Multiphysics Simulations with Spectral Element Methods:

Conjugate Heat Transfer, Fluid-Structure Interaction, and Acoustics

by

Yiqin Xu

A Dissertation Presented in Partial Fulfillment
of the Requirements for the Degree
Doctor of Philosophy

Approved July 2021 by the
Graduate Supervisory Committee:

Yulia T. Peet, Chair
Huei-Ping Huang
Marcus Herrmann
Ronald Adrian
Steven Baer

ARIZONA STATE UNIVERSITY

August 2021

ABSTRACT

Realistic engineering, physical and biological systems are very complex in nature, and their response and performance are governed by multitude of interacting processes. In computational modeling of these systems, the interactive response is most often ignored, and simplifications are made to model one or a few relevant phenomena as opposed to a complete set of interacting processes due to a complexity of integrative analysis. In this thesis, I will develop new high-order computational approaches that reduce the amount of simplifications and model the full response of a complex system by accounting for the interaction between different physical processes as required for an accurate description of the global system behavior. Specifically, I will develop multi-physics coupling techniques based on spectral-element methods for the simulations of such systems. I focus on three specific applications: fluid-structure interaction, conjugate heat transfer, and modeling of acoustic wave propagation in non-uniform media.

Fluid-structure interaction illustrates a complex system between a fluid and a solid, where a movable and deformable structure is surrounded by fluid flow, and its deformation caused by fluid affects the fluid flow interactively. To simulate this system, two coupling schemes are developed: 1) iterative implicit coupling, and 2) explicit coupling based on Robin-Neumann boundary conditions. A comprehensive verification strategy of the developed methodology is presented, including a comparison with benchmark flow solutions, h-, p- and temporal refinement studies. Simulation of a turbulent flow in a channel interacting with a compliant wall is attempted as well. Another problem I consider is when a solid is stationary, but a heat transfer occurs on the fluid-solid interface. To model this problem, a conjugate heat transfer framework is introduced. Validation of the framework, as well as studies of an interior thermal environment in a building regulated by an HVAC system with an on/off con-

trol model with precooling and multi-zone precooling strategies are presented. The final part of this thesis is devoted to modeling an interaction of acoustic waves with the fluid flow. The development of a spectral-element methodology for solution of Lighthills equation, and its application to a problem of leak detection in water pipes is presented.

ACKNOWLEDGMENTS

I would like to express my sincere gratitude to my dear adviser Dr. Yulia Peet for her trust, support and guidance for all these years. I still remember that it was Dr. Peet who trusted me with her only start-up when I had no way to go. And it was also Dr. Peet who always silently strives for our food and juice with her best so we could have fundings and computational resources of our own. Dr. Peet not only gave her brilliant thoughts and ideas in academic region which resolved my research difficulties many many times, she also acted like a lead from whom we could learn. Deep in my heart, I am very fortunate to be guided to the field I like to devote and raised up by Dr. Peet.

I express my deep appreciation to Dr. Huang, Dr. Herrmann, Dr. Adrian, Dr. Baer, Dr. Oswald, Dr. Peet and all my undergraduate school professors, especially Dr. Zhang, Dr. Song, Dr. Lu, for giving great lectures, and leading me to the ocean of knowledge. Without them, I would not be me.

I am very grateful to my wife, and my parents for their love.

TABLE OF CONTENTS

CHAPTER Page

CHAPTER Page

CHAPTER Page

LIST OF TABLES

Table Page

Table Page

Table Page

LIST OF FIGURES

Chapter 1

INTRODUCTION

In most fluid related realistic engineering, physical and biological systems, the governing equations or in other words the physical relations govern to the systems are not based on just one single physical phenomenon. It is more complex and coupled interaction between two or even more different governing equations which their coupled relation is hard to be stated as the whole physical relation is quite nonlinear and complex. One of the most common example of such fluid related complex system would be fluid-structural interaction. A situation where a tight interaction occurs between a fluid flow and a surrounding structure, the so called fluid-structure interaction (FSI) problem, is prevalent in many engineering and biological applications. One famous example of a destabilizing effect of the fluid-structure interaction is the failure of the Tacoma Narrows bridge (Billah and Scanlan (1991)), while many other examples can be found in aerospace (flutter of airplane wings (Livne (2018))), turbomachinery (turbine blade vibrations (Rao (2005))) and nuclear (fretting in nuclear reactors (Jones *et al.* (1985))) engineering. FSI effects can also be beneficial; for example, compliant surfaces can delay laminar-to-turbulent transition (Carpenter and Garrad (1985); Dixon *et al.* (1994)), and, perhaps, reduce skin friction drag (Gad-el-Hak (2002)). Fluid mechanics problems are mostly studied by its own governing equations solely and some of the physical problem are simplified by ignoring the interaction with structural mechanics. In most of the cases, it is reasonable enough to ignore the structural response as it is rigid and barely moves. But in some cases, it leads to a hard time understanding the integrative physical phenomenon. For example, stenotic flows are well studied by fluid mechanics simulations in DNS region

(Varghese *et al.* (2007a,b)). But whether the small motion from flexible vessel would cause the narrowing of the vessel or alter the flow structural in vivo condition should further be explained more when structural mechanics is coupled with fluid mechanics (Tang *et al.* (2003); Valencia and Baeza (2009)).

The problem of fluid-structure interaction is inevitably complex, featuring nonlinear interactions, tightly coupled multi-physical phenomena, and potential instabilities (Benjamin (1966)). Accurate numerical solution of the FSI problem, even in relatively simple situations, is thus increasingly challenging. In many of the applications, the flow that interacts with a deformable surface is in a turbulent regime, which makes the computation of the FSI problem even more complicated, due to a wide range length and time scales that need to be resolved. High-order methods, such as spectral-element methods (Deville *et al.* (2002)) and discontinuous Galerkin methods (Cockburn *et al.* (1991)), have proven to be accurate and efficient robust in application to scale-resolving simulations of turbulent flows (Wang *et al.* (2012)). Computational methodologies that achieve high rates of convergence in the presence of fluid-structure interactions would thus be increasingly useful to the engineering and physical communities.

There are only a few examples in the literature that are concerned with a numerical discretization of the FSI problem with high-order methods. The Refs of Pena and Prud'homme (2010); Baek and Karniadakis (2012) employ spectral-element methods in the FSI problem discretization, Froehle and Persson (2014) present an application of discontinuous Galerkin (DG) methods to a solution of the fluid-structure interaction problem involving compressible flows, Sheldon *et al.* (2016) use hybridizable DG methods in incompressible FSI (although only first- and second-order elements were employed in the fully coupled FSI test cases), while Verkaik *et al.* (2015) present an overlapping domain approach that couples low-order finite element meth-

ods in the vicinity of a deformable structure, with high-order spectral elements in a background mesh. One should also mention the work of Bazilevs *et al.* (2013) and references therein who use non-uniform rational B-spline isogeometric methods for fluid-structure interaction. While these developments have appeared, a strict verification of high-order convergence in the presence of complex multi-physics interactions remains a challenging task. Most of the researchers have resorted to a verification of the component solutions separately, such as only fluid or only solid. Thus, Yu *et al.* (2012) presents h/p-convergence of an elastostatics solid solver with spectral elements, while Dong and Yosibash (2009) shows both h/p- and temporal convergence of the corresponding elastodynamics solver. Several groups demonstrate h/p- and/or temporal convergence of their fluid components of the FSI solvers on stationary (Baek and Karniadakis (2011)) and deforming (Froehle and Persson (2014); Pena *et al.* (2012); Persson *et al.* (2009)) domains, Sheldon *et al.* (2016) presents a verification of h/p-convergence for both the fluid and the structural solvers separately using the method of manufactured solutions (MMS), while Verkaik *et al.* (2015) does not show any convergence studies.

Additional to the mass and momentum transfer of fluid-structure interaction, multi-physics problem also occurs in heat transfer. For example, in the cooling process of electronics, heat transfer not just should not only be considered within the electronics, it is also associated with fluid motion which makes the whole heat transfer process both convective and conductive. Thus a coupled heat transfer between fluid and solid should be properly simulated (Fedorov and Viskanta (2000); Toh *et al.* (2002)) for such study, which is also called conjugate heat transfer (CHT). Similar to FSI, the boundary conditions of the fluid-solid interface is solved through the thermal coupling of the two domains and the thermal boundary conditions between the interface is the continuity of heat flux and temperature. But differently, CHT approach

couples both fluid domain and solid domain and solves for the whole temperature field simultaneously developed in Patankar (1980) without any iterations. The solution of such coupled system has been developed from analytical expressions for certain problems (Perelman (1961); Siegel and Perlmutter (1963)) to one generalized expression for numerical simulations (Patankar (1980)). CHT simulations solving for velocity and temperature fields from one equation for the whole domain self satisfying the conjugate boundary conditions based on the expressions from Patankar (1980) have become a very powerful tool to simulate various multi-physics engineering problems which also provides certain simplicity for such multi-physics system rather than FSI. For example, CHT has been used for simulating engine combustion chamber (Li and Kong (2011)), microchannel heat sink for electronic packaging (Fedorov and Viskanta (2000)), and even for nuclear liquid metal-cooled reactor (Obabko *et al.* (2019)).

CHT has been developed in high-order methods (Obabko *et al.* (2019)), but it has not been widely used in HVAC simulation with the consideration of wall thickness coupled with high-order CFD. HVAC simulation are mostly done by low-order method for the fluid part. For example, multizone airflow models (Cetin *et al.* (2019); Wetter and Haugstetter (2006); Tabares-Velasco (2013)) assuming the air in each zone is well mixed (Chen (2009); Tian *et al.* (2017)). Such method is not CFD and it could not simulate any stratified flow distribution. Zhang and Chen (2007) uses CFD RANS model for simulating air distribution systems for aircraft carbins. Jahanbin and Semprini (2020) studied a room with air quality equipped with heat recovery ventilation using RNG $k-\epsilon$ model. Shan *et al.* (2019) uses RNG $k-\epsilon$ model to study full-scale room cooling where the thermal boundary condition is from experiments. Semprini *et al.* (2019) uses RNG $k-\epsilon$ model for simulating an office with fan coil. Nada *et al.* (2016) uses realizable $k-\epsilon$ model for steady-state results of a theater room. To be concluded, high-order CFD methods are not generally used for the huge

computational cost but without high-order methods, small-scale motion of fluid could not be resolved and the fidelity would be lowered.

Additional to the low-fidelity CFD tools used in building HVAC systems simulations, not many approaches have been made to couple the fluid part with the building envelope to have CHT simulation to obtain the wall surface temperatures. Cetin *et al.* (2019) coupled multizone airflow models with EnergyPlus. Pandey *et al.* (2021) couples EnergyPlus with ANSYS (realizable $k-\epsilon$ model). And Clarke *et al.* (1995); Nielsen and Trytvason (1998); Zhai *et al.* (2002); Zhai and Chen (2005) also shows the benefit of coupling CFD models with the building energy simulation tools to obtain the thermal information. However, building energy simulation tools is simplified model compared to energy equation which is also low in fidelity but high in saving cost. Buratti *et al.* (2017) couples CHT and $k-\epsilon$ model for a college classroom simulation and Ganesh *et al.* (2020) uses standard $k-\epsilon$ model for simulating indoor environment of an occupied office building. Thus, in this dissertation, we would fill in the gaps and apply high-order CFD tools combined with conjugate heat transfer for HVAC systems simulation for higher fidelity results.

Multiphysics simulations are not useful for physics-based problem. It is also useful for enhancing the computational capabilities. For example, flow-generated noise simulation is high in computational cost if solved in compressible code and one way to alleviate the burden is to couple acoustic analogy equation with Navier-Stokes equation (Wang *et al.* (2006); Khalighi *et al.* (2010)). The whole pressure field is decomposed into acoustic pressure and hydraulic pressure where the acoustic pressure is solved through Lighthill's equation and hydraulic pressure is solved in Navier-Stokes equation. Such methodology has been widely used in noise simulation but not in other applications, for example, pressure transients for leak detection. Computational Fluid Dynamics (CFD) analysis of pipe flows with leaks has been previously documented

(Ben-Mansour *et al.* (2012); Araujo *et al.* (2013); Lu *et al.* (2013); Shehaded and Shahata (2013); Reddy *et al.* (2016)), however these studies have not incorporated models of the pressure transients to study the performance of leak detection methods in conjunction with the CFD framework. Most of leak detection studies are using one-dimensional hydraulic equations (Liou (1998); Wang *et al.* (2002); Covas *et al.* (2005); Diao *et al.* (2019)). But researchers have found high-frequency and multi-path radial pressure waves should only be simulated in three-dimensional simulations (Brunone *et al.* (1995); Louati and Ghidaoui (2017); Che *et al.* (2018)). In Owowo and Oyadiji (2017), a finite element simulation of an acoustic wave propagation in a three-dimensional pipe model with rupture but without flow was presented, while Owowo (2016) has considered an application of an acoustic wave propagation method to a two-dimensional pipe flow using a commercial CFD code and a simplified model of leak as a vertical columnar extension without a fluid outflow. One purpose of this dissertation is to develop a three-dimensional (3D) modeling framework, based on a numerical solution of unsteady Navier-Stokes equations, coupled with a solution of an acoustic Lighthill's wave equation to model the dynamics of the pressure transient and its interaction with the fluid flow.

The objectives of my research are to first develop implicit and explicit fluid-structure coupling in spectral-element solver Nek5000 with its validation in spatial and temporal convergence and apply FSI approach for a turbulent channel with a compliant surface. Secondly, apply high-order CFD with conjugate heat transfer simulation to HVAC system with the consideration of the thickness and thermal contributions from the whole housing envelope. At last, develop high-order acoustic analogy equation solver in Nek5000 with its validation and apply such coupling for leak detection in a three-dimensional laminar pipe.

The dissertation would be structured as follows. In the second chapter, the

basics of spectral-element method would be introduced. In the third chapter, a newly developed implicit fluid-structure interaction coupling associated with nonlinear hyperelastic structural mechanics solver and implicit fluid solver with Arbitrary Lagrangian-Eulerian method would be presented with its validation. Additional to implicit fluid-structural interaction coupling, an explicit fluid-structure interaction based on Robin-Neumann boundary conditions would also be developed and presented for saving computational cost. It is further used in a simulation of a 3D turbulent channel with a compliant wall. In the fourth chapter, acoustic Lighthill's equation would be presented with its development and verification. An application for coupling such high-order acoustic solver in 3D pipe leak detection is presented. In the fifth chapter, conjugate heat transfer feature already developed in Nek5000 is used for a whole-housing HVAC system in regular cooling, whole-housing precooling and multi-zone precooling studies. And in the last chapter, summary, accomplishments of my work, and the future directions would be presented.

Chapter 2

SPECTRAL ELEMENT METHOD

In this chapter, a basic introduction to the spectral element method that our solver Nek5000 is based on, will be presented. Nek5000 has originally been developed by et al. (2016); Deville *et al.* (2002); Fischer (1997b). Similar to finite element method, spectral element method first introduced by A. Patera (1984) uses high-degree polynomials to have higher order accuracy than finite element method. The major difference would come from the choose of the basis functions. To begin with, let us first define the problem domain as Ω and let it decomposed into several elements subdomains as

$$\Omega \approx \bigcup_{e=1}^{n} \Omega^e, \tag{2.1}$$

where n and Ω^e denote to total number of elements and element subdomain. Since the domain may not be fully described by spectral element domain, thus approximation symbol is used instead of equivalence.

Also, same as Eq. (2.1), the domain boundary could also be decomposed correspondingly as

$$\Gamma \approx \bigcup_{e=1}^{n} \Gamma^e. \tag{2.2}$$

In each element, given the basis function π_i, any function u could be represented by

$$u(\xi) := \sum_{i=1}^{N} u_i^h \pi_i(\xi), \tag{2.3}$$

where i is the different basic polynomial function with its maximum degree N, u_i^h is its coefficients, and ξ is the coordinate in the reference domain $[-1, 1]$.

For example, if we are using linear element which contains two points in a domain $[2, 5]$, the polynomial basis would be

$$\begin{aligned} \pi_0(\xi) &= \frac{1-\xi}{2}, \\ \pi_1(\xi) &= \frac{1+\xi}{2}. \end{aligned} \tag{2.4}$$

The coefficient u_i^h would simply be the values on each element points which is

$$\begin{aligned} u_0^h &= 2, \\ u_1^h &= 5. \end{aligned} \tag{2.5}$$

If we want to know the value at reference domain 0, the results would be done by Eq. (2.3) as

$$u(0) := u_0^h \pi_i(0) + u_1^h \pi_1(0) = 2 * 0.5 + 5 * 0.5 = 3.5, \tag{2.6}$$

which is exactly the middle value of the domain $[2, 5]$. Similar to find other values in different locations by changing the coordinates in the reference domain.

As for the spectral element method, especially in Nek5000, the basis function would be (Deville *et al.* (2002))

$$\pi_i(\xi) = \frac{-1}{N(N+1)} \frac{(1-\xi^2) L_N^{'}(\xi)}{(\xi - \xi_i) L_N(\xi_i)}, \tag{2.7}$$

where ξ_i is the Gauss-Lobatto-Legendre (GLL) quadrature nodes on the reference domain $\hat{\Omega}$, L_N is the Legendre interpolation polynomial of order N and $L_N^{'}$ is its derivative.

Besides, GLL points could be acquired by solving

$$(1-\xi^2) L_N^{'}(\xi) = 0, \tag{2.8}$$

which is very different from finite element method since the quadrature nodes are explicit.

Additionally, the Legendre polynomial and its derivative could be solved by three-term recursion relationship (Deville *et al.* (2002)) as

$$\begin{aligned} &L_0(x) = 1, \\ &L_1(x) = x, \\ &(k+1)L_{k+1}(x) = (2k+1)xL_k(x) - kL_{k-1}(x), \quad k \geq 1, \\ &(2k+1)L_k(x) = L'_{k+1}(x) - L'_{k-1}(x), \quad k \geq 1. \end{aligned} \tag{2.9}$$

Also, as needs to be mentioned, coefficients u_i^h is usually be the grid points of finite element where at that point the summation of the basis function becomes 1, it is also the same here but here the location varies and they are not equally spaced which essentially based on the results of Eq. (2.7). With such basis function, the

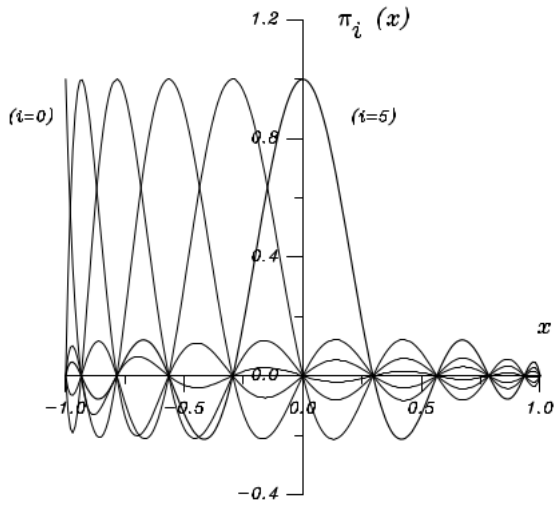

Figure 2.1: An Example of Legendre Spectral-element Basis Functions Corresponding to $n = 10$ from Deville *et al.* (2002).

derivative of one variable could also be represented by

$$\frac{\partial u(\xi)}{\partial x} = \sum_i^N u_i^h \frac{\partial \pi_i(\xi)}{\partial \xi} \frac{\partial \xi}{\partial x}, \tag{2.10}$$

where $\frac{\partial \xi}{\partial x}$ is usually called the inverse of the Jacobian matrix $J = [\frac{\partial x}{\partial \xi}]$. This is another advantage of using finite element based method that the derivative of a variable is

only related to its coefficients, since the derivative of a basis function is the same. The Jacobian of the geometry is also easy to acquired by applying the derivative of the basis function with the geometry. In this way, the derivative of a variable could be easily calculated.

In most of cases, an equation is not solved by its strong form for the boundary conditions are hard to be satisfied. While if using Galerkin method, a strong form equation could be converted to its weak form and the continuous problem could be converted to discrete problem. Besides, the boundary condition especially for Neumann boundary condition, it could be easily satisfied weakly. A weak form is usually got by multiplying a test function and integration over the domain. Thus, the integration could be performed by every decomposed elements as

$$\int_{\Omega} d\Omega = \sum_{e=1}^{n} \int_{\Omega^e} d\Omega. \tag{2.11}$$

Thus it brings to another important numerical method, numerical integration. It is stated as

$$\int_{\Omega^e} u(x)\ d\Omega = \sum_{j=0}^{N} u(\xi_j) W_j |J(\xi_j)|, \tag{2.12}$$

where W_j is the integration weight and $J(\xi_j)$ is the Jacobian as defined before. The numerical integration rule and the weight is calculated in the reference domain $\hat{\Omega}$, thus the Jacobian is only needs for changing the integration domain. In finite element method, the integration points should be picked by Gauss quadrature rule for numerical integration. The collocation points or we say the coefficients u_i^h is related to the basis functions. However, in spectral element method, the collocation points are the GLL points and we could also use the same for Gauss-Lobatto integration.

When we are using the test and trial functions for solving the weak form of one equation, between different elements, the derivative is not continuous for we have not made any effort on that. So they are only piecewise continuous. Plus the

integration capability, we would define a space of scalar-values functions that are square-integrable, $L^2(\Omega)$. Notice that piecewise continuous function in C^1 could not be integrable if contains second order derivative (Fish and Belytschko (2007)), thus integration by part to reduce one order of derivative is always being used.

Additionally to the solution solved by the weak form, since the test function is always vanishing on the Dirichlet boundary Γ_D, the solution would also be 0 on Γ_D. The reason why it vanishes on the essential boundary is for eliminating the extra terms appeared for integration by part. In that case, we would define another solution and test function space for a scalar function as

$$L_0^2(\Omega) := \left\{ q \middle| q \in L^2(\Omega), \int_\Omega q \; d\Omega = 0 \; if \; \Gamma = \Gamma_D \right\}, \tag{2.13}$$

which require the average of the field (pressure) over the domain Ω to be 0 if essential boundaries are all over the domain. The later constrain is not very to appear in normal simulation.

As for the velocity field, we would need a space of vector-valued functions with square-integrable derivatives. Same as the scalar space, the results on the Dirichlet would also be 0 as the vanishing of the test function. Thus, we would define it as

$$H_0^1(\Omega)^d := \left\{ u \middle| u \in H^1(\Omega)^d, u = 0 \; on \; \Gamma_D \right\}, \tag{2.14}$$

where d denotes the d components of the vector field such as 2 in 2D and 3 in 3D, and $H^1(\Omega)^d$ denotes to a Sobolev space with d components (Deville *et al.* (2002); Bazilevs *et al.* (2013)) defined as

$$H^1(\Omega)^d := \left\{ u \middle| u \in L^2(\Omega), \frac{du}{dx} \in L^2(\Omega) \right\}, \tag{2.15}$$

where $\frac{du}{dx}$ is the derivative of u. So, if using weak formulation, only 0 results would be acquired on the Dirichlet boundaries for the influence of the test function. Thus, the

equation calculated from the essential boundaries should be remained in the residual and the full solution should add the homogeneous part on the inhomogeneous part.

In Nek5000, as would be described in the later, there is another mesh option for pressure which is called $P_N - P_{N-2}$ (Deville *et al.* (2002)). It is a staggered mesh with spectral element method shown in Fig. (2.2). And the option for using the same mesh as the velocity field for pressure is called $P_N - P_N$.

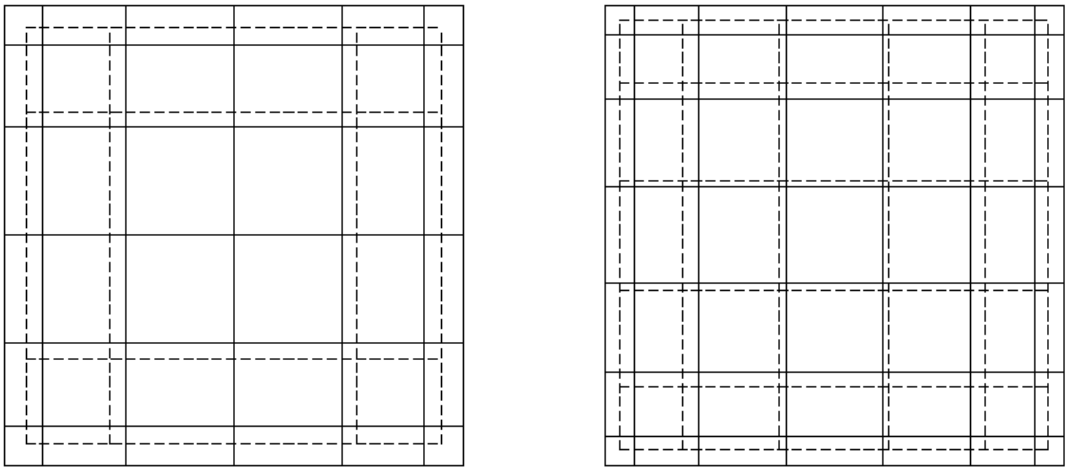

Figure 2.2: Staggered Spectral Element for N=6 (Left) and N=7 (Right) From Deville *et al.* (2002).

Chapter 3

FLUID-STRUCTURE INTERACTION

3.1 Introduction

This chapter presents a recently developed high-order in space computational methodology for a solution of the fluid-structure interaction problem, together with a comprehensive verification strategy demonstrating the high-order spatial accuracy and up to a second-order temporal accuracy of the approach. The methodology is based on a spectral-element implementation (Patera (1984)) of both the Navier-Stokes, and the solid mechanics equations, where a hyperelastic St. Venant-Kirchhoff material model is employed for the solid (Kim (2015); Holzapfel (2000)). The coupling between the fluid and solid components is performed in a partitioned manner, whereby a fixed point iteration (Küttler and Wall (2008)) with Aitken relaxation (Aitken (1926)) is employed to achieve a strong fluid-solid coupling. The fixed-point iteration with Aitken relaxation is not the state-of-the art method, and recent research has been devoted to a development of stable coupling methods with reduced amount of iterations. (see Ref. of Deparis *et al.* (2003); Badia *et al.* (2008), Degroote *et al.* (2009), and Yu *et al.* (2013); Banks *et al.* (2014)). In this chapter, explicit coupling based on Robin-Neumann boundary condition is also developed and presented.

A typical verification strategy of the FSI algorithms, apart from the component testing, is a simulation of a suite of accepted benchmark problems, one of which is a two-dimensional test case proposed by Turek and Hron (2006), where a flow-induced vibration of a flexible beam attached to a rigid circular cylinder is studied numerically. Another variant of a similar test problem exists where a circular cylinder is

replaced by a square cylinder (Wall and Ramm (1998)). In the absence of reliable experimental benchmarks for a fluid-structure interaction problem, the two aforementioned test cases have essentially taken a role of "validation experiments" in the FSI computational community, albeit the efforts to establish reliable experimental benchmarks for the FSI problems are underway (Dou *et al.* (2018)). While simulations on different levels of grid refinement are often performed with these two benchmarks (Sheldon *et al.* (2016); Verkaik *et al.* (2015); Turek and Hron (2006)), the verification of convergence rates is not demonstrated. Formaggia *et al.* (2001), as well as Bathe and Ledezma (2007), presented several three-dimensional computational test cases for the FSI problems, but, again, without demonstrating the formal rates of convergence. Fernández *et al.* (2015) used self-convergence studies with a finite-element method in a two-dimensional pressure-driven pipe flow with a flexible wall, while Banks *et al.* (2014) used both a method of manufactured solutions, as well as the traveling wave exact solutions of the 2D model FSI problems for the acoustic and linearly elastic solids to test their finite difference FSI code. Both studies were able to demonstrate a globally second-order spatial convergence on model FSI problems. A high-order convergence of the FSI methodologies on fully coupled FSI problems has not been demonstrated yet.

This chapter also presents a new three-dimensional computational benchmark, on which the convergence properties of the FSI algorithms can be studied. The benchmark is inspired by a problem of the interaction of compliant surfaces with the fluid flow (Gad-el-Hak *et al.* (1984); Kim and Choi (2014); Rosti and Brandt (2017)), and consists of a three-dimensional channel with one rigid and one flexible wall. We demonstrate the expected h/p-spatial convergence and the second order temporal convergence of the developed spectral-element FSI solver using this problem. Since the reference results are obtained with a high-order code on a well-resolved mesh,

these data can be used by the computational community to test the convergence rate of their FSI codes, both low- and high-order accurate. While the current fixed-point iteration fluid-solid coupling algorithm is fairly standard, it is nonetheless widely used in many commercial and research FSI codes, as the more efficient alternatives are hard to implement (Hou *et al.* (2012)). With a fixed-point iteration algorithm, the computational efficiency can always be achieved by increasing the solver tolerances. We demonstrate the effect of increasing the tolerances in both component and the coupling algorithms on the global computational errors. Additionally, we provide recommendations for acceptable tolerances with respect to their effect on the global errors. While convergence of the iterative algorithms in the FSI literature in terms of the iteration count has been studied extensively (Baek and Karniadakis (2012); Küttler and Wall (2008); Degroote *et al.* (2009)), the effect of these different strategies on errors has not been highlighted. The current chapter serves to fill this gap. At last, development and comparison between iterative fix-point iteration coupling and explicit Robin would be presented and we demonstrate the application of the developed high-order methodology to a Direct Numerical Simulation of a three-dimensional turbulent channel flow interacting with a hyperelastic solid wall, which shows the robustness of the methodology in the presence of the multiscale fluid-solid interactions.

3.2 Finite Strain Theory

Commonly, there are two frames of reference for specification of physical motion, `Eulerian` and `Lagrangian`. In the Lagrangian description, every parcel is labeled through time. It means that when the geometry is first described with certain parcels, the coordinate system is named by its initial set. As for the Eulerain description, only a certain domain of interest is specified. And usually the domain is fixed and bounded.

Lagrangian description is usually adapted to describing a structural deformation, since in an Eulerian formulation, where the domain is fixed, the bounds on the domain would be unknown to guarantee that it always contains the solid that can be significantly displaced from its original configuration. In addition, the grid points that are not currently within the structure would be wasted in an Eulerian formulation. On the contrary, Lagrangian description could easily track the location of material.

As for the fluid mechanics, it is possible to track every parcel within a certain domain but it is very hard or trivial to initially label the parcel from origin ready for inflow. Thus, Eulerian description is very commonly used for fluid problem to discard the inflow and outflow parcels with the focus on the flow in a certain domain. However, such domain is stationary. Thus, `Arbitrary Lagrangian-Eulerian Formulation` (`ALE`) (Hirt *et al.* (1997)) was proposed to help solving a fluid problem in a moving domain gathering the both benefit of two frames.

In problems that contain finite deformations, a linearly elastic approach for solid mechanics is not applicable and non-linear formulation is needed. As opposed to a linear elasticity approach, in the non-linear formulation, the Cauchy strain, or also called engineering strain (Fish and Belytschko (2007)), is not based on an infinitesimal strain assumption, thus allowing for large deformations.

In this section, preliminaries about nonlinear structural mechanics would be presented. Let two material domains of a structure be introduced first, Ω_0 and Ω_t. Ω_0 along with its boundary Γ_0 with subscription 0 is usually called initial domain, reference domain, or undeformed domain and Ω_t along with its boundary Γ_t with subscription t is called current domain, or deformed domain. It is not necessary for Ω_0 to be the very first geometry since every deformed domain could be undeformed relatively to the next time step.

Also, a very large globally Eulerian frame is concerned to describe the absolute

coordinates to simplify the description and thus the location of one parcel in initial domain could be described as $X(c_0)$ and the location in current domain could be described as $x(c_0)$. Here c_0 denotes the coordinate in the material Lagrangian frame and thus a displacement could be described as

$$d(c_0) = x(c_0) - X(c_0). \tag{3.1}$$

If every parcel has a unique mapping from Ω_0 to Ω_t continuously and differentiable, and thus an infinitesimal length dx in Ω_t could be described by dX in Ω_0 as

$$dx = \frac{\partial x}{\partial X} dX. \tag{3.2}$$

From Eqs. (3.1) and (3.2), and mapping assumption, deformation gradient F could be introduced as

$$F = \frac{\partial x}{\partial X} = I + \frac{\partial d}{\partial X} = I + \nabla_0 d, \tag{3.3}$$

where I is the identity matrix and $\nabla_0 = \frac{\partial}{\partial X}$ is taken on the initial domain. So, the length change could be derived as (Kim (2015))

$$\begin{aligned} ||dx||^2 - ||dX||^2 &= dx^T dx - dX^T dX \\ &= dX^T F^T F dX - dX^T dX \\ &= dX^T (F^T F - I) dX. \end{aligned} \tag{3.4}$$

Thus in finite strain theory, Green-Lagrange strain tensor to matched with engineering strain is defined as

$$E = \frac{1}{2}(F^T F - I) = \frac{1}{2}(\nabla_0 d + \nabla_0 d^T + \nabla_0 d^T \nabla_0 d), \tag{3.5}$$

which contains higher order term for rigid body motion and rotation.

Also, an integration domain change and surface area change could be expressed by

$$\begin{aligned} \int_{\Omega_t} d\Omega &= \int_{\Omega_0} J \; d\Omega, \\ \int_{\Gamma_t} n_t \; d\Gamma &= \int_{\Gamma_0} J F^{-T} n_0 \; d\Gamma, \end{aligned} \tag{3.6}$$

where n denotes the normal direction, and Jacobian $J = |F|$ denotes the determinant of deformation gradient F.

Same as strain and deformation analysis, stress description is also involved in undeformed geometry and deformed geometry. To start with, an assumption that a traction δf applied on a certain small area is not changing from undeformed to deformed area is made. So, the stress on the deformed geometry could be

$$\sigma \; n_t = \lim_{\delta\Gamma_t \to 0} \frac{\delta f}{\delta \Gamma_t}, \tag{3.7}$$

which is called Cauchy stress. And the stress on the undeformed geometry is

$$P^T \; n_0 = \lim_{\delta\Gamma_0 \to 0} \frac{\delta f}{\delta \Gamma_0}, \tag{3.8}$$

which is called first Piola-Kirchhoff stress. According to relation eqs. (3.6) to (3.8), the first Piola-Kirchhoff stress could be calculated the following

$$\begin{aligned} \delta f \; &= \delta f \\ \Rightarrow \sigma \; n_t \; \delta\Gamma_t \; &= P^T \; n_0 \; \Gamma_0 \\ \Rightarrow \sigma J F^{-T} \; n_0 \; \delta\Gamma_0 \; &= P^T \; n_0 \; \Gamma_0 \\ \Rightarrow \sigma J F^{-T} \; &= P^T \\ \Rightarrow P \; &= J F^{-1} \sigma^T = J F^{-1} \sigma, \end{aligned} \tag{3.9}$$

for σ is symmetric. However, first Piola-Kirchhoff stress P is not symmetric and to make it simpler to use, second Piola-Kirchhoff stress S is defined by

$$S = P F^{-T} = J F^{-1} \sigma F^{-T}, \tag{3.10}$$

which does not have specific physical meaning.

3.3 Governing Equations

The simulation domain $\Omega(t) \subset \mathbb{R}^3$ is decomposed into two separate nonoverlapping conforming subdomains $\Omega_s(t)$ and $\Omega_f(t)$, representing solid and fluid compo-

nents, with their respective Dirichlet and Neumann boundaries $\partial\Omega_{s_D}(t)$, $\partial\Omega_{s_N}(t)$ and $\partial\Omega_{f_D}(t)$, $\partial\Omega_{f_N}(t)$. Additionally, common boundary $\Gamma_{fsi}(t) = \Omega_s(t) \cap \Omega_f(t)$ denotes the interface between the solid and the fluid domains with a full connectivity. The remainder of this section presents a mathematical formulation a numerical discretization of the solid and fluid equations, and their coupling.

3.3.1 Nonlinear Structural Mechanics

A nonlinear elasticity formulation allows for finite-size deformations, as opposed to a linear elasticity approach, considered, e.g., in Peet and Fischer (2014). Nonlinearity can be introduced from a geometry, material properties, kinematics and force (Kim (2015); Holzapfel (2000)). Nonlinear solid equations in a strong form are written as

$$\rho_s \ddot{\mathbf{d}} = \nabla \cdot \sigma_s + \rho_s \mathbf{f} \text{ in } \Omega_s(t), \tag{3.11}$$

with the initial conditions

$$\begin{aligned} \mathbf{d}(\mathbf{x}, t = 0) &= \mathbf{d}_0(\mathbf{x}) \text{ in } \Omega_s(0), \\ \dot{\mathbf{d}}(\mathbf{x}, t = 0) &= \mathbf{v}_0(\mathbf{x}) \text{ in } \Omega_s(0), \\ \ddot{\mathbf{d}}(\mathbf{x}, t = 0) &= \mathbf{a}_0(\mathbf{x}) \text{ in } \Omega_s(0), \end{aligned} \tag{3.12}$$

and boundary conditions

$$\mathbf{d}(\mathbf{x}, t) = \mathbf{d}_D(\mathbf{x}, t) \text{ on } \partial\Omega_{s_D}(t), \tag{3.13}$$

$$\sigma_s(\mathbf{x}, t) \cdot \mathbf{n} = \mathbf{T}_N(x, t) \text{ on } \partial\Omega_{s_N}(t) \cup \Gamma_{fsi}(t), \tag{3.14}$$

where $\dot{\mathbf{d}}$, $\ddot{\mathbf{d}}$ denote the first and the second partial temporal derivatives of the displacement $\mathbf{d} = \{d_x, d_y, d_z\}$, σ is the Cauchy stress tensor, and $\mathbf{T} = \{T_x, T_y, T_z\}$ is the surface traction. To solve the equations (Eq. (3.11))–(Eq. (3.14)) in a spectral-element method, a weak form of Eq. (3.11) in a total Lagrangian formulation is stated

as: find $\mathbf{d} \in \mathcal{H}_0^1(\Omega_s)$, such that $\forall \mathbf{w} \in \mathcal{H}_0^1(\Omega_s)$,

$$\int_{\Omega_s(0)} \mathbf{w} \cdot \rho_{s(0)} \ddot{\mathbf{d}} \, \mathrm{d}\Omega + \int_{\Omega_s(0)} \nabla_0 \mathbf{w} : \mathbf{P} \, \mathrm{d}\Omega - \int_{\Omega_s(0)} \mathbf{w} \cdot \rho_{s(0)} \mathbf{f} \, \mathrm{d}\Omega - \int_{\Gamma_s(0)} \mathbf{w} \cdot \hat{\mathbf{T}} \, \mathrm{d}\Gamma = 0. \quad (3.15)$$

Here, $\mathcal{H}_0^1(\Omega_s)$ denotes the Sobolev space of vector functions, vanishing to zero on a Dirichlet boundary, the solid domain boundary surface is defined as $\Gamma_s(0) = \partial\Omega_{s_N}(0) \cup \partial\Omega_{s_D}(0) \cup \Gamma_{fsi}(0)$, $\rho_{s(0)}$ is the initial solid density, which, in general, is time-dependent, ∇_0 refers to a gradient operator taken with respect to an initial configuration, $\hat{\mathbf{T}}$ is the equivalent traction on the reference surface from the Nanson's formula (Bazilevs *et al.* (2013)), $\mathbf{P} = \mathbf{FS}$ is the first Piola-Kirchhoff stress, which could be expressed by the deformation gradient $\mathbf{F}$ and the second Piola-Kirchhoff stress $\mathbf{S}$. The terms in Eq. (3.15) are transferred to the initial domain $\Omega_s(0)$ using a large deformation theory (Kim (2015); Bathe (1996)) through a valid mapping from an undeformed material point $\mathbf{X}$ to a deformed point $\mathbf{x}$. Such deformation could be described by a deformation gradient as

$$\mathbf{F}(\mathbf{d}) = \frac{\partial \mathbf{x}}{\partial \mathbf{X}} = \mathbf{I} + \frac{\partial \mathbf{d}}{\partial \mathbf{X}} = \mathbf{I} + \nabla_0 \mathbf{d}. \quad (3.16)$$

Furthermore, the Green-Lagrange strain tensor matched with the engineering strain is defined as $\mathbf{E} = \frac{1}{2}(\mathbf{F}^T\mathbf{F} - \mathbf{I})$, and the determinant of the deformation gradient is $J = |\mathbf{F}|$, which indicates the volume change during the deformation.

St. Venant-Kirchhoff material Kim (2015); Holzapfel (2000) is used in this paper, which is an extension of the linear elasticity model that considers large deformations,

$$\mathbf{S} = \mathbf{D} : \mathbf{E}, \quad (3.17)$$

where $\mathbf{D}$ is a fourth-order stiffness tensor. For isotropic materials considered in the current paper, the stiffness tensor has only two independent material parameters λ_s and μ_s, and is written as

$$\mathbf{D} = \lambda_s \mathbf{I} \otimes \mathbf{I} + 2\,\mu_s \mathbf{I}_4, \quad (3.18)$$

where λ_s is the first Lame's coefficient, μ_s is the second Lame's coefficient (or shear modulus), $\mathbf{I}$ is the second-order identity tensor, $\otimes$ is the symbol for the tensor product, and $\mathbf{I}_4$ is the symmetric fourth-order identity tensor (Kim (2015)). Under the property of Eq. (3.18), Eq. (3.17) simplifies to

$$\mathbf{S} = \lambda_s \operatorname{tr}(\mathbf{E})\mathbf{I} + 2\mu_s\mathbf{E}. \tag{3.19}$$

3.3.2 Navier-Stokes ALE Formulation

Similar to non-linear structure mechanics, ALE formulation encounters deformed and undeformed geometry as well. Differently, the coordinate system is not Lagrangian but Eulerian only with a mesh movement. And the motion of the mesh is not necessarily following the fluid. To start with, the strong form of the incompressible flow for any t in a fixed Eulerian description is

$$\rho_f(\frac{\partial \mathbf{u}}{\partial t} + \mathbf{u}\cdot\nabla\mathbf{u} - \mathbf{f}) - \nabla\cdot\sigma = 0, \tag{3.20}$$

$$\nabla\cdot\mathbf{u} = 0, \tag{3.21}$$

where ρ_f, $\mathbf{u}$, $\mathbf{f}$ and $\sigma = -pI + \mu(\nabla\mathbf{u} + \nabla\mathbf{u}^T)$ are fluid density, velocity, body force, and Cauchy stress with pressure p and dynamic viscosity μ. Every derivative is taken when the geometry or interest domain is stationary. Using the same notation as structure mechanics, a reference domain Ω_0 and its motion is defined as $d(c_0) = x(c_0) - \hat{\mathbf{x}}(c_0)$ where x is the current domain Ω_t and $\hat{\mathbf{x}}$ is in the reference domain. The mapping is still conformal and differentiable. Since the motion of the frame is not taken into the consideration, the time derivative could not be evaluated well in the current domain for essentially $\frac{\partial \mathbf{u}}{\partial t}$ here is $\frac{\partial \mathbf{u}}{\partial t}\big|_x$. Like the total derivative $\frac{D}{Dt}$, the time derivative could be easily evaluated if calculated in a reference domain as

$$\left.\frac{\partial \mathbf{u}}{\partial t}\right|_{\hat{\mathbf{x}}} = \left.\frac{\partial \mathbf{u}}{\partial t}\right|_x + \frac{\partial \mathbf{u}}{\partial x}\frac{\partial x}{\partial t}, \tag{3.22}$$

and define a mesh velocity $\mathbf{w} = \left.\frac{\partial x}{\partial t}\right|_{\hat{\mathbf{x}}}$. Then rewrite Eq. (3.22)) with vector format same as Eq. (3.20) and rearrange as

$$\left.\frac{\partial \mathbf{u}}{\partial t}\right|_{x} = \left.\frac{\partial \mathbf{u}}{\partial t}\right|_{\hat{\mathbf{x}}} - \mathbf{w} \cdot \nabla \mathbf{u}. \tag{3.23}$$

Substitute the time derivative respect to current domain in Eq. (3.20), and take the incompressibility restrain in the Cauchy stress, the strong convective form of incompressible flow in ALE formulation would be

$$\rho_f(\left.\frac{\partial \mathbf{u}}{\partial t}\right|_{\hat{\mathbf{x}}} + (\mathbf{u} - \mathbf{w}) \cdot \nabla \mathbf{u} - \mathbf{f}) + \nabla p - \mu \Delta \mathbf{u} = 0 \text{ in } \Omega_f(t), \tag{3.24}$$

$$\nabla \cdot \mathbf{u} = 0 \text{ in } \Omega_f(t), \tag{3.25}$$

with the initial condition

$$\mathbf{u}(\mathbf{x}, t = 0) = \mathbf{u}_0(\mathbf{x}) \text{ in } \Omega_f(0), \tag{3.26}$$

and boundary conditions

$$\mathbf{u}(\mathbf{x}, t) = \mathbf{u}_D(\mathbf{x}, t) \text{ on } \partial\Omega_{f_D}(t) \cup \Gamma_{fsi}(t), \tag{3.27}$$

$$\nabla \mathbf{u}(\mathbf{x}, t) \cdot \mathbf{n} = 0 \text{ on } \partial\Omega_{f_N}(t), \tag{3.28}$$

where ρ_f, $\mathbf{u} = \{u_x, u_y, u_z\}$, $\mathbf{f} = \{f_x, f_y, f_z\}$, p, μ and $\mathbf{w} = \{w_x, w_y, w_z\}$ are the fluid density, velocity, external force, pressure, dynamic viscosity and the mesh velocity, respectively, while $\mathbf{n}$ is the outward-pointing unit vector normal to the surface. With the ALE formulation, the current configuration $\Omega_f(t)$ is defined through an ALE map, $\mathcal{A}_t$,

$$\mathcal{A}_t : \Omega_f(0) \in \mathbf{R}^d \rightarrow \Omega_f(t) \in \mathbf{R}^d, \ \mathbf{x}(\hat{\mathbf{x}}, t) = \mathcal{A}_t(\hat{\mathbf{x}}), \tag{3.29}$$

where d is the number of dimensions, which maps a reference configuration $\Omega_f(0)$ to a current configuration $\Omega_f(t)$,while associating the point $\hat{\mathbf{x}} \in \Omega_f(0)$ with the point $\mathbf{x}(\hat{\mathbf{x}}, t) \in \Omega_f(t)$ (Pena *et al.* (2012); Merrill and Peet (2019); Formaggia and Nobile (2004)). The ALE derivative in Eq. (3.24), $\left.\frac{\partial}{\partial t}\right|_{\hat{\mathbf{x}}}$, denotes the derivative with respect to time in the reference fluid domain $\Omega_f(0)$. The mesh velocity $\hat{\mathbf{w}}(\hat{\mathbf{x}}, t)$ with respect to a reference domain is defined as

$$\hat{\mathbf{w}}(\hat{\mathbf{x}}, t) = \left.\frac{\partial \mathbf{x}}{\partial t}\right|_{\hat{\mathbf{x}}}. \tag{3.30}$$

In the current formulation, the mesh velocity field $\hat{\mathbf{w}}(\hat{\mathbf{x}}, t)$ is obtained at each time instance t via a solution of a steady linear elastic equation (Deville *et al.* (2002); Peet and Fischer (2014))

$$\operatorname{div}\left(\lambda_e \operatorname{tr}(\boldsymbol{\epsilon})\,\mathbf{I} + 2\mu_e\,\boldsymbol{\epsilon}\right) = 0, \tag{3.31}$$

where

$$\boldsymbol{\epsilon} = \frac{1}{2}\left[\nabla\hat{\mathbf{w}} + \nabla(\hat{\mathbf{w}})^T\right], \tag{3.32}$$

λ_e, μ_e are user-defined elastic parameters, satisfying boundary conditions $\hat{\mathbf{w}}(\hat{\mathbf{x}}, t) = \hat{\mathbf{w}}_{int}(\hat{\mathbf{x}}, t)$ on the moving mesh boundary, $\Gamma_{fsi}(0)$, and $\hat{\mathbf{w}}(\hat{\mathbf{x}}, t) = 0$ on the other domain boundaries, such as inflow $\partial\Omega_{f_D}(0)$ and outflow $\partial\Omega_{f_N}(0)$. The mesh velocity $\hat{\mathbf{w}}(\hat{\mathbf{x}}, t)$ can be transformed into the current domain $\Omega_f(t)$ with the help of an inverse ALE map as

$$\mathbf{w}(\mathbf{x}, t) = \hat{\mathbf{w}}\left(\mathcal{A}_t^{-1}(\mathbf{x}), t\right) \text{ in } \Omega_f(t). \tag{3.33}$$

Note that, due to a no-slip condition at the solid boundaries of the fluid domain, including the fluid-structure interface, the mesh velocity $\mathbf{w}(\mathbf{x}, t)$ at the FSI interface $\Gamma_{fsi}(t)$ also represents the boundary condition for the fluid velocity in Eq. (3.27),

$$\mathbf{u}_D(\mathbf{x}, t) = \mathbf{w}(\mathbf{x}, t),\ \mathbf{x} \in \Gamma_{fsi}(t). \tag{3.34}$$

In the present work, a conservative formulation of the weak form of Eq. (3.24) and Eq. (3.25) is considered, which is stated as: find $\mathbf{u} \in \mathcal{H}_0^1(\Omega_f)$ and $p \in \mathcal{L}_0^2(\Omega_f)$ such that $\forall \mathbf{v} \in \mathcal{H}_0^1(\Omega_f)$ and $\forall q \in \mathcal{L}_0^2(\Omega_f)$,

$$\begin{aligned} &\frac{\partial}{\partial t}\int_{\Omega_f(t)} \mathbf{v}\cdot\rho_f\mathbf{u}\,\mathrm{d}\Omega + \int_{\Omega_f(t)} \mathbf{v}\cdot\rho_f[\mathbf{u}\cdot\nabla\mathbf{u} - \nabla\cdot(\mathbf{u}\,\mathbf{w}) - \mathbf{f}]\,\mathrm{d}\Omega \\ &- \int_{\Omega_f(t)} \nabla\mathbf{v}\cdot p\,\mathrm{d}\Omega + \int_{\Omega_f(t)} \mu\nabla\mathbf{v}:\nabla\mathbf{u}\,\mathrm{d}\Omega - \int_{\Gamma_f(t)} \mathbf{v}\cdot(\mu\nabla\mathbf{u} - p)\mathbf{n}\,\mathrm{d}\Gamma = 0, \end{aligned} \tag{3.35}$$

$$\int_{\Omega_f(t)} q\cdot\nabla\mathbf{u}\,\mathrm{d}\Omega = 0. \tag{3.36}$$

Here $\mathcal{H}_0^1(\Omega_f)$ denotes the Sobolev space of vector functions, vanishing to zero on a Dirichlet boundary, and $\mathcal{L}_0^2(\Omega_f)$ denotes the Hilbert space of vector functions that are square-integrable and have a zero mean value over the essential (pressure) boundary. $\Omega_f(t)$ and $\Gamma_f(t) = \partial\Omega_{f_D}(t) \cup \partial\Omega_{f_N}(t) \cup \Gamma_{fsi}(t)$ refer to a fluid current integration domain and its boundary surface, respectively. Further details, including the derivation of the conservative ALE formulation, can be found, for example, in Merrill and Peet (2019); Formaggia and Nobile (2004).

3.3.3 Fluid-Structure Interaction

In a fluid-structure interaction problem, the solution of the solid and fluid equations is coupled through appropriate boundary conditions, which can be stated as

$$\mathbf{u}_D(\mathbf{x},t) = \dot{\mathbf{d}}(\mathbf{x},t) \text{ on } \Gamma_{fsi}(t), \tag{3.37}$$

$$\sigma_s(\mathbf{x},t)\cdot(-\mathbf{n}_s) = \sigma_f(\mathbf{x},t)\cdot\mathbf{n}_f \text{ on } \Gamma_{fsi}(t). \tag{3.38}$$

Here, σ_s is the Cauchy stress tensor of the solid, see Eq. (3.11), Eq. (3.14), and σ_f is the Cauchy stress tensor of the fluid defined as

$$\sigma_f(\mathbf{x},t) = -p\mathbf{I} + \mu\left(\nabla\mathbf{u} + (\nabla\mathbf{u})^T\right), \tag{3.39}$$

and the outward unit surface normal vectors $\mathbf{n}_s$ and $\mathbf{n}_f$ for the solid and the fluid domains defined on the $\Gamma_{fsi}(t)$ boundary are pointing in opposite directions. The first boundary condition, Eq. (3.37), represents the kinematic constraint that the velocity on the interface $\Gamma_{fsi}(t)$ should be same in the fluid and the solid domains, and the second boundary condition, Eq. (3.38), reflects the continuity of the traction force across the interface.

Implicit fluid-structure coupling in a partitioned manner is accomplished via a Dirichlet-Neumann approach, where the fluid uses velocity provided by the solid solution at the FSI interface as the Dirichlet boundary conditions, and the solid employs the traction supplied by the fluid as the Neumann boundary conditions, as reflected in Eq. (3.14), Eq. (3.27). While explicit fluid-structure coupling is accomplished via Robin-Neumann approach which the details would be presented in Sec. (3.8).

3.4 Numerical Method

3.4.1 Temporal Discretization

The current section describes the temporal discretization of the ALE fluid equations and the nonlinear solid mechanics equations. Both solid and fluid domains are discretized with the second-order methods. For the solid equations which contain the second order temporal derivative, a Newmark β-method with a constant average acceleration is employed (Newmark (1959)), which is a second-order accurate implicit method commonly used for the time discretization of the structural dynamics equations (Bathe (1996)). For the fluid equations, a second-order accurate backward-differentiation scheme (BDF2) is employed (Deville *et al.* (2002); Merrill and Peet (2019)). The rest of this section provides the details of the two discretization schemes and the iteration procedures.

Solid Temporal Discretization

A. Newmark β method For the solid temporal discretization, we employ the Newmark β scheme (Newmark (1959)) with the parameters $(\beta, \gamma) = (0.25, 0.5)$, also known as a constant average acceleration method, wherein the velocity and acceleration at time step $n+1$ can be expressed through the unknown displacements $\mathbf{d}^{n+1}$ as

$$\begin{aligned} \dot{\mathbf{d}}^{n+1} &= \frac{2}{\delta t}\left(\mathbf{d}^{n+1} - \mathbf{d}^{n}\right) - \dot{\mathbf{d}}^{n}, \\ \ddot{\mathbf{d}}^{n+1} &= \frac{4}{\delta t^2}(\mathbf{d}^{n+1} - \mathbf{d}^{n}) - \frac{4}{\delta t}\,\dot{\mathbf{d}}^{n} - \ddot{\mathbf{d}}^{n}, \end{aligned} \tag{3.40}$$

where δt is the time step. For $(\beta, \gamma) = (0.25, 0.5)$, the Newmark scheme is second-order accurate and unconditionally stable under linear analysis. As in Dong and Yosibash (2009), we have found this scheme to be stable with spectral-element discretization for the nonlinear structural dynamics problems simulated. When these expressions are substituted into the structural dynamics equation, Eq. (3.15), it becomes a nonlinear equation for displacement $\mathbf{d}^{n+1}$, which can be solved iteratively.

B. Newton-Raphson iterative procedure To solve the nonlinear structural dynamics equation for displacements $\mathbf{d}^{n+1}$ with the implicit Newmark method, a Newton-Raphson iterative procedure (Bazilevs *et al.* (2013); Bathe (1996); Xu and Peet (2021a, 2017)) will be used. Instead of solving Eq. (3.15) directly, we solve for the increment of the displacement $\delta\mathbf{d}_{i+1}^{n+1}$ at each iteration $i+1$ at a time step $n+1$, i.e. we define $\delta\mathbf{d}_{i+1}^{n+1} = \mathbf{d}_{i+1}^{n+1} - \mathbf{d}_{i}^{n+1}$, and use linearization of Eq. (3.15) as

$$\left.\frac{\partial \mathbf{N}}{\partial \mathbf{d}}\right|_{\mathbf{d}_i^{n+1}} \delta\mathbf{d}_{i+1}^{n+1} = -\mathbf{N}(\mathbf{d}_i^{n+1}), \tag{3.41}$$

where $\mathbf{N}(\mathbf{d}_i^{n+1})$ is the left-hand side of Eq. (3.15) evaluated at the previously known displacement $\mathbf{d}_i^{n+1}$, and the Jacobian matrix $(\partial\mathbf{N}/\partial\mathbf{d})\big|_{\mathbf{d}_i^{n+1}}$ is evaluated by solving

the equation (Kim (2015))

$$\left.\frac{\partial \mathbf{N}}{\partial \mathbf{d}}\right|_{\mathbf{d}_i^{n+1}} \delta\mathbf{d}_{i+1}^{n+1} = \left.\frac{\partial}{\partial\epsilon}\mathbf{N}(\mathbf{d}_i^{n+1} + \epsilon\delta\mathbf{d}_{i+1}^{n+1})\right|_{\epsilon=0}. \tag{3.42}$$

Setting the initial value $\mathbf{d}_0^{n+1}$ to be equal to a converged value of the displacement $\mathbf{d}^n$ from the previous time step, and after a linearization using Eq. (3.41) and Eq. (3.42), a nonlinear structural dynamic equation, Eq. (3.15), can then be solved as

$$\begin{aligned}(\frac{4\mathbf{M}}{\delta t^2} + \mathbf{K})\ \delta\mathbf{d}_{i+1}^{n+1} &= \int_{\Omega_s(0)} \mathbf{w}\cdot\rho_{s(0)}\mathbf{f}^{n+1}\ \mathrm{d}\Omega + \int_{\Gamma_s(0)} \mathbf{w}\cdot\hat{\mathbf{T}}^{n+1}\ \mathrm{d}\Gamma \\ - \int_{\Omega_s(0)} \mathbf{S}_i^{n+1} : \bar{\mathbf{E}}_i^{n+1}\ \mathrm{d}\Omega &- \mathbf{M}[\frac{4}{\delta t^2}(\mathbf{d}_i^{n+1} - \mathbf{d}^n) + \frac{4}{\delta t}\dot{\mathbf{d}}^n - \ddot{\mathbf{d}}^n],\end{aligned} \tag{3.43}$$

with the mass matrix $\mathbf{M}$, stiffness matrix $\mathbf{K}$, and the other corresponding matrices defined as

$$\begin{aligned}\mathbf{M}\delta\mathbf{d}_{i+1}^{n+1} &= \int_{\Omega_s(0)} \mathbf{w}\cdot\rho_{s(0)}\delta\mathbf{d}_{i+1}^{n+1}\ \mathrm{d}\Omega, \\ \mathbf{K}\delta\mathbf{d}_{i+1}^{n+1} &= \int_{\Omega_s(0)} (\delta\mathbf{S}_{i+1}^{n+1} : \bar{\mathbf{E}}_i^{n+1} + \mathbf{S}_i^{n+1} : \delta\bar{\mathbf{E}}_{i+1}^{n+1})\ \mathrm{d}\Omega, \\ \mathbf{S}_i^{n+1} &= \mathbf{D} : \mathbf{E}_i^{n+1}, \\ \bar{\mathbf{E}}_i^{n+1} &= \frac{1}{2}[\nabla_0\mathbf{w}^T\mathbf{F}(\mathbf{d}_i^{n+1}) + (\nabla_0\mathbf{w}^T\mathbf{F}(\mathbf{d}_i^{n+1}))^T], \\ \delta\mathbf{S}_{i+1}^{n+1} &= \mathbf{D} : \delta\mathbf{E} = \mathbf{D} : \frac{1}{2}[\nabla_0(\delta\mathbf{d}_i^{n+1})^T\mathbf{F}(\mathbf{d}_i^{n+1}) + (\nabla_0(\delta\mathbf{d}_i^{n+1})^T\mathbf{F}(\mathbf{d}_i^{n+1}))^T], \\ \delta\bar{\mathbf{E}}_{i+1}^{n+1} &= \frac{1}{2}[\nabla_0\mathbf{w}^T\nabla_0\delta\mathbf{d}_{i+1}^{n+1} + (\nabla_0\mathbf{w}^T\nabla_0\delta\mathbf{d}_{i+1}^{n+1})^T].\end{aligned} \tag{3.44}$$

Once the increment of the displacement $\delta\mathbf{d}_{i+1}^{n+1}$ is obtained via solving Eq. (3.43) with the preconditioned conjugate gradient method (PCG), where the inverse of a spectral-element mass matrix is used as a preconditioner (mass matrix is diagonal in spectral elements), the solid displacement field can be updated as $\mathbf{d}_{i+1}^{n+1} = \mathbf{d}_i^{n+1} + \delta\mathbf{d}_{i+1}^{n+1}$. The iteration process is terminated when $\kappa_{s,\,i+1} = \left\|\delta\mathbf{d}_{i+1}^{n+1}\right\|_2 / \left\|\mathbf{d}_i^{n+1}\right\|_2$ reaches a prescribed tolerance value κ_s. The value of the solid solver tolerance $\kappa_s = 10^{-12}$ is used in all the test cases in the current paper. Solid equations manifest good convergence properties,

which permits such a tight tolerance to be set without affecting the overall solver cost. Note that the unknown surface traction $\hat{\mathbf{T}}^{n+1}$ at the FSI interface is provided by the solution of the fluid equations, and is updated implicitly during the partitioned fixed-point iteration coupling approach as discussed in Sec. (3.4.3).

Fluid Temporal Discretization

A. Backward-differentiation scheme A backward-differentiaion scheme of the second-order accuracy (BDF2) is used for the temporal discretization of the fluid equations. Applying BDF2 to Eq. (3.35) and Eq. (3.36) while denoting the current unknown time step with the superscript $n+1$ and the time step size as δt, transforms the fluid equations into the following semi-discrete form

$$\begin{aligned}
&\frac{3}{2\delta t}\int_{\Omega_f(t^{n+1})} \mathbf{v}\cdot\rho_f\mathbf{u}^{n+1}\ \mathrm{d}\Omega - \frac{2}{\delta t}\int_{\Omega_f(t^{n})} \mathbf{v}\cdot\rho_f\mathbf{u}^{n}\ \mathrm{d}\Omega + \frac{1}{2\delta t}\int_{\Omega_f(t^{n-1})} \mathbf{v}\cdot\rho_f\mathbf{u}^{n-1}\ \mathrm{d}\Omega \\
&= -\int_{\Omega_f(t^{n+1})} \mu\nabla\mathbf{v} : \nabla\mathbf{u}^{n+1}\ \mathrm{d}\Omega - \int_{\Omega_f(t^{n+1})} \mathbf{v}\cdot\rho_f(\mathbf{u}^{n+1}\cdot\nabla\mathbf{u}^{n+1})\ \mathrm{d}\Omega + \\
&\int_{\Omega_f(t^{n+1})} \mathbf{v}\cdot\rho_f\mathbf{f}^{n+1}\ \mathrm{d}\Omega + \int_{\Omega_f(t^{n+1})} \nabla\mathbf{v}\cdot p^{n+1}\ \mathrm{d}\Omega + \int_{\Gamma_f(t^{n+1})} \mathbf{v}\cdot(\mu\nabla\mathbf{u}^{n+1} - p^{n+1})\mathbf{n}\ \mathrm{d}\Gamma \\
&+ \int_{\Omega_f(t^{n+1})} \mathbf{v}\cdot\rho_f[\nabla\cdot(\mathbf{u}^{n+1}\mathbf{w}^{n+1})]\ \mathrm{d}\Omega,
\end{aligned} \tag{3.45}$$

$$\int_{\Omega_f(t^{n+1})} q\cdot\nabla\mathbf{u}^{n+1}\ \mathrm{d}\Omega = 0. \tag{3.46}$$

B. ALE geometry update Note that in this, implicit, formulation, the Eq. (3.45) and Eq. (3.46) are solved in the current, updated configuration $\Omega_f(t^{n+1})$, associated with the current ALE map $\mathcal{A}_t^{n+1}(\hat{\mathbf{x}})$. Since the ALE map is closely linked to the mesh velocity via Eq. (3.30), a temporal discretization of the evolution equation, Eq. (3.30), would define the temporal discretization of the ALE map, which can, in principle, be decoupled from the temporal discretization of the governing fluid equations, Eq. (3.45)

and Eq. (3.46). One obvious choice for a temporal discretization of Eq. (3.30) would be to use the BDF scheme of the same order as the discretization of the governing fluid equations, i.e. BDF2, as is done, for example, in stand-alone ALE developments (Pena *et al.* (2012); Patel *et al.* (2019)). However, in a fluid-structure interaction problem, the fluid geometry update should match the solid geometry update, otherwise there would be a discontinuity in the interface position which is undesirable. With the current constant average acceleration Newmark method for the solid discretization, it is seen from Eq. (3.40) that the solid geometry update

$$\mathbf{d}^{n+1} = \mathbf{d}^n + \frac{\delta t}{2}(\dot{\mathbf{d}}^{n+1} + \dot{\mathbf{d}}^n) \tag{3.47}$$

is essentially equivalent to a semi-implicit trapezoidal (or Crank-Nicholson) scheme. To match this update, we have explored two possibilities for the ALE map discretization:

1. First-order implicit Euler (IE) update: IE-ALE scheme,

$$\mathcal{A}_t^{n+1}(\hat{\mathbf{x}}) = \mathcal{A}_t^n(\hat{\mathbf{x}}) + \hat{\mathbf{w}}^{n+1}(\hat{\mathbf{x}})\,\delta\, t. \tag{3.48}$$

   To match the solid and fluid displacement at the FSI boundary, the FSI interface velocity for the time interval $[t^n, t^{n+1}]$ is defined as

$$\hat{\mathbf{w}}_{int}^{n+1}(\hat{\mathbf{x}}) = \frac{1}{2}\left[\dot{\mathbf{d}}^{n+1}(\hat{\mathbf{x}}) + \dot{\mathbf{d}}^n(\hat{\mathbf{x}})\right] \in \Gamma_{fsi}(0), \tag{3.49}$$

   which is equivalent to approximating the integral

   $\hat{\mathbf{w}}_{int}^{n+1}(\hat{\mathbf{x}})\,\delta\, t = \int_{t^n}^{t^{n+1}} \dot{\mathbf{d}}(\hat{\mathbf{x}}, t)\, dt,\ \hat{\mathbf{x}} \in \Gamma_{fsi}(0)$, with the trapezoidal rule.

2. Second-order semi-implicit (Crank-Nicholson) update: CN-ALE scheme,

$$\mathcal{A}_t^{n+1}(\hat{\mathbf{x}}) = \mathcal{A}_t^n(\hat{\mathbf{x}}) + \frac{\delta t}{2}\left[\hat{\mathbf{w}}^{n+1}(\hat{\mathbf{x}}) + \hat{\mathbf{w}}^n(\hat{\mathbf{x}})\right], \tag{3.50}$$

where the mesh velocity at the interface $\hat{\mathbf{w}}_{int}^{n+1}(\hat{\mathbf{x}})$ is set equal to the corresponding structure velocity at a time step t^{n+1} from the solid solver:

$$\hat{\mathbf{w}}_{int}^{n+1}(\hat{\mathbf{x}}) = \dot{\mathbf{d}}^{n+1}(\hat{\mathbf{x}}),\ \hat{\mathbf{x}} \in \Gamma_{fsi}(0). \tag{3.51}$$

In both methods, after the FSI interface velocity conditions are set up by Eq. (3.49) or Eq. (3.51), the ALE mesh velocity $\hat{\mathbf{w}}^{n+1}(\hat{\mathbf{x}})$ in the entire domain is obtained via a solution of an elastic equation, Eq. (3.31), with the boundary conditions $\hat{\mathbf{w}}^{n+1}(\hat{\mathbf{x}}) = \hat{\mathbf{w}}_{int}^{n+1}(\hat{\mathbf{x}})\,\text{on}\Gamma_{fsi}\,(0)$. Upon updating the ALE configuration via Eq. (3.48) or Eq. (3.50), the mesh velocity in the current configuration $\Omega_f(t^{n+1})$ used in Eq. (3.45) is obtained as

$$\mathbf{w}^{n+1}(\mathbf{x}) = \hat{\mathbf{w}}^{n+1} \circ \left(\mathcal{A}_t^{-1}(\mathbf{x})\right)^{n+1}. \tag{3.52}$$

C. Geometric conservation law Note that the BDF2 scheme applied to a conservative formulation of the ALE equations, Eq. (3.45), does not satisfy the geometric conservation law (GCL) (Formaggia and Nobile (2004)), which means that it can not reproduce a constant solution exactly. The role of GCL with respect to the accuracy and stability of numerical schemes on moving grids was investigated extensively in, e.g. Formaggia and Nobile (2004); Thomas and Lombard (1979); Guillard and Farhat (2000); Geuzaine *et al.* (2000). It was shown in Formaggia and Nobile (2004); Geuzaine *et al.* (2000) that, in general, a satisfaction of the GCL is neither a necessary nor sufficient condition for either accuracy or stability. However, in some situations, depending on a particular numerical scheme, GCL might be required to ensure certain numerical properties. For example, as shown in Formaggia and Nobile (2004), a BDF2 scheme that does not satisfy the GCL law can achieve only first order time-accuracy if the ALE mesh geometry is updated linearly in time (as with Eq. (3.48)). It is, however, fairly straightforward to modify the BDF2 scheme

given by Eq. (3.45))–Eq. (3.46), so that the Geometric Conservation Law is satisfied (Formaggia and Nobile (2004); Koobus and Farhat (1999)), as

$$\begin{aligned}
&\frac{3}{2\delta t}\int_{\Omega_f(t^{n+1})} \mathbf{v}\cdot\rho_f\mathbf{u}^{n+1}\,\mathrm{d}\Omega - \frac{2}{\delta t}\int_{\Omega_f(t^{n})} \mathbf{v}\cdot\rho_f\mathbf{u}^{n}\,\mathrm{d}\Omega + \frac{1}{2\delta t}\int_{\Omega_f(t^{n-1})} \mathbf{v}\cdot\rho_f\mathbf{u}^{n-1}\,\mathrm{d}\Omega \\
&= -\int_{\Omega_f(t^{n+1})} \mu\nabla\mathbf{v}:\nabla\mathbf{u}^{n+1}\,\mathrm{d}\Omega - \int_{\Omega_f(t^{n+1})} \mathbf{v}\cdot\rho_f(\mathbf{u}^{n+1}\cdot\nabla\mathbf{u}^{n+1})\,\mathrm{d}\Omega + \\
&\int_{\Omega_f(t^{n+1})} \mathbf{v}\cdot\rho_f\mathbf{f}^{n+1}\,\mathrm{d}\Omega + \int_{\Omega_f(t^{n+1})} \nabla\mathbf{v}\cdot p^{n+1}\,\mathrm{d}\Omega + \int_{\Gamma_f(t^{n+1})} \mathbf{v}\cdot(\mu\nabla\mathbf{u}^{n+1} - p^{n+1})\mathbf{n}\,\mathrm{d}\Gamma \\
&+ \frac{3}{2}\int_{\Omega_f(t^{n+1})} \mathbf{v}\cdot\rho_f[\nabla\cdot(\mathbf{u}^{n+1}\mathbf{w}^{n+1})]\,\mathrm{d}\Omega - \frac{1}{2}\int_{\Omega_f(t^{n})} \mathbf{v}\cdot\rho_f[\nabla\cdot(\mathbf{u}^{n+1}\mathbf{w}^{n})]\,\mathrm{d}\Omega,
\end{aligned} \tag{3.53}$$

$$\int_{\Omega_f(t^{n+1})} q\cdot\nabla\mathbf{u}^{n+1}\,\mathrm{d}\Omega = 0. \tag{3.54}$$

It was shown in Formaggia and Nobile (2004) that, for a model linear advection-diffusion equation discretized with finite-element methods, the GCL-satisfying BDF2 scheme in the form of Eq. (3.53) was able to attain a second-order temporal accuracy even with the linear in time ALE mesh update. Note that, with the ALE mesh interpolation scheme of order higher than one, satisfaction of the GCL is, in general, not necessary for achieving a global second-order temporal accuracy on moving meshes, as was the case, for example, in stand-alone ALE formulations (no FSI) (Pena *et al.* (2012); Patel *et al.* (2019)), where the ALE geometry was updated with the BDF scheme of the same order as used for the discretization of the Navier-Stokes equations. While the behavior of the BDF2 schemes with the Crank-Nicholson (CN) type geometry update (see Eq. (3.50)) was not previously analyzed, the current numerical experiments show that, as expected, the GCL law is not necessary with the CN mesh update for achieving a global second-order time accuracy on moving grids on an example of a convecting eddy viscous flow solution. Consequently, the GCL BDF2 scheme, Eq. (3.53), is used with the first-order IE-ALE geometry update, and the

no-GCL BDF2 scheme, Eq. (3.45), is used with the second-order CN-ALE geometry update.

D. Sub-iteration method This section deals with the treatment of the non-linear convective term $\int_{\Omega_f(t^{n+1})} \mathbf{v} \cdot \rho_f(\mathbf{u}^{n+1} \cdot \nabla \mathbf{u}^{n+1})\, \mathrm{d}\Omega$ (also, mesh velocity term $\int_{\Omega_f(t^{n+1})} \mathbf{v} \cdot \rho_f[\nabla \cdot (\mathbf{u}^{n+1}\mathbf{w}^{n+1})]\, \mathrm{d}\Omega$ with moving domains) in Eq. (3.45), Eq. (3.53). One approach would be to treat this term (terms) explicitly via an extrapolation from the previous time steps, as is done, e.g., in Merrill and Peet (2019); Patel *et al.* (2019); Fischer (1997b). This method produces stable and accurate results on stationary domains, and on moving domains where the movement of the domain boundary at the next time instance can be well predicted by extrapolation, as is the case, for example, with prescribed domain motions parameterized by a known function of time (Merrill and Peet (2019); Patel *et al.* (2019)). Previous work (Xu and Peet (2021a)) has shown, however, that with domain motions that can not be well predicted by extrapolation, such as, for example, with sudden, or impulsive, motions, the explicit approach fails to reproduce a stabilized pressure field in a short enough time. While the pressure recovery would eventually follow after a certain time lag, in a fully coupled FSI loop, a short-term disturbance of the pressure field would get amplified via an FSI iteration and lead to numerical instabilities. To avoid this situation, we follow, after Baek and Karniadakis (2011), an implicit approach for the treatment of the non-linear convective term in the BDF2 formulation, in the form of sub-iterations.

In Baek and Karniadakis (2011); Xu and Peet (2017), sub-iterations are described in a strong form. Here, we develop a more appropriate mathematical formulation by introducing a sub-iteration approach in a weak form, since this is precisely the form that is being solved numerically in the weighted-residual based methods, such as a spectral-element method (Deville *et al.* (2002)). Following a similar approach

as described in Sec. (3.4.1) in regards to an iterative solution of the nonlinear solid dynamics equations, both no-GCL and CGL ALE formulations given by Eq. (3.45)–Eq. (3.46) and Eq. (3.53)–Eq. (3.54), respectively, can be written in a form,

$$\begin{aligned} \mathbf{N_M}(\mathbf{u}^{n+1}, p^{n+1}) = 0, \\ \mathbf{N_C}(\mathbf{u}^{n+1}) = 0, \end{aligned} \tag{3.55}$$

where $\mathbf{N_M}$ is a non-linear variational functional corresponding to the momentum equations, and $\mathbf{N_C}$ is the non-linear functional for the continuity equation, defined as the difference between the left-hand side and the right-hand side of Eq. (3.45), Eq. (3.53) for $\mathbf{N_M}$, and as the left-hand side of Eq. (3.46), Eq. (3.54) for $\mathbf{N_C}$. Note that the continuity equation does not contain pressure, so that the functional $\mathbf{N_C}$ in Eq. (3.55) is independent of the pressure term.

As in Sec. (3.4.1), introducing iterative corrections to the independent problem variables at each time step $n+1$ and each iteration $i+1$

$$\begin{aligned} \mathbf{u}_{i+1}^{n+1} = \mathbf{u}_{i}^{n+1} + \delta\mathbf{u}_{i+1}^{n+1}, \\ p_{i+1}^{n+1} = p_{i}^{n+1} + \delta p_{i+1}^{n+1}, \end{aligned} \tag{3.56}$$

and linearizing the system given by Eq. (3.55) around the previous known values $(\mathbf{u}_i^{n+1}, p_i^{n+1})$, a solution of the following linearized equations in a Newton-Raphson form is being sought,

$$\begin{aligned} \left.\frac{\partial \mathbf{N_M}}{\partial \mathbf{u}}\right|_{\mathbf{u}_i^{n+1}} \delta\mathbf{u}_{i+1}^{n+1} + \left.\frac{\partial \mathbf{N_M}}{\partial p}\right|_{p_i^{n+1}} \delta p_{i+1}^{n+1} = -\mathbf{N_M}(\mathbf{u}_i^{n+1}, p_i^{n+1}), \\ \left.\frac{\partial \mathbf{N_C}}{\partial \mathbf{u}}\right|_{\mathbf{u}_i^{n+1}} \delta\mathbf{u}_{i+1}^{n+1} = -\mathbf{N_C}(\mathbf{u}_i^{n+1}). \end{aligned} \tag{3.57}$$

For evaluation of the Jacobian matrices, we omit nonlinear terms from the calculation of the Jacobians but keep them in the right-hand side of the iterative equation, Eq. (3.57), since Jacobians are not required to be exact with the implicit iterations procedure (Baek and Karniadakis (2011); Xu and Peet (2017)). The linearized

system, however, contains the implicit pressure-velocity relationship inherent to the incompressible Navier-Stokes equations system (Deville *et al.* (2002)):

$$\begin{bmatrix} \mathcal{F} & \mathcal{G} \\ \mathcal{D} & 0 \end{bmatrix} \begin{bmatrix} \delta\,\mathbf{u}_{i+1}^{n+1} \\ \delta p_{i+1}^{n+1} \end{bmatrix} = \begin{bmatrix} -\mathbf{N}_{\mathbf{M}_i}^{n+1} \\ -\mathbf{N}_{\mathbf{C}_i}^{n+1} \end{bmatrix}, \tag{3.58}$$

where

$$\begin{aligned}
\mathcal{F}\,\delta\mathbf{u}_{i+1}^{n+1} &= \frac{3}{2\delta t}\int_{\Omega_f(t^{n+1})} \mathbf{v}\cdot\rho_f\,\delta\mathbf{u}_{i+1}^{n+1}\;\mathrm{d}\Omega + \int_{\Omega_f(t^{n+1})} \mu\nabla\mathbf{v} : \nabla\delta\mathbf{u}_{i+1}^{n+1}\;\mathrm{d}\Omega, \\
\mathcal{G}\,\delta p_{i+1}^{n+1} &= -\int_{\Omega_f(t^{n+1})} \nabla\mathbf{v}\cdot\delta p_{i+1}^{n+1}\;\mathrm{d}\Omega, \\
\mathcal{D}\,\delta\mathbf{u}_{i+1}^{n+1} &= -\int_{\Omega_f(t^{n+1})} q\cdot\nabla\delta\mathbf{u}_{i+1}^{n+1}\;\mathrm{d}\Omega, \\
-\mathbf{N}_{\mathbf{M}_i}^{n+1} &= \frac{2}{\delta t}\int_{\Omega_f(t^{n})} \mathbf{v}\cdot\rho_f\mathbf{u}^{n}\;\mathrm{d}\Omega - \frac{1}{2\delta t}\int_{\Omega_f(t^{n-1})} \mathbf{v}\cdot\rho_f\mathbf{u}^{n-1}\;\mathrm{d}\Omega \\
&\quad - \int_{\Omega_f(t^{n+1})} \mathbf{v}\cdot\rho_f(\mathbf{u}_i^{n+1}\cdot\nabla\mathbf{u}_i^{n+1})\;\mathrm{d}\Omega + \int_{\Omega_f(t^{n+1})} \mathbf{v}\cdot\rho_f\mathbf{f}^{n+1}\;\mathrm{d}\Omega \\
&\quad + \int_{\Omega_f(t^{n+1})} \nabla\mathbf{v}\cdot p_i^{n+1}\;\mathrm{d}\Omega + \int_{\Gamma_f(t^{n+1})} \mathbf{v}\cdot(\mu\nabla\mathbf{u}^{n+1} - p^{n+1})\mathbf{n}\;\mathrm{d}\Gamma \\
&\quad + \mathbf{g}_{\mathbf{w}}(\mathbf{u}_i^{n+1}, t_i^{n+1}), \\
-\mathbf{N}_{\mathbf{C}_i}^{n+1} &= 0,
\end{aligned} \tag{3.59}$$

and the mesh velocity term $\mathbf{g}_{\mathbf{w}}(\mathbf{u}_i^{n+1}, t_i^{n+1})$ is equal to

$$\mathbf{g}_{\mathbf{w}}(\mathbf{u}_i^{n+1}, t_i^{n+1}) = \begin{cases} \frac{3}{2}\int_{\Omega_f(t^{n+1})} \mathbf{v}\cdot\rho_f[\nabla\cdot(\mathbf{u}_i^{n+1}\mathbf{w}^{n+1})]\;\mathrm{d}\Omega - \frac{1}{2}\int_{\Omega_f(t^{n})} \mathbf{v}\cdot\rho_f[\nabla\cdot(\mathbf{u}_i^{n+1}\mathbf{w}^{n})]\;\mathrm{d}\Omega, \\ \int_{\Omega_f(t^{n+1})} \mathbf{v}\cdot\rho_f[\nabla\cdot(\mathbf{u}_i^{n+1}\mathbf{w}^{n+1})]\;\mathrm{d}\Omega, \end{cases} \tag{3.60}$$

where the upper is for IE update with GCL and the lower is for IE or CN update with no GCL.

To solve the system of Eq. (3.58), following Deville *et al.* (2002); Quarteroni *et al.* (2000), we use inexact block LU factorization procedure as

$$\begin{bmatrix} \mathcal{F} & \mathcal{G} \\ \mathcal{D} & 0 \end{bmatrix} \approx \begin{bmatrix} \mathcal{F} & 0 \\ \mathcal{D} & -\mathcal{D}\,\mathcal{Q}_1\,\mathcal{G} \end{bmatrix} \begin{bmatrix} \mathbf{I} & \mathcal{Q}_2\,\mathcal{G} \\ 0 & \mathbf{I} \end{bmatrix}, \tag{3.61}$$

where $\mathcal{Q}_1$, $\mathcal{Q}_2$ serve to approximate an inverse of the matrix $\mathcal{F}^{-1}$, and in the current method are chosen as

$$\mathcal{Q}_1 = \mathcal{Q}_2 = \frac{\delta\, t}{\beta_0}\mathcal{M}^{-1}, \tag{3.62}$$

while other choices are possible (Deville *et al.* (2002); Quarteroni *et al.* (2000)). Here, $\beta_0 = 3/2$ is the leading coefficient in the BDF scheme, and $\mathcal{M}$ is the mass matrix defined as

$$\mathcal{M}\,\delta\mathbf{u}_{i+1}^{n+1} = \int_{\Omega_f(t^{n+1})} \mathbf{v}\cdot\rho_f\,\delta\mathbf{u}_{i+1}^{n+1}\;\mathrm{d}\Omega. \tag{3.63}$$

Note that an approximation of the matrix $\mathcal{F}^{-1}$ by inexact matrices $\mathcal{Q}_1$, $\mathcal{Q}_2$ generally (with explicit methods) results in splitting errors that can affect the overall accuracy of the temporal scheme. The splitting error with the current choice of $\mathcal{Q}_1$, $\mathcal{Q}_2$ would be of the order of $(\delta\, t)^2$ with the pressure-correction algorithm (Deville *et al.* (2002); Kan (1986)) and would not affect the accuracy of BDF2 in any case. However, in the current implicit method, the inexact factorization affects only the convergence of the iterations, and not a temporal accuracy of the scheme, which is not affected by the structure of the iteration matrix, so the choice of an inexact factorization in implicit methods is more forgiving.

With this inexact LU-factorization, a solution of the original system, Eq. (3.58), is equivalent to a solution of three split equations, with an intermediate velocity field $\delta\tilde{\mathbf{u}}_{i+1}^{n+1}$ introduced as an auxiliary variable (Deville *et al.* (2002); Quarteroni *et al.* (2000))

$$\begin{aligned}
\mathcal{F}\,\delta\tilde{\mathbf{u}}_i^{n+1} &= -\mathbf{N}_{\mathbf{M}i}^{n+1},\\
\mathcal{D}\,\mathcal{M}^{-1}\mathcal{G}\,\delta p_{i+1}^{n+1} &= \mathcal{D}\,\delta\tilde{\mathbf{u}}_{i+1}^{n+1},\\
\mathcal{M}\,\delta\mathbf{u}_{i+1}^{n+1} &= \mathcal{M}\,\delta\tilde{\mathbf{u}}_{i+1}^{n+1} - \mathcal{G}\,\delta p_{i+1}^{n+1}.
\end{aligned} \tag{3.64}$$

The first equation in the system of Eq. (3.64) is in the form of a Helmholtz equation, and is solved by the PCG method with the inverse mass and stiff matrix as

the preconditioner, and the second Poisson-like equation is solved by the Generalized Minimal Residual Method (GMRES) with a multi-grid preconditioning (Deville *et al.* (2002)). Note that in the current implementation of the spectral-element method, a discrete Helmholtz operator is symmetric positive definite (Deville *et al.* (2002); Fischer (1997b)), which makes it possible to use PCG solver for the Helmholtz equation. The velocity and the pressure fields are updated iteratively until $\kappa_{f,\,i+1} = \left\|\delta \mathbf{u}_{i+1}^{n+1}\right\|_2 / \left\|\mathbf{u}_i^{n+1}\right\|_2 \leq \kappa_f$ and $\kappa_{p,\,i+1} = \left\|\delta p_{i+1}^{n+1}\right\|_2 / \left\|p_i^{n+1}\right\|_2 \leq \kappa_p$. The baseline values of velocity and pressure tolerances are set to $\kappa_f = 10^{-6}, \kappa_p = 10^{-5}$ in most of the test cases unless specified, for which they are varying. When the velocity tolerance κ_f varies, the pressure tolerance is always set up as $\kappa_p = 10\,\kappa_f$. To accelerate convergence of the iterations, Aitken relaxation (Aitken (1926)) is used, but acting on the velocity and pressure fields, $\mathbf{u}_i^{n+1}, p_i^{n+1}$.

3.4.2 Solid and Fluid Spatial Discretization

To solve the solid domain equations of Eq. (3.15), with the Newmark method, Eq. (3.40), initial condition of Eq. (3.12), and boundary conditions of Eq. (3.13), Eq. (3.14), and the fluid domain equations in a no-GCL form of Eq. (3.45), Eq. (3.46), or a GCL form of Eq. (3.53), Eq. (3.54), initial condition, Eq. (3.26), and boundary conditions, Eq. (3.27), Eq. (3.28), a spectral element method (SEM) implemented in a solver Nek5000 (Deville *et al.* (2002)) is employed, that ensures a high-order spectral convergence in space with p-refinement.

In a spectral-element formulation, the computational domain Ω_s or Ω_f is decomposed into a set of nonoverlapping adjacent elements Ω^e mapped from a reference element $\hat{\Omega}$. Variables from different search spaces $\mathcal{H}^1(\hat{\Omega})$ or $\mathcal{L}^2(\hat{\Omega})$ are projected onto subspaces $\mathbb{P}_N$, $\mathbb{P}_M$, where $M = N - 2$ in the current formulation. Thus, in a solid domain, the displacement field at a time step t^{n+1}, $\mathbf{d}_e^{n+1}(\boldsymbol{\xi}) \in \mathcal{H}^1(\hat{\Omega}_s)$ is discretized

as

$$\mathbf{d}_e^{n+1}(\boldsymbol{\xi}) = \sum_{i=0}^{N}\sum_{j=0}^{N}\sum_{k=0}^{N} \mathbf{d}_{e,\,ijk}^{n+1}\pi_{N,i}(\xi_1)\pi_{N,j}(\xi_2)\pi_{N,k}(\xi_3), \quad \boldsymbol{\xi} \in \hat{\Omega}_s, \tag{3.65}$$

and in a fluid domain, the velocity field at a time step t^{n+1}, $\mathbf{u}_e^{n+1}(\boldsymbol{\xi}) \in \mathcal{H}^1(\hat{\Omega}_f)$, and the pressure $p_e^{n+1}(\tilde{\boldsymbol{\xi}}) \in \mathcal{L}^2(\hat{\Omega}_f)$ are represented as

$$\mathbf{u}_e^{n+1}(\boldsymbol{\xi}) = \sum_{i=0}^{N}\sum_{j=0}^{N}\sum_{k=0}^{N} \mathbf{u}_{e,\,ijk}^{n+1}\pi_{N,i}(\xi_1)\pi_{N,j}(\xi_2)\pi_{N,k}(\xi_3), \quad \boldsymbol{\xi} \in \hat{\Omega}_f, \tag{3.66}$$

$$p_e^{n+1}(\tilde{\boldsymbol{\xi}}) = \sum_{i=1}^{N-1}\sum_{j=1}^{N-1}\sum_{k=1}^{N-1} p_{e,\,ijk}^{n+1}\tilde{\pi}_{N-2,i}(\tilde{\xi}_1)\tilde{\pi}_{N-2,j}(\tilde{\xi}_2)\tilde{\pi}_{N-2,k}(\tilde{\xi}_3), \quad \tilde{\boldsymbol{\xi}} \in \hat{\Omega}_f. \tag{3.67}$$

Here, $\mathbf{d}_{e,\,ijk}^{n+1}$, $\mathbf{u}_{e,\,ijk}^{n+1}$, $p_{e,\,ijk}^{n+1}$, are the nodal values of displacements (for solid), velocity and pressure (for fluid), in the corresponding elements at a time step t^{n+1}, the basis functions $\pi_{N,\alpha}(\xi_\beta)$, $\tilde{\pi}_{N-2,\alpha}(\tilde{\xi}_\beta)$, $\alpha = \{i,j,k\}$, $\beta = \{1,2,3\}$, are the interpolating polynomials of degree N, $N-2$, respectively. For a high-order integration, the quadrature nodes are defined as the Gauss-Lobatto-Legendre (GLL) nodes, $\xi_{\beta m,\,m=0,\,\ldots N}$, for $\mathbb{P}_N$ integration, and the Gauss-Legendre (GL) nodes, $\tilde{\xi}_{\beta m,\,m=1,\,\ldots N-1}$, for $\mathbb{P}_{N-2}$ integration. The interpolating polynomials $\pi_{N,\alpha}(\xi_\beta)$, $\tilde{\pi}_{N-2,\alpha}(\tilde{\xi}_\beta)$, satisfy the properties

$$\begin{aligned} \pi_{N,\,\alpha}(\xi_{\beta m}) &= \delta_{\alpha m} \\ \tilde{\pi}_{N-2,\,\alpha}(\tilde{\xi}_{\beta m}) &= \delta_{\alpha m}, \end{aligned} \tag{3.68}$$

where $\delta_{\alpha m}$ is the Kronecker delta function.

With this discretization, the inner products in the governing equations for the solid and the fluid, Eq. (3.15), Eq. (3.45), Eq. (3.46), Eq. (3.53), Eq. (3.54), are evaluated using Gauss integration on the corresponding GLL or GL nodes on an element-by-element basis, and then assembled across the union of elements encompassing the solid and the fluid domains, respectively. Upon discretization and assembly, the inner products take a form of discrete matrix-vector products, where the matrices correspond to a discretized form of the mass, stiffness, and other spectral-element matrices

as defined in Eq. (3.44), Eq. (3.58), while the vectors correspond to the unknown arrays $\mathbf{d}_{e,ijk}^{n+1}$, $\mathbf{u}_{e,ijk}^{n+1}$, $p_{e,ijk}^{n+1}$ across the solid and fluid elements. For deformed geometries, spectral-element matrices contain the Jacobian terms of the mapping functions between the physical element Ω^e and the reference element $\hat{\Omega}$. For a global assembly of the inner products across the elements, a connectivity operator $\mathcal{C}$ is used, which defines a gather, $\mathbf{d}^{n+1} = \mathcal{C}^T \mathbf{d}_L^{n+1}$, and scatter, $\mathbf{d}_L^{n+1} = \mathcal{C}\, \mathbf{d}^{n+1}$ operations, where $\mathbf{d}_L^{n+1}$ represent the local, unassembled, arrays, and $\mathbf{d}^{n+1}$ represent the global, assembled arrays, similarly for velocity and pressure. The gather-scatter operators then appear multiplicatively at the left and the right of the corresponding spectral-element matrix operators in the discretization of the inner products, see, Refs. Deville *et al.* (2002); Merrill and Peet (2019); Fischer (1997b); Merrill *et al.* (2016a) for more details. With the discretizations Eq. (3.66)–Eq. (3.65) and the property Eq. (3.68), the mass matrix is diagonal in spectral-element methods, and consists of the corresponding Gauss integration quadrature weights on the diagonal (Deville *et al.* (2002); Merrill *et al.* (2016a)).

3.4.3 Fluid-Structure Interaction with Iterative Partitioned Coupling

One way for fluid-structure coupling is accomplished via a partitioned approach, which advances the fluid and solid equations iteratively with a fixed-point iteration algorithm using Aitken relaxation (Küttler and Wall (2008); Aitken (1926)) to accelerate convergence of the iterations. The solid and fluid spectral-element meshes are matched at the FSI boundary, $\Gamma_{fsi}(0)$, at time $t = 0$, and, due to an ALE geometry update that guarantees the continuity of the displacements between the solid and fluid domains in a discrete sense, as described in Sec. (3.4.1), the congruence of the solid and fluid meshes is preserved at $\Gamma_{fsi}(t)$ at $t \geq 0$. Therefore, a simple exchange of the nodal values between the meshes is performed to communicate the corresponding

solid and fluid variables to satisfy the coupling boundary conditions, and no spatial interpolation is required. The algorithm for the fluid-structure coupling that implicitly satisfies the fluid-structure interface boundary conditions, Eq. (3.37) and Eq. (3.38), thus reads as follows: at each new time step t^{n+1}

1. **Fluid**: Solve for $\mathbf{u}_{k=1}^{n+1}$ and $p_{k=1}^{n+1}$ via Eq. (3.53), Eq. (3.54) (IE-ALE update), or Eq. (3.45), Eq. (3.46) (CN-ALE update), with the mesh velocity $\mathbf{w}_{k=1}^{n+1}$ calculated from Eq. (3.31), Eq. (3.52) using boundary conditions

$$\hat{\mathbf{w}}_{int,\,k=1}^{n+1}(\hat{\mathbf{x}}) = \frac{\delta t}{2}\left[\dot{\mathbf{d}}^{n}(\hat{\mathbf{x}}) + \dot{\mathbf{d}}^{n-1}(\hat{\mathbf{x}})\right] \in \Gamma_{fsi}(0), \tag{3.69}$$

for IE-ALE update, or

$$\hat{\mathbf{w}}_{int,\,k=1}^{n+1}(\hat{\mathbf{x}}) = \dot{\mathbf{d}}^{n}(\hat{\mathbf{x}}) \in \Gamma_{fsi}(0), \tag{3.70}$$

for CN-ALE update. Calculate ${\sigma_f}_{k=1}^{n+1}$.

2. **Solid**: Solve for $\mathbf{d}_{k=1}^{n+1}$, $\dot{\mathbf{d}}_{k=1}^{n+1}$, $\ddot{\mathbf{d}}_{k=1}^{n+1}$ via Eq. (3.40), Eq. (3.43) with ${\sigma_f}_{k=1}^{n+1}$ on $\Gamma_{fsi}(t^{n+1})$.

   Start FSI iterations in k from $k = 1$ until the FSI iteration convergence tolerance κ is reached:

3. **Fluid**: Calculate the new unrelaxed interface velocity as

$$\bar{\mathbf{w}}_{int,\,k+1}^{n+1}(\hat{\mathbf{x}}) = \frac{\delta t}{2}\left[\dot{\mathbf{d}}_{k}^{n+1}(\hat{\mathbf{x}}) + \dot{\mathbf{d}}^{n}(\hat{\mathbf{x}})\right] \in \Gamma_{fsi}(0), \tag{3.71}$$

for IE-ALE update, or

$$\bar{\mathbf{w}}_{int,\,k+1}^{n+1}(\hat{\mathbf{x}}) = \dot{\mathbf{d}}_{k}^{n+1}(\hat{\mathbf{x}}) \in \Gamma_{fsi}(0), \tag{3.72}$$

for CN-ALE update.

4. **Fluid**: Evaluate the FSI iteration convergence criteria κ_{i+1} based on the interface velocity

$$\kappa_{i+1} = \left\| \bar{\mathbf{w}}_{int,\,k+1}^{n+1} - \hat{\mathbf{w}}_{int,\,k}^{n+1} \right\|_2 / \left\| \hat{\mathbf{w}}_{int,\,k}^{n+1} \right\|_2 . \tag{3.73}$$

   Exit the loop if κ_{i+1} is below a predefined threshold κ.

5. **Fluid**: Relax the interface velocity as

$$\hat{\mathbf{w}}_{int,\,k+1}^{n+1} = \omega_k \bar{\mathbf{w}}_{int,\,k+1}^{n+1} + (1-\omega_k)\hat{\mathbf{w}}_{int,\,k}^{n+1}, \tag{3.74}$$

   where

$$\begin{aligned} \omega_k &= -\omega_{k-1} \frac{\mathbf{R}_k \cdot \delta\mathbf{R}_k}{\delta\mathbf{R}_k \cdot \delta\mathbf{R}_k}, \\ \mathbf{R}_k &= \bar{\mathbf{w}}_{int,\,k+1}^{n+1} - \hat{\mathbf{w}}_{int,\,k}^{n+1}, \\ \delta\mathbf{R}_k &= \mathbf{R}_k - \mathbf{R}_{k-1}, \end{aligned} \tag{3.75}$$

   with $\omega_1 = 0.75$.

6. **Fluid**: Solve for $\mathbf{u}_{k+1}^{n+1}$ and p_{k+1}^{n+1} via Eq. (3.53), Eq. (3.54) (IE-ALE update), or Eq. (3.45), Eq. (3.46) (CN-ALE update), with the mesh velocity $\mathbf{w}_{k+1}^{n+1}$ calculated from Eq. (3.31), Eq. (3.52) using the relaxed interface velocity $\hat{\mathbf{w}}_{int,\,k+1}^{n+1}$ calculated in Step 5 from Eq. (3.74) as boundary conditions. Calculate $\sigma_{f\,k+1}^{n+1}$.

7. **Solid**: Solve for $\mathbf{d}_{k+1}^{n+1}$, $\dot{\mathbf{d}}_{k+1}^{n+1}$, $\ddot{\mathbf{d}}_{k+1}^{n+1}$ via Eq. (3.40), Eq. (3.43) with $\sigma_{f\,k+1}^{n+1}$ on $\Gamma_{fsi}(t^{n+1})$.

   End FSI iterations.

The FSI iteration convergence tolerance κ is set to $\kappa = 10^{-5}$ in all the test cases presented except specified.

3.4.4 Fluid-Structure Interaction with Explicit Partitioned Coupling

Iterative partitioned coupling based on Dirichlet-Neumann boundary works fine and accurate but the cost is tremendous especially when fluid and solid density ratio is

close for the added-mass effect. Added-mass effect is a physical phenomenon happens when a solid object is moving surrounded by fluid. As the motion of the solid changes the motion of fluid, the surrounded fluid is accelerated by the solid which is additional mass which is called virtual mass added to the whole system. When fluid and solid density is close, the acceleration between them would be strong and it requires more iterations to solve the FSI coupling issue and that would make the FSI coupling more costly. To accelerate FSI coupling, more and more non-iterative explicit methodology has been developed based on Robin boundary on the cost of accuracy (Burman and Fernández (2009); Badia *et al.* (2008); Nobile and Vergara (2008); Gerardo-Giorda *et al.* (2010); Fernández *et al.* (2015)). The method developed in this paper is generalized Robin-Neumann explicit coupling scheme from Fernández *et al.* (2015), which using Robin boundary condition for fluid and Neumann boundary condition for solid. The algorithm is stated as follows: at each new time step t^{n+1}

1. **Fluid**: Solve for $\mathbf{u}^{n+1}$ and p^{n+1} via Eq. (3.78) (BDF1) (we would show why BDF2 is not used in Sec. (3.8)), and Eq. (3.46) (CN-ALE update), with Robin boundary conditions

$$\begin{aligned} &\int_{\Gamma_f(t^{n+1})} \mathbf{v}\cdot\sigma_f^{n+1}\mathbf{n}_f \,\mathrm{d}\Gamma + \int_{\Gamma_f(t^{n+1})} \mathbf{v}\cdot\rho_s\frac{\partial \mathbf{u}^{n+1}}{\partial t}\,\mathrm{d}\Gamma \\ =&\int_{\Gamma_f(t^{n+1})} \mathbf{v}\cdot\rho_s\frac{\partial \dot{\mathbf{d}}^{n+1}}{\partial t}\,\mathrm{d}\Gamma - \int_{\Gamma_f(t^{n+1})} \mathbf{v}\cdot\sigma_s^{n+1}\mathbf{n}_s\,\mathrm{d}\Gamma, \end{aligned} \tag{3.76}$$

   and mesh velocity $\mathbf{w}^{n+1}$ calculated from Eq. (3.31), Eq. (3.52) using boundary conditions

$$\hat{\mathbf{w}}_{int}^{n+1}(\hat{\mathbf{x}}) = \dot{\mathbf{d}}^n(\hat{\mathbf{x}}) \in \Gamma_{fsi}(0). \tag{3.77}$$

2. **Solid**: Solve for $\mathbf{d}^{n+1}$, $\dot{\mathbf{d}}^{n+1}$, $\ddot{\mathbf{d}}^{n+1}$ via Eq. (3.40), Eq. (3.43) with ${\sigma_f}^{n+1}$ on $\Gamma_{fsi}(t^{n+1})$.

   End FSI coupling.

$$
\begin{aligned}
&\frac{1}{\delta t}\int_{\Omega_f(t^{n+1})} \mathbf{v}\cdot\rho_f\mathbf{u}^{n+1}\ \mathrm{d}\Omega - \frac{1}{\delta t}\int_{\Omega_f(t^{n})} \mathbf{v}\cdot\rho_f\mathbf{u}^{n}\ \mathrm{d}\Omega \\
&= -\int_{\Omega_f(t^{n+1})} \mu\nabla\mathbf{v} : \nabla\mathbf{u}^{n+1}\ \mathrm{d}\Omega - \int_{\Omega_f(t^{n+1})} \mathbf{v}\cdot\rho_f(\mathbf{u}^{n+1}\cdot\nabla\mathbf{u}^{n+1})\ \mathrm{d}\Omega + \\
&\int_{\Omega_f(t^{n+1})} \mathbf{v}\cdot\rho_f\mathbf{f}^{n+1}\ \mathrm{d}\Omega + \int_{\Omega_f(t^{n+1})} \nabla\mathbf{v}\cdot p^{n+1}\ \mathrm{d}\Omega + \int_{\Gamma_f(t^{n+1})} \mathbf{v}\cdot(\mu\nabla\mathbf{u}^{n+1} - p^{n+1})\mathbf{n}\ \mathrm{d}\Gamma \\
&+ \int_{\Omega_f(t^{n+1})} \mathbf{v}\cdot\rho_f[\nabla\cdot(\mathbf{u}^{n+1}\mathbf{w}^{n+1})]\ \mathrm{d}\Omega,
\end{aligned}
\tag{3.78}
$$

The algorithm looks pretty straightforward but Robin boundary Eq. (3.76) is not discretized. According to Fernández *et al.* (2015), the implicit treatment of the LHS is enough for added-mass effect stability and the explicit treatment of RHS enables the full fluid-solid splitting without compromising stability. Thus, in the simulation, Eq. (3.76) would be further discretized as

$$
\begin{aligned}
&\int_{\Gamma_f(t^{n+1})} \mathbf{v}\cdot\sigma_f^{n+1}\mathbf{n}_f\ \mathrm{d}\Gamma + \int_{\Gamma_f(t^{n+1})} \mathbf{v}\cdot\frac{\rho_s}{\delta t}\mathbf{u}^{n+1}\ \mathrm{d}\Gamma \\
&= \int_{\Gamma_f(t^{n+1})} \mathbf{v}\cdot\frac{\rho_s}{\delta t}(\dot{\mathbf{d}}^{n} - \dot{\mathbf{d}}^{n-1} + \mathbf{u}^{n})\ \mathrm{d}\Gamma - \int_{\Gamma_f(t^{n+1})} \mathbf{v}\cdot\sigma_s^{n}\mathbf{n}_s\ \mathrm{d}\Gamma,
\end{aligned}
\tag{3.79}
$$

where $\mathbf{u}^n$ could be expressed by $\dot{\mathbf{d}}^n$ from the FSI interface boundary condition.

Using Robin boundary condition could avoid FSI instability so there is no need for iteration in FSI coupling. However, the fluid solver is still solved iteratively as although it would not affect FSI stability but it would affect accuracy, which would be mentioned in Sec. (3.8).

3.5 Verification of h/p and Temporal Convergence of Component Solvers

This section presents verification of h/p- and temporal convergence of the solid and fluid solvers, respectively, using known analytical solutions.

3.5.1 Solid Solver: Nonlinear Elasticity

Here we present a verification of the developed nonlinear solid solver based on a St. Venant-Kirchhoff material model using both steady and unsteady nonlinear structural mechanics test cases.

Nonlinear Elastostatics

For a nonlinear elastostatics problem, a cubic solid block with dimensions $[0,1] \times [0,1] \times [0,1]$ is deformed by imposing a displacement field on all of the six faces as boundary conditions described as

$$\begin{aligned} d_x(X,Y,Z) &= A\mathrm{e}^{aX} - A, \\ d_y(X,Y,Z) &= B\mathrm{e}^{bY} - B, \\ d_z(X,Y,Z) &= 0, \end{aligned} \tag{3.80}$$

where non-dimensional constants $A = B = 0.1$, $a = b = 1$, and X, Y, Z denote the undeformed geometry coordinates. The method of manufactured solutions is used, which takes displacements defined by Eq. (3.80) as the analytic solution, and introduces a body force field $\rho_s \mathbf{f}$ to the right-hand side of the elastostatics equations to satisfy the given solution. In the current case, the body force is determined by

$$\begin{aligned} \rho_s f_x(X,Y,Z) &= -C_1(2A\mu_s a^2 \mathrm{e}^{aX} C_1 + Aa^2\lambda_s \mathrm{e}^{aX} C_1) \\ &\quad - Aa^2\mathrm{e}^{aX}[\lambda_s(\frac{C_1^2}{2} + \frac{C_2^2}{2} - 1) + 2\mu_s(\frac{C_1^2}{2} - \frac{1}{2})], \\ \rho_s f_y(X,Y,Z) &= -C_2(2B\mu_s b^2 \mathrm{e}^{bY} C_2 + Bb^2\lambda_s \mathrm{e}^{bY} C_2) \\ &\quad - Bb^2\mathrm{e}^{bY}[\lambda_s(\frac{C_1^2}{2} + \frac{C_2^2}{2} - 1) + 2\mu_s(\frac{C_2^2}{2} - \frac{1}{2})], \\ \rho_s f_z(X,Y,Z) &= 0, \\ C_1 &= Aa\mathrm{e}^{aX} + 1, \\ C_2 &= Bb\mathrm{e}^{bY} + 1, \end{aligned} \tag{3.81}$$

where the shear modulus μ_s and Lamé first parameter λ_s are calculated using a dimensionless Young's modulus $E = 1000$, Poisson's ratio $\nu_s = 0.3$ and density $\rho_s = 1$.

The original cubic geometry is uniformly discretized with spectral elements, using the same number of elements in X, Y and Z directions. The elements are therefore also cubic, with equal sizes in X, Y and Z directions in an undeformed configuration. The element size δX in the spatial convergence studies thus refers to an element size in any direction, and in regards to the original, undeformed, configuration. The spatial convergence for the nonlinear elastostatics problem using the L^2-error norm of the displacement defined as

$$L^2(\mathbf{d}) = \sqrt{\frac{\int_{\Omega_s} (\mathbf{d}_{ex} - \mathbf{d}_{comp})^2 \, \mathrm{d}\Omega}{V_s}}, \tag{3.82}$$

where, $\mathbf{d}_{comp}$ are the displacements obtained from the computations, $\mathbf{d}_{ex}$ are the corresponding exact values taken from Eq. (3.80), V_s is the volume of Ω_s in the undeformed configuration, is shown in Fig. (3.1). we observe a polynomial-order convergence with h-refinement, and a spectral convergence with p-refinement. Note that for h-refinement, the observed order of convergence is $O(\delta x^{N+2})$. The deviation of plots from an expected order of convergence starts when the errors due to spatial discretization drop below machine precision. Errors close to machine precision were observed previously in elastostatics problems with spectral element methods (Dong and Yosibash (2009); Peet and Fischer (2014)), which might be related to favorable properties of the matrix operators resulting from a discretization of the elastostatics equations.

Nonlinear Elastodynamics

A nonlinear elastodynamics test case is performed to demonstrate the spatial and the temporal accuracy of the solid solver on the time-dependent problems. It shares

the same geometry and material properties as the elastostatics test case described in Sec. (3.5.1). The analytic solution, however, is given by

$$\begin{aligned} d_x(X,Y,Z,t) &= A\sin(aX)\sin(\pi t), \\ d_y(X,Y,Z,t) &= d_z(X,Y,Z,t) = 0, \end{aligned} \tag{3.83}$$

where the constants $A = 0.1$ and $a = 2$. Boundary conditions are, again, defined as Dirichlet boundary conditions on displacements, obtained by evaluating Eq. (3.83) at the domain boundary faces. For the time-dependent problem, we also need initial conditions that are given by

$$\begin{aligned} d_x(X,Y,Z,0) &= 0, \\ \dot{d}_x(X,Y,Z,0) &= A\pi\sin(aX), \\ \ddot{d}_x(X,Y,Z,0) &= 0, \end{aligned} \tag{3.84}$$

and zero displacements, velocities and accelerations in Y and Z directions. Similarly, to enforce the displacement field defined by Eq. (3.83) as the analytic solution of the elastodynamics equation, Eq. (3.11), the body force is introduced as

$$\begin{aligned} \rho_s f_x(X,Y,Z,t) &= 0.5Aa^2\sin(\pi t)\sin(aX)(2\mu_s+\lambda_s)[6Aa\sin(\pi t)\cos(aX) \\ &\quad + 3A^2a^2\sin^2(\pi t)\cos^2(aX) + 2] - A\pi^2\sin(\pi t)\sin(aX), \\ \rho_s f_y(X,Y,Z,t) &= \rho_s f_z(X,Y,Z,t) = 0. \end{aligned} \tag{3.85}$$

In the elastodynamics problem, the L^2 errors are defined as

$$L^2(\mathbf{d}) = \sqrt{\frac{\int_{\Omega_s}(\mathbf{d}_{ex}-\mathbf{d}_{comp})^2\ \mathrm{d}\Omega}{V_s}}\Big|_{t=t_f}, \tag{3.86}$$

where the exact value of displacements $\mathbf{d}_{ex}$ is taken from Eq. (3.83), and the notation $\big|_{t=t_f}$ signifies that the error is evaluated at the final time of the simulations t_f, where the final time is set to $t_f = 2$. Fig. (3.2) shows the results of a spatial refinement study for a nonlinear elastodynamics problem at the final time $t_f = 2$. Since a spatial

error is significantly smaller compared to a temporal error in this problem, the time step size is set to a very small value of $\delta t = 10^{-5}$ to avoid an error interference. As with the static test, an order of convergence for the h-refinement tests is $O(\delta X^{N+2})$. The curve with higher-order polynomials starts to deviate from the expected slope at smaller element sizes due to the fact that the spatial discretization errors start interfering both with temporal and with machine precision errors. p-refinement plots show a clear spectral convergence all the way down to machine precision. Fig. (3.3) demonstrates the temporal convergence of the displacements at the same final time of $t_f = 2$. All three displacement components exhibit a second-order convergence in time, as expected. A temporal convergence study is performed using the mesh with the element size $\delta X = 1/4$ and 7^{th} - order polynomials.

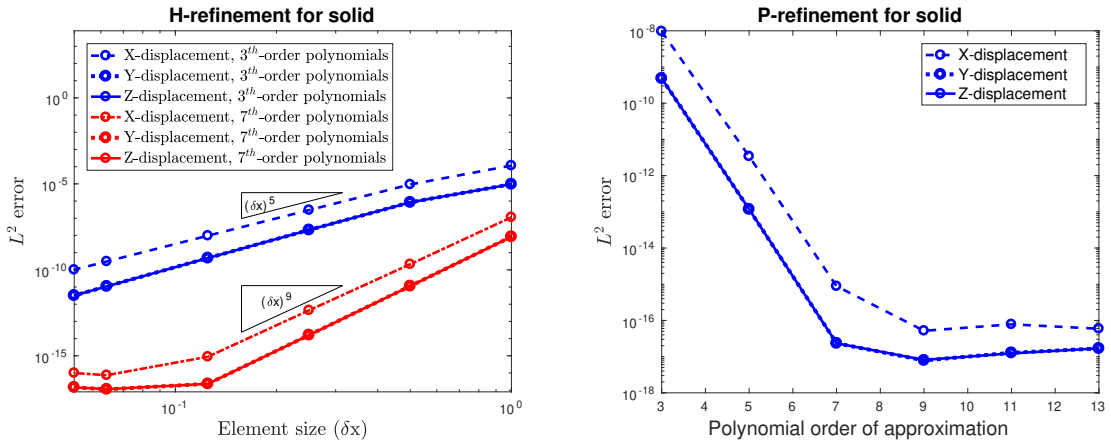

(a) H-refinement.

(b) P-refinement.

Figure 3.1: Spatial Convergence for a Nonlinear Elastostatics Problem Using Nonlinear St. Venant-Kirchhoff Material Model. Element Size Refers to an Undeformed Configuration. P-refinement is Performed with the Element Size $\delta X = 1/4$.

3.5.2 Fluid Solver: Convecting Walsh's Eddies

Walsh (1992) proves that if an initial condition $\mathbf{a}$ satisfies $\Delta\mathbf{a} = \lambda\mathbf{a}$ and $\nabla \cdot \mathbf{a} = 0$, then $\mathbf{u} = \mathrm{e}^{\nu\lambda t}\mathbf{a}$ and $\nabla p = -\mathbf{u} \cdot \nabla\mathbf{u}$ would be a solution of the incompressible Navier-

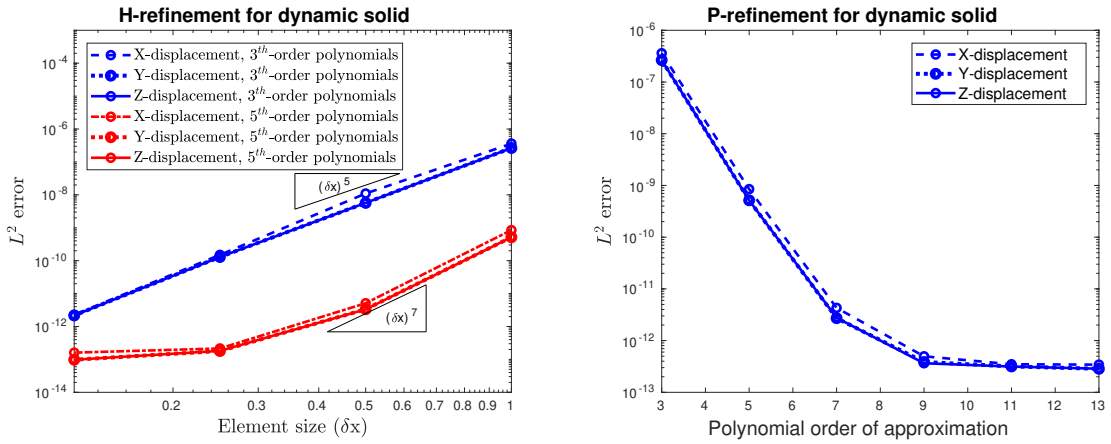

(a) H-refinement. (b) P-refinement.

Figure 3.2: Spatial Convergence for a Nonlinear Elastodynamics Problem Using Nonlinear St. Venant-Kirchhoff Material Model at Time $t_f = 2$ Using Time Step $\delta t = 10^{-5}$. Element Size Refers to an Undeformed Configuration. P-refinement is Performed with the Element Size $\delta X = 1$.

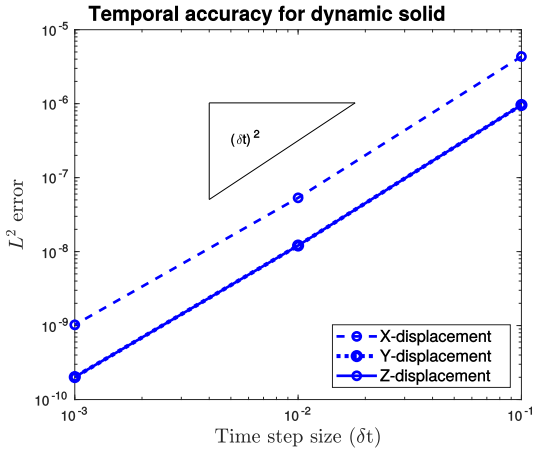

Figure 3.3: Temporal Convergence for an Elastodynamics Problem Using Nonlinear St. Venant-Kirchhoff Material Model at Time $t_f = 2$. Element Size $\delta X = 1/4$ with 7^{Th}-order Polynomials. Element Size Refers to an Undeformed Configuration.

Stokes equations in an unbounded domain. Here, ν is the kinematic viscosity, and λ are the eigenvalues associated with the Walsh's eigenfunction solutions. Thus, a linear combination of several eigenfunctions could be used as an analytical exact solution for assessing spatial and temporal accuracy. To make the test case more interesting, a convecting version of Walsh's solution could be implemented by applying a convecting

frame of reference to the original solution (Walsh (1992)) by means of a coordinate transformation. Here, we use the same exact solution as in Merrill *et al.* (2016a) that employs a coordinate transformation $x = \tilde{x} + c_x t$, $y = \tilde{y} + c_y t$, where (c_x, c_y) is the convecting velocity, $(\tilde{x}, \tilde{y})$ is the convecting frame of reference, where an original Walsh's solution is imposed, and (x, y) is the stationary frame of reference. The convecting Walsh's eddy solution, with the corresponding initial conditions given by the stream function

$$\psi(x, y, 0) = -\frac{1}{5}\cos(5\,x) - \frac{1}{5}\sin(5\,y) + \frac{1}{4}\sin(3\,x)\cos(4\,y) + c_x\,y - c_y\,x, \tag{3.87}$$

is then expressed as (see Merrill *et al.* (2016a) for more details):

$$\begin{aligned}
u_x(x, y, t) &= \mathrm{e}^{-25\nu t}[-\cos(5\tilde{y}) + \cos(4\tilde{y})\sin(3\tilde{x})] + c_x, \\
u_y(x, y, t) &= \mathrm{e}^{-25\nu t}[-\sin(5\tilde{x}) - \frac{3}{4}\cos(3\tilde{x})\sin(4\tilde{y})] + c_y, \\
p(x, y, t) &= \frac{1}{64}\mathrm{e}^{-50\nu t}[-16 + 16\cos(6\tilde{x}) + 8\cos(8\tilde{x} - 4\tilde{y}) - 32\cos(2\tilde{x} - 4\tilde{y}) \\
&\quad + 9\cos(8\tilde{y}) - 8\cos(8\tilde{x} + 4\tilde{y}) + 32\cos(2\tilde{x} + 4\tilde{y}) - 4\sin(3\tilde{x} - 9\tilde{y}) \\
&\quad + 32\sin(5\tilde{x} - 5\tilde{y}) + 36\sin(3\tilde{x} - \tilde{y}) - 32\sin(5\tilde{x} + 5\tilde{y}) \\
&\quad + 36\sin(3\tilde{x} + \tilde{y}) - 4\sin(3\tilde{x} + 9\tilde{y})].
\end{aligned} \tag{3.88}$$

We use $(c_x, c_y) = (1, 0.3)$ for a convecting velocity, $\nu = 0.05$ for viscosity, and a square domain of $\Omega_f = [0, 2\pi] \times [0, 2\pi]$ for a geometry. The original square geometry is uniformly discretized with spectral elements, using the same number of elements in x and y directions. The elements are therefore also square, with equal sizes in x and y directions in an undeformed configuration. The element size δX in the spatial convergence studies thus refers to an element size in any direction, and in regards to the original, undeformed, configuration. Boundary conditions at the edges of Ω_f are set up as Dirichlet conditions on velocity evaluated from Eq. (3.88), while pressure boundary conditions in the current $P_N - P_{N-2}$ formulation are not required, and are

evaluated internally using homogeneous Neumann boundary conditions (Deville *et al.* (2002)).

To test the performance of the developed ALE fluid solver on deformable meshes, a domain deformation shown in Fig. (3.4) based on undeformed mesh coordinates X and Y is imposed as

$$\begin{aligned} w_x(X,Y,t) &= \frac{1.2\pi}{5}\sin(X)\sin(Y)\cos(\frac{2\pi}{5}t), \\ w_y(X,Y,t) &= \frac{2.4\pi}{5}\sin(X)\sin(Y)\cos(\frac{4\pi}{5}t). \end{aligned} \tag{3.89}$$

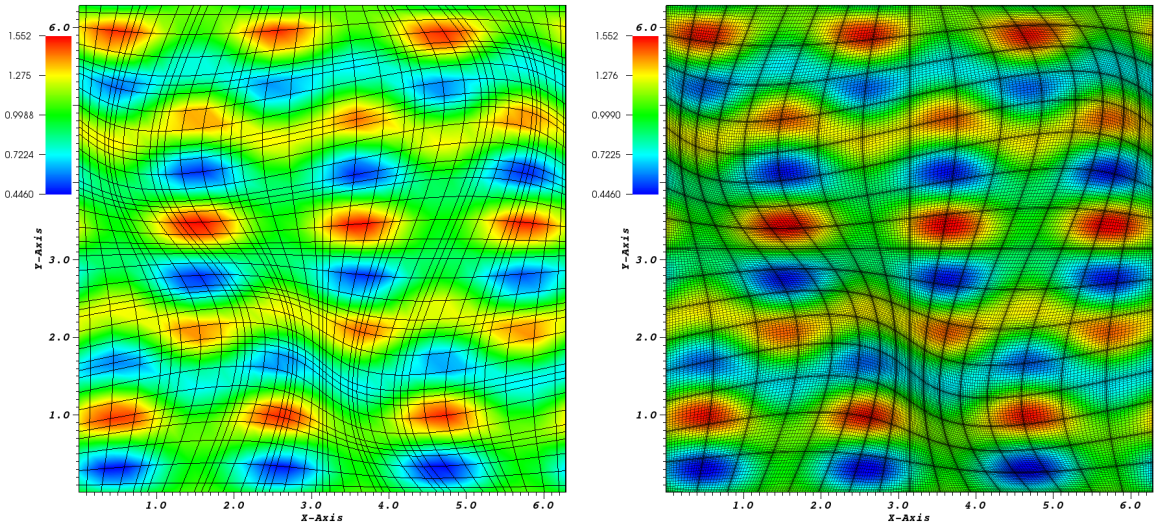

(a) Element size $\delta X = 2\pi/8$ with 5^{th}-order polynomials.

(b) Element size $\delta X = 2\pi/16$ with 17^{th}-order polynomials.

Figure 3.4: Mesh Deformation and the x-velocity Solution for the Convecting Walsh's Eddies Case at $t = 1$. Element Size Refers to an Undeformed Configuration.

Note, since ALE equations (3.24), (3.25) transform back to the original Navier-Stokes equations in a stationary domain when the ALE derivative $\left.\frac{\partial}{\partial t}\right|_{\hat{\mathbf{x}}}$ is converted back to the Eulerian derivative $\left.\frac{\partial}{\partial t}\right|_{\mathbf{x}}$, the flow solution in both stationary and deformed domains is the same, as long as the domain deformation does not influence the flow through a modification of the boundary conditions (as would be the case if actual

moving or deforming objects were present). Since, in the current case, the mesh movement is entirely "virtual" (no actual solid surfaces are moving), the flow solution given by Eq. (3.88) still holds on a deforming domain.

The spatial and temporal convergence for both velocity and pressure fields is investigated through an L^2 error norm defined as

$$\begin{aligned} L^2(\mathbf{u}) &= \sqrt{\frac{\int_{\Omega_f}(\mathbf{u}_{ex}-\mathbf{u}_{comp})^2 \, \mathrm{d}\Omega}{V_f}}\Big|_{t=t_f}, \\ L^2(p) &= \sqrt{\frac{\int_{\Omega_f}(p_{ex}-p_{comp})^2 \, \mathrm{d}\Omega}{V_f}}\Big|_{t=t_f}, \end{aligned} \tag{3.90}$$

where V_f is the volume of the domain Ω_f, subscript *comp* is the result from the computations, *ex* is the analytical value that refers to Eq. (3.88) in this case, and the notation $\big|_{t=t_f}$ signifies that the error is evaluated at the final time of the simulations t_f.

Spatial convergence study is performed with time step $\delta t = 10^{-4}$. Fig. (3.5(a)) shows the L^2 error norm convergence of velocity and pressure fields with regard to the varying element sizes δX by 5^{th} and 7^{th} order polynomials. The convergence rates of velocity and pressure fields demonstrate the expected $O(\delta X^N)$ polynomial order of convergence. The p-refinement plot shown in Fig. (3.5(b)) confirms a spectral convergence for both velocity and pressure fields. Both plots confirm the expected spectral-element convergence rates on deforming meshes. The deviation of plots from an expected order of convergence starts when the errors due to spatial discretization drop below a temporal error of about $O(\delta t^2) \sim 10^{-8} - 10^{-7}$ as expected.

The temporal convergence shown in Fig. (3.6) contains the results at $t_f = 5$ from BDF2 background temporal scheme with three options for the interface update: 1) IE-ALE interface update with GCL, 2) IE-ALE interface update with no GCL, 3) CN-ALE interface update with no GCL. A temporal convergence study is performed using the mesh with the element size $\delta X = 2\pi/16$ and 13^{th} - order polynomials.

As expected, BDF2 with IE-ALE interface update does not achieve second order temporal accuracy without GCL, since the geometry is updated linearly (Formaggia and Nobile (2004)). The two other schemes show the expected second-order temporal convergence rates on deforming meshes.

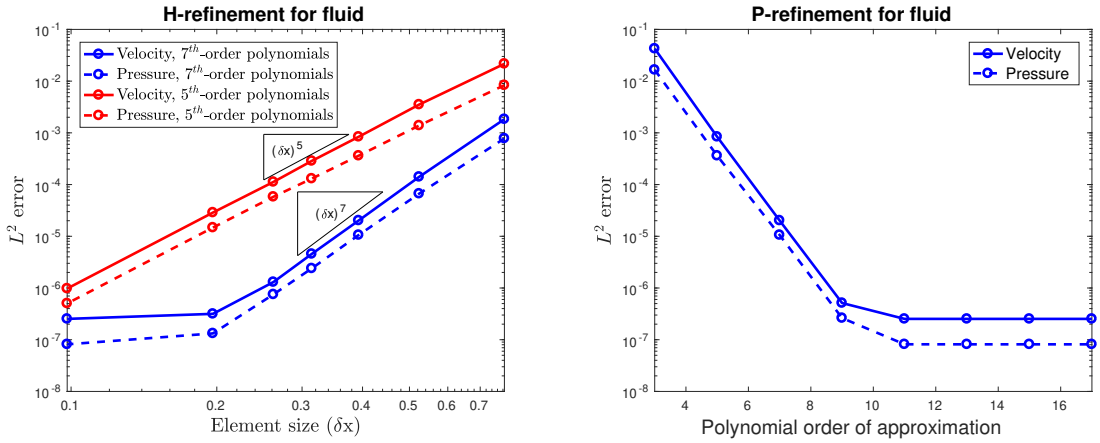

(a) H-refinement. (b) P-refinement.

Figure 3.5: Spatial Refinement for the Convecting Walsh's Eddies Case at Time $t_f = 1$ Using Time Step $\delta t = 10^{-4}$. Element Size Refers to an Undeformed Configuration. P-refinement Is Performed with the Element Size $\delta X = 2\pi/16$.

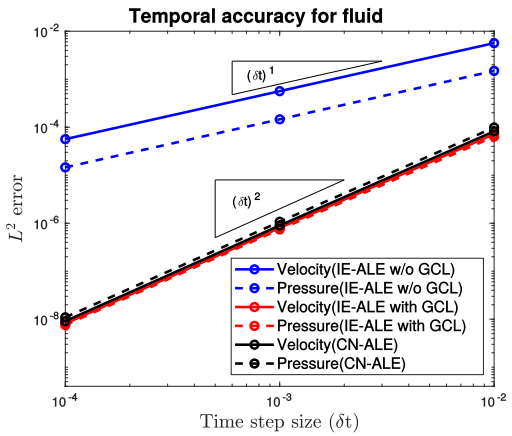

Figure 3.6: Temporal Convergence for the Convecting Walsh's Eddies Case at Time $t_f = 5$. Element Size $\delta X = 2\pi/16$ with 13^{Th}-order Polynomials. Element Size Refers to an Undeformed Configuration.

3.6 Verification of the Iterative Fluid-Structure Interaction Solver against Available Benchmark Solutions

This section concerns with a verification of the developed high-order fluid-structure interaction solver against available numerical benchmarks solutions. we start with a two-dimensional test case proposed by Turek and Hron (2006), and then proceed to a three-dimensional pressure wave propagation test case considered in Refs. Formaggia *et al.* (2001); Fernández *et al.* (2015). In all the test cases presented below, fluid and solid spectral-element meshes are conforming, and the same degree of the polynomial approximation is used for both the fluid and the solid solvers, i.e. the information between the corresponding fluid and solid nodes at the interfaces can be directly exchanged, without the need for an interpolation.

3.6.1 2D Turek-Hron FSI Benchmark

A common fluid-structure interaction benchmark, versus which a performance of the fluid-structure interaction codes is often assessed (Sheldon *et al.* (2016); Verkaik *et al.* (2015); Chabannes *et al.* (2013)), involves a two-dimensional problem proposed by Turek and Hron (2006), which consists of an interaction of an incompressible fluid with a geometrically nonlinear structure, where a fluid flowing over a rigid cylinder excites a flexible cantilever beam attached to a cylinder, as shown in a geometrical setup in Fig. (3.7), where all geometrical parameters have been non-dimensionalized by the cylinder diameter. The fluid solver boundary conditions are set as a parabolic velocity inlet given by Eq. (3.91) below; a constant-pressure derivative-free outlet; and no-slip, rigid and stationary top, bottom and cylinder walls. A flexible elastic solid bar with a curved left side for a no-gap connection is fully attached to the cylinder. The boundary conditions between the fluid and the flexible elastic bar are the FSI

interface conditions defined by Eqs. (3.37), (3.38).

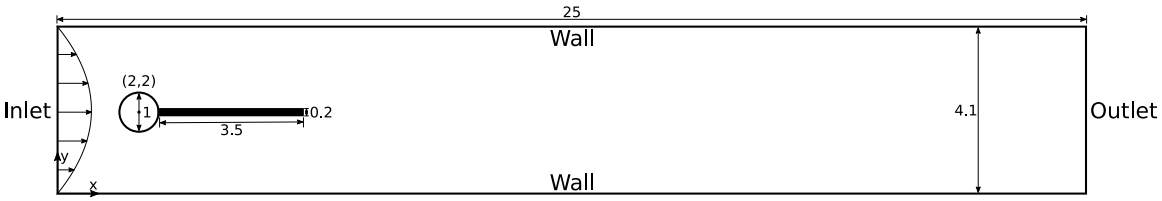

Figure 3.7: Non-dimensional 2d FSI Benchmark Geometry Following Ref. Turek and Hron (2006).

Following Turek and Hron (2006), the inlet flow velocity profile is prescribed as

$$u_x = \begin{cases} 1.5\mathrm{U}\,\dfrac{y(4.1-y)}{(4.1/2)^2}\,\dfrac{[1-\cos(\pi t/t_u)]}{2} & 0 \le t < t_u, \\ 1.5\mathrm{U}\,\dfrac{y(4.1-y)}{(4.1/2)^2} & t \ge t_u, \end{cases} \tag{3.91}$$

where a nonlinear ramping function is applied to an inlet velocity over a time period t_u to alleviate the numerical issues associated with an abrupt start-up motion.

A nonlinear St. Venant-Kirchhoff structural dynamics equation, Eq. (3.11), is solved within the flexible bar, but not within the rigid cylinder, and the solid boundary conditions for the bar are set as the zero displacements at the left curved side, and FSI interface boundary conditions (3.37) and (3.38), at all the other three sides of the bar interacting with the fluid. The fluid mesh contains a total of 760 spectral elements, and the solid mesh contains 34. The solution for all the test cases is obtained with the 6^{th} order polynomial approximation.

In this paper, we compare the results of Turek and Hron with the current spectral-element results for the solid-only, fluid-only, and the FSI test cases, termed as `CSM3`, `CFD3` and `FSI3` in Turek and Hron. In the `CSM3` test case, the geometry of the problem contains only the solid bar with the left side fixed, and an additional gravity force. In the `CSM3` test, the original, non-rescaled, geometry by Turek and Hron is used, with the non-dimensional structure properties set as the solid density $\rho_s = 1000$, Poisson's ratio $\nu_s = 0.4$, Young's modulus $E = 1400000$, and a gravity force $f_y = -2$.

For the CFD3 and FSI3 test cases, the geometry is used as shown in Fig. (3.7), non-dimensionalized by the cylinder diameter, and the other non-dimensional parameters are set as $t_u = 2$, $U = 20$, $\rho_f = \rho_s = 1$ as fluid and solid density, fluid viscosity $\mu = 0.1$, Young's modulus for the solid is $E = 560000$, Poisson's ratio is $\nu_s = 0.4$, and the outflow pressure is set to a reference value of 0. In the CFD3 case, the geometry is as in Fig. (3.7), but the solid bar is kept stationary. In FSI3, a complete fluid-structure interaction of the presented geometry is studied.

The CSM3 results documenting the temporal history of X and Y displacements of the point located at the rightmost tip of the bar along the centerline for Nek5000 as compared to Turek and Hron are shown in Fig. (3.8). For the CFD3 test case, the total lift and drag over the cylinder and the bar are compared in Fig. (3.9). For both test cases, the results shown in Fig. (3.8) and Fig. (3.9) confirm excellent agreement with Ref. Turek and Hron (2006).

The visualization of the streamwise velocity field for the FSI3 test case computed by Nek5000 is presented in Fig. (3.10) for two selected times of $t = 4.475$ and $t = 4.575$. A corresponding mesh deformation pattern, zoomed in around the solid structure is shown in Fig. (3.11). The comparison of both the total lift and drag, as well as the streamwise and vertical displacement of the rightmost tip of the bar along the centerline, for the FSI3 test case, are shown in Fig. (3.12) and Fig. (3.13). Again, an excellent agreement between the current computations and Turek and Hron results are observed, with only 38,906 total degrees of freedom in the current mesh.

3.6.2 3D FSI Pressure Wave Propagation Benchmark

In this section, we compare the results of our three-dimensional spectral-element FSI implementation with the previous numerical solutions using a 3D FSI test case that considers a pressure wave propagation in a flexible pipe proposed in Formaggia

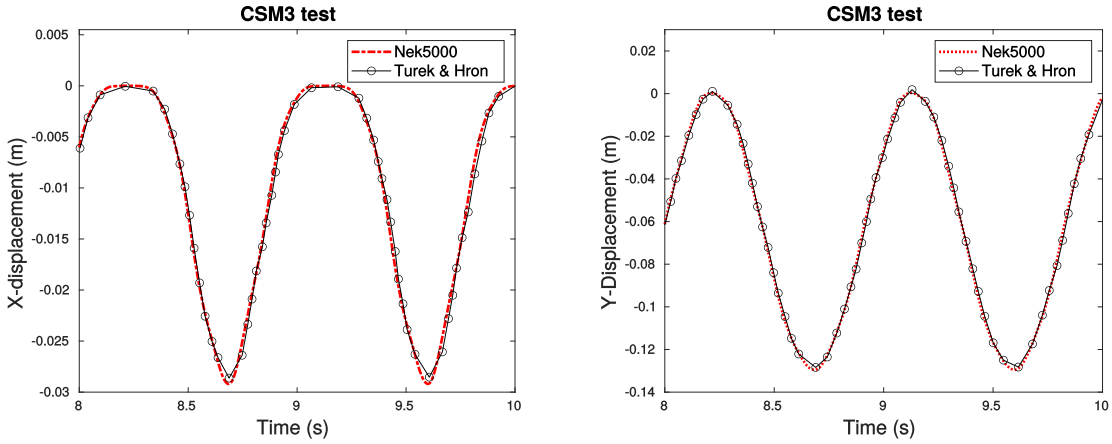

(a) X-displacement comparison for CSM3 test. (b) Y-displacement comparison for CSM3 test.

Figure 3.8: CSM3 Test Case Comparison for the Solid Solver with the Results of the FSI Benchmark (Turek and Hron (2006)). Displacements Are for the Point Located at the Rightmost Tip of the Bar along the Centerline.

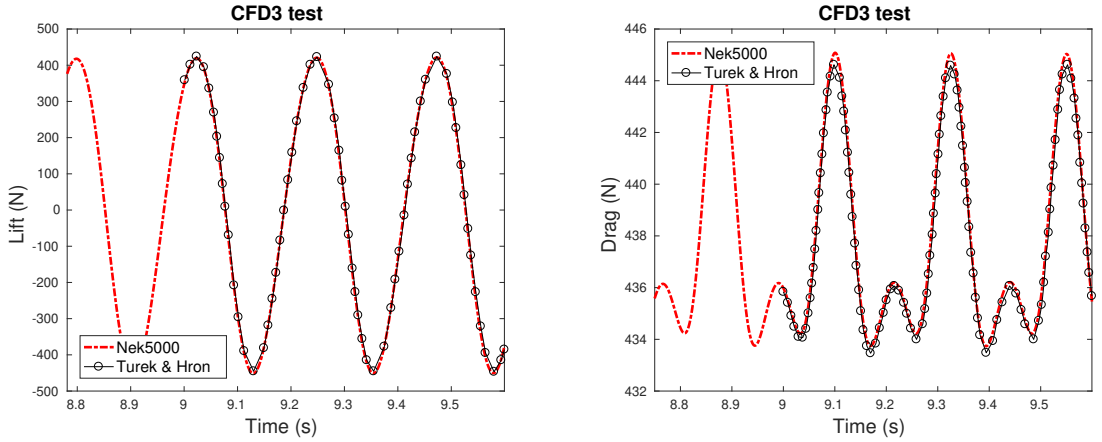

(a) Lift comparison for CFD3 test. (b) Drag comparison for CFD3 test.

Figure 3.9: CFS3 Test Case Comparison for the Fluid Solver with the Results of the FSI Benchmark (Turek and Hron (2006)).

et al. (2001) and later studied in Fernández *et al.* (2015). The geometry consists of a cylindrical pipe with a flexible thin wall of a thickness $d = 0.1D$, where D is the the inner diameter of the pipe. The pipe has a length of $5D$ and is filled with an incompressible fluid. The three-dimensional pipe geometry is presented in Fig. (3.14(a)), and a spectral-element mesh for the fluid and solid is shown in Fig. (3.14(b)), where

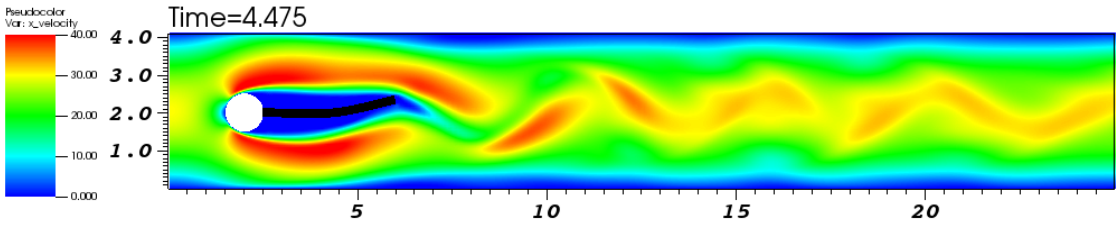

(a) Streamwise velocity at time $t = 4.475$.

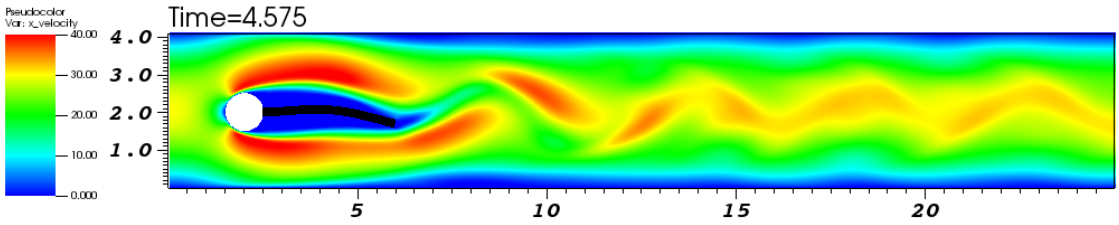

(b) Streamwise velocity at time $t = 4.575$.

Figure 3.10: Visualization of Streamwise Velocity for FSI3 Test Case.

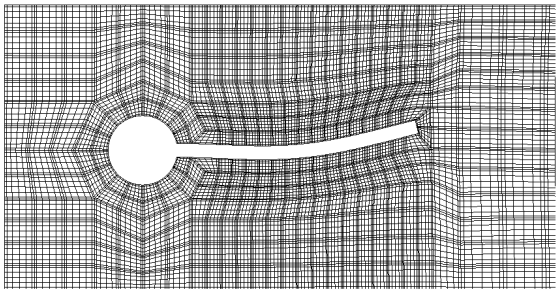

(a) Mesh deformation visualization for FSI3 test at time $t = 4.475$.

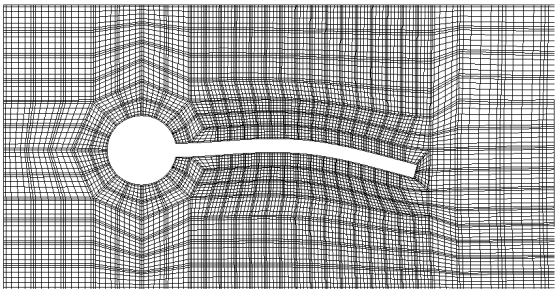

(b) Mesh deformation visualization for FSI3 test at time $t = 4.575$.

Figure 3.11: FSI3 Test Case Mesh Deformation Visualization with 6^{th}-order Polynomials.

the blue color corresponds to the fluid mesh, and the green color to the solid mesh. The fluid mesh contains 32 elements along the circumference, two layers of elements between the radial distance of 0.45 to 0.5 (normalized with the pipe diameter), one layer of elements between the radial distance of $[0.4, 0.45]$, and the core of the cross-sectional circular mesh consists of approximately uniform quadrilateral elements with the average element size of ~ 0.08. The fluid mesh has a total of 224 elements inside the cylindrical cross-section, and 40 equally spaced elements in the streamwise direc-

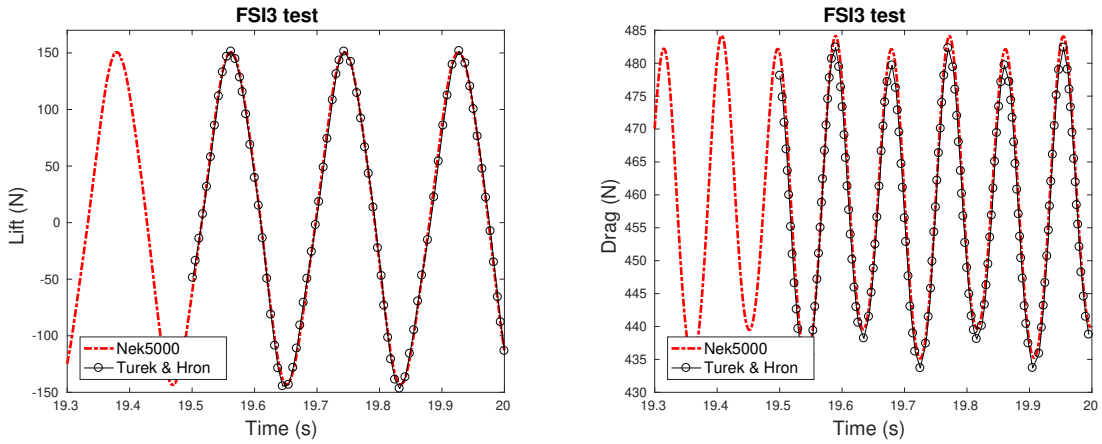

(a) Lift comparison for FSI3 test. (b) Drag comparison for FSI3 test.

Figure 3.12: FSI3 Test Case Comparison with the Results of the FSI Benchmark (Turek and Hron (2006)).

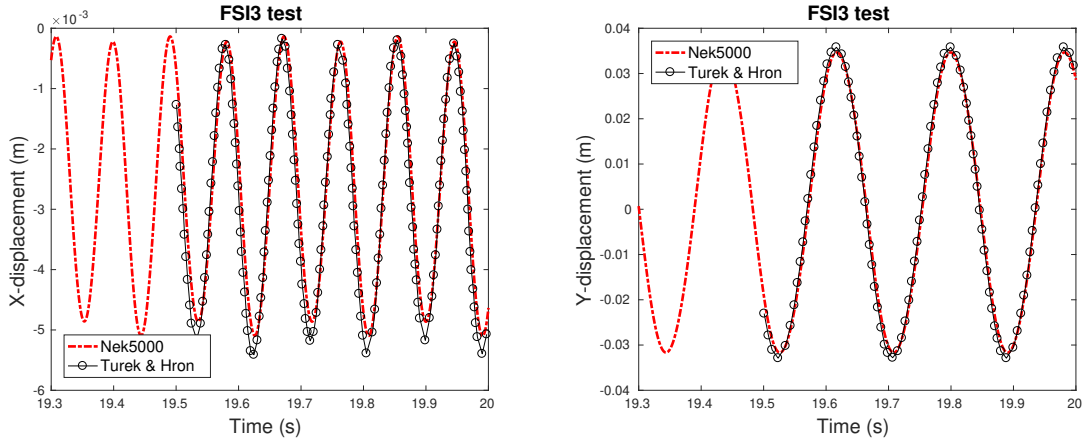

(a) X-displacement comparison for FSI3 test. (b) Y-displacement comparison for FSI3 test.

Figure 3.13: FSI3 Test Case Comparison with the Results of the FSI Benchmark (Turek and Hron (2006)). Displacements are for the Point Located at the Rightmost Tip of the Bar along the Centerline.

tion. The solid is discretized with one layer of elements across the wall thickness, while the element distribution along the circumferential and streamwise directions match that of the fluid. The fluid is assumed to be incompressible, as before, and the solid is discretized with a nonlinear St. Venant-Kirchhoff material model. In the current test case, the fluid has the non-dimensional density $\rho_f = 1$ and viscosity

$\mu = 0.035$. The solid has a density $\rho_s = 1.2$, Young's modulus $E = 3 \times 10^6$ and a Poisson's ratio $\nu_s = 0.3$. Both fluid and solid parameters, as well as the initial and boundary conditions described below, match the parameters of Refs. Formaggia *et al.* (2001); Fernández *et al.* (2015). The pipe flow in the current test case is driven by an inlet pressure, the outlet pressure is kept at zero, and the rest of the fluid boundary is the FSI interface. For the solid, the inner surface is interacting with the fluid through the FSI boundary conditions, the outer surface is stress-free, and the structure is clamped at the inlet and outlet.

To initialize the pressure wave propagation benchmark, the fluid, originally at rest, is disturbed by a sudden inlet pressure impulse of the magnitude of 1.3332×10^4 applied for the time period $[0, 0.005]$, after which the inlet pressure goes back to zero. This pressure impulse sends a pressure wave into the domain, which propagates downstream and causes the deflection of the pipe surface as shown in Fig. (3.15). In the current setup, the z axis is in the streamwise direction, while x and y axes are in the pipe cross-sectional plane. In the current test case, the maximum fluid streamwise velocity achieved is $U_{max} = 28$, which gives a Reynolds number estimate of $Re_{max} = U_{max}D/\nu = 800$, based on the pipe diameter. This ensures that the flow stays in a laminar regime, and the pipe deformation is axisymmetric. Following Fernández *et al.* (2015), we track a temporal evolution of the point with coordinates $(X, Y, Z) = (0.5, 0, 2.5)$ in the undeformed configuration, which corresponds to a point at the fluid-structure interface in the middle of the tube. Again, since the motion is axisymmetric, any interface point with $Z = 2.5$ should give the same results.

The simulations are performed with 4^{th} and 6^{th}-order polynomials and time steps $\delta t = 10^{-4}$ and $\delta t = 4.4721 \times 10^{-5}$. The temporal evolution of the displacement of the middle point of the pipe FSI interface is compared with the results of the implicit method of Fernández *et al.* (2015), which uses second-order accurate in space finite

element (FEM) discretization, in Fig. (3.16). The interface displacement occurs both in the radial and in the streamwise directions, so that the displacement magnitude is compared. We first note that Nek5000 results with $p = 4$ and $p = 6$ are nearly identical, which testifies of an adequate spatial resolution for this problem. While the agreement with the results of Fernández et al. is generally very good, slight differences are noted. We first remark that both the current results and the results of Fernández et al. are sensitive to the time step value, with a consistent trend of an upward shift of the peak at smaller time steps. We also note a time lag of the peak in SEM versus FEM, testifying that the spatial discretization also affects the temporal dynamics. Sensitivities to the time step and the influence of spatial discretization on the time shift in a structure response in the FSI problems will be further discussed in Sec. (3.7). While the 2D Turek and Hron FSI benchmark was studied extensively, results for this 3D FSI benchmark are scarce. More numerical solutions are needed to establish the uncertainty bounds on the results produced so far by these two numerical methods, FEM by Fernández et al. and the current SEM.

3.7 New Proposed 3D FSI Benchmark: Flow in a Compliant Wall Channel

3.7.1 Problem Formulation

Geometry

In this section, we present a new three-dimensional benchmark for studying a fluid-structure interaction problem, which uses consistent initial and boundary conditions, continuous both in space and time, and is quite simple to implement. The benchmark is inspired by a physical problem of a fluid flow in a channel interacting with a compliant wall, which has potential applications in flow control related to a delay of a laminar-to-turbulent transition (Carpenter and Garrad (1985), Dixon *et al.* (1994)),

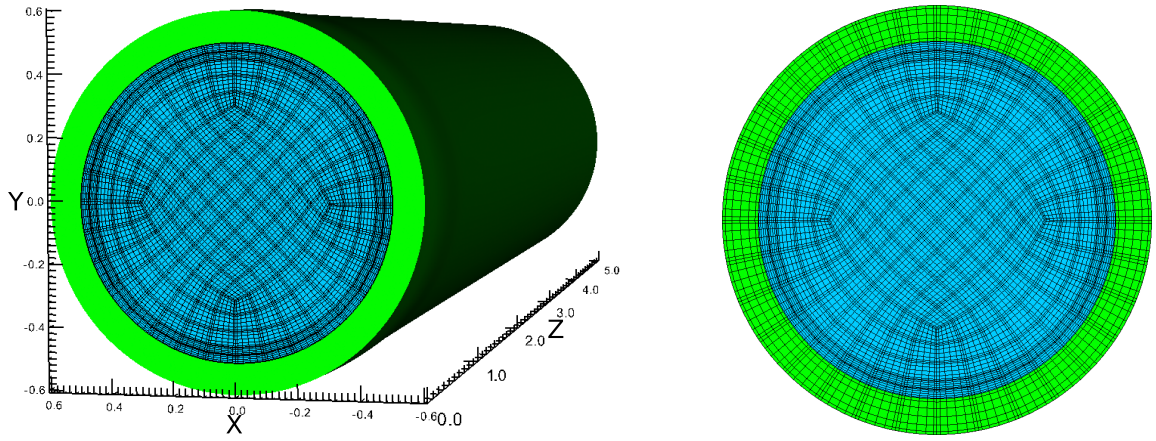

(a) Pipe geometry, mesh and a pressure field visualization computed with 6^{th}-order polynomials.

(b) A close-up view of the spectral-element mesh across the pipe cross-section. Blue color corresponds to the fluid mesh, and green – to the solid mesh.

Figure 3.14: 3D Pipe Geometry and the Computational Mesh for the SEM Simulations of the 3D FSI Pressure Wave Propagation Benchmark.

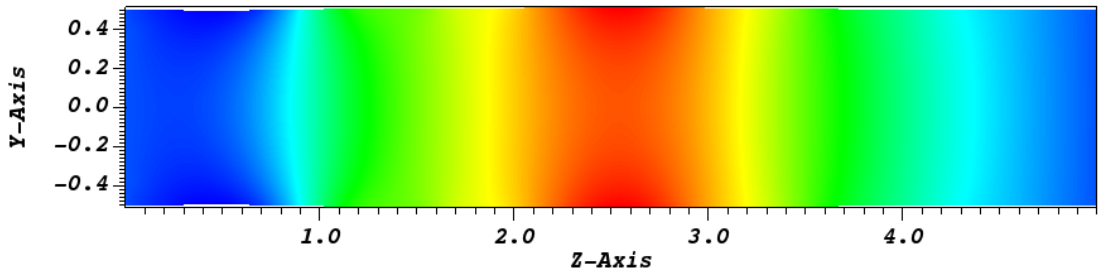

Figure 3.15: Visualization of the Pressure Field and a Pipe Deflection in the Streamwise-radial Plane at Time $t = 0.0075$ for the 3D FSI Pressure Wave Propagation Benchmark. Solution is Computed with 6^{th}-order Polynomials Both for the Fluid and for the Solid.

as well as skin friction drag reduction (Gad-el-Hak (2002)).

The proposed benchmark is studied in this section to verify the h/p- and temporal convergence of a high-order spectral element solver on a globally-coupled FSI problem using self-convergence tests. The effect of the solver tolerances on the numerical errors in the FSI setting is also discussed.

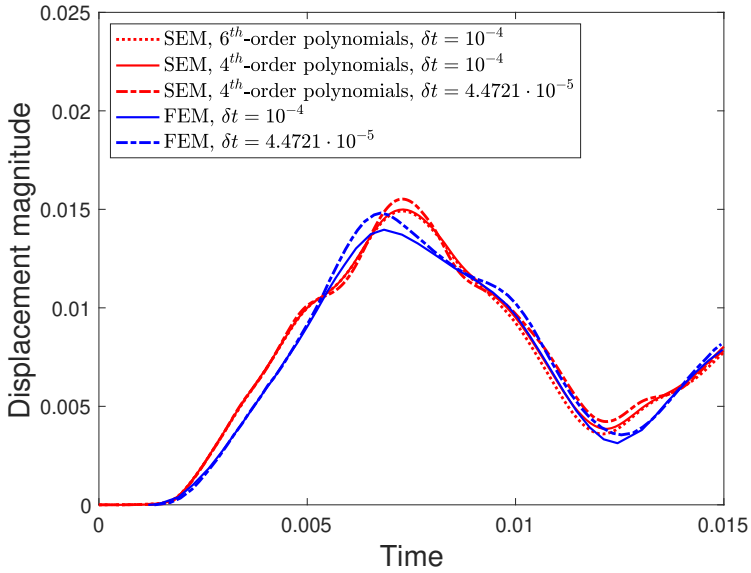

Figure 3.16: Comparison of the Magnitude of Midpoint Displacement versus Time with Fernández *et al.* (2015) for the 3D FSI Pressure Wave Propagation Benchmark. Fernández *et al.* (2015) results are from Their Implicit Coupling Method.

The geometry for the proposed FSI benchmark consists of a rectilinear channel flow domain of the dimensions $[0, 6] \times [-1, 1] \times [-1, 1]$ filled with incompressible fluid (all distances are normalized with the channel half-width), and a flexible solid layer with dimensions $[0, 6] \times [1, 1.2] \times [-1, 1]$ added on top of the fluid domain. Note, in this setting, only one (top) channel wall is elastic, while the other (bottom) wall is rigid, a configuration typical in previous studies of a compliant wall channel (Kim and Choi (2014); Rosti and Brandt (2017)). The bottom rigid wall is thus not modeled by a solid solver, but rather represented by the no-slip boundary conditions in the fluid domain. The other boundary conditions for the fluid are periodic in a spanwise direction, fluid-structure interface for the top compliant wall, inlet velocity boundary conditions, and outflow boundary conditions with a constant pressure set to zero at the outlet. The solid domain added to the top of the fluid domain also has periodic boundary conditions in a spanwise direction, it is clamped at the inlet and outlet (zero displacements), its top surface is stress-free, and its bottom surface that interacts with

the fluid has the FSI interface boundary condition.

The initial condition for the fluid flow is a laminar parabolic velocity profile $(u_x, u_y, u_z) = (U(y), 0, 0)$, where the non-dimensional velocity profile is specified as

$$U(y) = 0.15\,(1 - y^2), \tag{3.92}$$

while the solid starts at rest (zero displacements, velocities, and accelerations). The non-dimensional material properties for the fluid are $\rho_f = 1$, $\mu = 0.0001$ (corresponding to a flow Reynolds number of 1500 based on a channel half-width and an unperturbed centerline velocity), and for the solid the parameters are $\rho_s = 5$, $\nu_s = 0.3$, $E = 300$, with a St. Venant Kirchhoff material model used to model nonlinearly-elastic solid behavior. The unsteady interaction between the fluid and the structure is initiated by sending a transient velocity perturbation through the inlet into the flow domain, in the form of

$$u_x(0, y, z, t) = \begin{cases} U(y) + u'(y, z, t), & 0 \le t < t_u, \\ U(y) & t \ge t_u, \end{cases} \tag{3.93}$$

where the perturbation $u'(y, z, t)$ is given by

$$u'(y, z, t) = 0.075(1 - y^2)\frac{1 - \cos\,(2\,\pi\,t)/t_u}{2}, \tag{3.94}$$

which corresponds to an unsteady velocity perturbation with a peak amplitude of 0.0075 (5% of the undisturbed centerline velocity). This perturbation, also in a form of a parabolic profile consistent with the fluid domain boundary conditions, is added to the undisturbed flow profile $U(y)$ given by Eq. (3.92) for a duration of a time period $t_u = 2$. The perturbation is designed to gradually increase while $t \in [0, t_u/2]$ and then gradually decrease until zero at $t = t_u$, after which the perturbation is turned off, and the flow inlet velocity assumes its undisturbed value. The simulations are run

from the beginning of the transient ($t = 0$) until the final time of $t_f = 25$. A three-dimensional view of the simulated flow velocity and the solid deformation at a time $t = 20$ is provided in Fig. (3.18). The temporal series of the midpoint wall vertical displacement and the flow drag on the compliant wall (fluid force in a streamwise direction, see Eq. (3.95)), using the series of meshes described below, are shown in Fig. (3.17). Fig. (3.17) and Fig. (3.18) demonstrate that although the original perturbation is switched off at a time $t = 2$, an unsteady cycle of the fluid structure interaction persists far beyond the time during which the original perturbation is active.

Table 3.1: Meshes Set for the Self-convergence Studies in the Proposed Compliant Wall Channel 3D FSI Benchmark.

Mesh level	$M1$	$M2$	$M3$	$M4$	$M5$	$M6$	$M7$
Element size, δY, solid	1/10	1/10	1/10	1/10	1/10	1/10	1/10
Element size, δX, fluid and solid, all other directions	1/2	1/3	1/4	1/5	1/6	1/7	1/8
Total number of elements (fluid and solid)	288	864	1920	3600	6048	9408	13824

Table 3.2: Meshes with One Vertical Layer of Solid Elements.

Mesh level	$m1$	$m2$	$m3$
Element size, δY, solid	1/5	1/5	1/5
Element size, δX, fluid and solid, all other directions	1/2	1/3	1/4
Total number of elements (fluid and solid)	240	756	1728

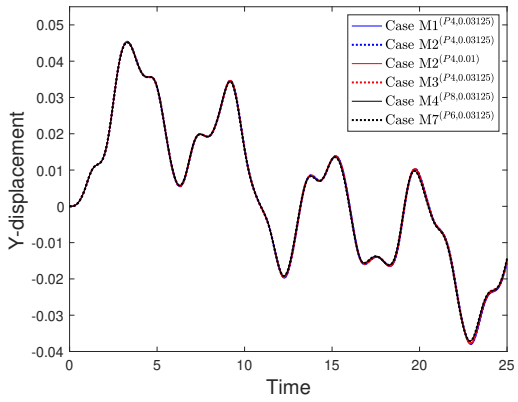

(a) Midpoint wall vertical displacement for the baseline (M) meshes.

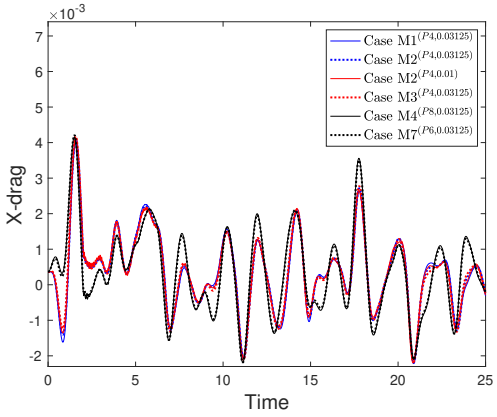

(b) Total flow drag on the compliant wall for the baseline (M) meshes.

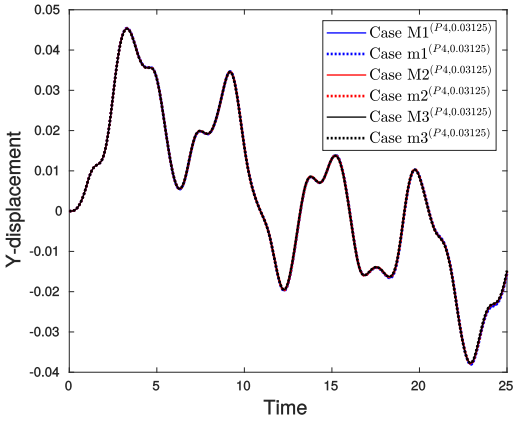

(c) Midpoint wall vertical displacement. Comparison of meshes with one vertical layer (m) and two vertical layers (M) of solid elements.

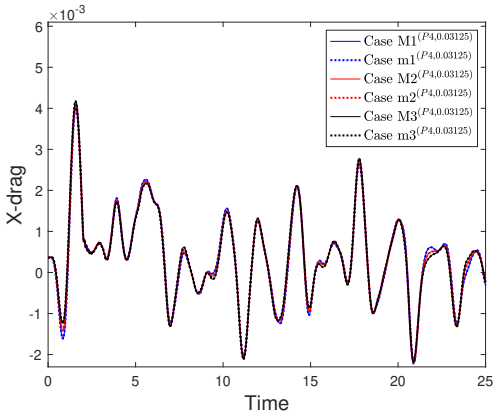

(d) Total flow drag on the compliant wall. Comparison of meshes with one vertical layer (m) and two vertical layers (M) of solid elements.

Figure 3.17: Temporal Series of the Midpoint Wall Vertical Displacement and the Total Flow Drag (Pressure and Viscous Drag) on the Compliant Wall for Different Meshes.

Description of Meshes

In this section, We perform a spatial and a temporal refinement study using a series of meshes, $M1 - M7$. For the meshes $M1 - M7$, the number of solid elements in the y direction is fixed at two (size of $\delta Y = 1/10$ in wall-normal direction). We also add

Table 3.3: Test Meshes and a Reference Mesh for Each Type of the Refinement Studies Performed in the Proposed Compliant Wall Channel 3D FSI Benchmark.

Type of study	Mesh level	Polynomial order	Time step, δt	Tolerances, κ_s, κ_f, κ	Reference mesh
H-refinement	$M1 - M4$	$P4$	0.03125	$10^{-12}, 10^{-6}, 10^{-5}$	$M5^{(P4,\,0.03125)}$
P-refinement	$M4$	$P4, P6, P8$	0.03125	$10^{-12}, 10^{-6}, 10^{-5}$	$M7^{(P6,\,0.03125)}$
Time-refinement	$M2$	$P4$	0.03125, 0.0625, 0.125	$10^{-12}, 10^{-6}, 10^{-5}$	$M2^{(P4,\,0.01)}$

three additional meshes, $m1$, $m2$ and $m3$, with one vertical layer of solid elements instead of two, to check a spatial refinement of the solid, see Table. (3.2). The size of the elements in all other directions (x and z for the solid, and x, y and z for the fluid) is the same within each mesh level, and is uniformly refined across the meshes, following a relation $\delta(Mk) = 1/(k+1)$, $\delta(mk) = 1/(k+1)$. As before, the element size δX refers to an element size in any direction for the fluid, and to either x or z direction for the solid (while $\delta Y = 1/10$ or $\delta Y = 1/5$ for the solid meshes), and in regards to an original, undeformed, configuration. Table. (3.1) and Table. (3.2) show the corresponding element sizes and the total number of elements (in fluid and solid meshes combined) for all the meshes simulated.

In a series of verification studies presented below, including h-refinement, p-refinement and temporal refinement, the meshes from Table. (3.1) are used with a varying polynomial order and time step of the simulation. To keep the notation clear, We define the mesh at a level k with the polynomial order p and a time step δt as $Mk^{(Pp,\,\delta t)}$. For example, the mesh M2 using 4^{th} order polynomials and a time step $\delta t = 0.03125$ is denoted as $M2^{(P4,\,0.03125)}$. Furthermore, for a consistent refinement study, the reference solution is taken from a mesh that has a highest level of refinement in a variable with respect to which the refinement is studied. Table. (3.3) gives a list of the test meshes and a mesh used for a reference solution for each type of the refinement studies performed. The tolerances in the spatial and temporal refinement

studies are set to their baseline values of $\kappa_s = 10^{-12}$, $\kappa_f = 10^{-6}, \kappa = 10^{-5}$ in all the test meshes and the reference mesh, as shown in Table. (3.3), while they vary in the tolerance sensitivity study as described below.

Error Metrics

To evaluate the performance of the coupled solver and the errors of approximation pertinent to an unsteady fluid-structure interaction problem, we monitor the time-dependent errors of the two relevant quantities: 1) vertical displacement of the mid-point of the FSI interface, $d_y\left(X_m, Y_m, Z_m, t\right)$, where $(X_m, Y_m, Z_m) = (3, 1, 0)$ in the undeformed configuration, 2) the flow drag at the FSI interface defined as the integral of the x-component of the local fluid force,

$$F_d(t) = -\int_{\Gamma_{fsi}(t)} (\sigma_f \, \vec{n}_f) \cdot \vec{i} \, d\,\Gamma, \tag{3.95}$$

where σ_f is the Cauchy stress tensor of the fluid defined by Eq. (3.39), $\vec{n}_f$ is the outward-pointing unit normal vector at the FSI interface, $\vec{i}$ is the unit vector in a streamwise direction. Since the fluid Cauchy stress tensor consists of the pressure and viscous components, pressure and viscous drag can be defined, correspondingly, as

$$F_p(t) = \int_{\Gamma_{fsi}(t)} (p \, \vec{n}_f) \cdot \vec{i} \; d\,\Gamma, \tag{3.96}$$

$$F_v(t) = -\int_{\Gamma_{fsi}(t)} [\mu(\nabla \mathbf{u} + (\nabla \mathbf{u})^T) \, \vec{n}_f] \cdot \vec{i} \, d\,\Gamma, \tag{3.97}$$

with

$$F_d(t) = F_p(t) + F_v(t). \tag{3.98}$$

I note that the number of elements in streamwise and spanwise directions is always even for all the meshes, so that no interpolation is required to obtain the midpoint

displacement, since it is located at the intersection between the elements, where a GLL node always exists.

In this study, we investigate two error norms, L^2 and L^∞, defined as

$$L^2(q) = \sqrt{\frac{\int_0^{t_f} \left(q_{ref}(t) - q_{comp}(t)\right)^2 \, \mathrm{d}\, t}{t_f}}, \tag{3.99}$$

$$L^\infty(q) = \max_{t\in[0,t_f]} \left|q_{ref}(t) - q_{comp}(t)\right|, \tag{3.100}$$

where q_{comp} is the quantity taken from the simulations at a particular refinement level, and q_{ref} is the corresponding reference value taken from a reference mesh solution, and the time $t_f = 25$ is set in the current simulations.

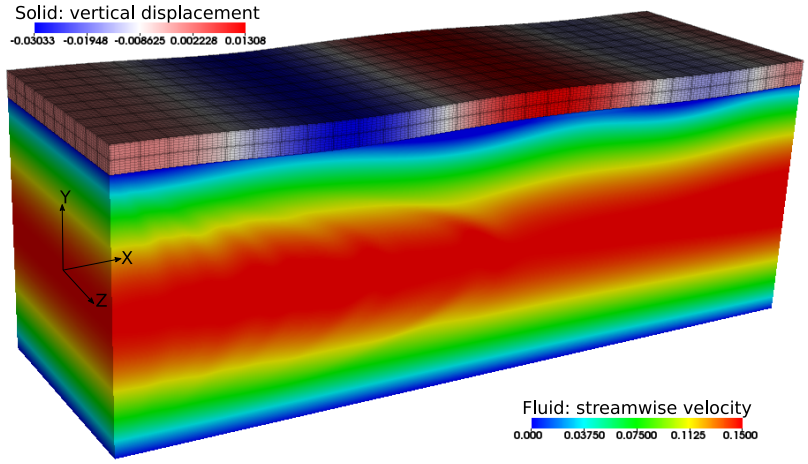

Figure 3.18: The Fluid Flow and the Solid Deformation at a time $t = 20$ for the Proposed Compliant Wall Channel 3D FSI Benchmark Using the Mesh $M4^{(P8,0.03125)}$, See Table. (3.1). Fluid Field: Streamwise Velocity; Solid Field: Vertical Displacement.

3.7.2 Results

H-Refinement

The results of the h-refinement study with the meshes $M1 - M5$ using 4^{th}-order polynomials and a time step size of $\delta t = 0.03125$ are shown in Fig. (3.19(a)), where

the $M5$ results with the same polynomial order and the time step are considered as a reference value, and the errors for the meshes $M1 - M4$ with respect to $M5$ mesh values are plotted. Fig. (3.19(a)) shows that both L^2 and L^∞ errors of displacement exhibit expected 4^{th}-order of convergence in the asymptotic limit. The order of convergence of the drag value is however reduced to the 3^{rd} order, both for L^2 and L^∞ error norms. In order to investigate what hampers the convergence of the drag values, we look into the L^2 errors for the pressure and viscous drag separately, also plotted in Fig. (3.19(a)). The results show that while the pressure drag shows the expected 4^{th}-order of convergence, it is the viscous drag that converges with the 3^{rd} order. The reason is that the viscous drag includes the first-order spatial derivatives of the velocity quantities in its definition. While velocities are approximated with the p^{th}-order polynomials functions, their derivatives are consequently approximated by the $(p-1)^{st}$ order polynomials, which drops the rate of convergence of a quantity that depends on the spatial derivatives of the solution variables by an order of a derivative Kirby *et al.* (2014).

P-Refinement

To study the implicit FSI solver convergence with p-refinement, we choose the mesh $M4$ with 4^{th}, 6^{th} and 8^{th} order polynomials and the same time step of $\delta t = 0.03125$, see Table. (3.3), while the reference solution is provided by the mesh $M7$ with the 6^{th} order polynomials and $\delta t = 0.03125$. The results of the p-refinement convergence study are shown in Fig. (3.19(b)). The expected exponential order of convergence (linear in a semi-log plot) is observed for both displacement and drag. As expected, the slope of the convergence plot is steeper for the displacement versus drag errors, commensurate with the fact that displacements are approximated with higher-order polynomial functions as discussed above.

Temporal Refinement

For a temporal convergence verification, the mesh $M2$ with 4^{th}-order polynomials is used, with the time steps $\delta t = 0.125$, $\delta t = 0.0625$ and $\delta t = 0.03125$, with a reference solution taken from $M2^{(P4,\,0.01)}$, as specified in Table. (3.3). In the temporal convergence study, the two schemes which showed a second-order convergence in the fluid-only tests, namely, the IE-ALE with GCL, and CN-ALE (see Sec. (3.4.1)) are compared. The results are shown in Fig. (3.20). It is interesting to see that, although IE-ALE with GCL showed a second-order temporal convergence in fluid-only tests on deforming meshes, its accuracy drops to the first order in the fully coupled FSI problem, while the CN-ALE scheme preserves the second order accuracy in the fully coupled problem. For a better estimation of the convergence slope, we perform a Richardson extrapolation of errors with the three chosen time steps, and calculate the convergence rate r as

$$r\left(q\right) = \frac{1}{\ln(2)} \ln\left(\frac{\left| q(M2^{(P4,0.125)}) - q(M2^{(P4,0.0625)}) \right|}{\left| q(M2^{(P4,0.0625)}) - q(M2^{(P4,0.03125)}) \right|} \right), \tag{3.101}$$

where q is the quantity to be estimated, evaluated with the different meshes. In the current study, q is taken to be the time-averaged value of the midpoint displacement and the total flow drag on the compliant surface. The results of Richardson extrapolation are shown in Table. (3.4) and Table. (3.4) confirms the conclusion that CN-ALE scheme preserves the second-order of accuracy, while IE-ALE scheme does not. This shows that, in order to keep a nominal order of convergence in the fully coupled problem, not only do both component codes have to have a time stepping scheme of the required nominal order of accuracy, but the interface coupling scheme of the same order of accuracy is also required. This also shows the importance of verification studies and convergence tests on the fully coupled FSI problem. We also

note a slightly lower rate of a temporal convergence of drag in both schemes compared to a displacement, which can also be seen in Fig. (3.20). The reason for this reduction might be associated with the fact that the drag is related to the velocity variables rather than displacements, and the nominal order of accuracy of the Newmark scheme is lower for velocities than for displacements.

Table 3.4: Temporal Convergence Rates r Obtained with the Richardson Extrapolation for the Midpoint Displacement and the Total Flow Drag on the Compliant Surface Evaluated Using the Meshes $M2^{(P4,0.03125)} - M2^{(P4,0.125)}$.

Scheme	Midpoint displacement	Total flow drag
IE-ALE with GCL	0.9440	0.6387
CN-ALE	1.8272	1.5008

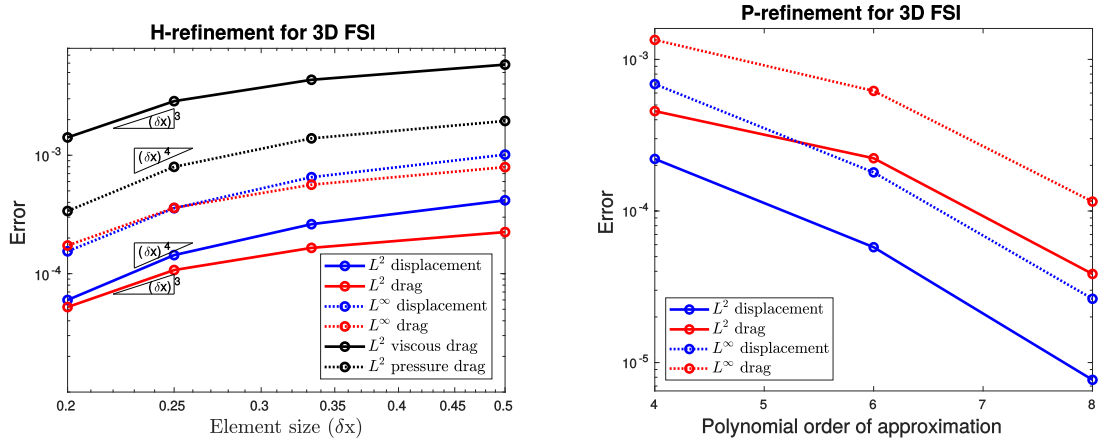

(a) H-refinement. $M1^{(P4,0.03125)}$–$M4^{(P4,0.03125)}$ are used.

(b) P-refinement. $M4^{(P4,0.03125)}$–$M4^{(P8,0.03125)}$ are used.

Figure 3.19: Spatial Convergence for the Compliant Wall Channel 3D FSI Benchmark.

Temporal Dynamics

To evaluate the effect of spatial and temporal refinement on the dynamics of the quantities of interest, we plot the temporal series of the vertical midpoint wall dis-

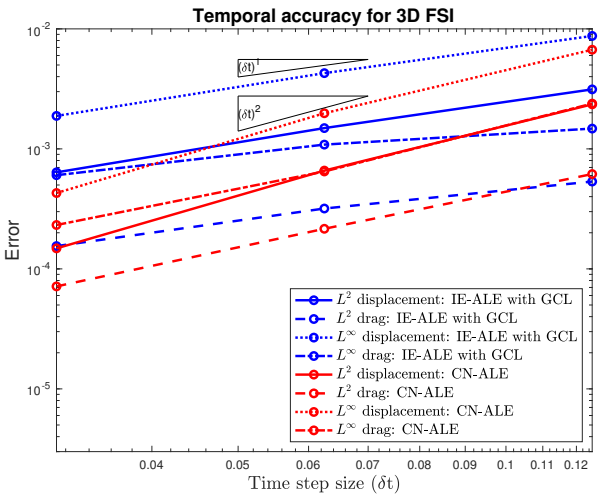

Figure 3.20: Temporal Convergence for the Compliant Wall Channel 3D FSI Benchmark. Meshes $M2^{(P4,0.03125)}$–$M2^{(P4,0.125)}$ are Used.

placement and the total flow drag on the compliant surface in Fig. (3.17) for the different meshes. For the displacement evolution, Fig. (3.17(a)) demonstrates that all the cases with different levels of h-refinement, p-refinement and time step, show essentially identical values. The drag evolution shown in Fig. (3.17(b)) is, however, more sensitive to a spatial refinement, showing that it requires finer meshes and/or higher polynomial orders to converge the values of drag. From Fig. (3.17(c)) and Fig. (3.17(d)), it can also be seen that the meshes with one and two layers of solid elements produce identical results, testifying that the two layers of solid elements provide an adequate resolution for the solid. Since displacement is less sensitive to a spatial refinement compared to a drag, this means that in the situations where primarily a displacement of the structure is of interest, the mesh size (the total number of degrees of freedom) could be reduced to save cost.

This high sensitivity of drag to a spatial resolution can explain why it is difficult to obtain ideal convergence slopes with $h-$ and $p-$refinements across a large range of h, p levels in the FSI problem, i.e., for meshes that differ significantly in their spatial resolutions, as observed in Fig. (3.19). Since the drag force is the one that

drives the motion of the solid, which in turns drives the fluid, the spatial resolution of drag now also effects the temporal dynamics, and not only the spatial accuracy. A slightly different temporal dynamics at different spatial resolutions results in a fact that the values that are being compared are now also shifted in time which is shown in Fig. (3.21). For the error estimates such as these obtained with Eq. (3.99), Eq. (3.100), when the errors are compared at the same time step, the outcome is that the temporal differences introduced by different spatial resolutions now implicitly enter the spatial convergence results, which makes it difficult to separate temporal and spatial errors, and obtain an anticipated spatial convergence rate across a wide range of resolutions. It would be interesting to devise improved error metrics, for example, using a temporal convolution of the values at different spatial resolutions, to assess the applicability of such enhanced error measures to the coupled multi-physics problems, which will be investigated in the future work.

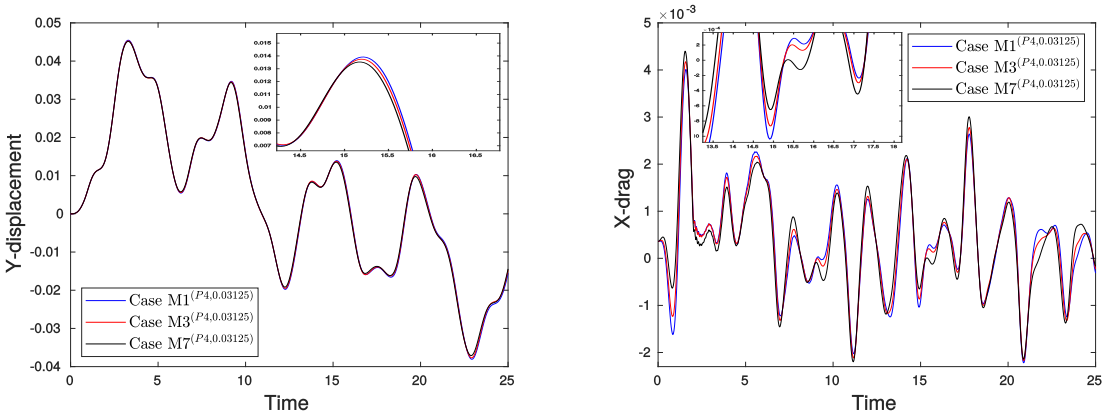

(a) Midpoint wall vertical displacement for the baseline (M) meshes.

(b) Total flow drag on the compliant wall for the baseline (M) meshes.

Figure 3.21: Temporal Series of the Midpoint Wall Vertical Displacement and the Total Flow Drag (Pressure and Viscous Drag) on the Compliant Wall for Different Meshes for Shift Observation.

Tolerance Study

We now turn our attention to the effect of the FSI convergence criteria κ and the fluid solver tolerance κ_f on the L^2 and L^∞ errors of the quantities of interest in the FSI problem. It is important to quantify this effect, since higher tolerances can be associated with faster solver execution times but can incur larger global errors. Understanding the tradeoff is helpful for practical applications. In the current study, the mesh $M2^{(P4,0.05)}$ is used with various values of the FSI and fluid solver tolerances κ, κ_f ranging from 10^{-2} to 10^{-6} as given in Table. (3.5). Solid solver tolerance is fixed at 10^{-12} in all the studies. The reason we do not vary the solid tolerance is because the solid iterations account for a small fraction of the total computational time of the coupled FSI solver, due to a dominance of the computational cost by the pressure Poisson solution of the Navier-Stokes equations, and due to a relatively small size of a solid domain compared to a fluid domain. Keeping a solid solver tolerance at a very low level as in the current tests ensures that the errors from the iterative convergence of the solid solver are minimized, at essentially no additional cost.

The L^2 and L_∞ errors for the vertical wall displacement and the total flow drag on a compliant surface at various fluid and FSI tolerances are shown in Fig. (3.22) (note that there is no data point for the $(\kappa_s, \kappa_f, \kappa) = (10^{-12}, 10^{-6}, 10^{-6})$ case, which corresponds to the reference mesh, and for which the error is identically zero). One can see that for both displacement and the drag, the effect of the fluid solver tolerance κ_f is negligible as long as the tolerance does not exceed the value of $\kappa_f = 10^{-3}$, which means that this value of the fluid tolerance should in general be sufficient for convergence.

The strong effect of the FSI tolerance κ is pronounced for both quantities, with errors decreasing by three to four orders of magnitude when κ is reduced from 10^{-2} to

10^{-6}. However, for the lowest fluid solver tolerance $\kappa_f = 10^{-2}$, the effect of tightening the FSI solver tolerance κ is of diminishing return, since the error is then dominated by a poor fluid solver convergence and is not improved by a stronger fluid-solid coupling.

To assess the increase in the computational cost associated with the tightening of the convergence criteria, the number of iterations taken by the component solvers and by the FSI interface coupling routine in response to different values of the convergence tolerances is shown in Fig. (3.23). The number of iterations taken by the solvers at each time step is averaged over the entire time of the simulations, thus an averaged number of iterations is presented. we see that, as expected, the number of FSI iterations do not depend on the fluid solver tolerance κ_f, while increasing the FSI tolerance κ from 10^{-6} to 10^{-2} reduces the average number of iterations from ten to four, thus reducing the global solver cost by approximately 2.5 times. Fig. (3.23(b)) shows that the number of solid solver iterations depends neither on the fluid tolerance nor the FSI tolerance, as expected. The number of fluid solver iterations does not depend on the FSI tolerance either, however, it does depend on the fluid tolerance. While Fig. (3.22) showed that the fluid tolerance can be increased from 10^{-6} to 10^{-3} without affecting the accuracy, Fig. (3.23(b)) shows that this increase will decrease the number of iterations from four to two which will, essentially, cut the total computational cost by two, since the cost of the fluid solver, due to a Poisson equation solution, far exceeds that of the solid solver. Therefore, for practical FSI implementations where a cost versus accuracy tradeoff may be considered, we recommend increasing the fluid solver tolerance while keeping the FSI tolerance as low as possible.

Table 3.5: Mesh, Tolerance Values, and a Reference Solution Used for the Solver Tolerance Study in the Proposed Compliant Wall Channel 3D FSI Benchmark.

Mesh level	Polynomial order	Time step, δt	κ_s	κ_f	κ	Reference mesh
M2	P4	0.05	10^{-12}	$[10^{-6} : 10^{-2}]$	$[10^{-6} : 10^{-2}]$	$M2^{(P4,\,0.05)}$ with $(\kappa_s, \kappa_f, \kappa) = (10^{-12}, 10^{-6}, 10^{-6})$

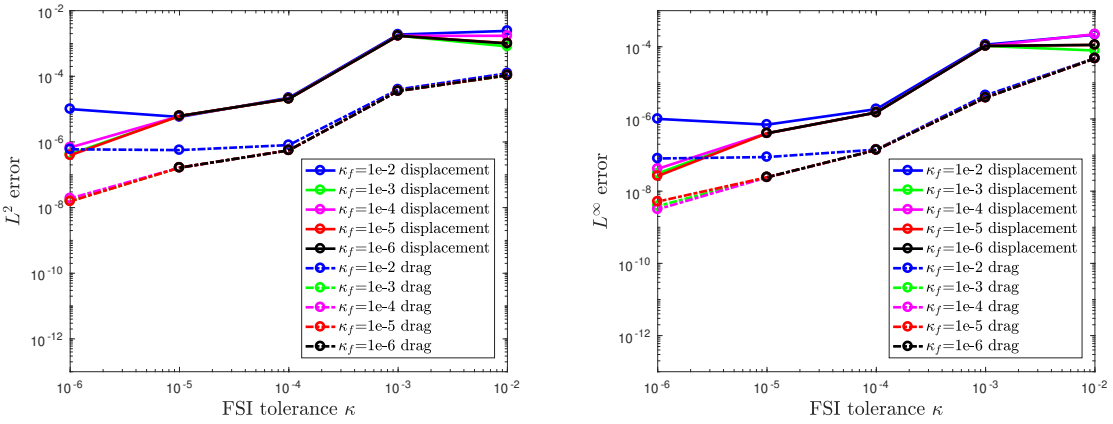

(a) L^2 error. (b) L^∞ error.

Figure 3.22: Effect of Tolerances on the Solution Errors for Compliant Wall Channel 3D FSI Benchmark.

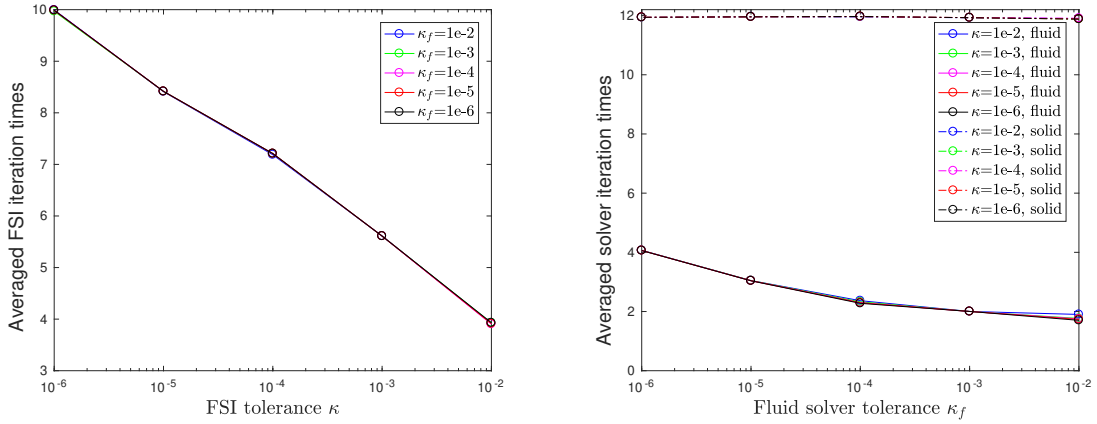

(a) Effect on FSI iterations. (b) Effect on component solver iterations.

Figure 3.23: Effect of Tolerances on the Number of Solver Iterations for Compliant Wall Channel 3D FSI Benchmark.

3.8 Validation of Generalized Robin-Neumann Explicit FSI Coupling Scheme

In this section, we present the validation of generalized Robin-Neumann explicit FSI coupling scheme via the case we proposed in Sec. (3.7) and Walsh's eddy(Sec. (3.5.2)).

For Walsh's eddy, we set one of the boundary to be Robin, and use current time step stress and velocity from analytical solution for the RHS of Eq. (3.79). The mesh here is no longer moving and the fluid solver is not iterative to avoid additional uncertainty. The h-refinement results at time $t_f = 1$ with $\delta t = 10^{-4}$ are shown in Fig. (3.24). It shows losing one order of accuracy for both velocity and pressure. This is due to the fact that $P_N - P_{N-2}$ formulation is used in the case and the simulation is not iterative. Additionally, since combined stress and velocity boundary condition is used, lower order of pressure affects the order of velocity as consequent. Although Robin boundary condition does not provide expected order of velocity, but the convergence order of pressure is increased.

To step further for the validation of FSI coupling based on Robin-Neumann boundary conditions, time series of displacement/drag, h/p and temporal convergence studies of flow in a compliant wall channel case Sec. (3.7) would be performed.

As mentioned earlier, implicit FSI coupling requires an iterative fluid solver for stability, and explicit FSI coupling ensures stability. But it is still unknown how much tolerance or inner fluid iteration times should be used for explicit FSI coupling and whether it would affect the results. To validate it, we show displacement and drag results from $M4^{(P6,0.03125)}$ with implicit FSI, explicit FSI with 3 iterations, 6 iterations and 10 iterations shown in Fig. (3.25). It shows that with more iterations, explicit FSI coupling could achieve closer results compared to implicit FSI coupling. It makes sense as still iterative procedure helps to have more accurate results in fluid although inaccurate results would not affect the stability of explicit FSI coupling.

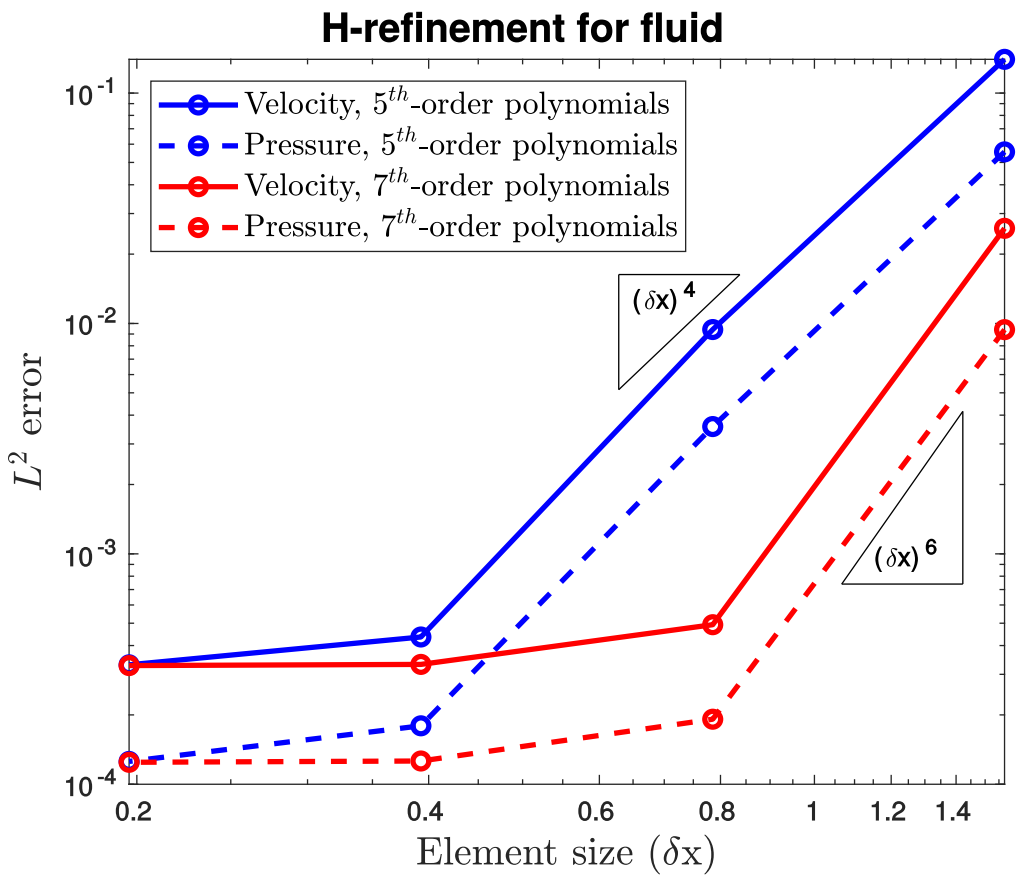

Figure 3.24: H-refinement for the Convecting Walsh's Eddies Case at Time $t_f = 1$ Using Time Step $\delta t = 10^{-4}$ for Validation of Robin Boundary Condition.

But in general, the accuracy of explicit FSI coupling even with 10 iterations is still acceptable in a engineering based point of view.

Before drawing the conclusion that explicit coupling is inaccurate, one important thing to compare is the computational cost. For implicit FSI coupling ($M4^{(P6,0.03125)}$), it requires 248246 seconds with certain amount of processors, while for explicit FSI coupling (6 iterations), it only takes 14607 seconds for the same amount of processors and same cluster. That is about $\frac{1}{17}$ cost of the implicit FSI coupling. Thus, although explicit FSI coupling is losing accuracy, but it is acceptable compared to the cost saving as FSI coupling is quite expensive. It is also mentionable here that since explicit FSI coupling is cheap, to achieve the accuracy, we here use certain amount

of fluid iteration rather than convergence criteria for certain accuracy control.

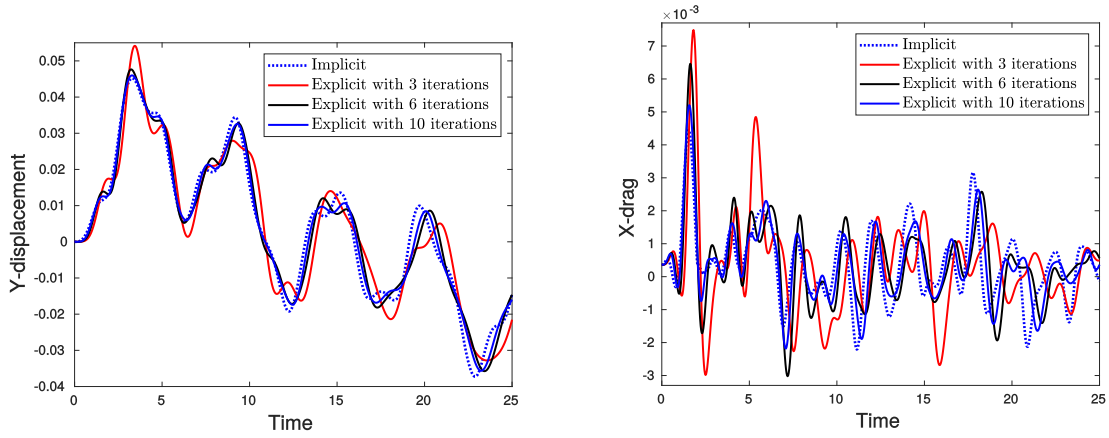

(a) Midpoint wall vertical displacement. (b) Total flow drag on the compliant wall.

Figure 3.25: Temporal Series of the Midpoint Wall Vertical Displacement and the Total Flow Drag (Pressure and Viscous Drag) on the Compliant Wall for Different Meshes for Explicit FSI Coupling Validation.

For temporal convergence verification, the mesh $M2$ with 4^{th}-order polynomials is used, with 6 fluid iteration, the time steps $\delta t = 0.125$, $\delta t = 0.0625$ and $\delta t = 0.03125$. We perform a Richardson extrapolation of errors with the three chosen time steps, and calculate the convergence rate as Eq. (3.101) and the results are shown in Table. (3.6). The reason half time is used for flow drag time series is that it is too unstable to get order of convergence about the end of simulation with $\delta t = 0.03125$. This is due to the structural instability with coarse mesh and small time step as observed during testing. It is shown that the temporal convergence is well achieved for both displacement and drag for BDF1 scheme while only 1st order convergence is observed for BDF2. It may be due to the first order temporal discretization used for the RHS of Eq. (3.76). However, instability is observed for higher order scheme in Fernández *et al.* (2015). Thus, only first order temporal scheme is used in explicit FSI coupling.

As for h-refinement study of explicit FSI coupling, the meshes $M2 - M7$ using 4^{th}-order polynomials and a time step size of $\delta t = 0.03125$ are shown in Fig. (3.26(a)),

Table 3.6: Temporal Convergence Rates r Obtained with the Richardson Extrapolation for the Midpoint Displacement and the Total Flow Drag on the Compliant Surface Evaluated Using the Meshes $M2^{(P4,0.03125)} - M2^{(P4,0.125)}$.

Scheme	Midpoint displacement	Total flow drag (half time)
BDF1	1.1456	1.0510
BDF2	0.8873	0.6408

where the $M7$ results with the same polynomial order and the time step are considered as a reference value, and the errors for the meshes $M2-M6$ with respect to $M5$ mesh values are plotted Fig. (3.26(a)) shows that both L^2 and L^∞ errors of displacement and drag exhibit expected 4^{th}-order of convergence in the asymptotic limit. The consistent convergence of displacement and drag should be related to using combine Robin boundary conditions and solving iteratively.

To study the explicit FSI solver convergence with p-refinement, the mesh $M4$ with 4^{th}, 6^{th}, and 8^{th} order polynomials and the same time step size of $\delta t = 0.03125$ are used. The reference solution is provided by the mesh $M7$ with the 6^{th} order polynomials and $\delta t = 0.03125$. Shown in Fig. (3.26(b)), the expected exponential order of convergence (linear in a semi-log plot) is observed for both displacement and drag although the slope of the convergence plot is not that steep as the same reason mentioned in Sec. (3.7.2).

From above we could conclude that, generalized explicit FSI coupling scheme based on Robin-Neumann boundary conditions is validated. The accuracy might be low but it could be improved by increasing the number of fluid solver iteration and most importantly, the cost savings is tremendous.

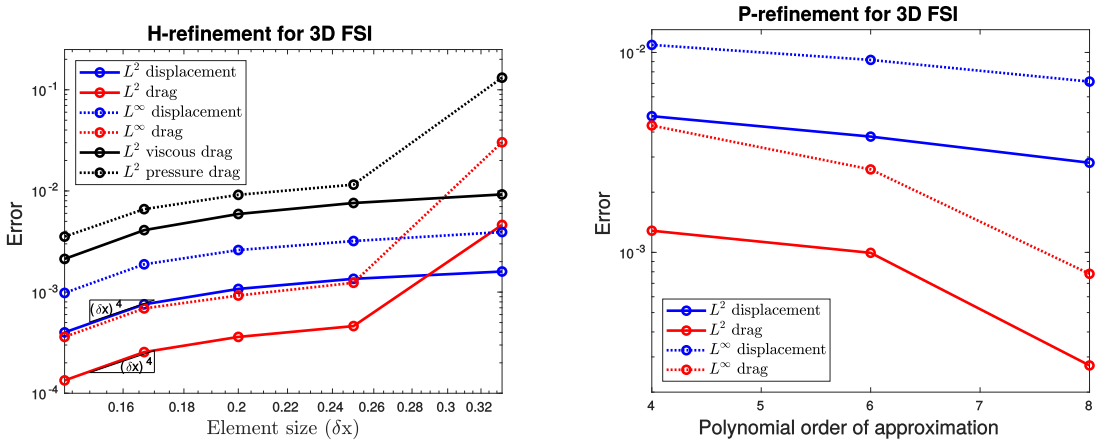

(a) H-refinement. $M2^{(P4,0.03125)}$–$M6^{(P4,0.03125)}$ are used.

(b) P-refinement. $M4^{(P4,0.03125)}$–$M4^{(P8,0.03125)}$ are used.

Figure 3.26: Spatial Convergence for the Compliant Wall Channel 3D FSI Benchmark with Explicit FSI Coupling.

3.9 Fluid-Structure Interaction in a 3D Turbulent Channel with a Compliant Wall

3.9.1 Problem Formulation

In this section, we extend the developed explicit FSI solver to a Direct Numerical Simulation of an interaction of a turbulent flow with a nonlinearly elastic compliant wall. The reason of using explicit FSI coupling scheme instead of the implicit one is the huge cost of such problems as the interface needs to be refined more than stationary one for capturing the small scale surface motion.

Previous computational studies of the interaction between the turbulent flow and an elastic surface were primarily confined to a zero-thickness spring-backed membrane model for the solid material (Kim and Choi (2014); Xu *et al.* (2003); Xia *et al.* (2017)). In addition to being a very simplistic model that neglects many important effects pertinent to structural dynamics related to multi-dimensionality and non-linearity, the spring-backed membrane model does not allow for longitudinal wall motions, which have been found to be important (Benschop *et al.* (2019)), especially during the

interaction with turbulence, where the properties of the fluctuating field are crucial in determining the global structure of turbulence, and their artificial suppression might draw an incomplete picture. In a recent computational study, Rosti and Brandt (2017) used a monolithic FSI approach combined with a 2^{nd}-order finite difference scheme to model the interaction of an incompressible flow in a channel with a hyperelastic Mooney-Rivlin material wall. With a monolithic approach, an FSI interface is not resolved, but implicitly embedded into the computational cells analogously to the methodology of immersed boundary techniques (Mittal and Iaccarino (2005)). This leads to a low-order representation of the interface and the surrounding near-wall velocities, which can create some numerical deficiencies in a case of a turbulent flow.

The presented simulation is the first attempt to apply a high-order interface-resolving FSI solver to a Direct Numerical Simulation of a turbulent channel flow interacting with a nonlinear, hyperelastic wall. The setup of the problem is similar to the one described in the previous section. A fluid flow in an originally rectilinear box of the length $(L_x, L_y, L_z) = (6H, 2H, 3H)$ interacts with a nonlinearly elastic solid layer of the thickness $D = 0.6H$ at its top boundary. The boundary conditions for the fluid are: 1) periodic in streamwise and spanwise directions, 2) a no-slip wall enforced at the bottom boundary $Y = -H$, 3) fluid-structure interface at the top wall $Y = H$. A forcing function is applied in a streamwise direction to keep the mass flow rate constant (Merrill *et al.* (2016a)). The Reynolds number of the flow based on the bulk mean velocity U and a channel half-width H is set as $Re = UH/\nu = 2800$, which for channel flow is in the turbulent regime (Kim *et al.* (1987)). An illustration of the domain geometry for the fluid and the solid layers and the overall problem setup is presented in Fig. (3.27).

A fully-developed turbulent channel flow with rigid walls is first obtained before the interaction with a compliant solid is initiated. To trigger the transition to

turbulence in a channel, the following initial conditions for the fluid flow are specified(citesprague)

$$\begin{aligned} u_x/U &= 5(1-(\tilde{y})^4)/4 + 0.3\cos(12\tilde{z})e^{0.5-32.4(1-|\tilde{y}|)^2}(1-|\tilde{y}|), \\ u_y/U &= 0, \\ u_z/U &= 21.6\sin(12\tilde{x})e^{-32.4(1-|\tilde{y}|)^2}(1-|\tilde{y}|), \end{aligned} \tag{3.102}$$

where $\{\tilde{x},\tilde{y},\tilde{z}\} = \{x/H, y/H, z/H\}$. Initial perturbations are necessary in this case, since discretization errors in a spectral-element method are intrinsically low and, by themselves, are unable to trigger transition to turbulence. Additionally, the channel flow with the current relatively low Reynolds number is linearly stable. The specified initial conditions correspond to an initial perturbation in a form of elongated high- and low- speed streaks with superimposed spanwise velocity perturbations. According to a recent research, this type of perturbations triggers auto-generating mechanisms of turbulence, via which the turbulence is initiated and sustained Butler and Farrell (1992); Jiménez (1994); Hamilton *et al.* (1995).

The simulations are run on a mesh with the number of fluid elements is $(n_{f,x}, n_{f,y}, n_{f,z}) = (40, 11, 20)$, while the polynomial order of $N = 7$ is used for a spectral element discretization in space. The element spacing in the y direction is given in Sprague *et al.* (2010) with additional half-size layer for the first element of the FSI interface , while the element sizes in x and z directions are uniform. Note that Sprague *et al.* (2010) used the same spectral-element code Nek5000 in their study of a turbulent rigid-wall channel flow with $Re = 2800$. After running the decoupled fluid solver for $250H/U$ time units, turbulence becomes statistically stationary (Sprague *et al.* (2010)). Turbulent statistics are subsequently gathered over $50H/U$ time units. Before moving on to the FSI study, turbulent statistics were validated against the results of Sprague *et al.* (2010) and Kim *et al.* (1987), and a good agreement was obtained (not shown here). Based on the calculated wall shear

stress, the obtained grid resolution in wall units is documented in Table. (3.7).

After a simulation time of $250H/U$ time units, the fluid-structure interaction is initiated with time reset to $0H/U$. An elastic solid layer added on top of the fluid domain covers the whole extent of the top channel boundary and has the dimensions of $(L_x, L_y, L_z) = (6H, 0.6H, 3H)$. A solid layer is modeled by a nonlinear hyperelastic St. Venant-Kirchhoff material model as described in Sec. (3.3.1). The boundary conditions for the solid are: 1) periodic in streamwise and spanwise directions, 2) fluid-structure interface at the lower solid boundary $Y = H$, 3) clamped wall at the top solid boundary $Y = 1.6\,H$. The solid boundary locations are given in an undeformed configuration. The number of elements for the solid are: $(n_{s,x}, n_{s,y}, n_{s,z}) = (40, 4, 20)$ with the polynomial order of $N = 7$. The element sizes are uniform in all three directions.

The material properties for the solid are set for three cases, (E1) density $\rho_s = 20\,\rho_f$, Young's modulus as $E = 2\,\rho_f U^2$, and Poisson's ratio as $\nu_s = 0.4$, (E2) density $\rho_s = 20\,\rho_f$, Young's modulus as $E = 5\,\rho_f U^2$, and Poisson's ratio as $\nu_s = 0.4$, and (E3) density $\rho_s = 2\,\rho_f$, Young's modulus as $E = 20\,\rho_f U^2$, and Poisson's ratio as $\nu_s = 0.4$.

These material properties can be converted into λ_s and μ_s as Lamé constants in a constitutive relation, Eq. (3.19). A measure of the wall inertia relative to the fluid is often presented as the non-dimensional parameter $C_m = (\rho_s\, D)/(\rho_f\, H)$. The higher C_m is, the heavier is the wall and the fewer interactions are expected between the solid and the fluid, while for a lower C_m the situation is the opposite. In the current simulations, the value of $C_m = 12$ for E1, $C_m = 12$ for E2, $C_m = 1.2$ for E3 is used, which corresponds to a moderately light wall considered in previous theoretical studies (Luhar *et al.* (2015)) and in simulations (Kim and Choi (2014)). Another material parameter that characterizes a potential of the structure to stimulate strong coupling processes with the fluid is the shear wave speed. Previous studies have

shown that a strong interaction can be expected if the elastic shear wave speed is less than the flow speed (Gad-el-Hak *et al.* (1984); Lee *et al.* (1995)). Shear wave speed for the current solid is $c_t = \sqrt{E/(2\,(1+\nu)\,\rho_s)} = 0.189\,U$ for E1 and $c_t = 0.2988\,U$ for E2, which corresponds to a soft wall capable of interactions with the fluid. But $c_t = 1.8898\,U$ for E3 is on the contrary. The initial conditions for the solid are at zero displacements, velocities and acceleration. The FSI simulations are advanced with the time step $\delta t = 0.001\,H/U$, which leads to a Courant number of approximately 0.134. Three fluid iterations were found sufficient for stability and accuracy. The simulation is run till time $70H/U$ and we name A1, A2...A7 for the average data from time $0H/U - 10H/U$, $10H/U - 20H/U$...$60H/U - 70H/U$ correspondingly.

Table 3.7: Mesh Resolution in Wall Units in Undeformed Configuration for the Fluid Mesh Used in the Turbulent Channel Flow Case Based on u_τ of the Corresponding Rigid Wall Case. Wall Units are Defined as $L^+ = L\,u_\tau/\nu$, with $u_\tau = \sqrt{\tau_w/\rho}$ Being Wall Friction Velocity, τ_w is Wall Shear Stress, $Re_\tau = u_\tau H/\nu$. ΔL^+, min Corresponds to a Minimum Distance Between the Grid Points Across All Elements and GLL Points, While ΔL^+, max Corresponds to a Maximum Distance. Difference in Uniform x and z Directions is Solely Due to a Non-uniform GLL Points Distribution.

Re_τ	ΔX^+, min	ΔX^+, max	ΔY^+, min	ΔY^+, max	ΔZ^+, min	ΔZ^+, max
180.4436	1.7359	5.6659	0.3124	18.1318	1.7359	5.6648

3.9.2 Results

Although the solid material surface in contact with the fluid is originally flat, a fluid-solid interface soon develops small-scale deformations from the influence of the fluctuating pressure and viscous forces in a turbulent flow for case E1 and E2.

Figs. 3.28 and 3.29 show a visualization of the instantaneous streamwise vorticity and a top surface deformation at time $50H/U$ and $70H/U$ from the beginning of the

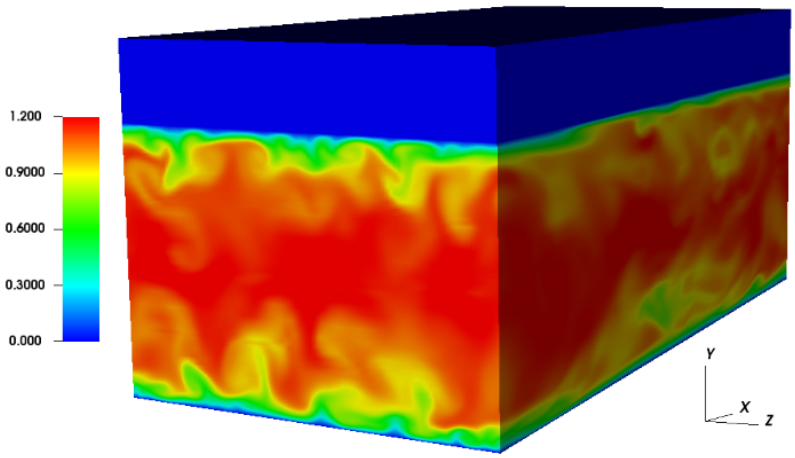

Figure 3.27: FSI in a Turbulent Channel Domain Geometry and Problem Setup. The Blue Layer on Top Corresponds to a Hyperelastic Solid Coating. The Snapshot of the Streamwise Fluid Velocity (Refer to the Colorbar for Values) Shows a Streamwise-spanwise View of High- and Low-speed Streaks in a Turbulent Channel Flow.

FSI simulations for material E1, where the small-scale wrinkle originating in the top surface deformation field can be observed. Compared to Figs. 3.30 and 3.31 which has slightly higher stiffness (Young's modulus), E1 shows more surface small-scale wrinkle and while E2 shows more large-scale wrinkle. For both E1 and E2, their wrinkle generated from flat surface especially from time $50H/U$ to $70H/U$ indicating the system energy increase dramatically during that period. From Fig. (3.32), we could see that the surface barely moves but the streamwise vortex shown on the interface is different from what we could observe from a rigid wall, which is elongated like the downstream region of Fig. (3.32). The broken down vortices indicates very large scale motion with very small displacement of the interface. Although stiffness indicates hardness of deformation, but for such coupled system, high stiffness shows more of large scale motion rather than small scale.

The unsteady interaction processes between the fluid flow and a hyperelastic compliant wall significantly change the structure of turbulence as can be seen from Fig. (3.33), Fig. (3.34), and Fig. (3.35), where streamwise vorticity slices at $Y^+ = 5.4$

(based on the Re_τ in Table. (3.7)) from the lower and upper walls are presented to show the difference between the bottom rigid and the top flexible surfaces in the current simulations at a time of $70H/U$, while Fig. (3.36), Fig. (3.37), and Fig. (3.38) are from the slices at $Y^+ = 12.6$. Note that the location of the slices for visualization refers to an undeformed configuration. It can be seen that elongated quasi-streamwise vortices typical of a classical near-wall turbulence in a presence of a rigid wall (Adrian (2007)) (see Figs. 3.33(a), 3.34(a) and 3.35(a)) are broken down by a flexible wall in Figs. 3.33(b), 3.34(b) and 3.35(b), and a significant amount of small-scale vorticity is generated, forming structures that are no longer primarily aligned with the mean flow direction. It could be understandable for E1 and E2 for observable deformation but apparently according to E3 (Fig. (3.35(b))), quite small deformation at a certain location would be enough to cause vortices broken down.

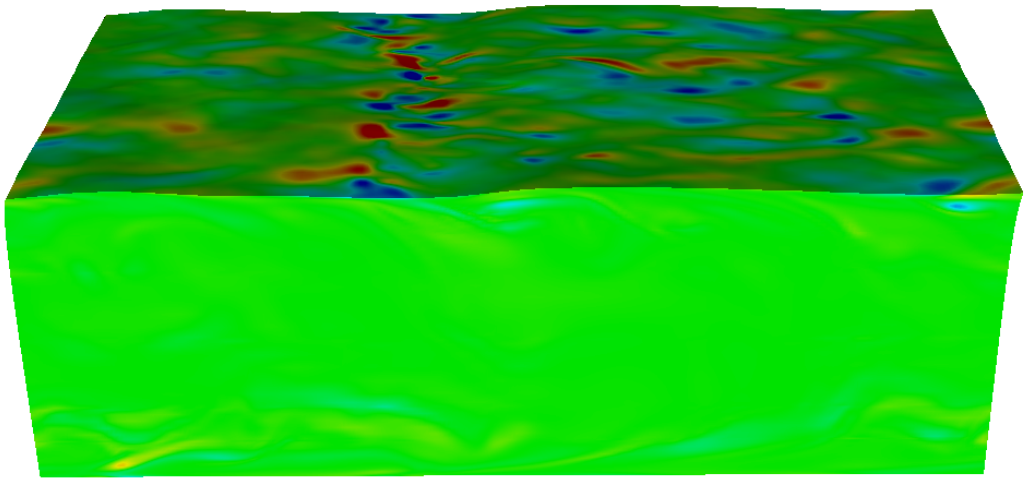

Figure 3.28: Instantaneous Streamwise Vorticity and the Deformation of the Fluid-solid Interface for Material E1 at Time $50H/U$, Color Bar from -20 (Blue) to 20 (Red).

We next present the time series of the total flow drag defined in Eq. (3.95) for both the bottom and top walls for the FSI (E1, E2, E3) and no-FSI turbulent channel flow cases in Fig. (3.39). Without FSI, the flow drag among the lower and upper walls exhibits similar, relatively smooth and constant time dynamics. For all FSI

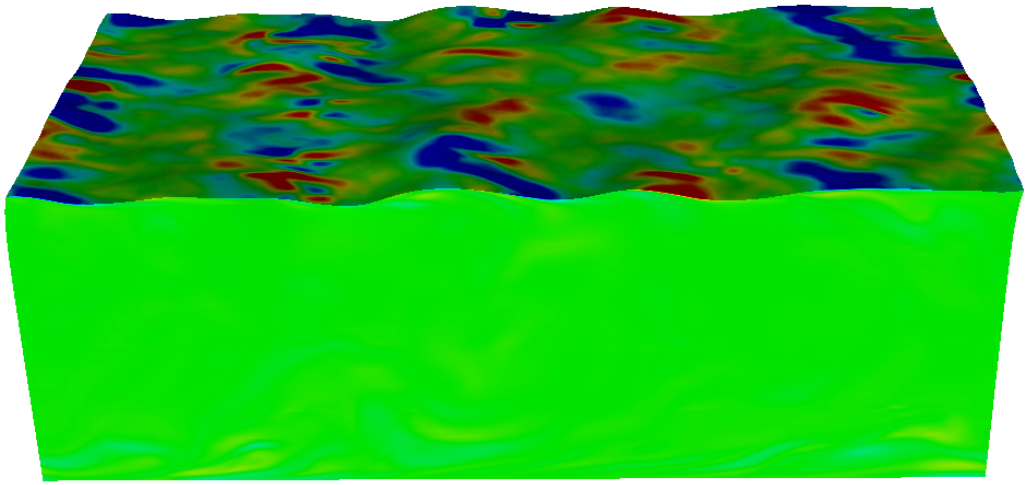

Figure 3.29: Instantaneous Streamwise Vorticity and the Deformation of the Fluid-solid Interface for Material E1 at Time $70H/U$, Color Bar from -20 (Blue) to 20 (Red).

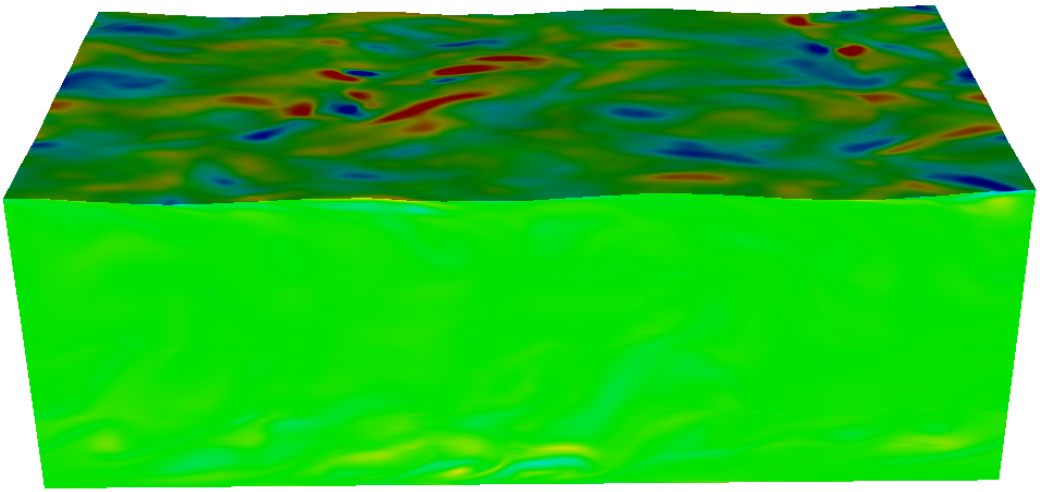

Figure 3.30: Instantaneous Streamwise Vorticity and the Deformation of the Fluid-solid Interface for Material E2 at Time $50H/U$, Color Bar from -20 (Blue) to 20 (Red).

cases, surface drag of lower wall tends to be slightly smaller compared to lower wall without FSI. The drag on the upper wall shows completely different dynamics when FSI is introduced compared to the lower wall. Both three cases (E1, E2, E3) show a conceptually similar trend of the drag force at elastic walls in an FSI flow as they all becomes larger than the rigid wall. For E1 and E2, the drag increases about exponentially and higher stiffness (E2) tends to have much more drag on the upper

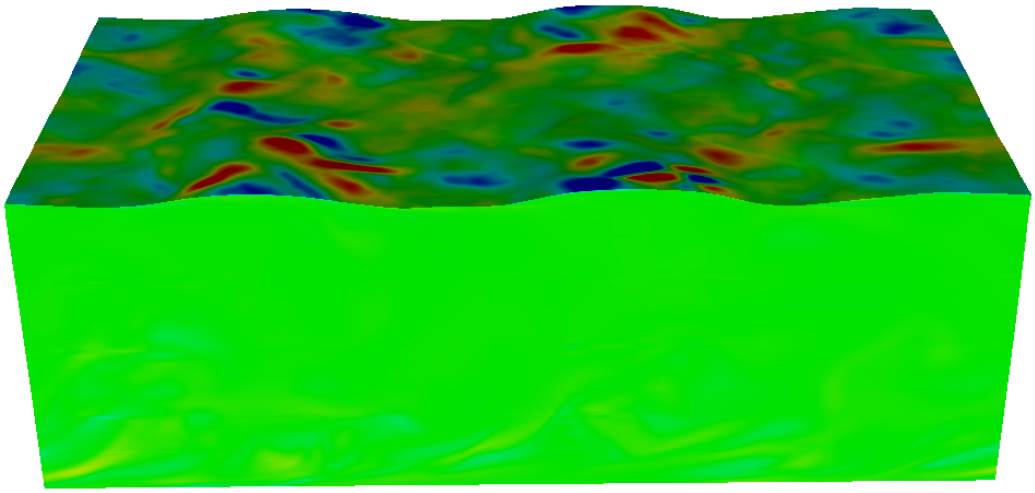

Figure 3.31: Instantaneous Streamwise Vorticity and the Deformation of the Fluid-solid Interface for Material E2 at Time $70H/U$, Color Bar from -20 (Blue) to 20 (Red).

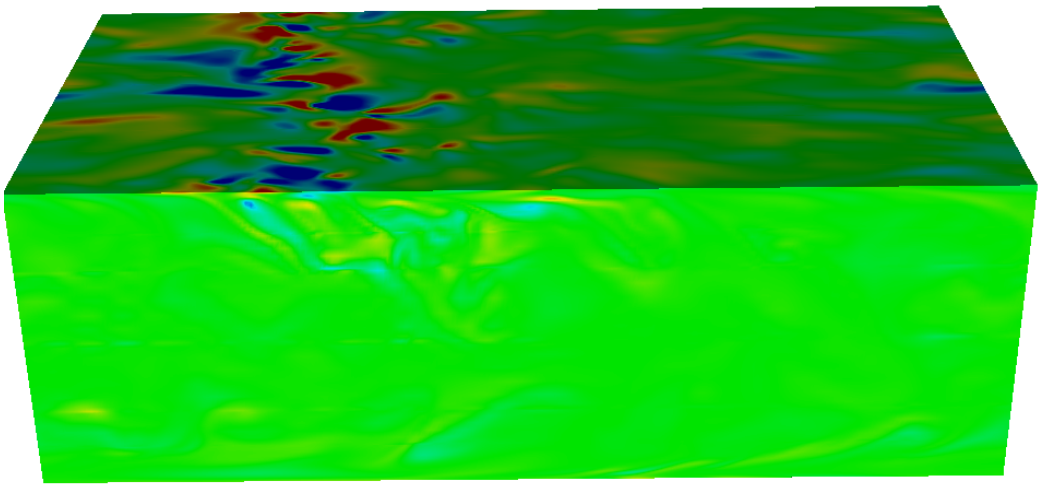

Figure 3.32: Instantaneous Streamwise Vorticity and the Deformation of the Fluid-solid Interface for Material E3 at Time $70H/U$, Color Bar from -20 (Blue) to 20 (Red).

FSI interface for larger riblets interface structures. While for E3, although the surface motion is almost stationary, the drag on the FSI interace is still higher than the rigid wall indicating a small surface motion.

Regardless of large drag for FSI turbulent channel flow cases, total forcing shown in Fig. (3.40) gives different trend. The initial bump from the time $0H/U$ to about $10H/U$ is caused by restart discontinuity. Both E1 and E2 show increased forcing

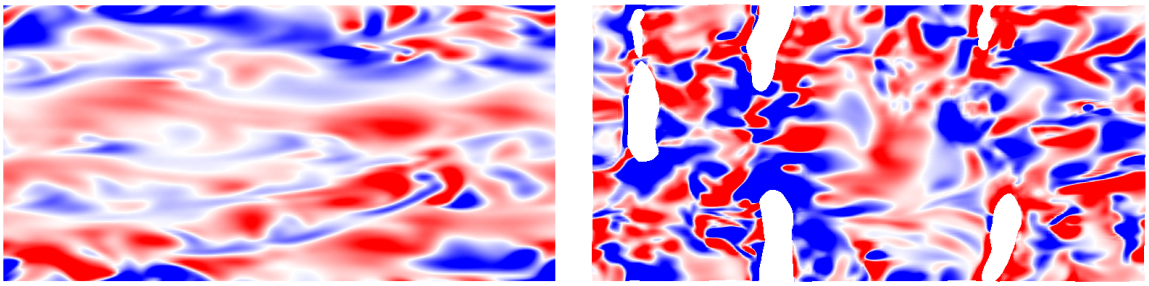

(a) Lower wall streamwise vortcity at $Y = -0.97H$ for the FSI case.

(b) Upper wall streamwise vorticity at $Y = 0.97H$ for the FSI case.

Figure 3.33: Instantaneous Snapshots of Streamwise Vorticity at $Y^+ = 5.4$ for E1 from the Lower and Upper Surfaces in a Turbulent Channel Flow at Time $70H/U$, Color Bar from -2 (Blue) to 2 (Red). Note the Change in the Color Bar Compared to Fig. (3.29). The Location of the Planes for Visualization Refers to an Undeformed Configuration. The White Area Contains No Data for Surface Deformation.

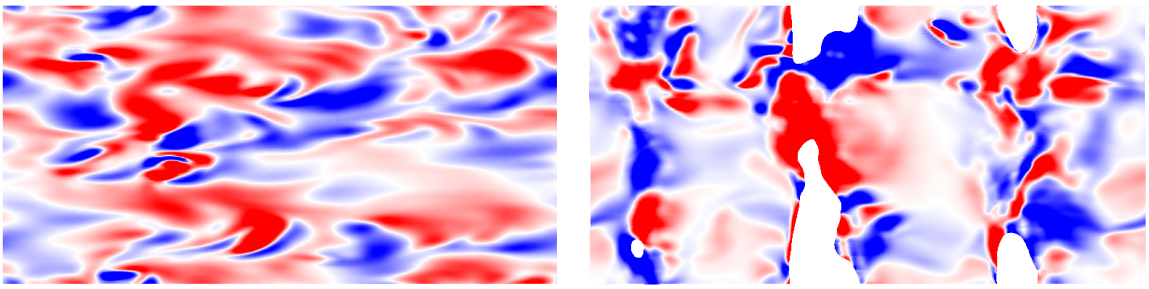

(a) Lower wall streamwise vortcity at $Y = -0.97H$ for the FSI case.

(b) Upper wall streamwise vorticity at $Y = 0.97H$ for the FSI case.

Figure 3.34: Instantaneous Snapshots of Streamwise Vorticity at $Y^+ = 5.4$ for E2 from the Lower and Upper Surfaces in a Turbulent Channel Flow at Time $70H/U$, Color Bar from -2 (Blue) to 2 (Red). Note the Change in the Color Bar Compared to Fig. (3.31). The Location of the Planes for Visualization Refers to an Undeformed Configuration. The White Area Contains No Data for Surface Deformation.

from the time about $10H/U$ to about $35H/U$ compared to the turbulent channel without FSI, which is relatively steady. But after the time $35H/U$, the forcing of E1 and E2 decreases. Considering to the fact of drag increases monotonically for E1 and E2, it suggests that some part of the drag induces the motion of solid material, and since it is hyper-elastic, it gives its energy back to flow field and causes the decrease of forcing when drag is increasing. Take fluid and solid system as a whole, the total

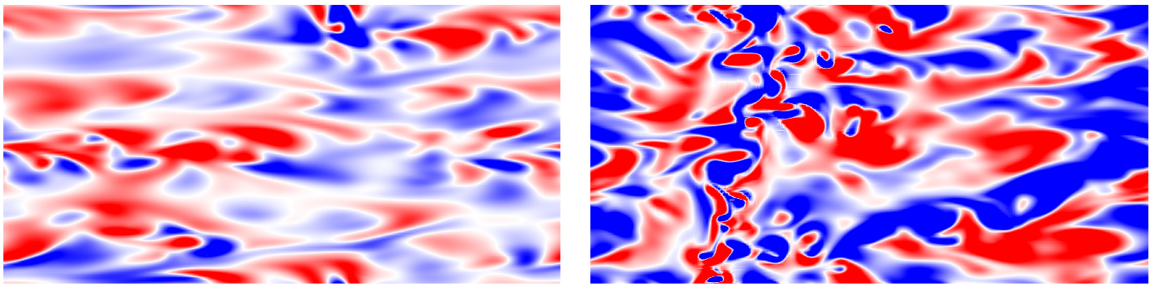

(a) Lower wall streamwise vortcity at $Y = -0.97H$ for the FSI case.

(b) Upper wall streamwise vorticity at $Y = 0.97H$ for the FSI case.

Figure 3.35: Instantaneous Snapshots of Streamwise Vorticity at $Y^+ = 5.4$ for E3 from the Lower and Upper Surfaces in a Turbulent Channel Flow at Time $70H/U$, Color Bar from -2 (Blue) to 2 (Red). Note the Change in the Color Bar Compared to Fig. (3.32). The Location of the Planes for Visualization Refers to an Undeformed Configuration.

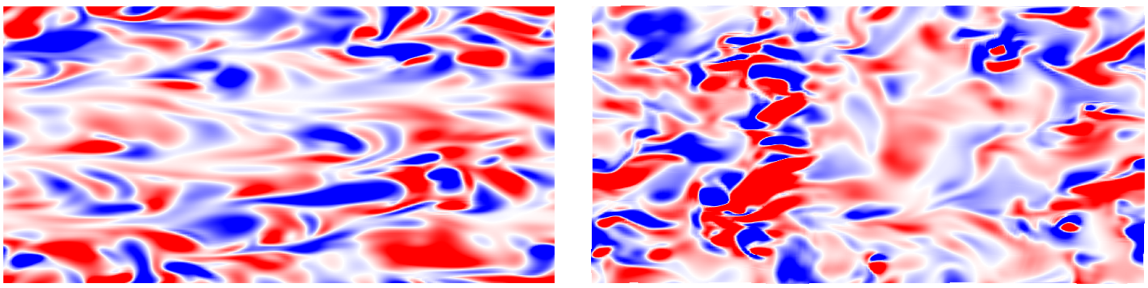

(a) Lower wall streamwise vortcity at $Y = -0.93H$ for the FSI case.

(b) Upper wall streamwise vorticity at $Y = 0.93H$ for the FSI case.

Figure 3.36: Instantaneous Snapshots of Streamwise Vorticity at $Y^+ = 12.6$ for E1 from the Lower and Upper Surfaces in a Turbulent Channel Flow at Time $70H/U$, Color Bar from -2 (Blue) to 2 (Red). Note the Change in the Color Bar Compared to Fig. (3.29). The Location of the Planes for Visualization Refers to an Undeformed Configuration.

energy of motion almost remains the same. During the period of the increased forcing, fluid is giving energy to solid. And during the period of the decreased forcing, solid is giving back its energy from fluid to fluid. As for E3, which forcing is always larger, it may have not enter the stage when solid gives back its energy to fluid for high stiffness. From the energy interaction between fluid and solid, we may conclude that for such coupled system, steady state with certain amount of surface fluctuations may

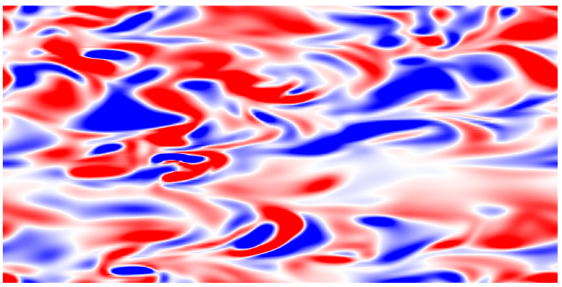

(a) Lower wall streamwise vortcity at $Y = -0.93H$ for the FSI case.

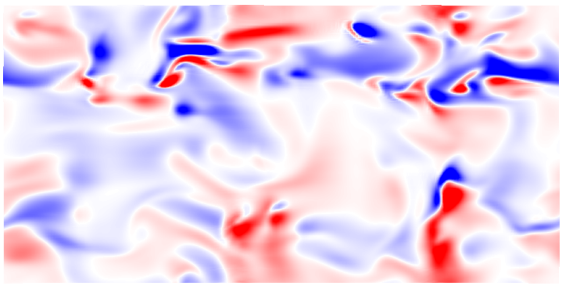

(b) Upper wall streamwise vorticity at $Y = 0.93H$ for the FSI case.

Figure 3.37: Instantaneous Snapshots of Streamwise Vorticity at $Y^+ = 12.6$ for E2 from the Lower and Upper Surfaces in a Turbulent Channel Flow at Time $70H/U$, Color Bar from -2 (Blue) to 2 (Red). Note the Change in the Color Bar Compared to Fig. (3.31). The Location of the Planes for Visualization Refers to an Undeformed Configuration.

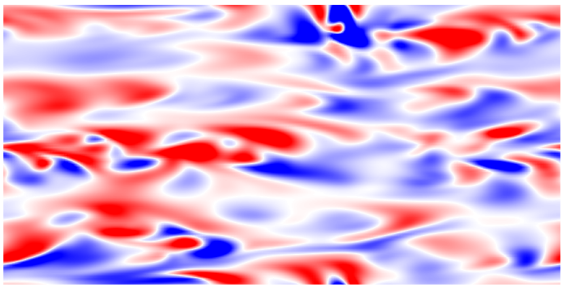

(a) Lower wall streamwise vortcity at $Y = -0.93H$ for the FSI case.

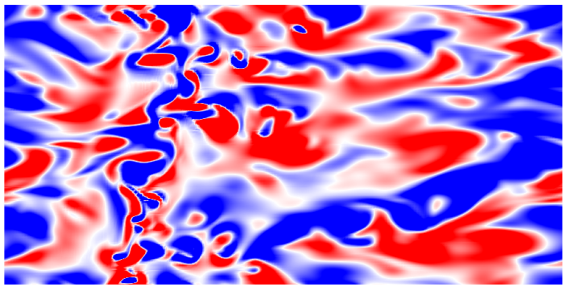

(b) Upper wall streamwise vorticity at $Y = 0.93H$ for the FSI case.

Figure 3.38: Instantaneous Snapshots of Streamwise Vorticity at $Y^+ = 12.6$ for E3 from the Lower and Upper Surfaces in a Turbulent Channel Flow at Time $70H/U$, Color Bar from -2 (Blue) to 2 (Red). Note the Change in the Color Bar Compared to Fig. (3.32). The Location of the Planes for Visualization Refers to an Undeformed Configuration.

not be reached as solid would gain more and more energy from fluid.

To further look into the surface motion, we average y-displacement of the mesh layer in y-direction which is originally flat in different time period (A3, A5 and A7). Fig. (3.41) shows that for E3, although we could not tell any deformation from Fig. (3.32), but FSI interface increases small amount averagely. As for E1 and E2, the averaged surface displacement is increasing through time which indicates the

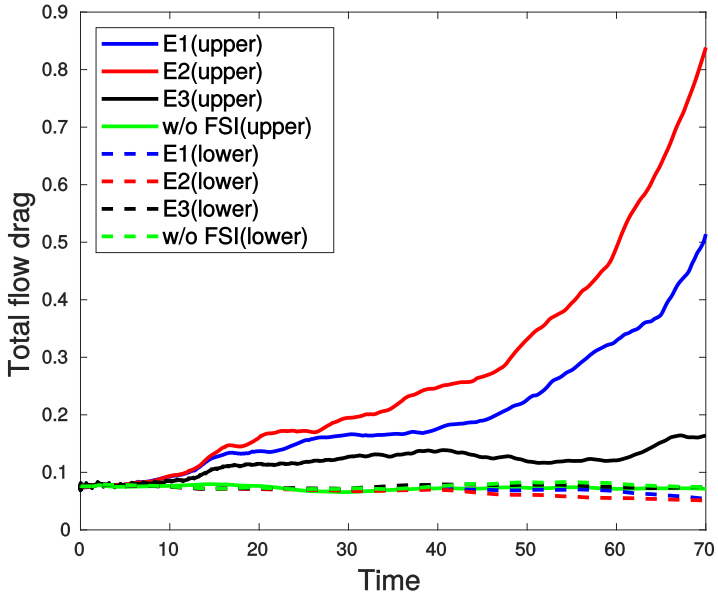

Figure 3.39: Comparison of the Total Flow Drag for the Lower and Upper Walls with and without FSI in a Turbulent Channel Flow. Time is Normalized with H/U.

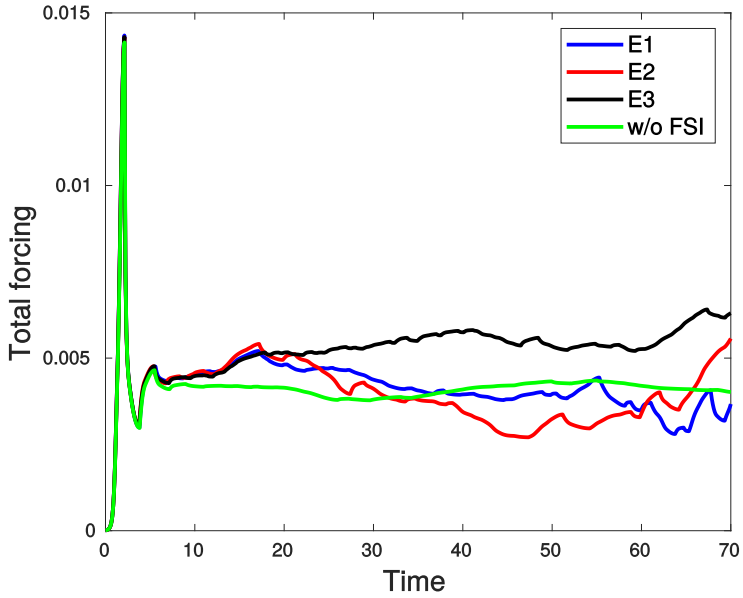

Figure 3.40: Comparison of the Total Forcing with and without FSI in a Turbulent Channel Flow. Time is Normalized with H/U.

solid is squeezed by the fluid regardless of fluctuated surface motion.

The streamwise mean velocity profiles of E1, E2, and E3 in time period A3, A5

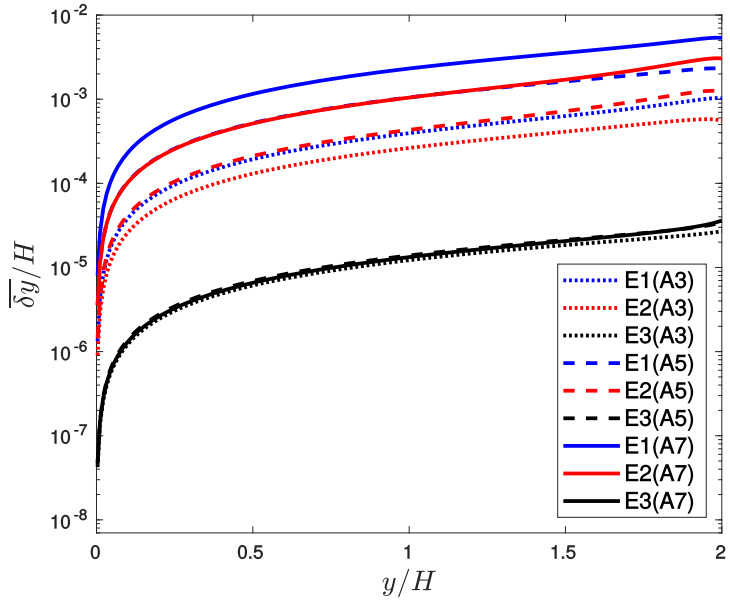

Figure 3.41: Comparison of the Time Averaged y-displacement of E1, E2, and E3.

and A7 compared with the whole time averaged profile of rigid turbulent channel without FSI, are shown in Fig. (3.42) versus the original y location. For E1 and E2, streamwise mean velocity is shifting towards the FSI interface for the surface motion gradually through time, while the streamwise mean velocity for E3 is shifting other way. Notice that for A3, the steamwise mean velocity profiles of E1 and E2 have the same trend and shift towards the rigid lower wall. So this may relate to the period that energy is transferring from fluid to solid, and when the energy is transferring from solid to fluid (low forcing), streamwise mean velocity profiles would be higher close to the FSI interface.

Fig. (3.43) shows the streamwise mean velocity profile scaled by u_τ from the bottom rigid wall versus the logarithm of the distance from the bottom rigid wall in wall units. Notice that u_τ is calculated for each cases in its own time period, and the averaged y-plane location is also from the current time period. Generally, the streamwise mean velocity profiles from FSI cases still satisfy the same log-law

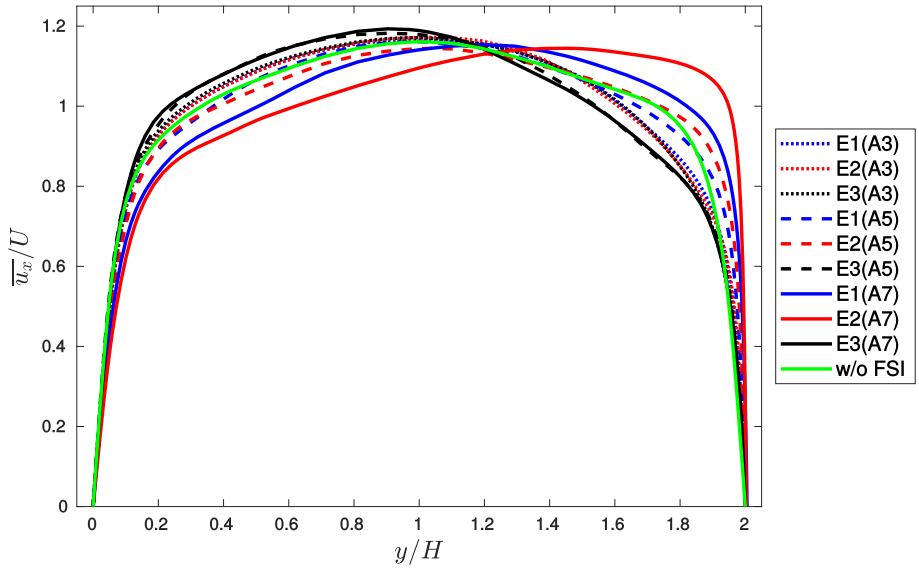

Figure 3.42: Comparison of the Streamwise Mean Velocity Profile of E1, E2, E3 and without FSI versus the Distance from the Bottom Rigid Wall.

from rigid channel flow without FSI, except E1(A7) and E2(A7). The scaling of the streamwise mean velocity near rigid lower wall is not changed because of the deformable upper wall.

As for velocity fluctuations, we calculate the wall-normal profiles of different components of time-averaged Reynolds stress tensors from time $20H/U$ to $70H/U$ versus its original flat y location shown in Fig. (3.44). The streamwise diagonal component $\overline{u_x' u_x'}$ is overall increased compared to the case without FSI, while other diagonal components contains a lower value region near the rigid wall and higher region near the FSI interface. It obviously shows that introducing a compliant wall would not only affect the fluctuation near a compliant wall, but it would also affects the whole fluid field fluctuations even if the streamwise mean velocity profile is not affected that much near the rigid wall region. One thing to notice is that the Reynolds stress components profiles are acquired through the values from its original y position, it may cause discrepancy for the Reynolds stress with such plane averaging even if the

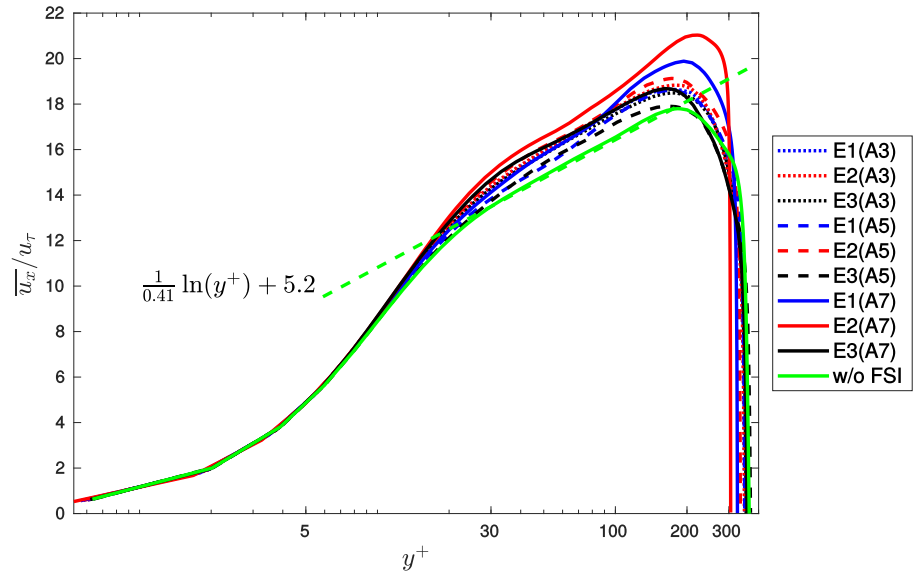

Figure 3.43: Comparison of the Streamwise Mean Velocity Profile Scaled by u_τ of E1, E2, E3 and Without FSI Versus the Distance from the Bottom Rigid Wall in Wall Units.

averaged y-displacement is small shown in Fig. (3.41). Even though, for all of the diagonal components including one off-diagonal term, fluctuation is much stronger near the FSI interface region and the peak position remains about the same, which shows a viscous layer with similar thickness occurs near the FSI interface for non-slip condition. Notice that E2 shows stronger fluctuation in $\overline{u'_x u'_x}$ compared to E1 and E3, while E3 shows stronger fluctuation in $\overline{u'_y u'_y}$ and $\overline{u'_z u'_z}$. It shows that very large scale motion of moving wall with small displacement would increase the fluctuations in spanwise and wall normal direction compared to small scale motion with large displacement. According to the vortices broken down by the moving wall illustrated in Figs. 3.33(b), 3.34(b) and 3.35(b), large disturbance of the moving wall would eventually create larger wall surface and it breaks down large vortices with strong fluctuations, which is the reason that spanwise and wall normal components are relatively smaller for E1 and E2 compared to E3. For off-diagonal term $\overline{u'_x u'_y}$, large values near FSI interface for E3 shows a strong streamwise mean velocity reduce which is also

found in Fig. (3.42). Apparently, turbulent kinetic energy $\kappa = (\overline{u'_x u'_x} + \overline{u'_y u'_y} + \overline{u'_z u'_z})/2$ are much stronger due to the moving wall compared to the case without FSI which is shown in Fig. (3.45). It is scaled by u_τ^2 of its own case from time $20H/U$ to $70H/U$. For E1 and E2, turbulent kinetic energy is strong near the moving wall region. While for E3, although it is still strong near the moving wall, it is unsymmetrically stronger near the upper half channel region which is not shown in E1 and E2. And the turbulent kinetic energy for E3 in lower half channel is almost the same as the case without FSI. This is another sign of turbulent kinetic energy has not been transfered from the upper moving wall to the bottom rigid wall for very large scale surface motion with small displacement. From the mean velocity profiles shown in Fig. (3.42), reduced mean velocity for E3 in the upper half channel region is also the reason for high turbulent kinetic energy as the large scale motion of the moving wall with small displacement is breaking the elongated streaks into small vortices causing the streamwise mean velocity reduced and fluctuation increased. But for E1 and E2, both streamwise mean velocity and fluctuations are strong near the moving wall region for intense surface motion.

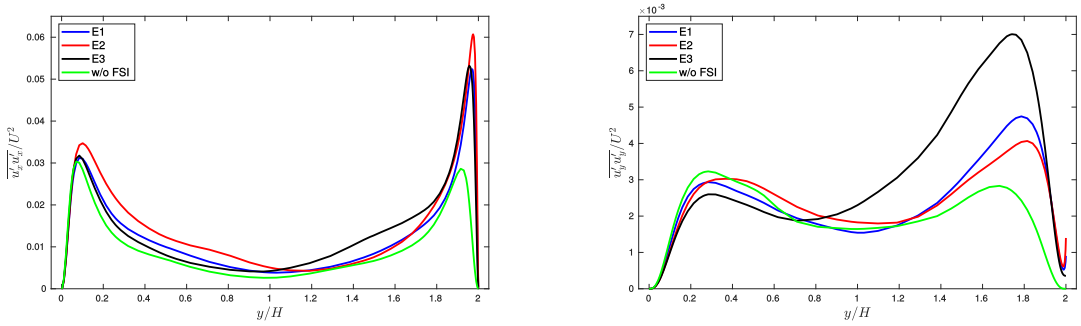

(a) Diagonal component $\overline{u'_x u'_x}$.

(b) Diagonal component $\overline{u'_y u'_y}$.

(c) Diagonal component $\overline{u'_z u'_z}$.

(d) Off-diagonal term $\overline{u'_x u'_y}$.

Figure 3.44: Comparison of Different Components of Reynolds Stress Tensor Profiles Scaled by U^2 for E1, E2, E3 and without FSI Versus its Position When it is Originally Flat.

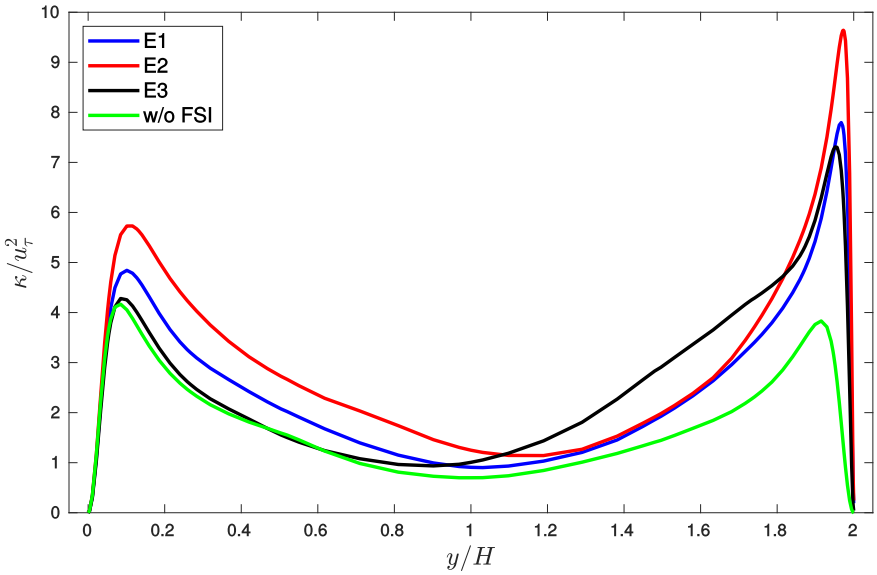

Figure 3.45: Comparison of the Turbulent Kinetic Energy Profile Scaled by u_τ^2 of E1, E2, E3 and without FSI Versus its Position When it is Originally Flat.

Chapter 4

ACOUSTICS FOR PIPE LEAK DETECTION

A transient-based method to detect single and multiple leaks in pipe flows is investigated computationally using a newly developed numerical framework, which couples a solution of an acoustic Lighthill's equation to the Navier-Stokes equations to model the transient pressure wave propagation in pipe flows with leaks. An analytic wavelet transform that uses a complex wavelet function, is used for signal analysis to detect leaks. New insights regarding a three-dimensional transient pressure wave dynamics in pipe flows with leaks are presented, and the sensitivity of the method to the azimuthal misalignment between the pressure sensor and the leak is analyzed. The results show good leak detection capabilities of the presented technology for single and multiple leaks in three-dimensional studies.

4.1 Introduction

Conservation and smart utilization of available water resources are essential in the current economy featured by a population growth and depleting water supplies. Water distribution systems often suffer from undesirable leaks and water losses, the so called unaccounted for water. A global survey conducted on the reported water loss from several different countries showed the values from as low as 9% in Germany to as high as 43% in Malaysia (Lai (1991)), 56% in Bangladesh (Chowdhury *et al.* (1999)), with most countries reporting water losses within 20 - 30% (Lai (1991)). In United States, almost 20% of the water supply is lost through leaking pipes (Brothers (2001); Thornton *et al.* (2008)). The loss of water resources represents a major environmental concern, and also puts economical burdens on society, due to an increased energy

cost of pumping water through fractured pipes (Colombo and Karney (2002)). Water leaks can also degrade the quality of the water by intrusion of the coliform and other harmful bacteria into the pipelines through backflow from the surrounding soils (Funk *et al.* (1999); Kirmeyer (2001); Karim *et al.* (2003)), and are associated with health and safety concerns to the population. Additional detrimental effects of undesirable water discharges into the ground are associated with flooding and erosion of the soils, damage to the transportation infrastructure, and impairing the foundation of buildings.

While ensuring the structural integrity of the distribution systems at construction stage is an important preventative measure, an eventual occurrence of leaks is, to some extent, an inevitable consequence, due to corrosion, joints wearing, and a gradual loss of integrity from operational events, such as pressure changes, surges and water hammer (Wang *et al.* (2001); Whittle *et al.* (2013)). Thus, efficient leak detection techniques to determine the existing leaks and potentially evaluate their sizes in the operating pipelines are required. Many different leak detection techniques have been proposed over the years, each with their own advantages and disadvantages, see Wang *et al.* (2001); Colombo *et al.* (2009); Adnan *et al.* (2015) for a comprehensive review, ranging from simpler methods such as a visual inspection (Folga (2007); Liu (2008)), to more sophisticated methods based on a signal analysis (Ghazali *et al.* (2012); Shucksmith *et al.* (2012); Adnan *et al.* (2015); Ovchinnikov and Lapshin (2016)).

The current chapter is concerned with the pressure transient based leak detection methods (Taghvaei *et al.* (2006); Ghazali *et al.* (2012); Brunone *et al.* (2013)), since they potentially can deliver high accuracy combined with a relative ease of implementation. Transient methods analyze the behavior of an unsteady transient pressure wave which is introduced into the system during a transient event, such as valve closing and opening, operation of the pump etc. Since the dynamics of a

transient event differs significantly if a leak is present in the system, the interaction of a transient pressure wave with the "anomaly" carries a certain signature that is potentially detectable even far away from the leak. While several pressure transient based techniques exist, such as a transient damping method (Wang *et al.* (2002)), an impulse response method in time (Liou (1998); Kim (2005)) or frequency (Mpesha *et al.* (2001); Wang *et al.* (2002); Ferrante and Brunone (2003a)) domains, the current study is concerned with the negative pressure wave (NPW) method (Taghvaei *et al.* (2006); Ghazali *et al.* (2012); Brunone *et al.* (2013)). The difference between the former and the latter techniques is that the impulse response methods are based on a comparison of the pipeline response to a pressure transient with the a-priori computed characteristics of the intact pipe, while the NPW method analyzes the pressure signal itself, and thus an a-priori model of the pipeline system is not required, which is a strong advantage, since such a model can be sometimes hard to obtain, or the system characteristics can change over time.

With the NPW method, the pressure wave created by a transient event is sent into the pipe, and a subsequent pressure signal is then measured by a sensor or multiple sensors. If encountering a leak, a reflected pressure signal will possess a lower amplitude due to a creation of the so called negative pressure wave, which can be detected by the sensor. By comparing the time lag between the forward and the reflected signal at a given location, the location of the leak can be pinpointed (Meniconi *et al.* (2011); Ghazali *et al.* (2012); Brunone *et al.* (2013)), while a strength of the reflected signal can help identify the size of the leak (Ferrante *et al.* (2014)). This technique has been first proposed in late 1990s, and the early studies concentrated on a direct analysis of time series of a measured pressure signal (Silva *et al.* (1996); Brunone *et al.* (2000)). A simple time domain approach, however, can be insufficient in realistic situations featuring noisy signals, multiple leaks, wave disper-

sion etc. In this case, more sophisticated techniques that analyze the signals in the frequency domain might be more suitable. To overcome the limitations given by a time domain method, different approaches, including cross-correlation analysis (Liou (1998); Beck *et al.* (2005)), wavelet (Ferrante and Brunone (2003b); Urbanek *et al.* (2011); Rashid *et al.* (2014)), or cepstrum (Taghvaei *et al.* (2006); Urbanek *et al.* (2011); Shucksmith *et al.* (2012); Motazedi and Beck (2018)) techniques, have been proposed. Surprisingly, there are very few studies that compare different analysis methods in application to a leak detection: Ghazali *et al.* (2012) compared a cepstrum analysis to several other instantaneous frequency based techniques, including Hilbert transform and a direct quadrature method, however a comparison involving wavelet methods is lacking.

While preliminary effectiveness of the NPW method has been demonstrated in laboratory experiments (Taghvaei *et al.* (2006); Brunone *et al.* (2013); Ferrante *et al.* (2014)), and even in life water distribution networks (Shucksmith *et al.* (2012); Brunone *et al.* (2013)), several questions about the optimum application of this technique still remain, for example, a choice of a signal processing method, an influence of a sensor location with respect to the leak, both along the longitudinal and azimuthal directions of the pipe, the latter especially important for large diameter pipes. To improve effectiveness of this technique, an availability of a physics-based model of the interaction between the pipe flow with leak and a transient pressure signal, is essential, so that different implementation strategies could be evaluated efficiently on a wide range of system parameters.

There were several numerical experiments of a transient leak detection analysis performed previously using one-dimensional hydraulic equations (the so-called Method of Characteristics – MOC) (Liou (1998); Wang *et al.* (2002); Covas *et al.* (2005); Diao *et al.* (2019)). One-dimensional model is computationally inexpensive,

and it can be applied efficiently to simulate major hydraulic events that are associated with a plane wave propagation in a pipe, such as a water hammer, whereas a leak can be modeled via introducing the pressure and flow rate losses. Wave reflection from the leak in this framework can only be approximated as a 1D plane wave, with no radial and azimuthal high frequency modes. However, more and more researchers have found the existence of such high-frequency and multi-path radial pressure waves, which can be induced by a nonuniform valve operation in realistic three-dimensional configurations, helpful for a more accurate leak detection (Brunone *et al.* (1995); Louati and Ghidaoui (2017); Che *et al.* (2018)).

This chapter presents a consistent numerical framework for the investigation of the pressure transient propagation in three-dimensional pipe flows with and without leaks for a leak detection analysis. In the current study, the fluid flow equations in a pipe are first solved with an open-source CFD code based on a spectral element method, while an acoustic pressure transient propagation is then calculated via a solution of an inhomogeneous Lighthill's equation forced by the fluid stresses. The developed computational framework is applied to study three-dimensional effects associated with the pressure transient wave propagation in pipe flows with leaks, which allows us to highlight new important phenomena, including an excitation of high-frequency radial and azimuthal wave reflection modes from the leak. In context with the three-dimensional pressure wave behavior, a sensitivity of the methodology to the azimuthal misalignment between the pressure probe and the leak is investigated for the first time. New insights regarding the role of frequency with regards to a leak detection in three dimensional flows are also presented. Another novel contribution of the current chapter is an application of the analytic wavelet transform method based on complex wavelets to a leak detection analysis.

The chapter is organized as follows. The developed computational model is pre-

sented first, including the Navier-Stokes solver, and the acoustic solver and its validation, followed by a description of signal analysis techniques that are compared in the current study. Subsequently, the three-dimensional test cases for the pipe flows with and without leaks, and their results are presented. Conclusions are drawn at the end.

4.2 Computational Model

A computational model proposed for the current problem consists of two parts: 1) Navier-Stokes equations are solved to compute the flow-field of a three-dimensional pipe flow with leak; 2) Lighthill's equation for a transient pressure wave propagation is solved, to investigate the interaction of a transient pressure signal with a pipe flow with leak. This section describes both these approaches, in turn.

4.2.1 Navier-Stokes Solver

The incompressible Navier-Stokes equations,

$$\rho\,(\frac{\partial \mathbf{u}}{\partial t} + \mathbf{u}\cdot\nabla\mathbf{u}) + \nabla\cdot p - \mu\nabla^2\mathbf{u} = 0, \tag{4.1}$$

$$\nabla\cdot\mathbf{u} = 0, \tag{4.2}$$

where ρ is the fluid density, $\mathbf{u} = \{u_x, u_y, u_z\}$ is the fluid velocity, μ is dynamic viscosity, and p is the pressure, along with the boundary conditions are solved in a weak formulation (obtained via a Galerkin projection), using a highly scalable, exponentially accurate high order spectral element solver Nek5000 (Patera (1984); Fischer (1997b); Fischer *et al.* (2015); Merrill *et al.* (2016b); Tomboulides *et al.* (1997)).

For a spatial discretization, we use a framework of a $\mathbb{P}_N - \mathbb{P}_N$ formulation (Tomboulides *et al.* (1997)), in which a decomposition of the computational domain comprises of

subdividing $\bar{\Omega} = \Omega \cup \partial\Omega$ into E non-overlapping adjacent rectilinear elements such that $\bar{\Omega} = \cup_{e=1}^{E} \Omega_e$. Each Ω_e is the image of a reference subdomain under a mapping $\mathbf{x}^e(\mathbf{r}) \in \Omega_e \rightarrow \mathbf{r} \in \hat{\Omega}$, with a well defined inverse $\mathbf{r}^e(\mathbf{x}) \in \hat{\Omega} \rightarrow \mathbf{x} \in \Omega_e$, where a 3D reference subdomain is $\hat{\Omega} = [-1, 1]^3$. Velocity and pressure within each local element Ω_e are represented as m^{th} order tensor product polynomials on a reference subdomain $\hat{\Omega}$. The velocity (and pressure) functions in the spectral element method in each element can be expressed as follows

$$u(r_1, r_2, r_3)|_{\hat{\Omega}} = \sum_{i=0}^{m} \sum_{j=0}^{m} \sum_{j=0}^{m} u_{ijk}^e \pi_{m,i}(r_1) \pi_{m,j}(r_2) \pi_{m,k}(r_3), \quad r_1, r_2, r_3 \in [-1, 1]^3, \quad (4.3)$$

where u_{ijk}^e are the nodal values of the velocity (pressure) at each Gauss-Lobatto-Legendre (GLL) grid point at every element Ω_e (GLL points are the roots of the Legendre polynomials). $\pi_{m,i}(r_1)$,$\pi_{m,j}(r_2)$, $\pi_{m,k}(r_3)$ are the Lagrange polynomial based interpolants of a degree m (Deville *et al.* (2002)). Due to the invertible mapping between Ω_e and $\hat{\Omega}$ there exists a one-to-one correspondence between the nodal values of variables $u(x, y, z)|_{\Omega_e}$, $p(x, y, z)|_{\Omega_e}$ and the reference subdomain values $u(r_1, r_2, r_3)|_{\hat{\Omega}}$, $p(r_1, r_2, r_3)|_{\hat{\Omega}}$, $r_1, r_2, r_3 \in [-1, 1]^3$.

The time discretization of the Navier-Stokes solver in the current spectral element code Nek5000 involves 3^{rd} order backward difference/extrapolation scheme with an operator integrator factor splitting characteristic time stepping (Karniadakis *et al.* (1991)). The code is fully dealiased using 3/2 rule (Orszag (1980)). The Helmholtz problem for velocity is solved using a preconditioned conjugate gradient (PCG) method, and the pressure solver uses an iterative generalized mean residual solver (GMRES) method in Krylov subspace.

Nek5000 has been used extensively by the scientific and engineering community, and has been validated on many canonical and applied fluid mechanics problems, including laminar and turbulent pipe flows (El Khoury *et al.* (2013); Merrill *et al.*

(2016b); Coxe *et al.* (2019); Xu and Peet (2021b))and more complex configurations.

4.2.2 Transient Pressure Solver

Numerical Formulation

Transient pressure solver is developed in this chapter in a spectral-element framework native to Nek5000 to study transient based leak detection methods. The transient pressure wave propagation is modeled using an inhomogeneous hyperbolic wave equation, the so called Lighthill's equation (Lighthill (1952)). Lighthill's equation is derived under the assumptions that are known as the "acoustic analogy", whereby an acoustic pressure is considered as a small perturbation to a base flow pressure (hydrodynamic pressure), and the governing flow equations, the compressible Navier-Stokes equations, are linearized to yield the inhomogeneous wave equation for the sound propagation in the fluid medium. Acoustic pressure propagation is thus decoupled from the base fluid flow equations. Lighthill's equation and acoustic analogy have been popularly used in the past (Wang *et al.* (2006); Kaltenbacher *et al.* (2010); Khalighi *et al.* (2010)) in the field of aero- and hydro-acoustics involving compressible and incompressible flows. Note that, while this analogy is a good approximation to the acoustic-type disturbances considered in the current chapter, it would also be applicable, for example, for studying the effects of the water hammer (Wylie and Streeter (1983); Wichowski (2006)), where transient effects that cause the change in the water flow can be modeled in a Lighthill's equation by adding an additional damping from an unsteady friction.

The Lighthill's equation for a transient pressure propagating through an incom-

pressible fluid medium can be written as,

$$\frac{1}{c_0^2}\frac{\partial^2 p^{\mathfrak{T}}}{\partial t^2} - \frac{\partial^2 p^{\mathfrak{T}}}{\partial x_i^2} = \frac{\partial^2(\rho u_i u_j)}{\partial x_i \partial x_j} - \frac{\partial^2 \sigma_{ij}}{\partial x_i \partial x_j}, \tag{4.4}$$

where u is the fluid velocity, c_0 is the speed of sound in a quiescent medium, $p^{\mathfrak{T}}$ denotes the transient pressure, which is different from the pressure term in the Navier-Stokes equation, and σ is the viscous stress tensor. A detailed derivation of the Lighthill's equation can be found, for example in Lighthill (1952); Blackstock (2000).

The left-hand side of Eq. (4.4) represents a three dimensional wave propagation operator, while the first term in the right-hand side is responsible for a noise generation from turbulent fluctuations. Most of the studies using a Lighthill's equation neglect the second term in the right-hand side, which represents the effect of viscosity in a flow-induced sound propagation. Under Stokes' hypothesis, viscous stress tensor can be expressed as

$$\sigma = -\frac{2\mu}{3}(\nabla \cdot u)\mathrm{I} + \mu(\nabla u + (\nabla u)^{\mathrm{T}}), \tag{4.5}$$

where I is the identity tensor. Using Eq. (4.5), the second term in the right-hand side of the Lighthill's equation, Eq. (4.4), becomes

$$\frac{\partial^2 \sigma_{ij}}{\partial x_i \partial x_j} = \frac{4\mu}{3}\nabla^2(\nabla \cdot \mathbf{u}), \tag{4.6}$$

Using the mass conservation equation under a small perturbation assumption,

$$\frac{\delta \rho}{\delta t} + \rho \nabla \cdot \mathbf{u} = 0, \tag{4.7}$$

and an equation of state $\delta p^{\mathfrak{T}} = c_0^2 \delta \rho$ to relate the velocity divergence in Eq. (4.7) to a time derivative of a transient pressure, Eq. (4.4) becomes

$$\frac{1}{c_0^2}\frac{\partial^2 p^{\mathfrak{T}}}{\partial t^2} - \frac{\partial^2 p^{\mathfrak{T}}}{\partial x_i^2} = \frac{\partial^2(\rho u_i u_j)}{\partial x_i \partial x_j} + \frac{4\mu}{3\rho c_0^2}\frac{\partial^2 \dot{p}^{\mathfrak{T}}}{\partial x_i^2}, \tag{4.8}$$

where $\dot{p}^{\mathfrak{T}} = \partial p^{\mathfrak{T}}/\partial t$.

A weak formulation of Eq. (4.8) to be used in a spectral-element framework involves integration with a test function w in a flow domain Ω as

$$\begin{aligned}
&\int_\Omega w(\frac{1}{c_0^2}\frac{\partial^2 p^{\mathfrak{T}}}{\partial t^2} - \frac{\partial^2 p^{\mathfrak{T}}}{\partial x_i^2} - \frac{\partial^2(\rho u_i u_j)}{\partial x_i \partial x_j} - \frac{4\mu}{3\rho c_0^2}\frac{\partial^2 \dot{p}^{\mathfrak{T}}}{\partial x_i^2}) \, \mathrm{d}\Omega \\
&= \int_\Omega w\frac{1}{c_0^2}\frac{\partial^2 p^{\mathfrak{T}}}{\partial t^2} \, \mathrm{d}\Omega + \int_\Omega \frac{\partial w}{\partial x_i}\frac{\partial p^{\mathfrak{T}}}{\partial x_i} \, \mathrm{d}\Omega - \int_\Gamma w\frac{\partial p^{\mathfrak{T}}}{\partial n} \, \mathrm{d}\Gamma + \int_\Omega \frac{\partial w}{\partial x_i}\frac{\partial(\rho u_i u_j)}{\partial x_j} \, \mathrm{d}\Omega \\
&+ \frac{4\mu}{3\rho c_0^2}\int_\Omega \frac{\partial w}{\partial x_i}\frac{\partial \dot{p}^{\mathfrak{T}}}{\partial x_i} \, \mathrm{d}\Omega - \frac{4\mu}{3\rho c_0^2}\int_\Gamma w\frac{\partial \dot{p}^{\mathfrak{T}}}{\partial n} \, \mathrm{d}\Gamma - \int_\Gamma w\frac{\partial(\rho u_i u_j)}{\partial x_j} n_i \, \mathrm{d}\Gamma = 0.
\end{aligned} \tag{4.9}$$

Here, both $p^{\mathfrak{T}}$ and the test function w are in $\mathcal{H}^1(\Omega)$, where $\mathcal{H}^1(\Omega)$ denotes the Sobolev space of square integrable functions whose first derivatives are also square integrable; $\int_\Omega$ denotes the integration over the flow domain volume Ω, while $\int_\Gamma$ denotes the boundary surface integral, which arises due to the integration by parts and converting the divergence term to the surface flux integral using Gauss's divergence theorem (Deville *et al.* (2002)), n is the outward pointing unit normal vector at the boundary surface. Note, the boundary integral, $\int_\Gamma$ can be partitioned into three integrals coming from the solid boundaries Γ_S (e.g., pipe walls), open boundaries Γ_o (water-water interfaces), and soft boundaries Γ_I (e.g., water-air interfaces), as described below, $\int_\Gamma = \int_{\Gamma_S} + \int_{\Gamma_o} + \int_{\Gamma_I}$.

Note that the last term in Eq. (4.9) vanishes if the boundary is located far from the acoustic sources or at non-slip wall surfaces, as in Kaltenbacher *et al.* (2010). In the past literature, the evaluation of the boundary integral corresponding to the open boundary has been popularly implemented via a perfectly matched layer (Berenger (1994)) or an absorbing boundary condition (Clayton and Engquist (1977); Engquist and Majda (1977)). In our current setup, we have used the first order approximation of a highly absorbing local boundary condition (Engquist and Majda (1977)) because of its simplicity of implementation and good flow stability characteristics near the outflow. In a perfectly absorbing formulation, the boundary conditions are based

on characteristic equations of the governing hyperbolic partial differential operator, which, to the first order approximation, are set to zero at the boundary,

$$\left(\frac{\partial p^{\mathfrak{T}}}{\partial n}+\frac{1}{c_0}\frac{\partial p^{\mathfrak{T}}}{\partial t}\right)\Bigg|_{\Gamma_o}=0, \tag{4.10}$$

where Γ_o stands for the open boundary.

In the current study, we encounter three types of interfaces for the acoustic wave propagation which need to be properly addressed: 1) open boundaries (water-water interfaces), 2) solid boundaries (walls), and 3) soft boundaries (water-air interfaces). Based on the first-order approximation, the unified formulation for these three types of boundary conditions can be given as

$$\frac{\partial p^{\mathfrak{T}}}{\partial n}\Bigg|_{\Gamma}=-\frac{\alpha}{c_0}\frac{\partial p^{\mathfrak{T}}}{\partial t}\Bigg|_{\Gamma}, \tag{4.11}$$

where the coefficient α depends on the type of interface and the corresponding reflection coefficient R (Blackstock (2000)) . The value of α is given as

$$\alpha=\frac{1-R}{1+R}, \tag{4.12}$$

where the reflection coefficient

$$R=\frac{Z_2-Z_1}{Z_2+Z_1}, \tag{4.13}$$

with the acoustic impedance in a wave traveling medium Z_1, and the acoustic impedance in a reflection medium Z_2. Three characteristic cases describing ideal, no-loss reflections, are given below:

(B1) Open boundary (no reflection): $R=0$, $\alpha=1$ to let the outgoing wave pass through, which recovers the original perfectly absorbing (non-reflecting) boundary condition of Eq. (4.10) (Clayton and Engquist (1977); Engquist and Majda (1977)).

(B2) Wall (reflection with no phase change): $R = 1$, $\alpha = 0$ to model the sound wave reflection from the wall or a higher acoustic impedance medium, which occurs without a phase change (Blackstock (2000)).

(B3) Water-air interface (reflection with a phase reversal): $R = -1$, $\alpha \to \infty$ to model the sound wave reflection from a lower acoustic impedance medium, which undergoes a phase reversal (180° shift) upon reflection (Blackstock (2000)). Numerically, to avoid a singularity, one could set R to a slightly larger number, such as $R = -1 + \epsilon$, with a small value of ϵ, and calculate α correspondingly from Eq. (4.12).

Simple theoretical arguments pertaining to a derivation of the acoustic boundary conditions in a one-dimensional approximation are given in Sec. (4.2.2). Note that in the test cases with pipe leaks, we set the values of the reflection coefficients R slightly off from their ideal values, as described below, to account for the losses inevitable in realistic applications.

Substituting the Eq. (4.11) into Eq. (4.9), the inhomogeneous Lighthill's equation in a variational form can be written as

$$\begin{aligned} &\int_\Omega w \frac{1}{c_0^2} \frac{\partial^2 p^{\mathfrak{T}}}{\partial t^2} \, \mathrm{d}\Omega + \int_\Gamma w \frac{\alpha}{c_0} \frac{\partial p^{\mathfrak{T}}}{\partial t} \, \mathrm{d}\Gamma + \int_\Omega \frac{\partial w}{\partial x_i} \frac{\partial p^{\mathfrak{T}}}{\partial x_i} \, \mathrm{d}\Omega + \frac{4\mu}{3\rho c_0^2} \int_\Omega \frac{\partial w}{\partial x_i} \frac{\partial \dot{p}^{\mathfrak{T}}}{\partial x_i} \, \mathrm{d}\Omega \\ &+ \frac{4\mu\alpha}{3\rho c_0^3} \int_\Gamma w \frac{\partial \dot{p}^{\mathfrak{T}}}{\partial t} \, \mathrm{d}\Gamma = -\int_\Omega \frac{\partial w}{\partial x_i} \frac{\partial (\rho u_i u_j)}{\partial x_j} \, \mathrm{d}\Omega + \int_\Gamma w \frac{\partial (\rho u_i u_j)}{\partial x_j} n_i \, \mathrm{d}\Gamma. \end{aligned} \tag{4.14}$$

The details of the numerical discretization of Eq. (4.14) are presented in Sec. (4.2.2).

Boundary Conditions

To derive the universal form of the boundary conditions for the transient acoustic wave reflection from the wall, air, or water in a one-dimensional case, we need to consider the interaction of the original and the reflected pressure waves close to the

boundary. Restricting the analytical solution of Eq. (4.25) to a one-dimensional case, the one-dimensional transient pressure field in the vicinity of the boundary, $p_b^{\mathfrak{T}}(x,t)$ can be written as

$$p_b^{\mathfrak{T}}(x,t) = f(t - x/c_0) + f_r(t + x/c_0). \tag{4.15}$$

Denoting $\xi_1 = t - x/c_0$, $\xi_2 = t + x/c_0$ as characteristic lines for the original and the reflected waves, and differentiating, we get

$$\begin{aligned} \frac{\partial p_b^{\mathfrak{T}}}{\partial x} &= -\frac{1}{c_0}\frac{\mathrm{d}f}{\mathrm{d}\xi_1} + \frac{1}{c_0}\frac{\mathrm{d}f_r}{\mathrm{d}\xi_2}, \\ \frac{\partial p_b^{\mathfrak{T}}}{\partial t} &= \frac{\mathrm{d}f}{\mathrm{d}\xi_1} + \frac{\mathrm{d}f_r}{\mathrm{d}\xi_2}. \end{aligned} \tag{4.16}$$

Now, considering that for a reflected wave $f_r(\xi) = Rf(\xi - 2x_r/c_0)$, i.e. $\mathrm{d}f_r/\mathrm{d}\xi = R\mathrm{d}f/\mathrm{d}\xi$, with R as a reflection coefficient, and that at the boundary $\xi_1 = \xi_2$, since this is where the two characteristics meet, substitution of these expressions into Eq. (4.16), yields that α in Eq. (4.11) can be written as $\alpha = (1 - R)/(1 + R)$.

Comparing these expressions with the general formulation of Eq. (4.11) for the boundary conditions and restricting it to one dimension, we immediately see that when $R = 1$ as $Z_2 \gg Z_1$, $\alpha = 0$ for the case of the wall reflection, (B2) condition. To derive the value of α for the air reflection, (B3) condition, we note that in this case $Z_2 \ll Z_1$, $R = -1$, which corresponds to $\alpha \to \infty$. One can also immediately see that, setting $f_r = 0$ for the non-reflecting case when $R = 0$, $Z_2 = Z_1$, one recovers that $\left(\partial\, p_b^{\mathfrak{T}}/\partial\, x + (\partial\, p_b^{\mathfrak{T}}/\partial\, t)/c_0\right)|_{\Gamma_o} = 0$ for the open boundary, (B1) condition, in agreement with Eq. (4.10). Extension of the above boundary conditions to multiple dimensions can be done by considering a paraxial approximation to the wave equation of various orders, as is done in Clayton and Engquist (1977); Engquist and Majda (1977), which, for a first-order approximation, would yield an expression given by Eq. (4.11).

Discrete Formulation of Lighthill's Equation

Spectral element implementation of the Lighthill's equation was developed into the open-source code Nek5000 (Fischer (1997b); Deville *et al.* (2002); Fischer *et al.* (2015)). Following the spectral element formulation (Deville *et al.* (2002)), the spatial domain is discretized by high-order polynomials associated with the Gauss-Lobatto-Legendre points. With such discretization, the variable p and the test function w (here we denote $p^{\mathfrak{T}}$ as p for the brevity of expressions) would be written as $p(t) = \sum N_i p_i(t)$ and $w = \sum N_i w_i$ where N_i denotes the spectral element interpolation functions, and $p_i,\ w_i$ are the GLL nodal values. A weak formulation of the Lighthill's equation, Eq. (4.14), can be written in a semi-discrete form as a damped mass-spring oscillator system

$$\left(\frac{M}{c_0^2} + \frac{4\mu}{3\rho c_0^2}\frac{C}{c_0}\right)\ddot{p} + \left(\frac{C}{c_0} + \frac{4\mu}{3\rho c_0^2}K\right)\dot{p} + Kp = f, \tag{4.17}$$

where the mass matrix M, surface matrix C arising due to boundary conditions, stiffness matrix K and sources term f are defined as

$$\begin{aligned}
M &= [M_{ij}] = \int_\Omega N_i N_j \ \mathrm{d}\Omega, \\
C &= [C_{ij}] = \int_\Gamma \alpha\, N_i N_j \ \mathrm{d}\Gamma, \\
K &= [K_{ij}] = \int_\Omega \frac{\partial N_i}{\partial x_k}\frac{\partial N_j}{\partial x_k} \ \mathrm{d}\Omega, \\
f &= \{f_i\} = -\int_\Omega \frac{\partial N_i}{\partial x_k}\frac{\partial(\rho u_k u_j)}{\partial x_j} \ \mathrm{d}\Omega + \int_\Gamma N_i \frac{\partial(\rho u_k u_j)}{\partial x_j} n_k \ \mathrm{d}\Gamma,
\end{aligned} \tag{4.18}$$

and the coefficient α comes from the boundary condition formulation, Eq. (4.12).

The time discretization is carried out using a Newmark predictor-corrector method (Newmark (1959)), which is a popular method for solving second-order differential equations. With the Newmark method, at a time step t^{n+1}, the pressure and its

derivatives, p^{n+1}, $\dot{p}^{n+1}$ and $\ddot{p}^{n+1}$ are expressed as

$$p^{n+1} = p^n + \delta t \dot{p}^n + \frac{\delta t^2}{2}[(1-2\beta)\ddot{p}^n + 2\beta\ddot{p}^{n+1}], \tag{4.19}$$

$$\dot{p}^{n+1} = \dot{p}^n + \delta t[(1-\gamma)\ddot{p}^n + \gamma\ddot{p}^{n+1}], \tag{4.20}$$

$$f^{n+1} = \left(\frac{M}{c_0^2} + \frac{4\mu}{3\rho c_0^2}\frac{C}{c_0}\right)\ddot{p}^{n+1} + \left(\frac{C}{c_0} + \frac{4\mu}{3\rho c_0^2}K\right)\dot{p}^{n+1} + Kp^{n+1}, \tag{4.21}$$

where δt is the time step, β and γ have been chosen to be 0.25 and 0.5, which yields a second order accuracy and an unconditional stability (Newmark (1959)). Substituting Eqs. (4.19) and (4.20) into Eq. (4.21) yields the equation

$$\begin{aligned}\left[\frac{M}{c_0^2} + (\gamma\delta t + \frac{4\mu}{3\rho c_0^2})\frac{C}{c_0} + (\beta\delta t^2 + \gamma\delta t\frac{4\mu}{3\rho c_0^2})K\right]\ddot{p}^{n+1} \quad &= \\ f^{n+1} - (\frac{C}{c_0} + \frac{4\mu}{3\rho c_0^2}K)\left[\dot{p}^n + (1-\gamma)\delta t\ddot{p}^n\right] - \quad K\left[p^n + \delta t\dot{p}^n + \tfrac{\delta t^2}{2}(1-2\beta)\ddot{p}^n\right],\end{aligned} \tag{4.22}$$

which is solved by either GMRES or PCG method with the diagonal matrix, $\mathrm{diag}(a_{11}^{-1}, a_{22}^{-1}, ..., a_{nn}^{-1})$, that consists of the inverse entries of the diagonal of the matrix $A = M/c_0^2 + \beta\delta t^2 K$, as a preconditioner. Subsequently, p^{n+1} and $\dot{p}^{n+1}$ are solved by Eqs. (4.19) and (4.20) with an updated $\ddot{p}^{n+1}$.

Validation

Since the transient pressure solver is a new development undertaken to benefit the current study, this section presents its validation which is a sound wave propagation in a quiescent state versus an analytical solution. The solver was validated using a test case of a sound wave propagation in water in its quiescent state (without the source terms) against the analytical solution. The validation case consists of a propagating wave in a two-dimensional open channel that reflects from the rightmost domain boundary. The wave propagation speed is set as $c_0 = 1000$ m/s which is 10 after nondimensionalization in the simulation. The boundary conditions at the

leftmost domain boundary for the pressure are specified as

$$p^{\mathfrak{T}}(x = 0, y, t) = f(t)g(y), \tag{4.23}$$

where the characteristic one-dimensional waveform function $f(t)$ is given by

$$f(t) = \frac{1}{0.4\sqrt{2\pi}} \exp\left(- \frac{(2 - c_0 t)^2}{0.08} \right), \quad t \in [0, 0.4] \tag{4.24}$$

and $g(y) = 1$. The computational domain dimensions are chosen as $x \in [0, 5], y \in [0, 1]$. Boundary conditions correspond to the open boundaries (B1) at $x = 0$ (inflow) when $t > 0.4$. $y = 0, y = 1$ (bottom and top boundaries) use (B2) boundary conditions which essentially means symmetric here when waveform in y direction is constant and uniform. For the rightmost boundary, $x = 5$, we have tested (B2) and (B3) boundary conditions, that correspond to the wall reflection (no phase change) and the air reflection (reversed phase). This was designed to test the interaction of the wave with materials of various acoustic impedance. Note that only the corresponding ideal (no-loss) values of the wall reflection coefficients are shown in this section.

The simulation ends at $t = 1.2$ and it presents a case that a wave coming from the leftmost boundary propagates from the left to the right and then gets reflected by the rightmost boundary. After the reflection, such wave propagates from right to left and vanishes its half after it reaches the leftmost boundary. The analytical solution for the acoustic wave propagation in a quiescent medium of a quasi-one-dimensional waveform described by Eqs. (4.23) and (4.24), with a reflection from the downstream boundary, is given by

$$p^{\mathfrak{T}}(x, y, t) = \left[f(t - x/c_0) + f_r(t + x/c_0) \right] g(y), \tag{4.25}$$

$g(y) = 1$, where the first term in the brackets of Eq. (4.25) represents the original right-going wave, the second term is the reflected left-going wave (reflected from the

right boundary), which is equal to

$$f_r(\xi) = \begin{cases} 0, & \text{for no reflection ((B1), open boundary)} \\ f(\xi - 2x_r/c_0), & \text{for same phase reflection ((B2), reflection from the wall)} \\ -f(\xi - 2x_r/c_0), & \text{for reversed phase reflection ((B3), reflection from the air)} \end{cases} \tag{4.26}$$

where x_r is the streamwise coordinate of the boundary and the reflection occurs, $x_r = 5$ in our case. The validation is presented with the second full same phase reflection condition of Eq. (4.26), which means $\alpha = 0$.

The simulation is carried out using various elements in the x direction and 10 elements in the y direction which is verified to make no contribution on mesh refinement. Mesh level, element size and total number of elements are listed in Table. (4.1). Except H-refinement, 3^{rd}, 4^{th}, 7^{th}, 10^{th}, 12^{th}, 13^{th}, 15^{th} order Lagrange interpolating polynomials are also used for P-refinement, which is named as P3, P4, P7, P10, P12, P13, P15 correspondingly. The temporal level and time step size are listed in Table. (4.2). Additionally, we use f to denote if the solution is filtered with a spectral filtering Fischer and Mullen (2001). For comparison, a probe at $(x, y) = (2.5, 0.5)$ records transient pressure at every time step.

Table 4.1: Meshes Used for the Convergence Study in the Lighthill Solver Validation Case.

Mesh level	M1	M2	M3	M4	M5	M6
Element size, δx	1/2	1/4	1/8	1/16	1/32	1/64
Total number of elements	100	200	400	800	1600	3200

Table 4.2: Time Step Size Used for the Convergence Study in the Lighthill Solver Validation Case.

Temporal level	T1	T2	T3	T4	T5
Time step size, δt	5e−5	1e−4	2e−4	4e−4	8e−4

The probe values from case $\mathrm{M1}^{(\mathrm{P3,T2})}$, $\mathrm{M1}^{(\mathrm{P3,T2,f})}$, $\mathrm{M6}^{(\mathrm{P4,T5})}$, $\mathrm{M6}^{(\mathrm{P4,T5,f})}$, are compared with analytic solution in Fig. (4.1(a)) and two waveforms are acquired. The first waveform is captured when the initial wave propagates from the left to the right while the second is the reflection waves propagates from the left to the right. When mesh is very coarse, for example $\mathrm{M1}^{(\mathrm{P3,T2})}$, dispersive error is quite noticeable. With artificial dissipation, $\mathrm{M1}^{(\mathrm{P3,T2,f})}$ shows less dispersive error but the magnitude of waveform is also reduced. But when the mesh is finer, either filtered and non-filtered solution could reduce dispersive and dissipation error and reach to analytical solution.

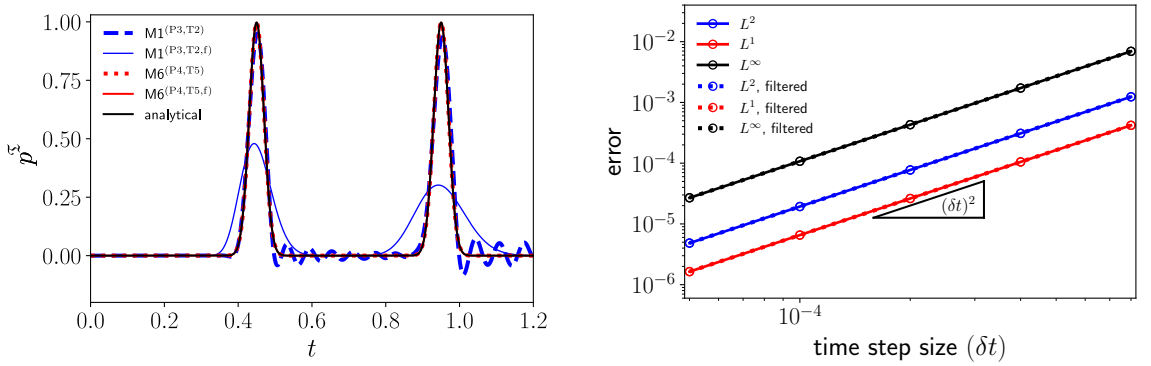

(a) Probe value of the transient pressure versus time compared to the analytical solution for the validation test case at $(x, y) = (2.5, 0.5)$.

(b) Temporal convergence for the Lighthill solver validation case with $\mathrm{M6}^{\mathrm{P4}}$.

Figure 4.1: Probe Value of the Transient Pressure and Temporal Convergence.

Snapshots of the transient pressure at several time intervals capturing the original wave and the subsequent reflection are shown in Fig. (4.2) from $\mathrm{M6}^{(\mathrm{P4,T1,f})}$. As predicted by the analytical solution, the original pulse travels from the left to right

right (first term in the brackets of Eq. (4.25)), See Figs. 4.2(a) and 4.2(b). At a time of 0.8 after the beginning of the simulation, the right-going wave undergoes a reflection from the right boundary captured in Fig. (4.2(c)), and it travels to the left, See Figs. 4.2(c) and 4.2(d).

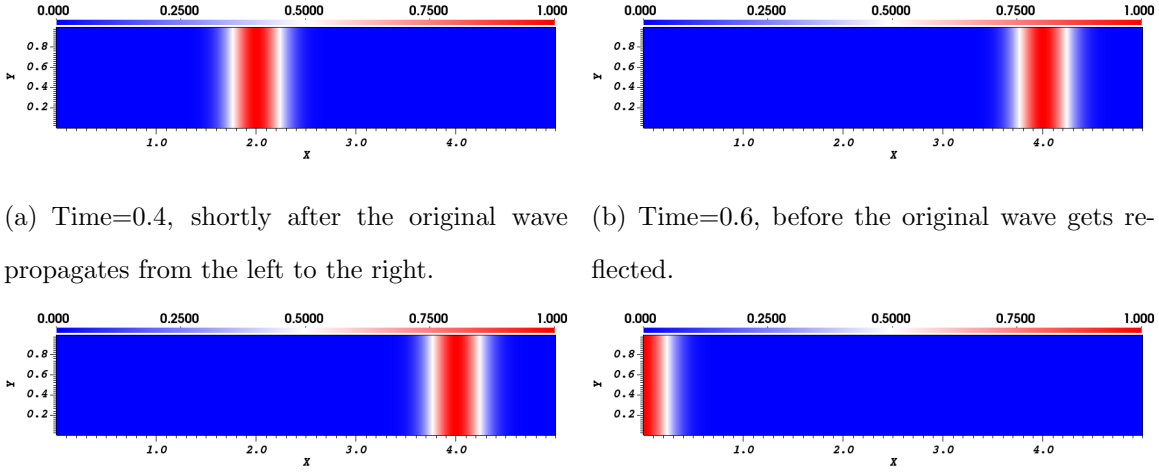

(a) Time=0.4, shortly after the original wave propagates from the left to the right.

(b) Time=0.6, before the original wave gets reflected.

(c) Time=0.8, reflection from the right boundary is observed.

(d) Time=1.2, reflection wave propagates from right to left.

Figure 4.2: Wave Propagation at Different Time Intervals for the Validation Test Case of the Lighthill Solver. Transient Pressure is Shown (Pressure is Normalized with $p_0^{\mathfrak{T}}$, x and y are Normalized). (B1) (Open, Left) After the Incoming Wave and (B2) (Reflection from Wall, Right) Boundary Conditions are Shown.

To further study the spatial and temporal convergence rate with or without filtering, H/P and temporal refinement study is performed. Temporal refinement study is done with mesh $\mathrm{M6}^{\mathrm{P4}}$ shown in Fig. (4.1(b)) with or without filtering. It shows expected second order convergence. For H-refinement, the results are shown in Fig. (4.3(a)) with $(\mathrm{P4}, \mathrm{T2})$. An unexpected 8^{th} order is observed when the filtering is off and expected 4^{th} order convergence is observed when the filtering is on. For P-refinement, the results are shown in Fig. (4.3(b)) with $\mathrm{M1}^{\mathrm{T2}}$. A good spectral convergence is observed with or without filtering.

Thus the Lighthill solver is validated with temporal and spatial convergence. Al-

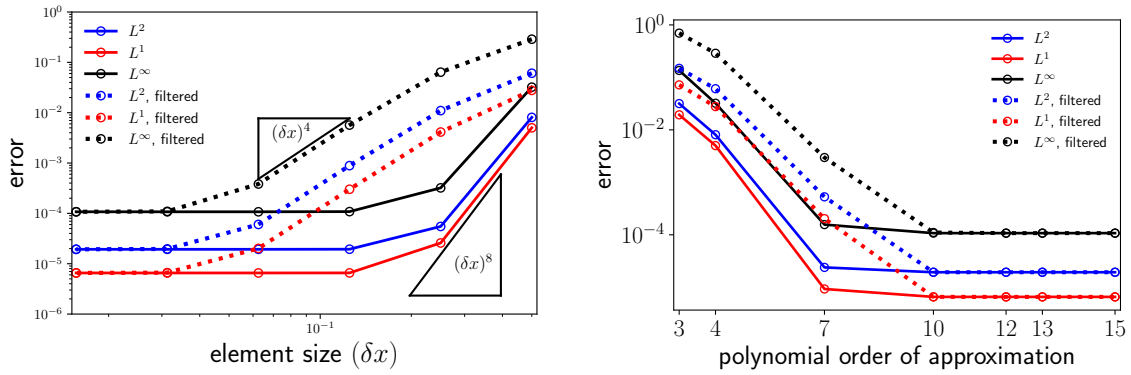

(a) H refinement for the Lighthill solver validation case with (P4, T2).

(b) P refinement for the Lighthill solver validation case with $\mathrm{M1}^{\mathrm{T2}}$.

Figure 4.3: Spatial Convergence Study for the Lighthill Solver Validation Case.

though filtering reduces the order of convergence, it is still used for adding artificial dissipation to stabilize the solution.

4.3 Unsteady Friction

In a derivation of Eq. (4.8), the effect of a change in the bulk velocity, and the corresponding wall shear stress, as the transient pressure wave is passing, has been neglected, as the flow equations and the pressure transient equations are decoupled in a Lighthill's approach. However, the effect of an additional wave damping from an unsteady pipe friction caused by high speed bulk velocity traveling (huge shear from wall)has been found important in 1D water hammer model studies (Zielke (1968); Ghidaoui *et al.* (2005); Martins *et al.* (2018)). To account for this effect, a friction parameter $\mathcal{F}(\mathbf{x}, t)$, $\mathbf{x} = \{x, y, z\}$, is introduced as

$$\frac{1}{c_0^2}\frac{\partial^2 p^{\mathfrak{T}}}{\partial t^2} - \frac{\partial^2 p^{\mathfrak{T}}}{\partial x_i^2} = \frac{\partial^2(\rho u_i u_j)}{\partial x_i \partial x_j} + \frac{4\mu\,\mathcal{F}}{3\rho c_0^2}\frac{\partial^2 \dot{p}^{\mathfrak{T}}}{\partial x_i^2}. \tag{4.27}$$

To estimate the friction parameter $\mathcal{F}(\mathbf{x}, t)$, we invoke an unsteady friction model that has been used successfully with water hammer equations (Brunone *et al.* (1991); Pezzinga (2000)), which shows that an unsteady friction term in a 1D momentum

equation can be estimated as

$$J_u(x,t) = k\left(\frac{\partial V}{\partial t} + \mathrm{sgn}(V\frac{\partial V}{\partial x})c_0\frac{\partial V}{\partial x}\right), \tag{4.28}$$

where x is the streamwise coordinate, $V(x,t)$ is the cross-sectional bulk mean velocity in the 1D model, and the Brunone's friction coefficient $k = \sqrt{7.41/Re^{k_1}}/2$ with $k_1 = \log(14.3/Re^{0.05})$, Re is the Reynolds number of the base flow.

To estimate the change of the cross-sectional bulk mean velocity V in our approach, Joukowsky's fundamental equation (Blackstock (2000); Ghidaoui *et al.* (2005)) is used as

$$\delta p^{\mathfrak{T}} = \pm\rho c_0 \delta V, \tag{4.29}$$

where a positive sign is applicable when the water hammer wave moves downstream, and a negative sign is applicable when the water hammer wave moves upstream. With the additional relations for the sign of the corresponding variables, Eq. (4.28) could be expressed in terms of a transient pressure $p^{\mathfrak{T}}$ as

$$J_u(x,t) = -k\left(\frac{\mathrm{sgn}(p^{\mathfrak{T}})\mathrm{sgn}(\dot{p}^{\mathfrak{T}})}{\rho c_0}\frac{\partial p^{\mathfrak{T}}}{\partial t} - \frac{\mathrm{sgn}(\dot{p}^{\mathfrak{T}})}{\rho}\left|\frac{\partial p^{\mathfrak{T}}}{\partial x}\right|\right). \tag{4.30}$$

When a steady-state friction J_s is estimated in a pipe flow with a steady-state velocity field V_s and a diameter D as

$$J_s = -\frac{32\mu}{D^2}V_s, \tag{4.31}$$

the friction parameter $\mathcal{F}(\mathbf{x},t)$ can be expressed as

$$\mathcal{F}(\mathbf{x},t) = 1 + \frac{J_u(\mathbf{x},t)}{J_s}, \tag{4.32}$$

which accounts for unsteady viscous forces from a transient wave propagation in a form of an additional, time-variant and localized damping. Note that in a three-dimensional model of the Lighthill's equation, an unsteady friction force $J_u(\mathbf{x},t)$ is

evaluated using a transient pressure value $p^{\mathfrak{T}}(\mathbf{x}, t)$ at a corresponding Cartesian location $\mathbf{x} = \{x, y, z\}$, however, using a streamwise derivative of pressure $\partial p^{\mathfrak{T}}/\partial x$ in Eq. (4.30).

4.3.1 Validation of Unsteady Friction

The validation case is a transient water hammer pressure surge analysis in a reservoir-pipe-valve system similar to the one studied in Ferrante and Brunone (2003b); Covas *et al.* (2005); Martins *et al.* (2018). The geometry and the mesh of a 3D pipe section with the pipe diameter $D = 0.1$ m, pipe length $L = 2$ m, and the Reynolds number based on the pipe diameter and a pre-surge bulk mean velocity $Re = 1000$. Velocity inlet and zero pressure outlet are used as boundary conditions in the fluid solver to obtain a baseline fluid flow, which is steady and fully developed originally. At a reference time of $t = 0$, an outflow boundary in the pipe suddenly changes to the wall boundary condition, when a strong transient pressure event is initiated at the pipe end. This condition is modeled in a Lighthill solver by setting the pressure wave reflection coefficients in Eq. (4.12) to $R = -0.9992$ at the pipe inlet (corresponding to a water-air interface), and $R = 0.98$ at the pipe outlet (corresponding to a wall reflection). Unsteady friction model from Eq. (4.28)–Eq. (4.32) is simulated to check the effectiveness of the developed methodology based on a modified Lighthill's equation Eq. (4.27) to model the water hammer effect. The transient water hammer simulations are performed for the time interval $t = [0,\ 5\,\tilde{t}]$, where the dimensional time unit $\tilde{t} = 4L/c_0$, with wave speed $c_0 = 1000$ m/s.

Normalized mid- and end-pipe center probe results for the water hammer validation case are shown in Fig. (4.4) compared with experimental results from Martins *et al.* (2018) at a similar Reynolds number. It can be seen that the current results are quite close the experiments presented in Martins *et al.* (2018). While longer pipes

are used in Martins *et al.* (2018), a good agreement with the present $L = 20D$ pipe domain computations testifies of an effectiveness of the developed acoustic boundary conditions for the truncated domains. As expected, spectral-element results yield very little dissipation, but some dispersive effects are noticed due to a sharp reflection of a surge pressure pulse from the boundaries (Deville *et al.* (2002)). The resulting pressure profiles are slightly smoother in Martins *et al.* (2018), perhaps due to a stronger effect of damping associated with longer domains.

This validation test cases confirms the ability of the developed transient pressure solver to realistically model the unsteady transient effects in hydraulic pipes, including the water hammer, as compared to experiments. But such unsteady friction is not used in Sec. (4.5) for the wave is not traveling back and forth for simplicity.

4.4 Analytic Wavelet Transform (AWT)

There are several analytic wavelets, such as an analytic Morlet wavelet, Bessel wavelet or a Cauchy wavelet (Lilly and Olhede (2010)), but still the choice of the wavelet becomes important for a specific case. This study adopts the use of a generalized Morse wavelet (Olhede and Walden (2002); Lilly and Olhede (2012)). Generalized Morse wavelets are the eigenfunction wavelets in a time-varying spectrum estimation via an averaging of the time-scale eigenscalograms (Olhede and Walden (2002)). Most commonly used analytic wavelets can be regarded as a special case of the Morse wavelet super family with certain parameters (Lilly and Olhede (2012)). Generalized Morse wavelets are typically defined in a frequency domain as

$$\Psi(\omega, \beta, \gamma) = H(\omega) a_{\beta,\gamma} \omega^{\beta} e^{-\omega^{\gamma}}, \tag{4.33}$$

where $H(\omega)$ is the Heaviside step function, $a_{\beta,\gamma} = 2(e\gamma/\beta)^{\beta/\gamma}$ is a normalization constant, and $\omega = 2\pi/f$. Two parameters, γ and β, determine the shape and the function

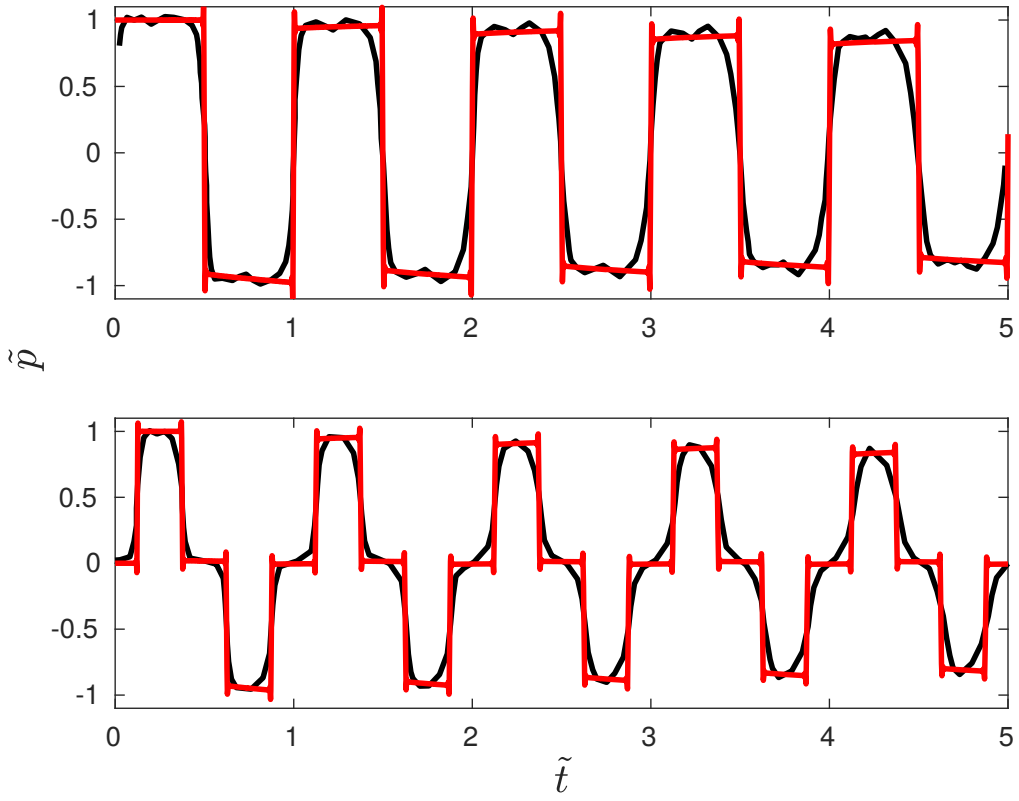

Figure 4.4: Normalized Transient Pressure Signal for the Water Hammer Validation Test Case. Red Line: Current Computational Results, Black Line: Experimental Results from Martins *et al.* (2018). Upper: Results from the End-pipe Centerline Probe$(0,\ 0, 20D)$; Lower: Results from the Mid-pipe Centerline Probe $(0,\ 0, 10D)$. Pressure is Normalized by $p_0^{\mathfrak{T}}$. Time is Normalized by $4L/c_0$ for Both the Current Simulations and the Results of Martins *et al.* (2018).

properties of the generalized Morse wavelet. Parameter γ controls the symmetry of the wavelet through the demodulate skewness, while parameter β is related to the time-bandwidth parameter $P^2 = \beta\gamma$, which controls the wavelet duration in time (Lilly and Olhede (2008)). It can be shown (Lilly and Olhede (2008)) that skewness is zero for $\gamma = 3$, representing a nearly symmetric wavelet. The value of $\gamma = 3$ also ensures the minimum Heisenberg area, i.e. the product of the standard deviations in the time and the frequency domains (minimum uncertainty). In the current work, the value of $\gamma = 3$ will be used. When γ is fixed, decreasing or increasing

time-bandwidth would effect which type of signals can be better detected, singular or oscillatory. In our case, since the signal we want to detect is oscillating, the maximum time-bandwidth $P^2 = 120$ will be used.

4.5 Problem Setup

4.5.1 Fluid Flow

In the current manuscript, we focus our analysis on laminar three-dimensional (3D) pipe flows with one or two leaks. Turbulent flow cases will be considered in future studies. A summary of all calculated test cases is presented in Table. (4.3), and the computational grid details (coarse, medium, fine meshes) are in Table. (4.4). A computational domain in a 3D case is a cylindrical pipe with a diameter $D = 0.1\,\mathrm{m}$ as shown in Fig. (4.5). The domain length in such cases is $L = 20D$. The axis z is in a streamwise direction, and the x, y axes correspond to a cross-sectional plane, withe the pipe centerline at $(x, y) = (0, 0)$. The boundary conditions are no-slip at the solid walls, a parabolic velocity profile at the inflow, and zero-pressure outflow boundary conditions at the outlet (Fischer *et al.* (2015)). A leak is modeled by removing one of the "wall" elements at the surface of the pipe and replacing it with an "outflow" element, which allows the fluid to flow through the leak orifice. In cases with one leak, the leak is placed at the middle of the pipe at $z_{leak} = 10D$, $x_{leak} = 0$, $y_{leak} = 0.5D$. In the description of the leak locations, we always refer to the leak front edge. The case with two leaks (Case L2) is also modeled, where the second leak is placed $5D$ downstream of the first leak, at $z_{leak} = 15D$, $x_{leak} = 0$, $y_{leak} = 0.5D$. The leaks are modeled as square orifices in all cases. The size of the leaks is $0.1D \times 0.1D$ (with a small cylindrical curvature due to a pipe wall). The size of the leaks corresponds to the size of one spectral element in the numerical grid. Based on the volumetric

flow loss through the leaks, See Table. (4.3), the leaks considered in the current study are classified as small leaks according to a criterion proposed in Bilmann and Isermann (1987) that considers a leak to be small if its flow rate is $< 5\%$ for liquids, and $< 12\%$ for gases. The choice of a leak size being $0.1D \times 0.1D$ in the current study is commensurate with the previous experimental investigations Meniconi *et al.* (2011); Urbanek *et al.* (2011); Ferrante *et al.* (2014); Rashid *et al.* (2014), where leak sizes between $0.08D$ and $0.24D$ typically have been considered. The working fluid is water with the density $\rho = 1000\,\mathrm{kg/m^3}$, dynamic viscosity $\mu = 10^{-3}\,\mathrm{kg/m/s}$, and the Reynolds number $Re_D = (\rho V D)/\mu = 1000$, where V is the fluid bulk mean velocity.

Case	No. of Leaks	Leak Location	% loss (Q_{leak}/Q_{inlet})	Probe Location
L1 (coarse)	1	$10D$	0.81	$(0D, 0.45D, 1D)$
L1 (medium)	1	$10D$	0.69	$(0D, 0.45D, 1D)$
L1 (fine)	1	$10D$	0.64	$z = 1D$, Multiple angles
L2 (fine)	2	$10D, 15D$	1.04	$(0D, 0.45D, 1D)$
L0 (fine)	0	$--$	0	$z = 1D$, Multiple angles

Table 4.3: Test Cases for Three-dimensional Laminar Pipe Flow Configurations. All Leak Sizes are $0.1D \times 0.1D$. For Leak Locations, a Location of the Leak Upstream Edge is Implied. Q_{inlet}, Q_{leak} are the Volumetric Flow Rates through the Inlet and the Leak(s) Respectively.

Mesh level	N^e	N^e_{stream}	N^e_{cross}	N	Δ_{stream}	Δ_{ortho}
coarse	960	30	32	126991	$0.67D$	$0.2D$
medium	7680	60	128	987581	$0.33D$	$0.1D$
fine	61440	120	512	7789561	$0.167D$	$0.05D$

Table 4.4: Details of the Computational Grids for the 3D Pipe Flow Simulations. Length: Domain Length in the Streamwise Direction. N^e : Number of Spectral Elements, N^e_{stream}, N^e_{cross}: Number of Elements in the Streamwise and Cross-sectional Directions, Respectively. N: Unique Number of Grid Points. Δ_{stream}, Δ_{ortho}: Average Grid Sizes in the Steamwise and Orthogonal Directions (Vertical Direction in 2D, Radial Direction in 3D). 6 GLL Nodes have been Used per Element per Cartesian Direction.

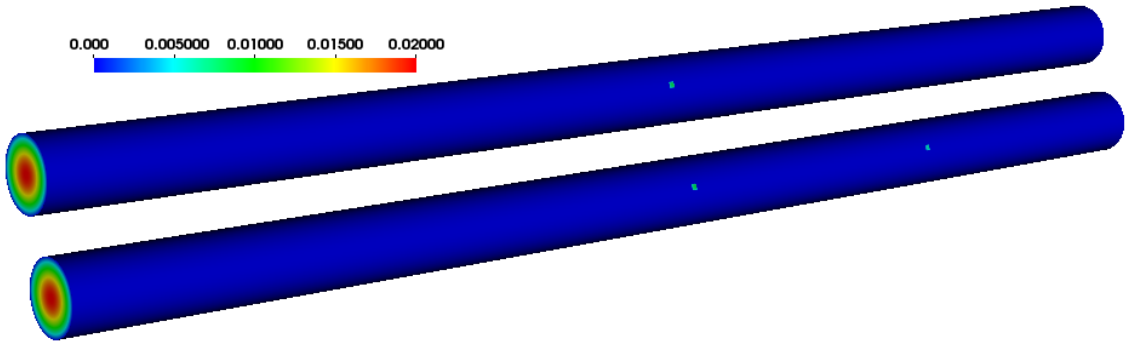

Figure 4.5: 3D Pipe Flow Domain with Velocity Magnitude for One and Two Leaks.

4.5.2 Pressure Transient

Pressure transient for all the test cases is modeled as a smooth plane wave from the pipe upstream inlet

$$p^{\mathfrak{T}}(x,y,0,t) = \begin{cases} -\dfrac{\mathcal{A}}{2}(1-\cos\dfrac{\pi t}{\mathcal{L}}), & t \in [0,\mathcal{L}], \\ -\mathcal{A}, & t \in (\mathcal{L},\mathcal{T}-\mathcal{L}], \\ \mathcal{A}\cos\pi(\dfrac{t+2\mathcal{L}}{2\mathcal{L}}), & t \in (\mathcal{T}-\mathcal{L},\mathcal{T}+\mathcal{L}], \\ \mathcal{A}, & t \in (\mathcal{T}+\mathcal{L},2\mathcal{T}-\mathcal{L}], \\ \dfrac{\mathcal{A}}{2}(1-\cos\dfrac{\pi t}{\mathcal{L}}), & t \in (2\mathcal{T}-\mathcal{L},2\mathcal{T}], \end{cases} \tag{4.34}$$

where $\mathcal{L} = 2\text{e}-5$ (s), $\mathcal{T} = 1\text{e}-4$ (s) and $\mathcal{A} = 10000$ (Pa).

This signal aims to imitate the pressure impulse introduced by closing and opening of the valve (Taghvaei *et al.* (2006)). The pressure wave speed propagation in a fluid-filled pipe, c_0, depends on various parameters, including the pipe diameter, stiffness and thickness of the pipe walls (less rigid pipe materials, such as plastic, resulting in lower wave speeds) etc. In the current study, we assume $c_0 = 1000\,\text{m/s}$ for simplicity (Louati and Ghidaoui (2017)), which is also a typical value for a pipe with a diameter $D = 0.1\,\text{m}$ with the walls made from a red brass.

Boundary conditions for the pressure transient propagation are set as a pressure inlet via Eq. (4.34) for $t \in [0, 2\mathcal{T}]$, which is then switched to an open boundary (B1) at $t = 2\mathcal{T}$, open boundary (B1) is used at the outflow, wall reflective boundary conditions (B2) at the pipe walls with the reflection coefficient $R = 1$, and the water-air interface (B3) at the surface of the leak with the reflection coefficient $R = -0.97$. A spectral filtering (Fischer and Mullen (2001)) is applied to stabilize the results with artificial dissipation.

4.6 Results

4.6.1 Single Leak

A three-dimensional flowfield for the pipe flow with a single leak is shown in Fig. (4.6), where a longitudinal cross-section across the pipe is presented in Fig. (4.6(a)), and an azimuthal cross-section in Fig. (4.6(b)). A diversion of the flow streamlines outwards in the vicinity of the leak is visible.

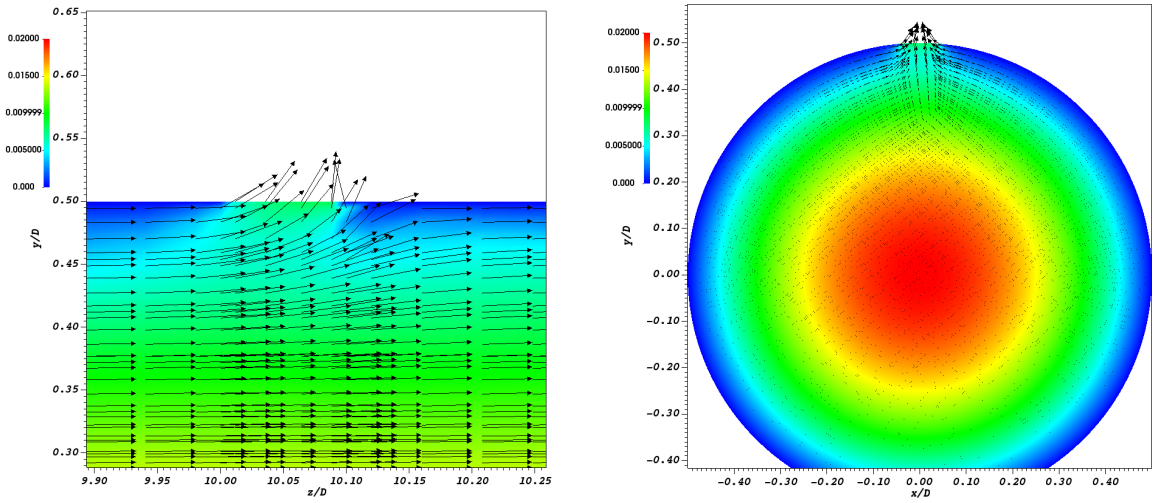

(a) Longitudinal $(y-z)$ cross-section

(b) Azimuthal $(x-y)$ cross-section at $z = 10.05D$.

Figure 4.6: Velocity Vector Plots Superimposed onto Velocity Magnitude Contours in the Vicinity of the Leak for the Fine Mesh Case with One Leak (Case L1). Velocity Values are in m/s.

For the transient pressure wave propagation, boundary conditions given by Eq. (4.34) were utilized. In the rest of the section, the pressure transient results from the probe located at $(0, 0.45D, D)$ will be presented first for the leak at $(0, 0.5D, 10D)$ (the order of coordinates listed are (x, y, z). To investigate the influence of this azimuthal misalignment, the remainder of this section will consider signals coming from different azimuthal locations for the probes at $z = D$, $r = 0.45\,D$, and different θ angles, and

a leak at $(x, y, z) = (0,\ 0.5D,\ 10D)$.

Azimuthally-Aligned Probe

For a baseline probe at $(x, y, z) = (0,\ 0.45D,\ D)$, azimuthally aligned with the leak, the transient pressure signals with three different meshes are shown in Fig. (4.7). The results illustrate that the pressure transient dynamics and reflections from the leak are similar for a 3D plane impulse. During the transient tests, a transient pressure signal is recorded at the sensor location at every time step, and a comparison between the leaking and non-leaking cases is shown. It is observed that, without leaking, the probe would only receive a signal coming from the initial pressure pulse. However, for the leaking pipe, a clear second peak at about time $t \sim 0.002$ (s) corresponding to 20 dimensional time units, 20 D/c_0 , or one acoustic flow through time, 1 L/c_0 , is observed, corresponding to the reflection from the leak. In agreement with the reversed phase mode of reflection from the water-air interface and the NPW methodology, as discussed above, the leading front of the reflected wave shows positive pressure, since the leading front of the original right-going impulse was negative, See Eq. (4.34). After the first reflection peak, several more pulses are observed, and the signal in general remains oscillatory. This is related to an excitation of non-plane high-frequency waves as discussed below. The magnitude of the first reflection wave is reduced compared to the initial impulse but subsequent oscillations maintain nearly the same amplitude, testifying that both the primary and secondary (non-plane) reflection waves carry comparable amounts of energy. In the next section, we gain more insight into an understanding of the behavior of the signals and the best practices of their evaluation using several signal analysis methods.

Signal from coarse mesh is quite dispersive compared to the fine mesh and it gives quite different pattern of oscillation. It is not yet confirmed from pressure signals to

see whether finer resolution for such simulation is needed.

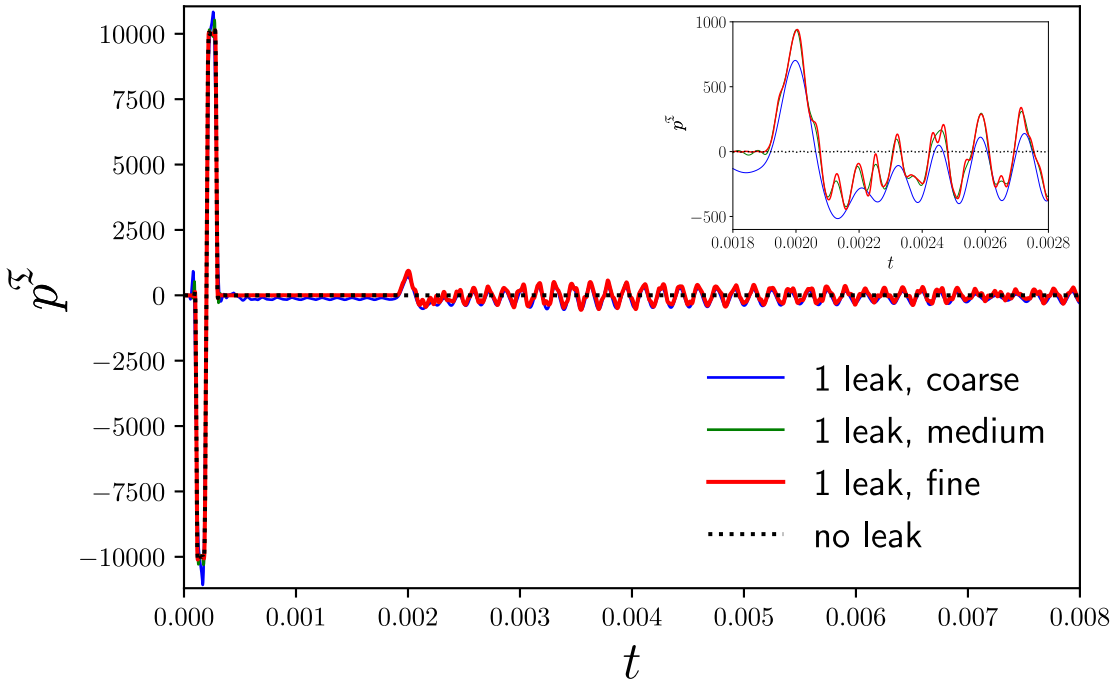

Figure 4.7: Signal Comparison from the Signal Reading at a Probe $(x, y, z) = (0, 0.45D, D)$ Between the Intact and the Leaking Pipe with the Leak at $(x, y, z) = (0, 0.5D, 10D)$ for the 3D Pipe. Inset: Zoom-in into the Time $t = (0.0024, 0.0028)$. Pressure is in Pascal, Time is in Seconds.

For a signal analysis, a signal analysis method based on an analytic wavelet transform (AWT) (Lilly and Olhede (2010)), is implemented here. As discussed above, analytic wavelet transform uses a complex-valued wavelet function as opposed to a real one. Its advantage is that it is able to provide both the magnitude and the phase of the signal at the same time, which alleviates the Heisenberg uncertainty and yields better signal detection capabilities when it comes to impulsive and oscillatory signals such as the ones found in the transient pressure wave signature reflected from the leak. Advantages of the AWT, specifically, for acoustic applications were previously discussed in Zhu and Kim (2006). Despite that fact, AWT was never previously applied to analyze the leaks in the fluid-carrying pipes.

Following this methodology, the contour plots of the wavelet transform amplitude and its line plots at frequencies $f_1 = 0.4726\, c_0/D$, $f_2 = 1.3367\, c_0/D$, and $f_3 = 2.3273\, c_0/D$ are shown in Figs. 4.8 and 4.9. These three frequency is based on three cut-off frequency for M0, M1 and M2 mode wave described in Louati and Ghidaoui (2017). M0 wave is plane wave, which is only concerned in classical one-dimensional water hammer model. Higher modes M1 and M2 wave are excited in three-dimensional case for wave traveling various path rather than in plane. In our set up, the first and second critical frequency according to Louati and Ghidaoui (2017) are $1.219c_0/D$ and $2.231c_0/D$ correspondingly. When frequency is between 0 and $1.219c_0/D$, it supposes to capture plane wave. When frequency is above $1.219c_0/D$ and below $2.231c_0/D$, it could also capture M1 wave. When frequency is above $2.231c_0/D$, it could additionally capture M2 wave. According to Eq. (4.34), the incoming wave is similar to heaviside step-function which contains large span from low frequency to high frequency.

In Fig. (4.8(a)), it shows that when the contour values are from 0 to 1000 with 200 spacing for both leaking and non-leaking cases, leaking case show significant different values in large frequency. While for low frequency, both cases vanish in time for not detecting any incoming wave. It shows that at the beginning, an incoming wave from Eq. (4.34) is detected which causes a large span of low frequency and high frequency energy spectrum. For leaking case, since it receives a signal from the leak which is also low mode wave, it shows energy spectrum from low frequency to high frequency as well. But after the leak signal, it only receives high frequency mode from non-plane wave and shows values only in high frequency region.

From Fig. (4.8(b)), at the frequency not being able to capture M1 wave, it clearly shows a bump indicating a leak from coarse, medium and fine mesh. To deduce the

leak location, we use

$$x_{leak} = x_{sensor} + \frac{c_0}{2}(t_2 - t_1), \tag{4.35}$$

with $error = \left|(x_{leak}^{est} - x_{leak}^{act})/x_{leak}^{act}\right| \times 100\%$, to estimate the leak location and error from the peak time of the magnitude. From Table. (4.5), it gives good estimation of the leak location.

For higher frequency shown in Fig. (4.8(b)), which is in the frequency range of M1 wave, it shows different energy from leak, but it is not recognizable about the plane wave reflection from the leak, or high modes reflection. Besides, although it does not show strong discrepancy from the signal plot in Fig. (4.7) for coarse mesh, it gives no energy in high frequency which shows incapability of detecting high frequency modes in the simulation. In other words, finer mesh is required for checking high frequency reflection. To estimate the leak location from high frequency, the first peak rather than the first bump is picked and from Table. (4.5), it shows its accuracy of leak detection.

For frequency $f_3 = 2.3273\, c_0/D$, it should contain M2 mode wave which is highly noisy for the reflection wave. Again, coarse mesh is unable to check any high frequency energy, and the accuracy of leak destination is good.

In reality, AWT at high frequency may not be able to find the leak as the signal should be noisy. Here, we have a clean case which you could not find any noise at all from non-leaking signal. So the first noise from leaking signal is definitely the disturbance from the leak. However, below M1 mode frequency, one could detect the leak with AWT to clearly see a bump, which is a major plane wave reflection from the leak to find the leak. Also, three-dimensional transient pressure wave simulation shows that small leak gives plane wave reflection rather than high frequency reflection when the test wave is plane. So traditional one-dimensional model works to some extent.

Case	Frequency (Hz)	Peak time t_1, (ms)	Peak time t_2, (ms)	Actual Leak (m)	Estimated Leak (m)	Error margin
L1	4726	0.303	2.017	$[1, 1.01]$	0.957	4.30-5.25%
L1	13367	0.162	2.022	$[1, 1.01]$	1.03	1.98-3.00%
L1	23273	0.2	2.018	$[1, 1.01]$	1.009	0.10-0.90%

Table 4.5: Estimation of the Peak Arrival Times, the Leak Locations, Eq. (4.35), and the Error Margins in L1 Case for an Azimuthally-aligned Probe.

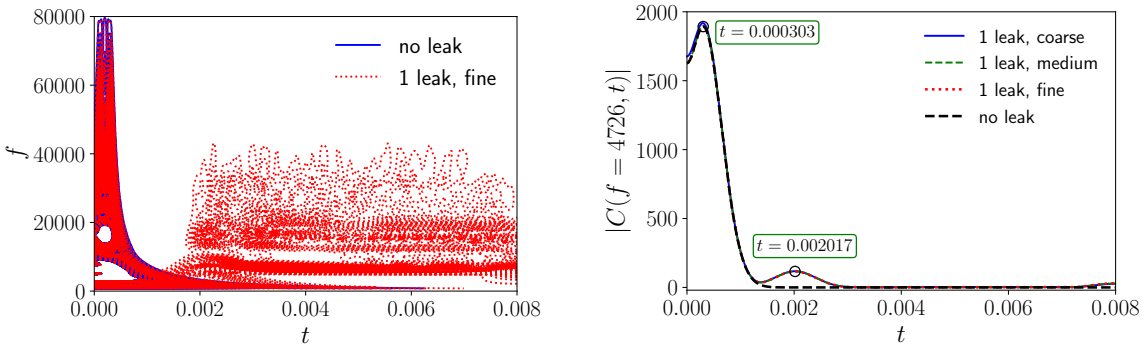

(a) Contour plots of the AWT magnitude in a time-frequency domain. Contour values are from 0 to 1000 with 200 spacing for both leaking and non-leaking cases.

(b) Magnitude plot of the AWT transform at a frequency 4726.

Figure 4.8: Analytic Wavelet Transform of the Pressure Signals from Fig. (4.7) with [3, 120] Morse Wavelet. Arrival Times for the Peaks are Shown in Boxes. Time is in Seconds, Frequency is in Hz.

Sensitivity to an Azimuthal Probe Misalignment

This section documents the influence of the azimuthal misalignment between the leak and the pressure sensor on the performance of the leak detection methodology and further explains the influence of the detection frequency on the obtained results. With the leak still being positioned at $(x, y, z) = (0, 0.5D, 10D)$, we place 11 azimuthal probes within one half of the pipe circumference (every $\Delta\,\theta = 18°$) between the angles

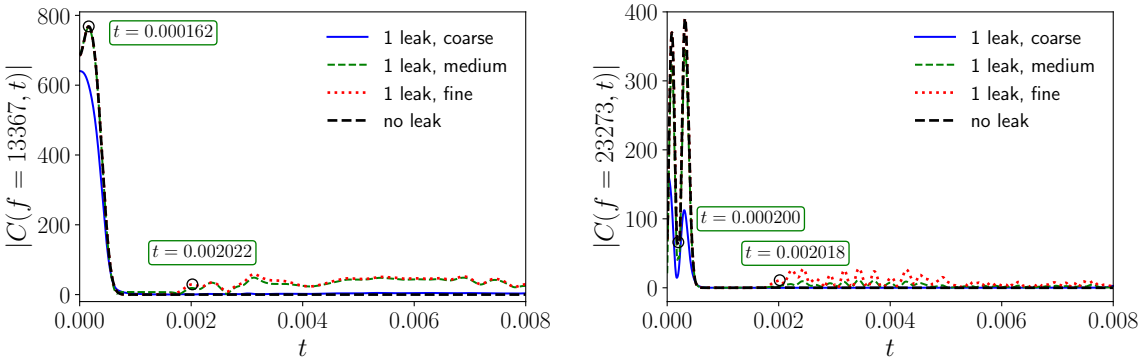

(a) Magnitude plot of the AWT transform at a frequency 13367.

(b) Magnitude plot of the AWT transform at a frequency 23273.

Figure 4.9: Analytic Wavelet Transform of the Pressure Signals from Fig. (4.7) with [3, 120] Morse Wavelet. Arrival Times for the Peaks are Shown in Boxes. Time is in Seconds, Frequency is in Hz.

$-90° \leq \theta \leq 90°$ in the cylindrical coordinate system, covering the possible scenarios of angle separations between the leak and the probe along the circumference, due to a reflectional symmetry of the geometry around a radial line passing through the leak. The location of the probes can be described by the coordinates $(x, y, z) = (0.45D\cos\theta, 0.45D\sin\theta, D)$, with the bottom probe at $\theta = -90°$ located on the opposite side of the leak, and the top probe at $\theta = 90°$ azimuthally collocated with the leak (a baseline probe investigated in the previous section). The signal analysis tool, AWT, remains the same, with the same input parameters.

The results of the AWT transform at both frequencies $f_1 = 0.4726\, c_0/D$ for the various azimuthal probes are shown in Fig. (4.10). It is seen that all probes give the same prediction at a frequency of $0.4726\, c_0/D$, resulting in a good estimation of the leak position for this frequency. Additionally, no azimuthal sensitivity of the signal is observed at this frequency.

The results are done in fine mesh only as coarse mesh is not sufficient from the previous discussion.

The probes at a frequency of $f_2 = 1.3367\, c_0/D$ shown in Fig. (4.11), however, give very different results. First, we note that a significant difference between the readings of the different azimuthal probes is now observed. Probes that are either aligned with the leak from it capture a stronger reflected signal. The timing of the arrival of this signal is also varied as compared to a low-frequency reading, which results in a various prediction of the leak location, as we do not observe in the previous section. The probe at $\theta = 0°$, a side probe, is, however, an exception. It does not show a strong peak at a later time of 0.003 s, which results in a relative accurate prediction of the leak position with less interference from high frequency noise compared to $90°$ or $-90°$. Also, note a reflectional symmetry in the probe signals around the $\theta = 0°$ line. M1 wave is in $x = 0$ plane so it is not captured by $\theta = 0°$ at frequency of $1.3367\, c_0/D$. The peak of the bump caused by reflection signal is shifted, which is due to the traveling path for high frequency wave is different.

At a frequency of $f_3 = 2.3273\, c_0/D$ shown in Fig. (4.12), weaker signal is still observed like frequency of $1.3367\, c_0/D$ at $\theta = 0°$, but it shows certain amount of magnitude which is also oscillatory. So M2 wave is sort of three-dimensional.

The aforementioned behavior is likely associated with the wave dispersion phenomenon mentioned above. At a low frequency of $0.4726\, c_0/D$, the primary mode of reflection is a plane wave, that propagates with the speed close to c_0 and does not exhibit an azimuthal variation. At a higher frequency of $1.3367\, c_0/D$ and $2.3273\, c_0/D$, the radial waves are additionally excited, which carry a significant amount of energy that overshadows the peak associated with a primary plane wave. The radial modes propagate at longer distance due to dispersion effects, resulting at later times of arrival.

The energy associated with these radial waves, which in this case likely resemble the quasi-two-dimensional waves that possess a reflectional symmetry around the

$x = 0$ plane and travel at an angle to a streamwise direction (Louati and Ghidaoui (2017)), decreases as one moves away from the 90° and −90° probe positions, thus explaining the azimuthal variation. This energy is essentially zero at a side probe, which captures only a primary plane wave. To illustrate this phenomenon further, a transient pressure signal received by the probes at 90°, 0° and −90° is plotted in Fig. (4.13). It is seen that all the three probes capture the primary reflection from the leak followed by an oscillatory signal. However, an inset in this figure shows that the energy in the oscillating signal is much higher at 90° and −90° probes, than at a 0° probe. This is commensurate with the results shown above that the top and the bottom probes detect strong high-frequency radial M1 mode wave, while the side probe does note. Note that in the current, three-dimensional situation, the azimuthal modes are excited as well (Baik *et al.* (2013); Rienstra and Hirschberg (2019)), and a side probe does show small oscillations associated with such an azimuthal mode.

The above results might lead to a conclusion that the AWT transform at a relatively low frequency must be used in order to reliably estimate the leak and its streamwise location regardless of the azimuthal probe location and the leak/probe misalignment. It also signifies that a simple one-dimensional theory for a leak detection based on the Method of Characteristics such as in Eq. (4.35) works reliably as long as the analyzed signal frequency is low. On the other hand, for the case of a low signal frequency, an information about the azimuthal leak location is completely lost. Thus, to pinpoint an azimuthal leak position, a higher-frequency information together with the readings from the multiple probes can be used. For example, finding a probe at a higher frequency with the shortest time of arrival would identify which probe is at 90° from the leak, which would help pinpoint the azimuthal leak location. This would be quite useful for the large diameter pipes, those that are hard to inspect visually, for example, if they are buried underground, and for automated leak repairs.

In general, a multi-mode probing at different frequencies can be proposed for the most effective results. However, while the low-frequency plane waves will likely be robustly detectable even in turbulent flows, the behavior of high-frequency signals and their azimuthal variance in the presence of leaks in turbulent flows warrants further investigation.

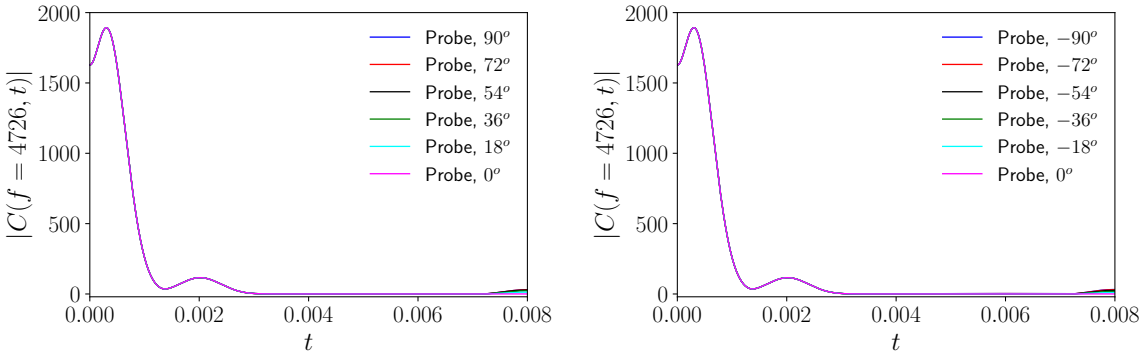

(a) Probes with $0° \leq \theta \leq 90°$ at a frequency 4726.

(b) Probes with $-90° \leq \theta \leq 0°$ at a frequency 4726.

Figure 4.10: Magnitude of the AWT Transform at a Frequencies 4726 for the Pressure Readings from Different Azimuthal Probes. Time is in Seconds, Frequency is in Hz.

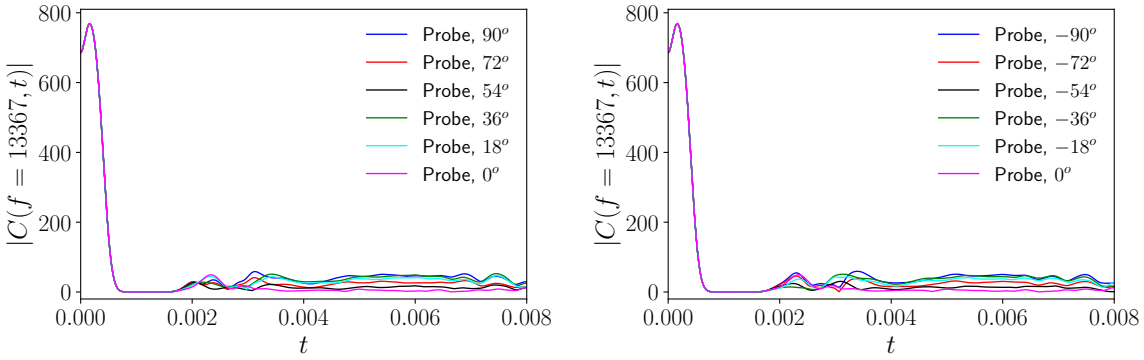

(a) Probes with $0° \leq \theta \leq 90°$ at a frequency 13367.

(b) Probes with $-90° \leq \theta \leq 0°$ at a frequency 13367.

Figure 4.11: Magnitude of the AWT Transform at a Frequencies 13367 for the Pressure Readings from Different Azimuthal Probes. Time is in Seconds, Frequency is in Hz.

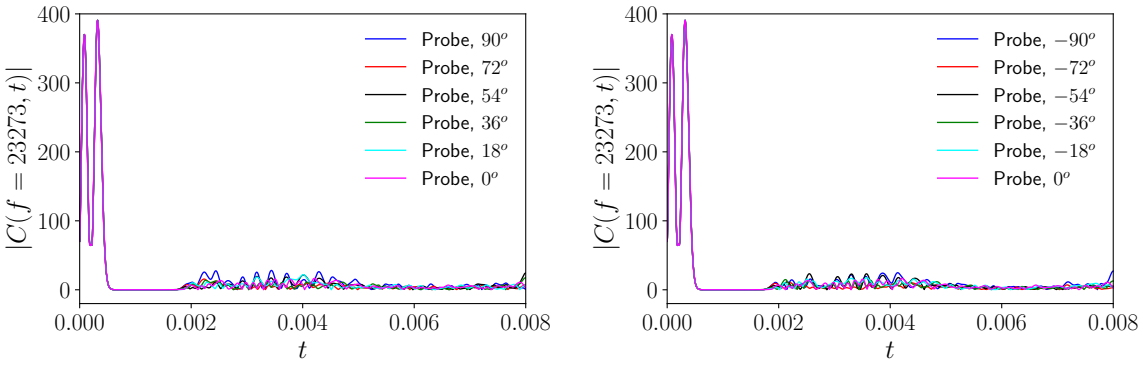

(a) Probes with $0° \leq \theta \leq 90°$ at a frequency 23273.

(b) Probes with $-90° \leq \theta \leq 0°$ at a frequency 23273.

Figure 4.12: Magnitude of the AWT Transform at a Frequencies 23273 for the Pressure Readings from Different Azimuthal Probes. Time is in Seconds, Frequency is in Hz.

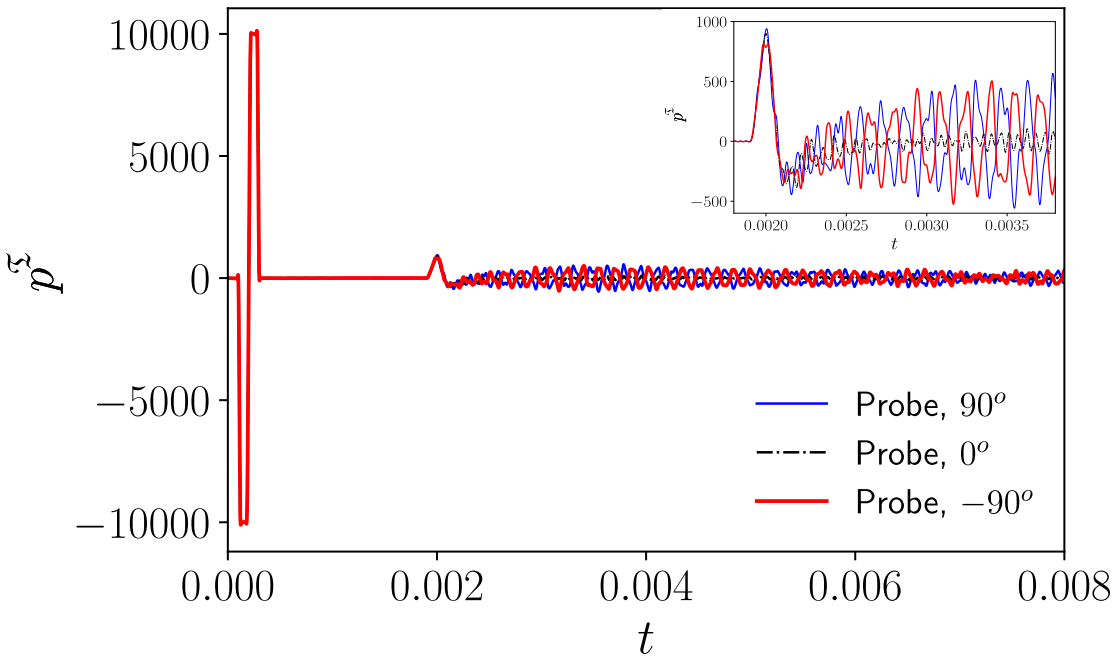

Figure 4.13: Signal Comparison from the Pressure Readings at Different Azimuthal Probes ($90°$, $0°$, and $-90°$). Inset: Zoom-in into the Time $t = (0.0018, 0.0038)$. Pressure is in Pascal, Time is in Seconds.

Three-Dimensional Dynamics of the Transient Pressure

To further characterize the pressure transient dynamics and its three dimensional effects, which, as we have seen in the previous section, might be important for a leak

detection, we plot the pressure snapshots across the $y-z$ and $x-z$ cross-sections of the pipe at selected time instances are shown in Figs. 4.14 and 4.15: $y-z$ cross-section passes through the centerline and the top/bottom probes, while the $x-z$ cross-section passes through the side probes opposite to each other. From these figures we can detect, indeed, a presence of a strong radial mode in the $y-z$ plane that causes significant pressure differences across the pipe cross-section. The $x-z$ plane shows only a mild cross-sectional variation, although non-vanishing, commensurate with a weak azimuthal mode.

Both Figs. 4.14 and 4.15 show a clear positive plane wave initiated by the leak propagating towards the left. The leak excites M1 mode wave at only $y-z$ plane which is the small oscillation observed strongly at $90°$ and $-90°$.

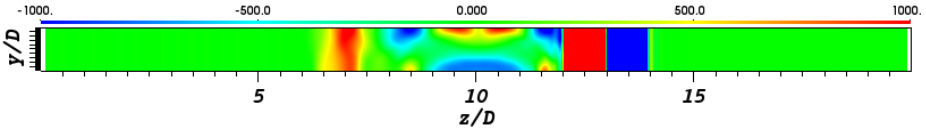

(a) Time = 0.0014

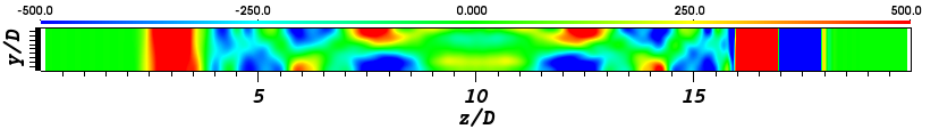

(b) Time = 0.0018

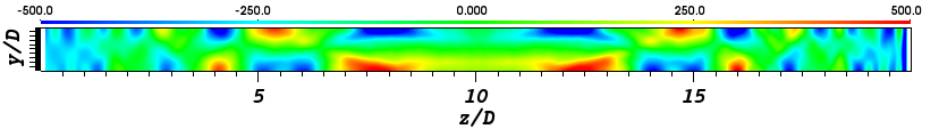

(c) Time = 0.0022

Figure 4.14: Snapshots of a Pressure Transient Signal across the $y-z$ Cross-section of the One Leak Pipe at Different Times, Zoomed into the Low Levels of Pressure between -1000 and 1000 for (a), -500 and 500 for (b) and (c). Pressure is in Pascal, Time is in Seconds.

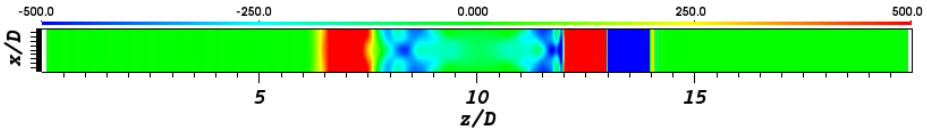

(a) Time = 0.0014

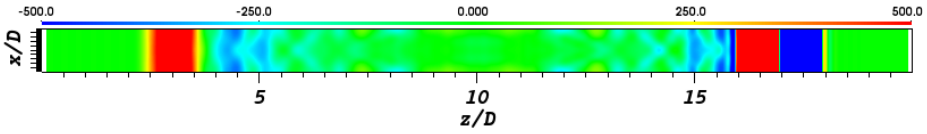

(b) Time = 0.0018

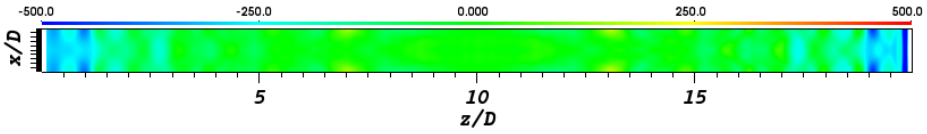

(c) Time = 0.0022

Figure 4.15: Snapshots of a Pressure Transient Signal across the $x-z$ Cross-section of the One Leak Pipe at Different Times, Zoomed into the Low Levels of Pressure between -500 and 500 for (a), (b) and (c). Pressure is in Pascal, Time is in Seconds.

4.6.2 Multiple Leaks

We now focus on investigating the capability of the presented methodology to detect multiple leaks in 3D laminar pipe flows with the same set up as one leak fine mesh but with additional $0.1D \times 0.1D$ leak located $z_{leak} = 15D$, $x_{leak} = 0$, $y_{leak} = 0.5D$. For the signal analysis, the probe is set at $(0, 0.45D, 1D)$, which is azimuthally aligned with both leaks. The transient pressure signal and the AWT analysis results are shown in Figs. 4.16 and 4.17. The transient pressure signal shows very similar reflecting patterns from the first leak in both cases shown in Fig. (4.16(a)). However, at a later time, the transient pressure in case L2 is different, clearly showing a third peak, corresponding to a reflection from the second leak. The AWT analysis presented in Fig. (4.16(b)) illustrates that the third pressure peak corresponding to a second leak can be identified clearly at the same frequency of $0.4726\, c_0/D$. Arrival times and a leak location estimation presented in Table. (4.6) demonstrate that both

leaks are predicted with a good accuracy by the current analysis method.

As for higher frequency $1.3367\,c_0/D$, and $2.3273\,c_0/D$ shown in Figs. 4.17(a) and 4.17(b) and Table. (4.6), the estimation of the second peak is relatively accurate when the timing of the first different peak is picked compared to case L1. But in general, if it is not compared with one leak signal analysis, the second peak is not noticeable compared to the frequency of $0.4726\,c_0/D$. In that case, frequency below M1 mode wave should only be concerned for signal analysis to check the plane wave reflection rather than high mode waves.

We also plot the pressure snapshots across the $y-z$ and $x-z$ cross-sections of the pipe at selected time instances are shown in Figs. 4.18 and 4.19, both show a second clear positive plane wave initiated by the second leak propagating towards the left.

Case	Frequency (Hz)	Peak time t_1, (ms)	Peak time t_2, (ms)	Peak time t_3, (ms)	Actual Leak (m)	Estimated Leak (m)	Error margin
L2	4726	0.303	2.002	3.032	$[1, 1.01]$, $[1.5, 1.51]$	0.95, 1.46	4.30-5.25%, 2.67-3.31%
L2	13367	0.162	2.022	2.806	$[1, 1.01]$, $[1.5, 1.51]$	1.03, 1.42	1.98-3.00%, 5.33-5.96%
L2	23273	0.2	2.018	2.928	$[1, 1.01]$, $[1.5, 1.51]$	1.009, 1.46	0.10-0.90%, 2.67-3.31%

Table 4.6: Estimation of the Peak Arrival Times, the Leak Locations, Eq. (4.35), and the Error Margins in L2 Case for an Azimuthally-aligned Probe.

4.6.3 Water Hammer Case

Previous results were obtained using a single instrumented pressure impulse that reflects from the leak, but is allowed to smoothly propagate out of the domain at both ends of the pipe via an open water-water interface boundary condition, which essentially models an infinitely-long pipe. With a finite-length pipe, the initial transient pressure impulse caused, for example, by opening or closing of the valve, would reflect from the ends of the pipe causing a phenomenon of the water hammer. Indeed, this situation would inevitably occur in laboratory or field experiments, where a re-

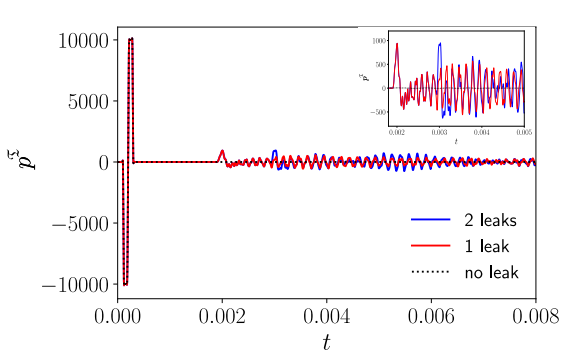

(a) Pressure transient signal at the probe $(D,\ 0.45D,\ D)$. Inset: zoom-in into the time $t = (0.0018, 0.005)$.

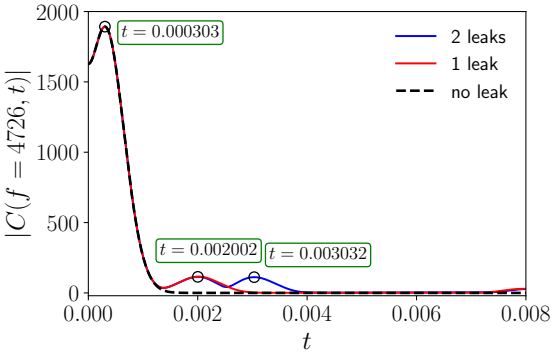

(b) Magnitude plot of the AWT transform at a frequency 4726.

Figure 4.16: Pressure Signal and the AWT Analysis Comparison for a Probe at $(0, 0.45D, D)$ for the Cases with No Leak, One Leak and Two Leaks (Cases L0, L1, L2) in Fine Mesh. Arrival Times for the Peaks are Shown in Boxes. Pressure is in Pascal, Time is in Seconds, Frequency is in Hz.

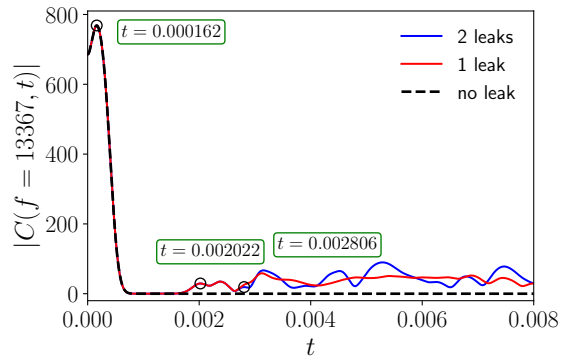

(a) Magnitude plot of the AWT transform at a frequency 13367.

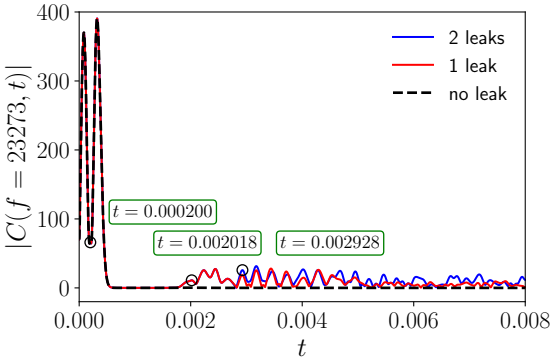

(b) Magnitude plot of the AWT transform at a frequency 23273.

Figure 4.17: AWT Analysis Comparison for a Probe at $(0, 0.45D, D)$ for the Cases with No Leak, One Leak and Two Leaks (Cases L0, L1, L2) in Fine Mesh. Arrival Times for the Peaks are Shown in Boxes. Pressure is in Pascal, Time is in Seconds, Frequency is in Hz.

flection from the pipe end or a water reservoir would cause a water hammer. In the case of a water hammer, the reflection from the leak would continuously interact with the bouncing pressure waves due to a water hammer, potentially making an analysis

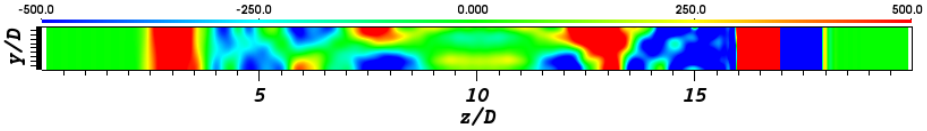

(a) Time = 0.0018

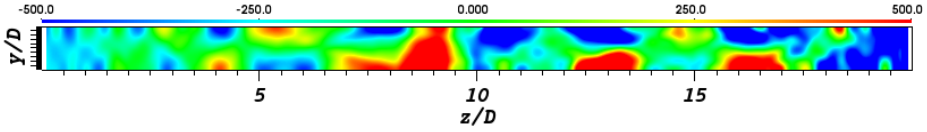

(b) Time = 0.0022

Figure 4.18: Snapshots of a Pressure Transient Signal across the $y-z$ Cross-section of the Two Leaks Pipe at Different Times, Zoomed into the Low Levels of Pressure between -500 and 500 for (a) and (b). Pressure is in Pascal, Time is in Seconds.

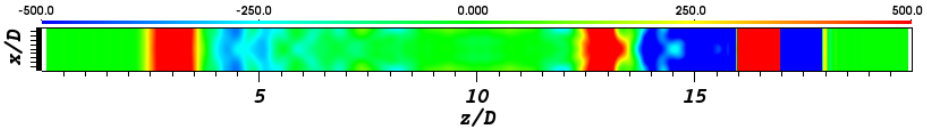

(a) Time = 0.0018

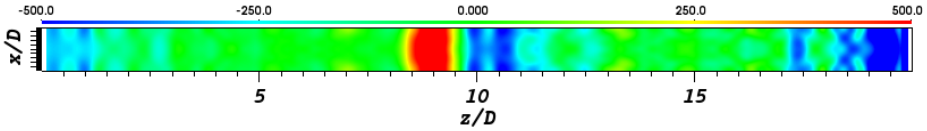

(b) Time = 0.0022

Figure 4.19: Snapshots of a Pressure Transient Signal across the $x-z$ Cross-section of the Two Leaks Pipe at Different Times, Zoomed into the Low Levels of Pressure between -500 and 500 for (a) and (b). Pressure is in Pascal, Time is in Seconds.

more complicated. The leak detection in a presence of a water hammer was studied experimentally and computationally in Brunone *et al.* (2000); Ferrante and Brunone (2003a); Brunone *et al.* (2013); Diao *et al.* (2019).

In this section, we assess the potential of our computational methodology to detect leaks in the situation of a water hammer. The ability of the current computations to correctly predict a water hammer in an intact pipe as compared to experiments (Martins *et al.* (2018)) was already demonstrated in the validation section. Here, we repeat the same computations in the presence of a leak. To model the water hammer

effects, we consider the 3DWH case with one leak, as described in Table 4.3. The major difference between this case and the case 3D1, also with one leak, is that the leak in the current case is moved upstream, to a location of $z_{leak} = 6D$, corresponding to $0.3\,L$ in terms of the pipe length. This is done in order to match one of the test cases in the study of Diao *et al.* (2019) for validation purposes. The water hammer is simulated in the same manner as in the validation section by closing the downstream end of the pipe (modeled with a wall reflection, (B2) condition with $R = 0.98$) and changing the upstream boundary condition to a water-air reflection, (B3) condition with $R = -0.9992$. Note that this computational setup aims to model a reservoir-pipe-valve system, frequently studied in the context of a water hammer experimentally and computationally Ferrante and Brunone (2003b); Covas *et al.* (2005); Diao *et al.* (2019). The reflection coefficient for the leak orifice is set to $R = -0.5$ which is chosen because it yields the closest match with the results of Diao *et al.* (2019) who performed 1D water hammer simulations with the MOC approach. Note that in the 1D MOC approach, a reflection from the leak is modeled via a flow loss coefficient, which is not exactly equivalent to a three-dimensional wave reflection model used here, therefore a one-to-one comparison of the methodologies is not possible.

The pressure transient signal through the pipe end centerline probe for the cases with and without a leak in the presence of a water hammer are shown in Fig. (4.20(a)). We note a similarity of the computed transient pressure signal in the case of a water hammer with the numerical results by Diao *et al.* (2019) obtained with 1D Method of Characteristics for the same relative leak location of 0.3 L . A good agreement between the current 3D simulations and the 1D MOC calculations of Diao *et al.* (2019) confirm the fact that a low-frequency water hammer problem is essentially a one-dimensional phenomenon (Louati and Ghidaoui (2017)).

The AWT transform of the pressure transient signals for a pipe with and without

a leak at a frequency of 0.447 c_0/D is shown in Fig. (4.20(b)). It is seen that while AWT detects strong peaks from the water hammer surges, it also clearly identifies the peaks due to a leak reflection within each water hammer cycle. As with a single transient impulse studied earlier, a main mode of reflection from the leak is relatively broadband and would show its signature at many different frequencies, while a detection frequency must be tuned for a good accuracy of leak detection. In the current water hammer case, the same optimum frequency of 0.447 c_0/D seems to provide a reasonable leak detection capability. The dependence of the optimum frequency on the model parameters, such as Reynolds number, pipe length, speed of sound etc. is of interest and would be studied in the future work.

We finally evaluate the ability of the proposed leak detection methodology based on the AWT transform of a transient pressure signal to be applied to realistic conditions taken from the experimental data, rather than from numerical simulations. To this end, we take experimental pressure transient signal from the laboratory tests of Ferrante and Brunone (2003b), both for an intact and a leaking pipe, and apply our AWT methodology to the decoded signals. The pressure traces from Ferrante and Brunone (2003b) are shown in Fig. (4.21(a)) for completeness. Note that, due to different model parameters, including the Reynolds number, pipe length, location of the leak, surge pressure amplitude etc. (determined by, e.g., a manner in which a valve is opened or closed) we do not expect an exact correspondence between the simulated and experimental signals, however, the trends with respect to Fig. (4.20(a)) are similar. The results of the AWT transform of the recorded signals from experiments (Ferrante and Brunone (2003b)) are shown in Fig. (4.21(b)). Again, while the exact reflection pattern is different (due to, for example, a different relative leak location from an upstream reservoir with respect to the pipe length: $0.3L$ in the current study and $0.634L$ in Ferrante and Brunone (2003b), which, according to previous studies

from Diao *et al.* (2019) has a significant effect on the details of the interaction during the water hammer), a clear peak due to leak can, again, be identified with the current methodology, when applied to the results from the experiments. This testifies of a potential robustness of the methodology in realistic laboratory and field conditions. As far as the scaling of a detection frequency is concerned, an optimum frequency as applied to the current numerical results was found to be $0.447c_0/D$, and an optimum frequency as applied to the experimental results (Ferrante and Brunone (2003b)) was found in the present work to be $23 \times c_0/(2L)$. If these both frequencies are scaled with c_0/L, they provide very similar values: 8.94 c_0/L for the simulations, and 11.5 c_0/L for the experiments. This suggests that a universal frequency scaling on the order of 10 c_0/L may potentially exist, which would provide a very useful guideline on a choice of an optimum frequency with the current AWT methodology, as well as a unification of implementation strategies across laboratory and field data. However, more studies are required to validate this assumption.

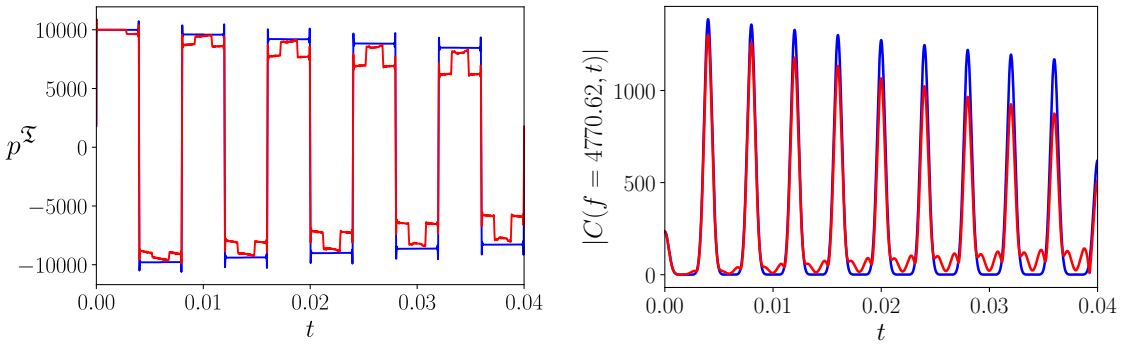

(a) Pressure signals at the downstream pipe end centerline probe (0, 0, 20D).

(b) Magnitude plot of the AWT transform at a frequency 4770.

Figure 4.20: Pressure Signal and the AWT Analysis Comparison for the 3D Water Hammer Cases with No Leak, and One Leak with the Reflection Coefficient of $R = -0.5$. Blue Line is From an Intact Pipe. Red Line is from a Single Leak Pipe. Pressure is in Pascal, Time is in Seconds, Frequency is in Hz.

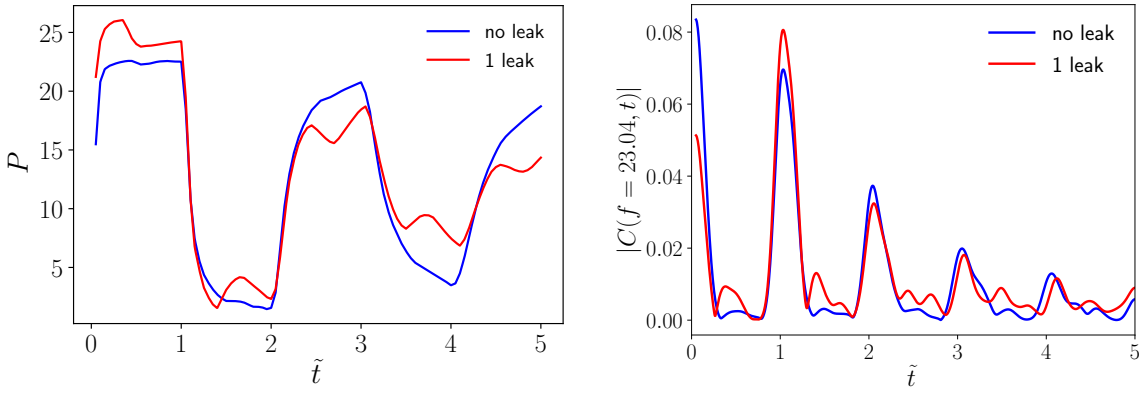

(a) Pressure signals at the pipe end centerline probe.

(b) Magnitude plot of the AWT transform at a frequency $23 \times c_0/(2L)$.

Figure 4.21: Pressure Signal and the AWT Analysis Comparison for the Experimental Water Hammer Cases for the Intact and Leaking Pipes from (Ferrante and Brunone 2003b). Pressure is a Piezometric Head in Meters. Time is Normalized by $2L/c_0$, Frequency by $c_0/(2L)$.

Chapter 5

CONJUGATE HEAT TRANSFER FOR HVAC SIMULATION

This chapter investigates an influence of an intermittent on/off operation of the air-conditioning (AC) equipment on the indoor temperature distribution, air flow and a cycle variability within a single-floor medium-size residential house. The analysis is performed using a recently developed and well validated computational tool based on a Computational Fluid Dynamics (CFD) method, coupled with conjugate heat transfer simulations within the building walls, and an HVAC on/off control model. The importance of including unsteady minute-level dynamic effects associated with the cycling of AC equipment into the energy and thermal analysis of residential and commercial buildings was recently recognized. Despite that, there were no studies that examined the effect of on-off cycling on the physics of the air mixing during both cooling and heating stages of the AC cycle, and how these unsteady interactions effect both the energy consumption and its variability, and the indoor thermal environment linked to a thermal comfort of the building occupants. This chapter focuses on analyzing the duration and variability of the cooling and heating cycles and their effect on the temperature distribution inside a residential house. It is found that both heat transfer from the walls, and turbulent intermittency of the indoor air affect the duration of the cooling and heating cycles. It is demonstrated that a central air system controlled by a single thermostat placed in the hallway results in a consistent overcooling of the interior spaces. These findings are important for the considerations of the electric grid management, and for the improvement of HVAC systems design and control.

5.1 Introduction

Heating, ventilation and air-conditioning (HVAC) systems represent an important component of a building infrastructure, and contribute significantly both to the building energetics (Pérez-Lombard *et al.* (2008); EIA (2015)), and to a quality of the living environment for its occupants (Tian *et al.* (2007); Chen (2009)). Consequently, studies devoted to a performance of ventilation and air-conditioning systems, as well as the corresponding indoor thermal comfort, received a significant attention in the recent literature (Chen (2009); Wang and Zhai (2016)). However, most of these studies considered a continuous operation of an HVAC system, where equipment was assumed to run uninterrupted for considerable periods of time.

HVAC control system is responsible for adjusting the equipment operation, so that the temperature is maintained within the narrow band (a "deadband") around a desired temperature, which is typically set by the thermostat setpoint (Mirinejad *et al.* (2008); Wang and Ma (2008)). Most of the HVAC units currently installed in the residential single-family homes in US and worldwide rely on a simple on/off switch to control the temperature (Wang and Ma (2008); Meier *et al.* (2011); Perera *et al.* (2014)). During an on/off temperature control, for example, for an air-conditioning (AC) mode, the unit operates at 100% capacity when the temperature is above the upper bound of the deadband, it turns off when the temperature reaches the lower bound of the deadband, and turns on again when the temperature exceeds the upper bound (Mirinejad *et al.* (2008); Li and Alleyne (2010); Cetin *et al.* (2019)). The time intervals during which the equipment is running or turned off, depends on many factors, including the outdoor temperature, the thermal characteristics of the building envelope, the size of the indoor space served by the unit, and the capacity of the unit (Cetin *et al.* (2019); Parken *et al.* (1977); Ulpiani *et al.* (2016)). For example, it was

noted that oversized units, facing part-load operating conditions, result in shorter cycles and, thus, more frequent on/off switches during the system operation (Ilic *et al.* (2001); Gorter (2012)). According to recent reviews, most of the units installed in the residential houses are oversized, i.e., they meet their design conditions only less than 2% of the time, and operate in a part-time load for 98% of their functional use (Proctor (1997); Rhodes *et al.* (2011)).

Part-load and cyclic operation of the HVAC units are important considerations that effect a variety of aspects associated with the performance and functionality of an indoor thermal management system, such as energy efficiency (Ilic *et al.* (2001); Tassou *et al.* (1983)), sensible and latent heat exchange capacity (Henderson *et al.* (2000); Winkler *et al.* (2018)), load variability (Cetin (2016); Tchuisseu *et al.* (2017)), and thermal comfort (Ulpiani *et al.* (2016); Park *et al.* (2019)). Henderson *et al.* (2007) and Booten *et al.* (2014) used building energy simulation tools to investigate the effect of part-load operation on energy efficiency and found that it is reduced. Henderson *et al.* (2000) introduced a new user defined function into a DOE-2 simulation tool to account for a change in sensible and latent capacity with part-load conditions and investigated the effect on moisture removal efficiency. Cetin *et al.* (2019) implemented a real-time on/off cycling control model into EnergyPlus and found that its inclusion improved the accuracy of prediction by as much as 20% for both the cooling power and the indoor air parameters (temperature and humidity), when compared with the actual field data for a residential house. While these studies have demonstrated an importance of inclusion of unsteady and short-time scale effects into the building energy simulations, as they are related to the power fluctuations and energy demand variability (Cetin *et al.* (2019); Wetter and Haugstetter (2006); Tabares-Velasco (2013)), they were based on the multizone airflow models, which assume that the air in each zone is well mixed (Chen (2009); Tian *et al.* (2017)).

However, for large multi-room building spaces, and where a stratified flow distribution is important (as in the presence of a natural heating driven by buoyancy when the AC system is off), the assumption of the multizone models fails (Chen (2009); Tian *et al.* (2017); Wang and Chen (2008)), and a Computational Fluid Dynamics (CFD) models becomes a better choice. Additionally, CFD models can provide the details of the airflow and temperature distribution inside the zones, which is important for the evaluation of the thermal comfort of the occupants. In recent studies, a Fast Fluid Dynamics (FFD) model (Zuo and Chen (2009); Zuo *et al.* (2012)) was coupled with the multizone airflow model and an HVAC control system model implemented in Modelica (Zuo *et al.* (2014, 2016); Tian *et al.* (2017)). However, in these studies only one zone in the house was modeled with the FFD while the other rooms relied on a multizone modeling approach.

The objective of the this chapter is to investigate the effects of the on/off operation of the AC equipment on the indoor airflow and temperature distribution inside a residential multi-room single-family building. Such information is of high demand for the building industry and thermal system design sector, and it serves two purposes. First, it allows one to evaluate the level of thermal comfort of the occupants in the presence of the cyclic AC operation. For example, Ulpiani *et al.* (2016) compared the effect of different thermostat control strategies on the energy consumption and indoor thermal comfort using an experimental single-room mock-up building model and concluded than an on/off HVAC controller resulted in the lowest comfort level. The current study provides a guidance on why an on/off AC control could result in a low thermal comfort level, and also makes suggestions about the measures that could be taken to improve the thermal comfort of the occupants. Second, the current study documents the role of an air turbulence on the duration and variability of the cooling and heating parts of the HVAC cycles. This information is crucial for understanding

the equipment cycling effects on operation and stability of electric grid networks, such as, for example, in regards to a demand response management, stability of the power supply, and electric grid frequency regulation (Tchuisseu *et al.* (2017); Tran-Quoc and Sabonnadiére (2009); Hummon *et al.* (2013)). In addition, the collected high-fidelity database can be used for validation and improvement of lower-fidelity building simulation tools in the presence of an on/off AC cycling.

It was shown in Clarke *et al.* (1995); Nielsen and Trytvason (1998); Zhai *et al.* (2002); Zhai and Chen (2005) that it is beneficial to couple CFD models with the building energy simulation tools to obtain the information regarding the wall surface temperature and heating/cooling loads. In the current study, we choose to couple the CFD simulation with the conjugate heat transfer (CHT) simulation to obtain the wall surface temperatures, while the heating and cooling loads are modeled directly by simulating the cooling jet using the on/off control model with the specified thermostat setpoints. CHT allows for an accurate prediction of a coupled dynamics of an airflow and heat transfer inside the house and through the building walls, and was previously used in two-dimensional and three-dimensional studies of an indoor thermal environment in steady and unsteady settings (Kaminski and Prakash (1986); Horikiri *et al.* (2014); Muftuoglu and Bilgen (2008); Kuznetsov and Sheremet (2011)).

The first part of the study considers a medium-size building typical of a single-family home in Arizona, using the operational conditions relevant for a summer day in a Phoenix climate. We use a well-validated open-source spectral-element fluid dynamics and heat transfer solver Nek5000 (Fischer *et al.* (2015)) for CHT simulations, while a turbulent air flow is modeled using a Large Eddy Simulation technique (Peet and Fischer (2010); Chatterjee and Peet (2018)).

5.1.1 Whole Housing Pre-Cooling

Most residential building type in the U.S. is wood light frame for being least expensive but durable (Allen and Iano (2019)). Other system such as heavy timber frame is discouraged to be used for example in Phoenix for being combustible (PHOENIX (1997)). The basic vertical components of wood light framing house is repetitive and vertical 2×4 or 2×6 framing studs with 16 or 24 inches spacing made from softwoods, for example, Douglas fir, Southern pine, etc and then sheathed with wood structure panel. Thermal insulation material is stuffed inside of wall for thermal insulation, such as batt, spray foam, fiberglass, vacuum panel or mineral wool (Allen and Iano (2019)). Studs, wood panels, and stuffed insulation material are the basic components of housing envelope and partitions. Although additional thermal insulation material for example, stucco would be applied for reducing radiation, most insulation essentially depends on stuffed thermal insulation material.

Thermal insulation material plays a major roll in keeping housing comfortable and less influenced by outer temperature. When thermal conductivity is high, rooms would be heated in a short time by outer heat through building envelop, and it would cause huge burden for air conditioner as heat is not blocked effectively. But when thermal conductivity is low, it would take some time for heat to pass through building envelope and give air conditioner some time to make room cooled.

So basically, for an air conditioned housing, it has two stages. When AC is off, room is heated through building envelope and glazing. When AC is on, room is still heated but AC cools hot air and distributed cooled air into rooms. Because of thermal insulation, outside heat could be sort of blocked or slowed down to transfer into inside housing. Thus, when people at home and set thermostat to a temperature, AC would run for example 3-4 minutes and then stop for example 10-12 minutes, which is called

dead-band.

One problem is when most of people come home from work and need air conditioning, electricity usage would be quite high. Such high usage is called peak hours. At that period, power plants have to be operated with highest burden, which is quite a challenge for electricity provider. To smooth out the power usage peak, becomes a research topic and one strategy is to over cool whole housing for about 6 °F for few hours before peak hours and then let house be naturally heated during peak hours (Turner *et al.* (2015); German and Hoeschele (2014); Arababadi (2016)). With thermal insulation material, it would take whole housing some time to be heated for 6 °F. So during peak hours, AC would not be turned off and peak hours would be smoothed out for such pre-cooling. The crucial part of such pre-cooling strategy is thermal insulation should be good enough to prevent housing heated so fast.

To study pre-cooling for whole housing, whole building energy simulation program, for example EnergyPlus is commonly used (Arababadi (2016)). It is useful and could give relatively realistic results compared to experiments. But it would not simulate dead-band and detailed flow and temperature distribution. In the second part of this study, we would show Nek5000 gives out similar results of pre-cooling simulation compared to other studies as validation.

5.1.2 Multi-Zone Housing Pre-Cooling

By installing dampers for ducted system to control flow rate, or installing multi-zone ductless mini-split system to provide different amount of refrigerant to different rooms, multi-zone cooling becomes a popular option nowadays for large housing as each room needs different temperature control.

For most of air conditioner, it uses single stage compressor which means AC runs at full power regardless of thermostat temperature setting. For example, when you set

thermostat to 70 °F, and return air temperature is 80 °F, air supply vent would give about $\Delta t = 20$ °F difference cold air all the time even if room temperature becomes closer to 70 °F. It turns on and off often and it is not that comfortable as air from supply vent is quite cold, and AC is only on when room temperature becomes higher than the setting.

But two stage and variable-speed compressors are different. Two stage compressor provides another low level of operation for keeping temperature variance smooth, and it would only run high level of operation when outside temperature is severe. Variable-speed compressor is even more robust and it can adjust its operating capacity depends on different situation.

Multi-zone ductless mini-split uses variable speed compressor and it could distribute different volume of refrigerant to each blower and let it perform differently. With such system, every room temperature could be set different rather than to be controlled by a center thermostat.

Such technology brings another thought of smoothing peak hours that it is not necessary to pre-cool a whole housing, but only room needed. In the last part of the study, we should show our estimation of heating time range for multi-zone pre-cooling.

5.2 Modeling Methodology

5.2.1 House Model

A housing model in this study is taken as a 755.11 square feet residential home with four rooms, featuring two bedrooms, an open-floor living area that includes the kitchen, and a long hallway dividing the bedrooms and the living area. The house floor plan is presented in Fig. (5.1) and Fig. (5.2), where green color represents the house interior, gray is the building envelope, black color represents the door,

and blue color corresponds to the windows. Room 1 and Room 2, the bedrooms, have the same area of 4 m × 3.6 m (155 square feet), albeit Room 2 has a window (0.8 m × 1.2 m) for testing the glazing effect, which can be seen in a three-dimensional view in Fig. (5.3(a)). The bottom edge of the window is located 1 m above the ground, and its closest vertical edge is 0.4 m away from the partition between the Rooms 1 and 2. The ceiling height of the house is 2.6 m. Room 1 and Room 2 both have an air supply vent (0.2 m × 0.2 m) in the ceiling located 1.4 m away from both interior partitions in each room (with Room 3 and between the Rooms 1 and 2), which can be viewed in Fig. (5.4).

Room 3 (1.2 m × 7.4 m) represents a hallway, and it does not have an air supply vent, but has an air return vent (0.4 m × 0.6 m) located at the ceiling in the center of Room 3 as can be seen in Fig. (5.4(a)). Room 3 also includes a front door (0.8 m × 1 m) colored in black, please, refer to Fig. (5.1) and Fig. (5.3).

Room 4 is considered as a living space with an area of 4 m × 7.4 m, and it includes two ceiling air supply vents, both of 0.2 m × 0.2 m, located 2 m away from the partition between the Rooms 3 and 4, and from each side of the building envelope. Room 4 also comes with two glass windows colored in blue, one for the kitchen (1 m × 1.2 m), and another for the balcony (1.8 m × 2.4 m), which can be viewed in Fig. (5.1) and Fig. (5.3(b)). The kitchen window's bottom edge is 1 m away from the ground, and the closest vertical edge is 0.8 m away from the building envelope. The balcony window extends all the way down to the ground, and has its closest vertical edge 2.8 m away from the envelope.

The partition walls adjacent to Room 3 are 0.14 m thick, and the partition between Rooms 1 and 2 is 0.2 m thick. The inner wall of the building envelope is 0.1 m thick, except for the inner roof wall, which is 0.2 m thick. The outer wall and the outer roof are both 0.1 m thick, as can be seen in Fig. (5.2). The total housing area is

70.152 m^2 (755.11 square feet) including the partitions. The house is modeled after a two-bedroom residential condo plan of the IMT Desert Palm Village in Tempe, AZ.

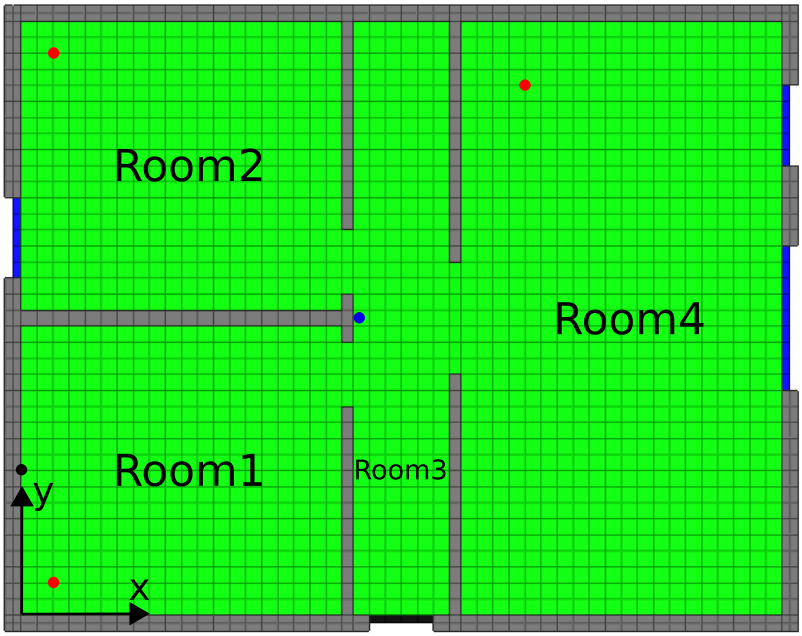

Figure 5.1: Floor Plan and the Building Envelope at a Height of 1.6 m. Blue Dot Corresponds to a Thermostat Probe; Red Dots, Remote Temperature Probes within the Rooms; Black Dot, a Wall Temperature Probe for the Initial Heating Stage of the Simulations.

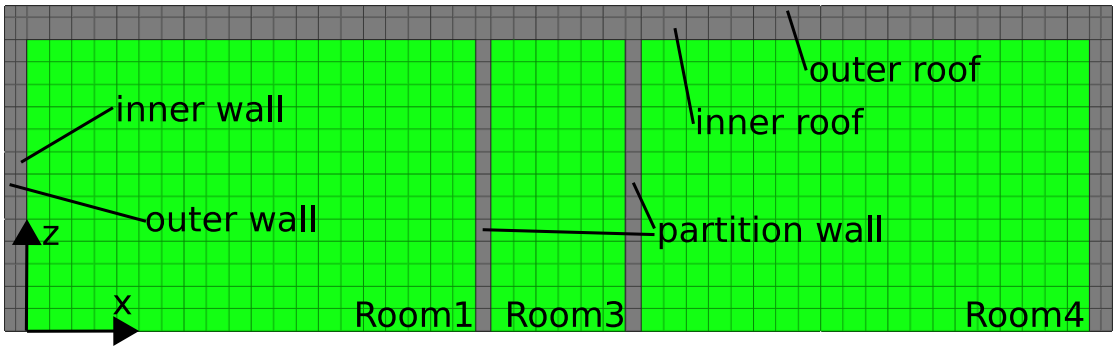

Figure 5.2: Cross Sectional View of the House Model Taken Through the Center of Room 1.

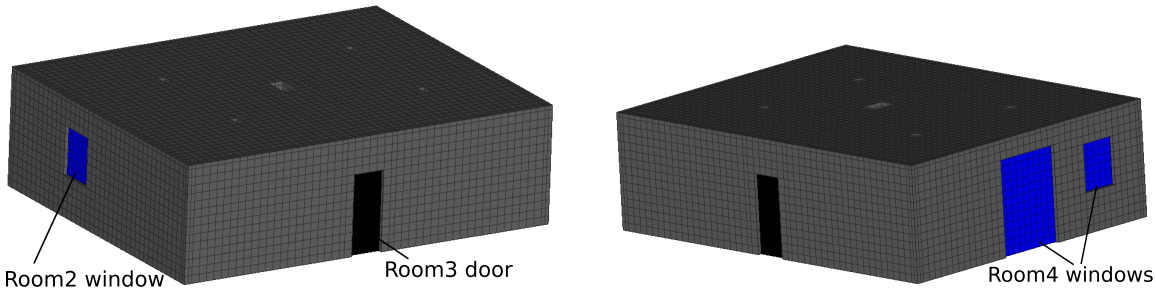

(a) Left view. (b) Right view.

Figure 5.3: Exterior View of the Building Envelope.

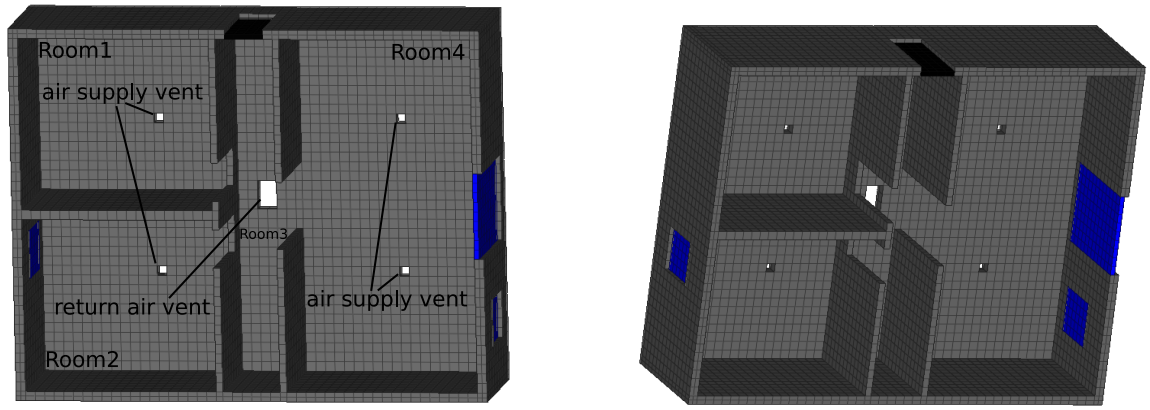

(a) Straight view. (b) Angled view.

Figure 5.4: Interior View of the Building Envelope.

5.2.2 Material Properties

There are three types of materials used to model the building envelope: Douglas Fir wood for the exterior walls, exterior roof and the door; LD-C-50 spray foam for the insulation; and glass for the windows. Insulation is used in all the inner walls, including the inner parts of the building envelope, inner roof, and the interior partitions between the rooms. The material parameters used in the current study are listed in Table. (5.1). The interior part of the house shown in green in Fig. (5.1), Fig. (5.2) is considered to be occupied by an incompressible air, whose parameters are also documented in Table. (5.1).

Material	Density (ρ_s)	Specific heat capacity (C_p)	Thermal conductivity (k)	Dynamic viscosity (μ)
Douglas Fir wood	$1200\,\mathrm{kg/m^3}$	$550\,\mathrm{J/(kg\cdot K)}$	$0.12\,\mathrm{W/(m\cdot K)}$	N/A
LD-C-50 spray foam	$8\,\mathrm{kg/m^3}$	$2000\,\mathrm{J/(kg\cdot K)}$	$0.038\,\mathrm{W/(m\cdot K)}$	N/A
Glass	$2500\,\mathrm{kg/m^3}$	$840\,\mathrm{J/(kg\cdot K)}$	$0.96\,\mathrm{W/(m\cdot K)}$	N/A
Air	$1\,\mathrm{kg/m^3}$	$1000\,\mathrm{J/(kg\cdot K)}$	$0.027\,19\,\mathrm{W/(m\cdot K)}$	$1.9\times10^{-5}\,\mathrm{N\cdot s/m^2}$

Table 5.1: Material Parameters for the Solid and the Fluid.

5.2.3 Numerical Method

Governing Equations

In this chapter, a coupled heat transfer problem between the building solid walls and the interior air is studied via a conjugate heat transfer (CHT) technique. In a CHT formulation, the governing equations for the air flow and the temperature are coupled with the heat conduction equation inside the solid. For both the fluid and the solid components, an open-source Computational Fluid Dynamics solver Nek5000 (Fischer *et al.* (2015)) is used in this study, which is based on a spectral element formulation of the governing equations (Patera (1984); Deville *et al.* (2002)). For a conjugate heat transfer problem, the simulation domain consists of the non-overlapping fluid and solid domains with its own material properties. In this study, the solid domain corresponds to the inner and outer parts of the building envelope as described in Sec. (5.2.1), and the fluid domain corresponds to the house interior with air as the working fluid.

The governing equations for the fluid are the incompressible Navier-Stokes equations described as

$$\nabla \cdot \mathbf{u} = 0, \tag{5.1}$$

$$\rho\,(\frac{\partial \mathbf{u}}{\partial t} + \mathbf{u}\cdot\nabla\mathbf{u}) + \nabla p = \mu\,\Delta\mathbf{u} + \rho\,\mathbf{f}, \tag{5.2}$$

$$\rho\,C_p\,(\frac{\partial T}{\partial t} + \mathbf{u}\cdot\nabla T) = k\Delta T, \tag{5.3}$$

where ρ, $\mathbf{u} = \{u_x, u_y, u_z\}$, $\mathbf{f} = \{f_x, f_y, f_z\}$, p, T, μ, C_p and k are the fluid density, ve-

locity, external force, pressure, temperature, dynamic viscosity, specific heat capacity, and thermal conductivity, respectively. A Boussinesq approximation is applied to the formulation (5.1)–(5.3), whereby the forcing term in Eq. (5.2) is set as $\mathbf{f} = \{0, 0, f_z\}$, $f_z = \beta g(T - T_0)$, where T_0 is the reference temperature taken as the initial uniform temperature of the interior air, T is the local temperature, $g = 9.8\,\mathrm{m/s^2}$ is the gravity constant, and β is the coefficient of the thermal expansion (Sakievich *et al.* (2016)).

In the solid domain, a heat conduction equation is solved as

$$\rho\, C_p \frac{\partial T}{\partial t} = k\Delta T, \tag{5.4}$$

where ρ is the density, C_p is the specific heat capacity, and k is the thermal conductivity of the solid. Since there are three different solid material zones in the current housing model, see Table. (5.1), Eq. (5.4) is applied to each zone with its separate material parameters.

Numerical Discretization

Equations (5.1)–(5.4) are spatially discretized with the spectral element method, where Lagrange-Legendre interpolating polynomials of degree N are employed within each element as the basis functions for velocity and temperature, and the equivalent polynomials of degree $N-2$ are used to discretize the pressure (Deville *et al.* (2002)). For the time advancement, an implicit second-order backward difference scheme is used for the diffusive terms, and an explicit second-order extrapolation scheme is used for the non-linear and the forcing terms. For pressure and velocity decoupling in the Navier-Stokes equations, an operator splitting approach is used (Deville *et al.* (2002); Fischer (1997a)), upon which the corresponding Helmholtz and Poisson solvers are solved via a preconditioned conjugate gradient, and a generalized minimal residual method, respectively. The coupling between the fluid and the solid domains is

done monolithically (Peet and Fischer (2010); Merzari *et al.* (2017)), where a single temperature field is composed for both the fluid and the solid domains, and the equations (5.3) and (5.4) are solved simultaneously, via a preconditioned conjugate gradient method, after solving for the fluid and the pressure fields in (5.1), (5.2). The presented conjugate heat transfer model and its numerical implementation is validated in Sec. (5.3.1) on a laminar, two-dimensional, natural convection problem in a square enclosure compared with the simulations of Kaminski and Prakash (1986).

Large Eddy Simulation

Considering the application of the presented methodology to high-Reynolds number flows associated with heating, ventilation and air-conditioning system operation, turbulent flow motions and their effect on the heat transfer must be taken into account. In the current study, a Large Eddy Simulation approach is used, with a spectral filtering regularization technique acting as a subgrid-scale model (Chatterjee and Peet (2018); Fischer and Mullen (2001)). With the filtering-based regularization, the governing equations of the fluid motion (5.1)–(5.3) are unchanged, while the explicit filtering of primitive variables in the modal space serves to remove the energy from the unresolved subgrid scales, thus mimicking a dissipative action of classical eddy-viscosity type subgrid models (Guermond and Prudhomme (2003); Berselli *et al.* (2006); Geurts *et al.* (2008)). Regularization based LES approaches are used extensively with high-order methods (Chatterjee and Peet (2018); Karamanos and Karniadakis (2000); Visbal *et al.* (2003); Geurts (2008)). Specifically, a filtering-based LES model for Nek5000 was extensively validated in the previous studies for a variety of turbulent flows (Peet and Fischer (2010); Fischer *et al.* (2008); Peet *et al.* (2013); Obabko *et al.* (2013)). It is additionally validated in Sec. (5.3.2) for a ventilated model room test case compared to experiments (Posner *et al.* (2003)) and LES

simulations (Tian *et al.* (2007)).

5.2.4 Simulation Details

Numerical Grid

The residential building model described in Sec. (5.2.1) is discretized with a spectral element mesh, where element boundaries are shown in black in Figures 5.1–5.4. As can be seen, the elements are mostly cubical, of the size $0.2\,\mathrm{m} \times 0.2\,\mathrm{m} \times 0.2\,\mathrm{m}$, except in a few places, where specific geometrical features prevent them from being cubical, such as, for example, in the exterior solid layer, which is 0.1 m thick, or in and around the interior partitions, which are 0.14 m thick. The number of elements are 22,037 in the fluid domain, and 9,715 in the solid domain, resulting in 31,752 elements total. Functions within each element are discretized with $N = 7^{th}$ order polynomials ($N = 5$ for pressure), which results in additional 8^3 collocation points per element (6^3 points for pressure). This yields an estimate of approximately 16 mln. grid points for the total LES simulation. A more detailed illustration is presented in Fig. (5.5).

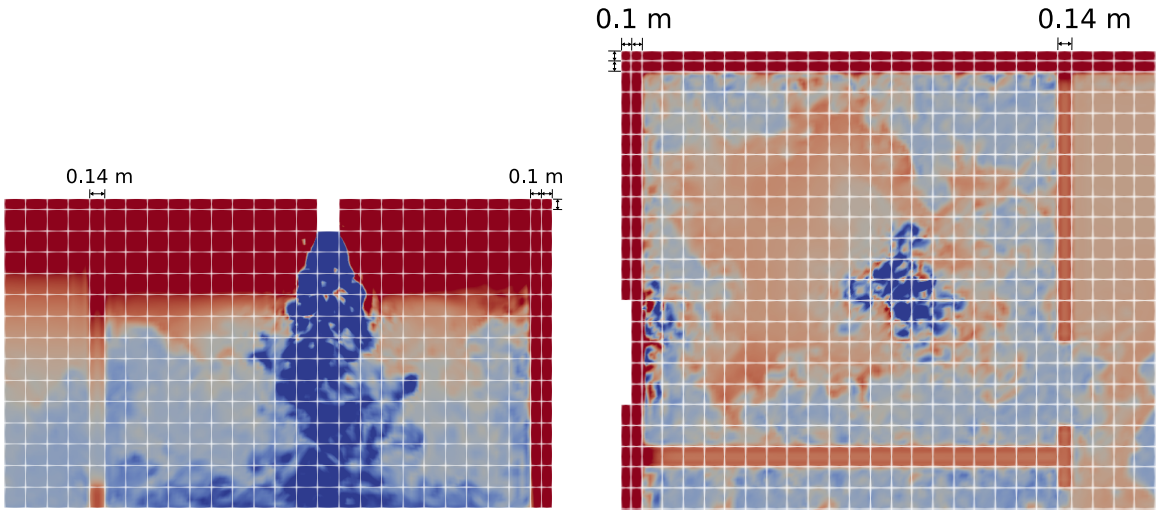

(a) Mesh view at y=2.1.

(b) Mesh view at z=1.6.

Figure 5.5: Mesh Size View.

Inlet Air Vent Model

For the air supply vents located in the Rooms 1, 2 and 4, we consider a standard four-way deflection square vent model schematically shown in Fig. (5.6). To model the air flow through the four-way deflection vent, the following velocity boundary conditions are used

$$\begin{aligned} &u_z = -v, \\ &u_x = vs, u_y = 0, \text{if } x > x_c, y > y_c, \\ &u_x = 0, u_y = -vs, \text{if } x > x_c, y < y_c, \\ &u_x = 0, u_y = vs, \text{if } x < x_c, y > y_c, \\ &u_x = -vs, u_y = 0, \text{if } x < x_c, y < y_c, \end{aligned} \tag{5.5}$$

with the scaling factor $s \geq 0$ being equal to

$$s = \left(1 - (2\,l_x - 1)^2\right)\left(1 - (2\,l_y - 1)^2\right), \tag{5.6}$$

where $v = 1\,\text{m/s}$, (x_c, y_c) is the center of each air supply vent, $l_x = |x - x_c|\,/h$, $l_y = |y - y_c|\,/h$, $l_x, l_y \in [0, 1]$ correspond to the non-dimensional distances from the vent center normalized by the vent half-width, and $h = 0.1\,\text{m}$ is the half-width of each square side of the vent. The scaling factor s is used to ensure the continuity of the tangential velocity component at the junctions between the quarter partitions, where it is set to zero, as well as at the outer edges of the partitions. The positive direction of z axis is pointing upwards (from the ground to the ceiling), the positive direction of x axis is pointing from Room 1 to Room 4, and the positive direction of y axis is pointing from Room 1 to Room 2 as can be seen in the floor plan shown in Fig. (5.1) and Fig. (5.2). The model (5.5) thus provides the flow that spreads outward in every direction, in agreement with the operation of the actual vent. The specified inlet velocity yields 95.56 CFM airflow per air supply vent, and 382.24 CFM airflow in total for the four vents considered in the current building model.

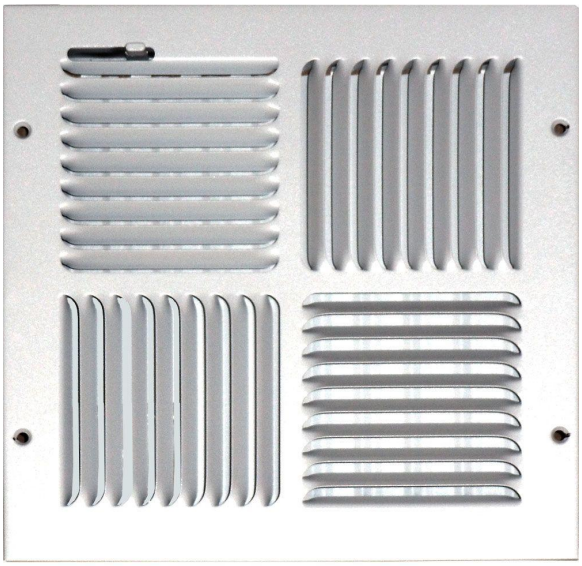

Figure 5.6: A Schematic of a Four-way Deflection Square Vent; Modeled after Speedi Grille - 1010 CW4 Ceiling Vent.

Simulation Setup

The current simulations model an on/off operation of the residential HVAC system, wherein each AC cycle consists of two stages: cooling stage characterized by a forced convection when AC is running, and heating stage characterized by a natural convection when AC is turned off. A variable time stepping strategy is adopted to increase the efficiency of the simulations, where the time step of $\Delta t = 5 \times 10^{-4}$ s is used for a cooling stage, and $\Delta t = 2.5 \times 10^{-3}$ s is used for a heating stage. The smaller time step is required for the cooling stage in order to resolve the motions of the small-scale turbulent eddies generated by the cooling jet associated with the short time scales. Additionally, time step needed for stability is inversely proportional to the flow velocity scale, according to the Courant-Friedrichs-Lewy condition (Courant *et al.* (1967)), which leads to smaller time steps for the cooling stage due to a higher jet velocity. The time step can be relaxed for the heating stage, associated with the air motion by natural convection, which is slower than the forced jet flow.

Boundary Conditions For the cooling stage, the inlet velocity given by Eq. (5.5) is specified at each air supply vent, with the air inlet temperature set to 60 °F (288.706 K). The air return vent in Room 3 is modeled as an outflow boundary condition during the cooling stage.

For the heating stage, the air inlet velocity at all the supply vents, and at the return vent is set to zero, with insulated boundary conditions for the temperature, modeling a shut-down of the flow through the ventilation duct. The flow during the heating stage is driven only by buoyancy force, corresponding to a situation of a natural convection.

For both stages, velocity boundary conditions at all the walls, partitions, windows and the door, are set as the no-slip. Insulated temperature boundary condition is applied on the bottom floor interfacing the ground, and on the lateral walls of the air vents. The temperature at the building exterior boundary, including the vertical solid walls, windows, door and the roof, is set to 100 °F (310.928 K).

This setup aims to model operational conditions for a residential household during an Arizona central valley summer day, where the outside temperature holds nearly constant for several hours (Svoma and Brazel (2010); Tewari *et al.* (2017)).

Initial Conditions Prior to a start of a regular on/off cycling of the air-conditioning equipment, the simulations undergo an initial development period. We wish to set up initial conditions, which correspond to an interior air temperature of $T_0 = 81$ °F (300.3722 K), and an outside temperature of 100 °F (310.928 K), to model a typical indoor environment of a residential house during the mid-day in Arizona central valley summer. However, the temperature distribution within the solid walls corresponding to these two bounding temperature points, is unknown.

Ideally, one would want to set up a temperature profile within the solid walls that

corresponds to a steady-state solution of the coupled heat transfer problem. But the only steady-state solution to this problem, without AC running, would correspond to an eventual heating of the interior air to 100 °F, while with AC running, we can not have a steady state due to cycling. To circumvent this problem, we start with the initial conditions of the fluid at rest, interior and exterior air temperatures as specified above (81 °F for interior and 100 °F for exterior), and the solid wall temperature at 81 °F, and we let the simulations run, with the AC turned off, until the temperature at the interface between the inner wall and the room air at a particular probe location in the center of Room 1 at a height of 1.6 m (shown in black in Fig. (5.1)) reaches 81.5 °F (300.65 K), which means that the outdoor heat started penetrating inside the building walls.

To speed up the initial heating process, we also turn off a natural convection within the house, i.e. we do not consider an effect of buoyancy force during this initial stage of the simulations, whose purpose is solely to provide reasonable wall temperature profile for the initiation of the on/off cycling. This initial heating stage can be viewed as a natural heating process corresponding to a mid-morning time, when the house is still sufficiently cooled from the night, but the building envelope gradually starts heating up from the warming weather outside.

AC Cycling Control Model

After this initial development stage, we start the AC cycling, originating with the cooling stage. To control the AC cycling, we consider a central air model, with a single thermostat probe located next to the center-left interior partition within the Room 3, as shown by a blue dot in Fig. (5.1). The thermostat probe is located 0.015 m away from the wall at a height of 1.6 m, and has a coordinate description as (4.155, 3.7, 1.6) in meters. We allow for a small offset between the thermostat probe and

the wall, so it would detect the air temperature, and not the wall temperature, for more reliable readings. The deadband is set between 79 °F and 81 °F, i.e. AC turns off when the temperature at the probe reaches 79 °F, and turns on again, when it reaches 81 °F.

Whole Housing Pre-Cooling

The simulation for whole housing pre-cooling and heating also contains three stages, initial stage, cooling stage and heating stage. And the difference is that the initial temperature, which is 297.0389 K (75 °F), as whole housing has cooled for a quite long time. The purpose of such initial stage is the same as heat is not distributed well among the building envelope. The initial stage would be stopped once the temperature probe of the inner left wall interface of Room1 at height 1.6 m reaches 297.3167 K (75.5 °F).

For pre-cooling in reality, when thermostat is set to a low temperature, for example from 299.817 K (80 °F) to 296.483 K (74 °F), AC would start to run until thermostat sensors 295.928 K (73 °F). However, since wall temperature is not cooled yet, room temperature would be raised very soon. Thus it is necessary to set thermostat to a low temperature for a while, for example, 2 hours, before peak hours in order to make room remained cold for a while. But if thermostat is set to low temperature for a long time, energy cost would be increased again. Thus the initial temperature for pre-cooling study is set under an ideal case that all rooms including the building envelope is cooled to 297.0389 K (75 °F) and it is assumed as upper bound. It gives the maximum shifting time for the room temperature to be heated back to 300.3722 K (81 °F) and it is also called recovery time in this study.

After the initial stage, a regular fixed thermostat AC cycle would be simulated in order to let the temperature distribution inside of the walls becomes steady and

heated more. In the cooling stage, cold air of temperature 285.372 K (64 °F) is blown and velocity profile, outside temperature remains the same as Sec. (5.2.4). Once thermostat sensors 295.928 K (73 °F), cooling stage ends, and heating stage starts. Heating stage ends once thermostat sensors 297.0389 K (75 °F).

Such regular AC cycle at lower temperature would be run for few cycles to let temperature distribution among the building envelop become stable. And then, a long heating stage would be run to simulate how much time it would take to be heated back to normal temperature and see how much peak hours could be shifted. The simulation would be stopped when the thermostat sensors 300.3722 K (81 °F).

Upper bound simulation only gives the maximum time about the recovery time as the housing is assumed to be cooled to 297.0389 K (75 °F). And in this study, a lower bound is also simulated to check the minimum recover time and give a range of whole housing pre-cooling performance. Different from upper bound simulation, lower bound starts with the previous few cycles of fixed thermostat regular AC cooling and heating and the thermostat is set to be 299.817 K (80 °F). Then, a long cooling stage is simulated till the thermostat sensors 295.928 K (73 °F) and the inlet temperature is set to be 285.372 K (64 °F). At last, a heating stage is simulated and it would be stopped when the thermostat sensors 300.3722 K (81 °F). It is called as lower bound as it is directly heated from a pre-cooling temperature back to a normal setting, which does not allow the housing to be cooled under a low temperature setting for a while. Compared to the upper bound, that housing is cooled under a low temperature for an extreme long time, the lower bound shows the opposite that the housing is cooled that low for only once. So it gives the minimum recovery time.

Multi-Zone Housing Pre-Cooling

Different from the whole housing pre-cooling, multi-zone housing pre-cooling focuses on Room1 pre-cooling only in this study. The temperature setup for Room1 is similar to the whole housing pre-cooling, but the rest is quite different as it would influence the temperature of Room1. In the whole housing pre-cooling, outside temperature is the heating source but in the multi-zone housing pre-cooling, surrounding rooms becomes the heating source of Room1 as well. If the surrounding room temperature is high, Room1 temperature would be raised faster when the surrounding room temperature is lower. And also, in reality, people would set different temperature for other rooms which would influence the performance of multi-zone pre-cooling.

In this study, two initial temperature setting is used to estimate the upper and lower bounds of the final heating time. For the upper bound, the initial temperature of Room1 is set to be 297.0389 K (75 °F) including the adjacent walls of the building envelope and the partition walls as Room1 is fully cooled for a long time. The initial temperature of the rest housing and building envelope is set to be 299.817 K (80 °F) as a normal temperature. For the lower bound, the initial temperature of Room1 and the same adjacent walls is still set to be 297.0389 K (75 °F) but the rest is set to be 310.928 K (100 °F). It is a extreme case of multi-zone housing pre-cooling that only Room1 is pre-cooled. With that setting, Room1 is much easier to be heated compared to the upper bound setting. The initial heating stage would be stopped for both bounds once the temperature probe of the inner left wall interface of Room1 at height 1.6 m reaches 297.3167 K (75.5 °F).

Same as whole housing pre-cooling, after the initial heating stage, regular cooling and heating stage would be performed for making heat distribution among the walls stable. But different from whole housing setup when thermostat in Room3 controls

AC on/off, a remote temperature probe at the coordinate of (1, 1, 1.6) would be the thermostat for Room1 instead, which is far away enough from the air supply vent and also the building envelope to avoid flow motion. The temperature of the cold air supply during the cooling stage is 285.372 K (64 °F), and it would be stopped once the remote thermostat in Room1 sensors 295.928 K (73 °F). And then, heating stage would be performed and it would be stopped once it sensors 297.0389 K (75 °F). After performing some regular cycles, a final heating stage would be simulated and it would be stopped when the remote thermostat sensors 300.3722 K (81 °F).

In the previous whole housing simulation, doors between rooms are not simulated for improving ventilation. But for multi-zone pre-cooling, as only one room matters, Room1 and Room2 should be isolated through door which is considered as wood. Thus, Room1 and Room2 no longer have large scale of air ventilation between Room3, except a small hole located at z= 1.8 m to 2 m, y= 3 m to 3.2 m and x=4 m to 4.14 m.

5.3 Validation

Before documenting the main results of the current study, we present a detailed validation of the computational method. First, we validate the conjugate heat transfer model versus previously published results (Kaminski and Prakash (1986)). Second, we validate the LES model on the case of a ventilated room model against experimental data (Posner *et al.* (2003)), and the results of the LES simulations of Tian *et al.* (2007). Third, we apply the developed full house model with an on-off HVAC control to the case study presented in Cetin *et al.* (2019), and compare Nek5000 results with both the field data, and the EnergyPlus simulations documented in Cetin *et al.* (2019).

5.3.1 Validation of Conjugate Heat Transfer Model

To validate the conjugate heat transfer model in Nek5000, a two-dimensional, laminar, natural convection flow in a square enclosure is simulated and compared with the previous numerical results of Kaminski and Prakash (1986). Fluid domain is a square with coordinates $[0,1] \times [0,1]$ that defines a characteristic length $L = 1$, and solid domain is an adjacent rectangle with the thickness of 0.2 attached to the right boundary of the fluid domain at $[1, 1.2] \times [0,1]$, as can be seen in Fig. (5.7(a)). The fluid-solid interface is a vertical line from $(1,0)$ to $(1,1)$ shown in black in Fig. (5.7(a)). In the simulation, following Kaminski and Prakash (1986), all the parameters are set to be non-dimensional with $\rho = 1$, $\mu = 1$, $C_p = 1$, and $k = 1/0.7$ for the fluid and the solid.

The initial condition is at rest with $T_0 = 0$. The lower horizontal wall from $(0,0)$ to $(1.2,0)$, and the upper horizontal wall from $(0,1)$ to $(1.2,1)$ are insulated. Isothermal temperature boundary conditions are defined on the left vertical wall from $(0,0)$ to $(0,1)$ with $T_C = 0$, and on the right vertical wall from $(1.2,0)$ to $(1.2,1)$ with $T_H = 1$. Grashof number $Gr = g\beta(T_H - T_C)L^3\rho^2/\mu^2$, is set to be 10^3, 10^5, 10^6 and 10^7, as in Kaminski and Prakash (1986).

The numerical mesh, which is shown in Fig. (5.7(a)), is uniform and consists of square elements of the size 0.2×0.2 employing 5^{th}-order polynomial basis functions for velocity and temperature within each element.

The time step size in Nek5000 simulations is set to 10^{-3}, 10^{-4}, 10^{-4}, 10^{-5}, for the four values of the Gr number, respectively. Since the results in Ref. Kaminski and Prakash (1986) are from a steady state model, and our simulations are transient, the results from Nek5000 are presented at the time $t = 2$, when the flow has reached a steady state. The comparison of the normalized temperature at the fluid-solid

interface between the current simulations and Kaminski and Prakash (1986) is shown in Fig. (5.7(b)), and an excellent agreement is observed.

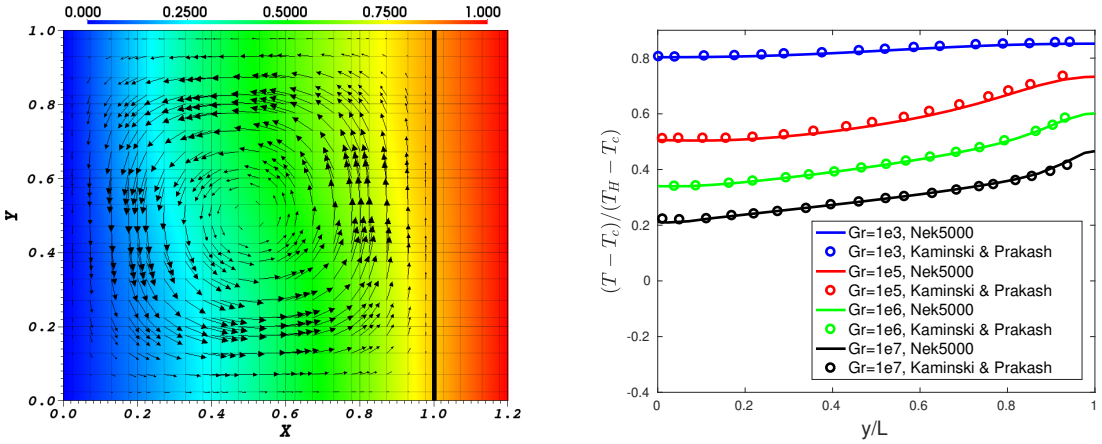

(a) Temperature distribution and velocity vectors at $Gr = 1000$ at time $t = 2$ from Nek5000. Numerical mesh showing the elements and the collocation points is also plotted.

(b) Temperature comparison at the fluid-solid interface between the current simulations at $t = 2$ and Ref. Kaminski and Prakash (1986).

Figure 5.7: Conjugate Heat Transfer Validation Test Case from Ref. Kaminski and Prakash (1986).

5.3.2 Validation of Large Eddy Simulation Model

The validation of the presented Large Eddy Simulation model is performed using a test case of a ventilated model room against experimental data (Posner *et al.* (2003)) and the LES simulations in Tian *et al.* (2007).

The model room corresponds to a rectangular box with the floor area of 0.914 m × 0.457 m and the height of 0.305 m, with a 0.03m thick wall partition of a height 0.15 m located in the middle of the room. The ceiling of the room features one air inlet and one air outlet, both of the size 0.1 m × 0.1 m. A steady plug flow with the velocity of 0.235 m/s is specified at the inlet. Based on the inlet velocity and the inlet

width, the Reynolds number of the inlet airflow is 1500. All geometrical and physical parameters of the study are taken exactly as in the references of Posner *et al.* (2003); Tian *et al.* (2007). The numerical mesh consists of cuboid elements of the average size 0.13m $\times$ 0.15m $\times$ 0.15m, which are correspondingly refined near the location of the air vents to conform to the geometry. Following Tian *et al.* (2007), we run the simulations with the time step of $\Delta t = 0.05$ s, for 2000 time steps, upon which a statistical information is collected for 10,000 time steps, corresponding to 500 s in physical time. Fig. (5.8) illustrates a mean airflow pattern in the room by plotting time-averaged velocity magnitude with the superimposed in-plane velocity vectors, where the Nek5000 computational grid including the elements and the collocation points is also shown.

Fig. (5.9(a)) compares time-averaged profile of vertical velocity along the center of the vertical inlet jet with the experiments (Posner *et al.* (2003)) and the simulations (Tian *et al.* (2007)), while Fig. (5.9(b)) compares time-averaged vertical velocity profile along the horizontal line at the mid-partitioned height and the mid-plane. In both cases, an excellent agreement is obtained.

5.3.3 Validation of House HVAC Control Model

In this section, we present a validation of our residential house model with the on/off HVAC temperature control implemented according to the strategy described in Sec. (5.2.4). We compare our simulations with both the field data and the EnergyPlus simulations documented in Ref. Cetin *et al.* (2019). The data in Ref. Cetin *et al.* (2019) is for a single story medium-size residential house located in Sacramento, CA Sparn *et al.* (2014). Sacramento, CA, the same as Phoenix, AZ, are both located in the Building America "hot-dry" climate zone Baechler *et al.* (2010). The data for the field study was collected in the month of August, when the largest cooling loads

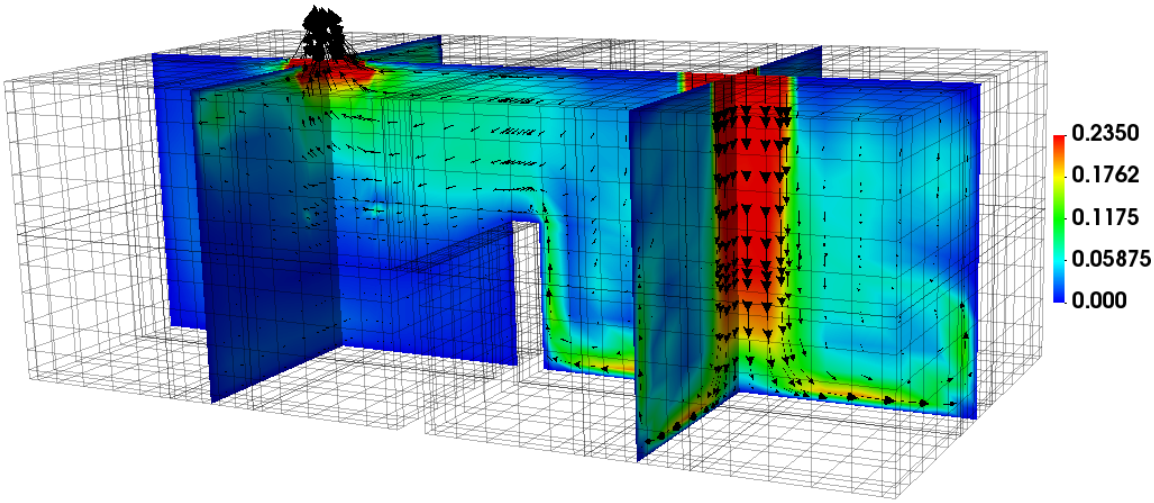

Figure 5.8: Time-averaged Velocity Magnitude with the Superimposed In-plane Velocity Vectors for the Ventilated Room Validation Test Case with Nek5000. Velocity is in m/s. Computational Grid including Elements and Collocation Points is also Shown.

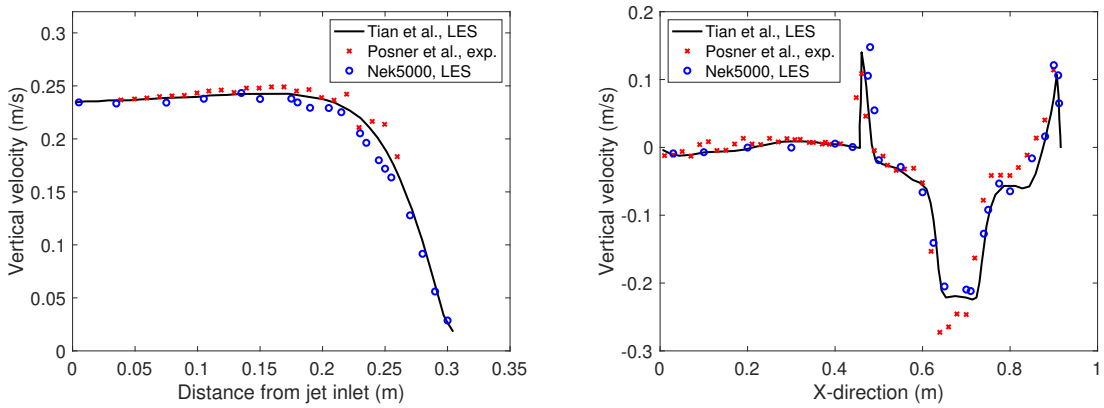

(a) Vertical velocity along the center of the vertical inlet jet.

(b) Vertical velocity along the horizontal line at the mid-partitioned height and the mid-plane.

Figure 5.9: Comparison of Time-averaged Velocity Profiles for the Ventilated Room Validation Test Case with the Data from Refs. Posner *et al.* (2003); Tian *et al.* (2007).

occur Cetin *et al.* (2019). For the validation of our AC cycling model, we chose to compare with the day-time temperature data of Ref. Cetin *et al.* (2019) corresponding to the time period between 10am and 3pm, when AC was running using an on/off temperature control, with a constant thermostat setpoint set to 70.52 °F (corresponding to an upper bound of a deadband) and a deadband interval of 1.8 °F. Since every

building has different thermal mass characteristics, following Cetin *et al.* (2019), we adjust the thermal mass to match the observed fluctuation of interior temperatures when the HVAC system is both on and off.

A comparison of the indoor temperature in our simulations with the field data and EnergyPlus simulations of Ref. Cetin *et al.* (2019) is shown in Fig. (5.10). Fig. (5.10) shows a very good agreement of Nek5000 data with both the field data and EnergyPlus simulations with on/off model. It can also be observed that the omission of on/off model in EnergyPlus simulations completely misses the cyclic temperature behavior as described in Ref. Cetin *et al.* (2019), showing the importance of inclusion of the dynamic HVAC control models into the building simulation software. It is interesting to note that the temperature reaches the values higher than the deadband for the field data, while it is controlled more precisely in both Nek5000 and EnergyPlus simulations. This might be due to the fact that the actual thermostat setpoint value in the field is unknown, as thermostat can have 1–2 °F uncertainty, or perhaps since the averaged room temperature between the living room, master bedroom and the den is plotted for the field data in Ref. Cetin *et al.* (2019), with the den, located quite far from a thermostat and not having its own cooling vent, potentially contributing to higher measured temperatures. In EnergyPlus, the on/off AC switch is controlled directly by the mean zone temperature and not by a temperature from a pointwise sensor location, while in Nek5000, Room 3 (whose temperature is plotted) and the thermostat are located close to each other, and there is no physical thermostat uncertainty in the simulations. On the other hand, Nek5000, as well as the field data, show a higher degree of cycle-to-cycle variability as opposed to the EnergyPlus data, which will be further discussed in Sec. (5.4).

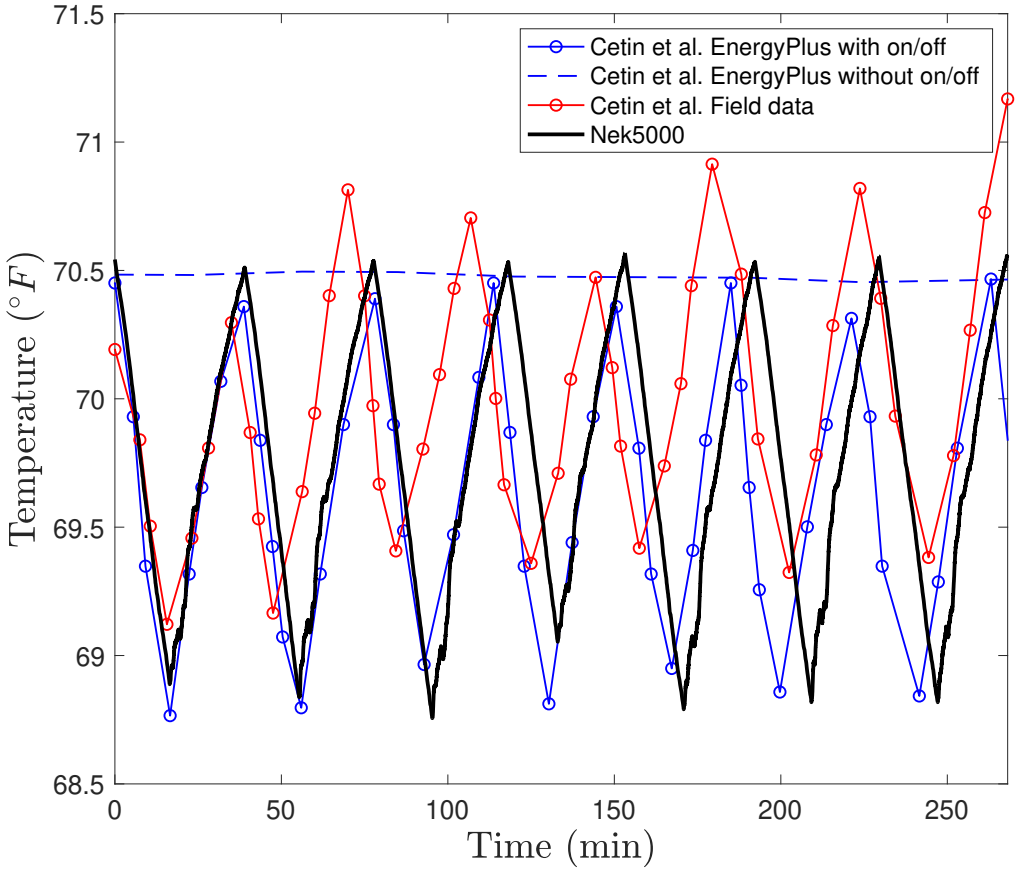

Figure 5.10: Comparison of the Interior Temperature Fluctuations with the on/off AC Control between the Current Simulations and the Field Data of Cetin *et al.* (2019) and the EnergyPlus Simulations with and without on/off AC Control (Cetin *et al.* (2019)). Horizontally-averaged Temperature in Room 3 at the Thermostat Level is Plotted for Nek5000; Data for the Field Measurements and EnergyPlus are as Described in Cetin *et al.* (2019).

5.3.4 Grid Refinement

Additional to LES and CHT validation, a grid refinement study has been performed for cooling stage of cycle 14 and 15 to check whether the mesh is fine enough for such high Reynolds cold jet from inlets. The comparison is done by reducing a polynomial order from $N = 7^{th}$ to $N = 6^{th}$ and the results are shown in Fig. (5.11). The initial condition of each cycle is the same from the previous heating stage with

$N = 7^{th}$ and spectral interpolation is done for $N = 6^{th}$ to read. It is shown that for both averaged temperature field and instantaneous reading are close. The final running time difference percentage based on $N = 7^{th}$ is 1.69% for cycle 14 and 0.59% for cycle 15. It could be concluded that the gird is enough to have relatively good results for such simulation.

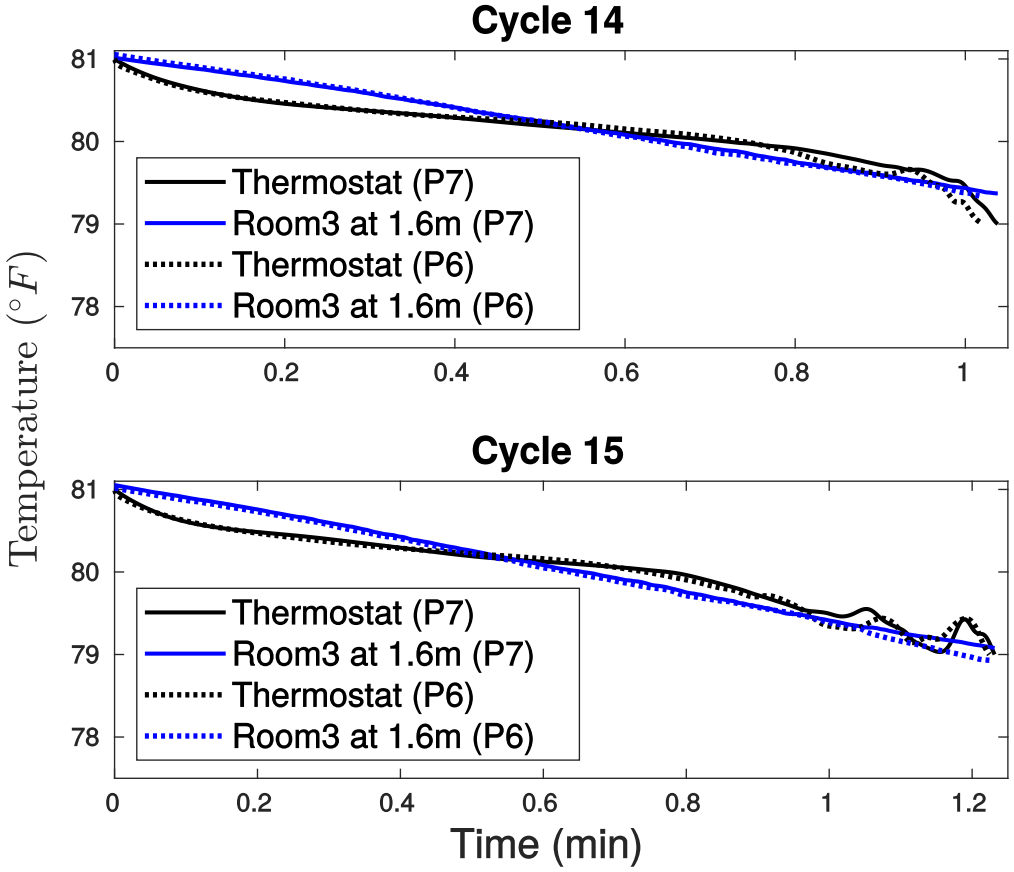

Figure 5.11: Thermostat Reading and Horizontally-averaged Temperature in Room 3 at the Thermostat Level with $N = 7^{th}$ Order Polynomials (P7) and $N = 6^{th}$ Order Polynomials (P6) Comparison from Cooling Stage of Cycle 14 and 15.

5.3.5 External Boundary Condition Equivalency

Mentioned Sec. (5.2.4), the external boundary condition is constantly set to 100 °F (310.928 K). However, it is more routinely to set up convection boundary condition

(Robin) for being more realistic. Here we would show the equivalency and similarity between setting a constant temperature and Robin boundary. For Robin boundary condition, $T_\infty = 100\,^\circ\mathrm{F}$ (310.928 K) and $h_c = 50\,\mathrm{Wm^{-2}K^{-1}}$ for all of the external surface, where h_c is convective heat transfer coefficient. The comparison is done for both cooling and heating stage for cycle 14 and 15 with the initial condition remains the same from constant temperature boundary condition results ($N = 7^{th}$). The results are shown in Fig. (5.12) and the final running time difference percentage based on constant temperature boundary is 6.15% and 4.82% for cooling stage 14 and 15, 0.55% and 1.97% for heating stage 14 and 15. Notice that convective heat transfer coefficient h_c varies from case to case based on environment and the value is considered to be common for air for mixing free and forced convection. From what could be concluded, constant temperature could represent convection boundary condition in this case.

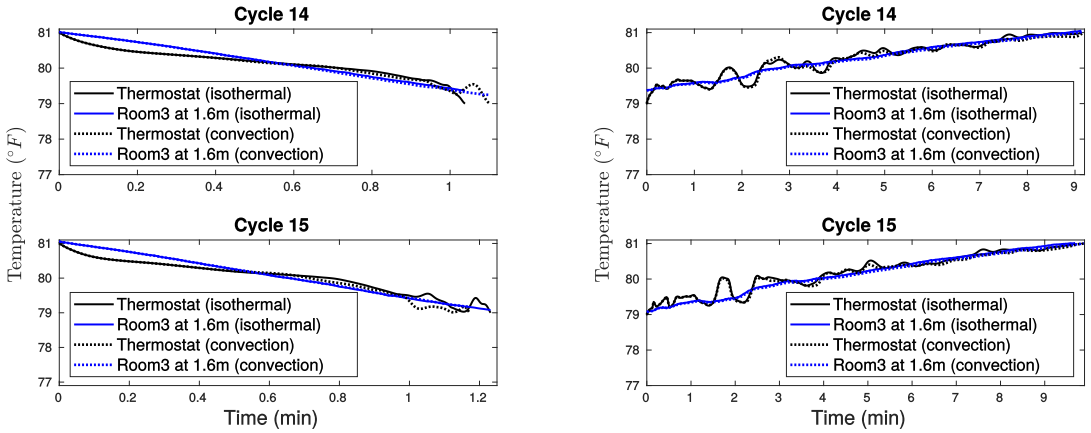

(a) Cooling stage from cycle 14 and 15.

(b) Heating stage from cycle 14 and 15.

Figure 5.12: Comparison of Horizontally-averaged Temperature in Room 3 at the Thermostat Level and Thermostat Reading between Constant Temperature Boundary and Robin Boundary.

5.4 Results

Having validated our conjugate heat transfer LES-HVAC simulation model versus the field data, we now apply the methodology to simulate a case study of a residential house model in Phoenix, AZ, presented in Sec. (5.2.1). As opposed to field measurements, which are hard to obtain in more than a few selected sensor locations, and to EnergyPlus simulations which only output the mean zone temperature, the advantages of our CFD approach is that the entire transient temperature field inside the house is available and can be easily probed.

5.4.1 Cooling and Heating Cycles

The total time of the simulations consists of an initial heating stage, followed by 30 cooling and heating cycles, which corresponds to the total of 467.37 minutes of physical time, or approximately 7.8 hours. The breakdown of the total simulation time into the heating and cooling stages, as well as the initial stage, is presented in Table. (5.2). It can be seen that the initial heating stage, which heats the inner wall by only 0.5 °F, takes 108.5 minutes, or 1.8 hours, which testifies of rather long time scales associated with the solid heat transfer process due to relatively high thermal mass ($\rho\, C_p$) of the exterior wood wall. One can notice from Table. (5.2) that the cooling stage occupies only 7.8% of the total elapsed time, signifying an extreme importance of incorporating AC idling and natural heating effects into the HVAC operation and building energy models, since no energy is consumed when AC is turned off, which corresponds to 90% time in the combined cycle.

Table. (5.3) gives a detailed breakdown of the cooling and heating time spent in each AC cycle for the 30 cycles simulated. For a convenience of analysis, we break the cycles into the three groups of 10 cycles each. It can be seen that the heating time

Stage	Initial heating	Total cycle cooling	Total cycle heating	Total
Time, min.	108.5	36.69	322.18	467.37
Percent of total	23.2%	7.8%	69%	100%

Table 5.2: Simulation Time and Percent Breakdown between Different Stages.

is significantly reduced between Group 1 (1–10 cycles) and Group 2 (11–20 cycles), while it is further reduced for Group 3 (21–30 cycles), but only slightly. Cooling time is slightly reduced between Group 1 and Group 2, while it is essentially unchanged for Group 3. To better illustrate these effects, Fig. (5.13) presents the bar plots for the calculated cooling and heating time periods. It can be clearly seen that the first 10 cycles correspond to the most significant reduction in the average cycle time both for cooling and for heating cycles, although the effect is more significant for heating than for cooling. This reduction in the average duration of the cooling and heating cycles, although similar in its perceived outcome, is caused by different phenomena. For the cooling, it corresponds to a better cooling efficiency once the cooling air gets better mixed with the warm room air. The reduction in the heating cycles is, however, due to a gradual heating of the building envelope by the outside air, which acts to increase the inner wall temperature and, thus, leads to a higher heat transfer rate through the building walls. These two different reasons can also explain why the cooling cycles stabilize after the first 10 cycles, while the heating cycles keep decreasing in time. The cooling cycles stabilize once the air is mixed to a sufficient degree, which yields a flow pattern that no longer significantly changes between cooling cycles. However, the heating cycles keep decreasing in time, because the building wall continues to heat, although the rate of this heating diminishes once the temperature gradient inside the solid wall starts approaching a constant value.

We can also notice a significant variability in the cooling and heating times, which

Cycle No.	1	2	3	4	5	6	7	8	9	10	Total
Cooling time	1.71	1.41	1.54	0.89	1.25	1.26	1.48	0.80	1.19	1.26	12.79
Heating time	17.96	20.60	19.86	12.51	15.01	13.98	15.49	8.07	11.23	11.48	146.19
Cycle No.	11	12	13	14	15	16	17	18	19	20	Total
Cooling time	1.15	1.14	1.23	1.04	1.23	1.18	1.23	1.17	1.46	1.04	11.87
Heating time	10.24	10.15	10.33	9.13	9.69	9.20	9.45	9.35	9.77	7.60	94.91
Cycle No.	21	22	23	24	25	26	27	28	29	30	Total
Cooling time	1.45	1.05	1.21	1.17	1.05	1.43	1.15	1.09	1.03	1.40	12.03
Heating time	9.85	7.61	8.70	8.05	7.27	9.01	7.18	7.66	6.98	8.77	81.08

Table 5.3: Cooling and Heating Time Consumption in Minutes for the 30 cycles.

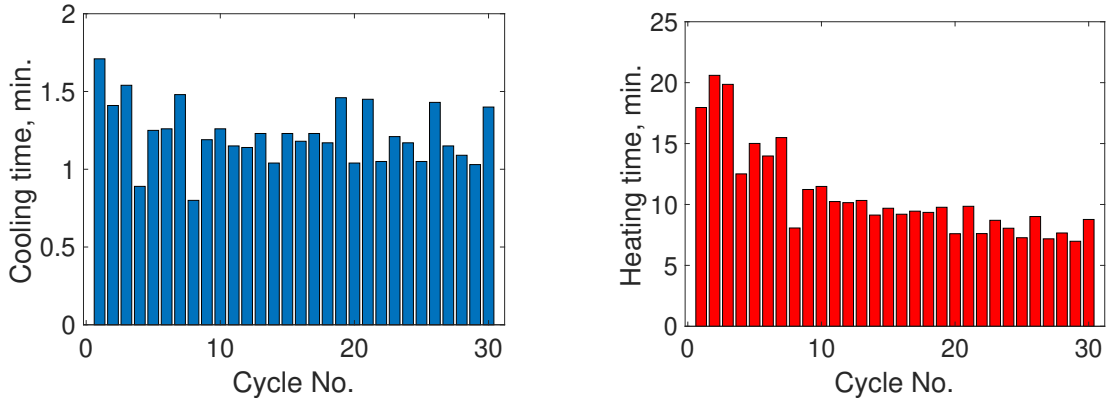

(a) Cooling time.

(b) Heating time.

Figure 5.13: Bar Plot of the Cooling and Heating Time Periods within the Simulated 30 Cycles.

is further illustrated in Table. (5.4), which lists the average value, the standard deviation, and the standard deviation as the percent of the average value, calculated separately for each Groups 1 to 3. It can be seen that the variability is especially pronounced during the first 10 cycles, reaching as much as 21.93% for cooling and 27.40% for heating, although a higher variability in the heating cycle times might also be explained by the fact that the slope of the overall reduction trend with time is higher for heating. However, Groups 2 and 3, while keeping relatively unchanged mean values,

demonstrate 10 – 13% variability, which is significant, especially in a consideration of electric grid stability and demand response. To further understand the nature of this variability, Table. (5.5) documents the percent deviation for each cooling and heating cycle from their corresponding in-group mean value. Surprisingly, it can be seen that, the positive and negative fluctuations from the mean in both cooling and heating cycles typically correlate with each other, i.e., if we had a significantly shorter cooling cycle, it is very likely that the following heating cycle will be shorter as well. Fig. (5.14) documents the quadrant plot of the cooling and heating time fluctuations, where we define $\Delta t_c = (t_c - \bar{t}_c)/\bar{t}_c \times 100\%$, $\Delta t_h = (t_h - \bar{t}_h)/\bar{t}_h \times 100\%$, with $\bar{t}_c$, $\bar{t}_h$ corresponding to the average cooling and heating times within each group, respectively. It can be seen from the figure that almost all the data falls into the Quadrants 1 or 3, meaning that we have a very good correlation between the same-sign fluctuations for the cooling and heating periods within the cycle. Thus, while it might be tempting to conclude that the shorter cooling cycles are beneficial because they save energy, it must be kept in mind that the follow-up heating cycle will likely be short as well, so that the time duration until the next energy consumption period is shortened, which negates the perceived original energy benefit. It will be shown in the next section that both positive and negative time fluctuations from the mean are caused by the temperature fluctuations at the thermostat level created by the turbulent motions associated with the interaction of the cooling jet and the in-room air.

5.4.2 Wall Temperature Distribution

To further study the heat transfer in building envelope, two profiles of temperature are presented in Fig. (5.15). The wall temperature profile is located at 1.6 m height, in the middle of the left building envelope of Room1 from outside to inside, and the roof temperature profile is located at the center of Room1 also from outside to inside. In

Cycle No.	1–10	Average, min.	STD, min.	STD, %
Cooling time		1.28	0.28	21.83 %
Heating time		14.62	4.00	27.40 %
Cycle No.	11–20	Average, min.	STD, min.	STD, %
Cooling time		1.19	0.12	10.02%
Heating time		9.49	0.79	8.33 %
Cycle No.	21–30	Average, min.	STD, min.	STD, %
Cooling time		1.20	0.16	13.71%
Heating time		8.11	0.94	11.57 %

Table 5.4: Average Value and Standard Deviation for the Cooling and Heating Time Periods for the 30 Cycles.

Cycle No.	1	2	3	4	5	6	7	8	9	10	Mean
Cooling time	33.70%	10.24%	20.41%	-30.41%	-2.27%	-1.49%	15.72%	-37.45%	-6.96%	-1.49%	1.28 min.
Heating time	22.85%	40.91%	35.85%	-14.43%	2.67%	-4.37%	5.96%	-44.80%	-23.18%	-21.47%	14.62 min.
Cycle No.	11	12	13	14	15	16	17	18	19	20	Mean
Cooling time	-3.12%	-3.96%	3.62%	-12.38%	3.62%	-0.59%	3.62%	-1.43%	22.30%	-12.38%	1.19 min.
Heating time	7.90%	6.94%	8.84%	-3.80%	2.10%	-3.07%	-0.43%	-1.490%	2.94%	-19.92%	9.49. min.
Cycle No.	21	22	23	24	25	26	27	28	29	30	Mean
Cooling time	20.53%	-12.72%	0.58%	-2.74%	-12.72%	18.87%	-4.41%	-9.39%	-14.38%	16.38%	1.20 min.
Heating time	21.48%	-6.14%	7.30%	-0.72%	-10.34%	11.12%	-11.42%	-5.53%	-13.91%	8.16%	8.11 min.

Table 5.5: Percent Deviation from the In-group Mean for the Cooling and Heating Time Periods.

coordinate, the wall profile is from $(-0.2, 1.8, 1.6)$ to $(0, 1.8, 1.6)$ and the roof profile is from $(2, 1.8, 2.6)$ to $(2, 1.8, 2.9)$. Each temperature profile from each material setting records five profiles right at the end of initial heating stage, 7th heating cycle, 14th heating cycle, 21st heating cycle, and 28th heating cycle.

For Fig. (5.15(a)), The outside temperature is fixed to be 310.928 K (100 °F) as boundary condition, but each profile ends at different but close temperature reading at the wall end. It is due to the fact that Room1 is cooled by AC and it helps to

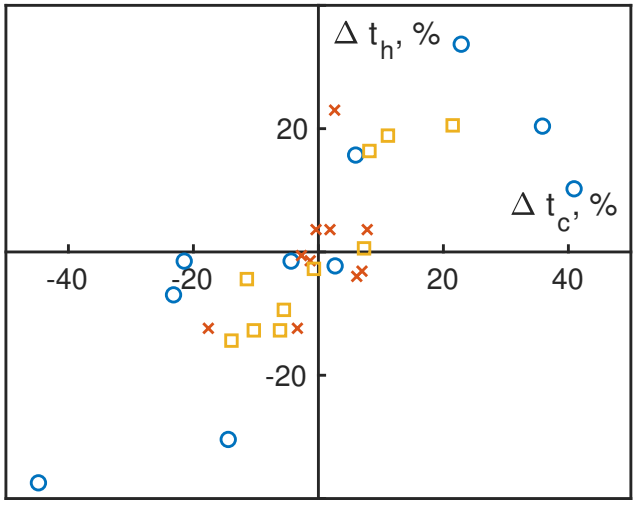

Figure 5.14: Correlation between Cooling and Heating Time Fluctuations. Blue Circles Correspond to the Data in Group 1, Red Crosses in Group 2, and Yellow Squares in Group 3.

maintain a low temperature boundary. However, one could notice that when cycle goes up, inner temperature distribution raises even if the inside wall surface is cooled at almost the same temperature. That means the wall gets heated by the outside and the AC cooling could not help to maintain steady state so that the wall temperature is maintained at certain heat distribution. Also in Table. (5.3), later cycles reduce the time of heating stage also suggests that building envelope itself is heated.

Similar phenomenon is also observed in Fig. (5.15(b)) that inner temperature raises while simulation of cycles runs longer. But the temperature of the inner surface of S1 roof increases a lot compared to S2. One explanation to that is roof is not cooled by AC compared to wall at 1.6 m height as cool air is not spread there. Another explanation is that insulation material has such low ρC_p compared to pure wood S2. So it raises its temperature easily although it has low thermal conductivity. For both Fig. (5.15(a)) and Fig. (5.15(b)), one could notice a sharp transition in S1 at distance 0.1 m where insulation material starts to be stuffed. Wood part for both S1 and S2

shows much smoother slope compared to insulation material part.

Notice that after the initial stage, both wall and roof are heated more time in S2 for large ρC_p, and temperature is much colder in S1. But after cooling and heating about the same amount of time, wall and roof temperature turns to be hotter in S1 than S2 even if part of building envelope is stuffed with low heat conductivity material, spray foam.

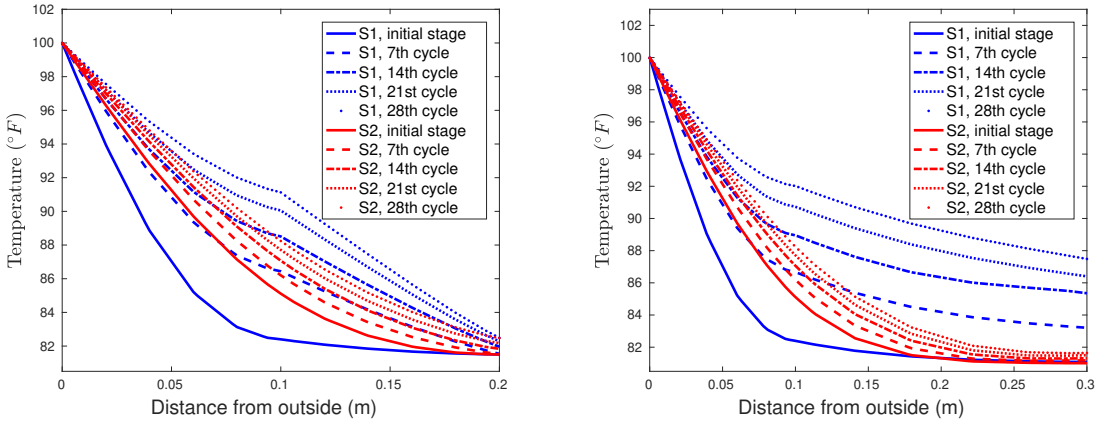

(a) Wall profile.

(b) Roof profile.

Figure 5.15: Wall Temperature.

5.4.3 Thermostat Readings

To further understand the nature of the cycle-to-cycle variability, in this section we examine the temperature signal as obtained from the thermostat probe during the cooling and heating periods for two representative cycles. We choose to compare cycles 25 and 26, which exhibit a large negative, and large positive, time fluctuations, respectively. Fig. (5.16) shows the temperature readings at the thermostat probe as compared to the temperature in the Rooms 1 - 4 averaged over horizontal planes at the thermostat height of $z = 1.6\,\mathrm{m}$. For a reference, we also plot the room temperatures averaged over a height of $z = 1\,\mathrm{m}$ and $z = 0.2\,\mathrm{m}$, respectively.

We see from Fig. (5.16(a)) that at the end of the cooling cycle the thermostat probe signal exhibits a large negative fluctuation from the corresponding Room 3 averaged temperature at that height, making a temperature at the thermostat reach the lower bound of a deadband of 79 °F early, thus ending the cooling cycle early. Note that, due to an early termination of the cycle, the actual Room 3 temperature is actually at a higher value than 79 °F at the end of the cycle 25. This also explains the shortening of the follow-up heating cycle, since Room 3 now needs to heat up by a smaller amount during the heating stage, since it starts with an elevated temperature at the beginning. For the cycle 26, where we have a positive shift in a cooling time duration, the situation is reversed – the thermostat probe encounters a large positive temperature fluctuation, which makes the AC unit keep cooling longer, with the resulting end-of-the-cycle averaged Room 3 temperature lower than the deadband value of 79 °F. As a result, the heating cycle needs to compensate for this overshoot, allowing the room to heat for a longer time.

Fig. (5.16) also shows that the temperature variability is the most significant at the end of the cooling cycle and the beginning of the heating cycle, when the cooling air reaches the thermostat location and results in large temperature fluctuations due to a strong turbulent mixing between the cold and warm air regions. When the AC is turned off, the effects of the turbulent mixing associated with the forced convection gradually disappear, and, once the natural convection sets up, it results in a more uniform temperature distribution across the given horizontal planes throughout the entire house, as can be seen by a very good collapse of the temperature plots across all the rooms at any given height during the later part of the heating cycle. We can thus conclude that the variability in the duration of the cooling cycles results from the turbulent nature of the cooling jet flow, while variability in the duration of the heating cycles is rather attributed to the over- or under-shoots of a preceding

cooling cycle, and not to the temperature fluctuations due to turbulence at the end of a heating cycle.

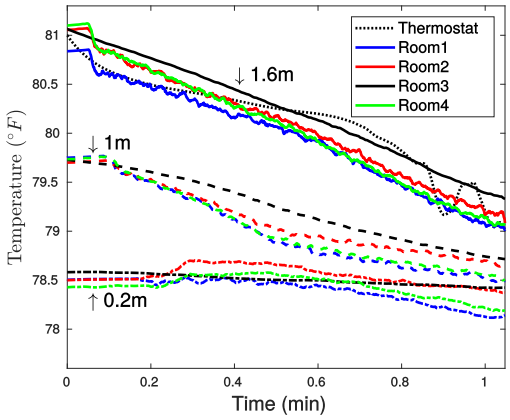

(a) Cycle 25: cooling.

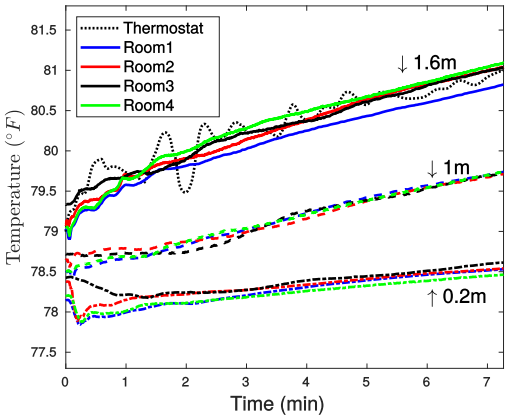

(b) Cycle 25: heating.

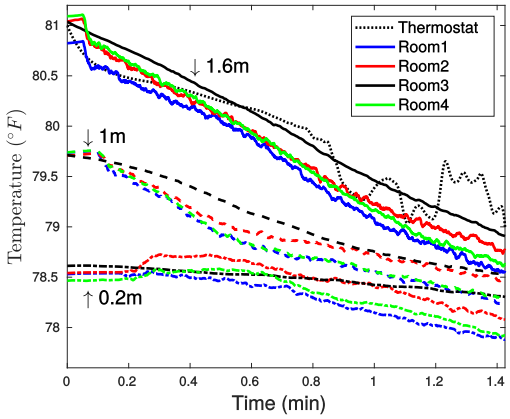

(c) Cycle 26: cooling.

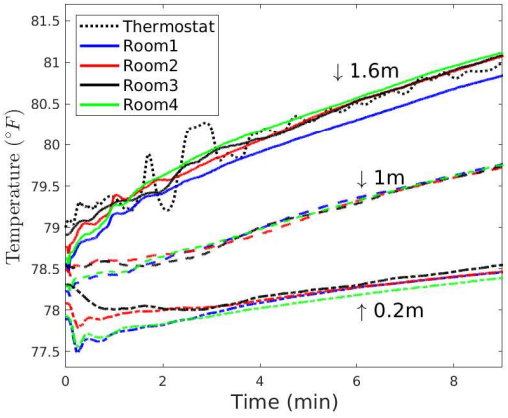

(d) Cycle 26: heating.

Figure 5.16: Thermostat Probe Readings as Compared to the Room Averaged Temperatures at Different Heights. Black Dotted Line: Thermostat Reading; Blue Lines: Room 1; Red Lines: Room 2; Black Lines: Room 3; Green Lines: Room 4. Top Plots (Solid Lines) are at a Height of 1.6 m; Middle Plots (Dashed Lines), at a Height of 1 m; Bottom Plots (Dash-dotted Lines), at a Height of 0.2 m.

5.4.4 Remote Room Temperature Probes

We now turn to examine the individual room temperatures that are established during the operation of the current HVAC system model with a central thermostat control setting. From Fig. (5.16) we see that the average temperature of Room 3 is typically higher during the cooling cycle than the temperature within the living room (Room 4) and the bedrooms (Rooms 1 and 2), since the thermostat is located in the hallway, which does not have its own air supply vent. This leads to the fact that Rooms 1, 2 and 4 typically experience colder temperatures at the end of the cooling cycle than that set by a thermostat setpoint, which can clearly be seen in Fig. (5.16(a)). From the data, we can infer that this overcooling occurs for most of the cycles, that is for all the cycles with positive, near-zero, and even some negative fluctuations in duration, as can be seen, for example, in Fig. (5.17), where cycles 14 and 24, both with negative fluctuations in duration, are plotted. The overcooling leads both to an excessive use of energy, when the rooms are cooled by an amount larger than needed, and to a reduced thermal comfort.

To propose a possible remedy, we investigate a potential efficiency of remote room sensors, which can be used either for a multi-zone control, or for a smart control of a central thermostat. Thus, we place remote sensor probes into the Rooms 1, 2 and 4, referred to as Probes 1, 2, 3. Probes 1, 2, 3, shown in red in Fig. (5.1), are located, correspondingly, at $(0.4, 0.4, 1.6)$, $(0.4, 7, 1.6)$, and $(6.28, 6.6, 1.6)$, which is away from each air supply vent and not too close to the walls, for reliable temperature readings. Fig. (5.18) compares the readings of the remote sensor probes with the room averaged temperatures taken over the same heigh of 1.6 m for the cycles 25 and 26. While turbulent fluctuations, especially at the end of the cooling cycle and the beginning of the heating cycle, as observed previously, are still pronounced, it can be seen, that on

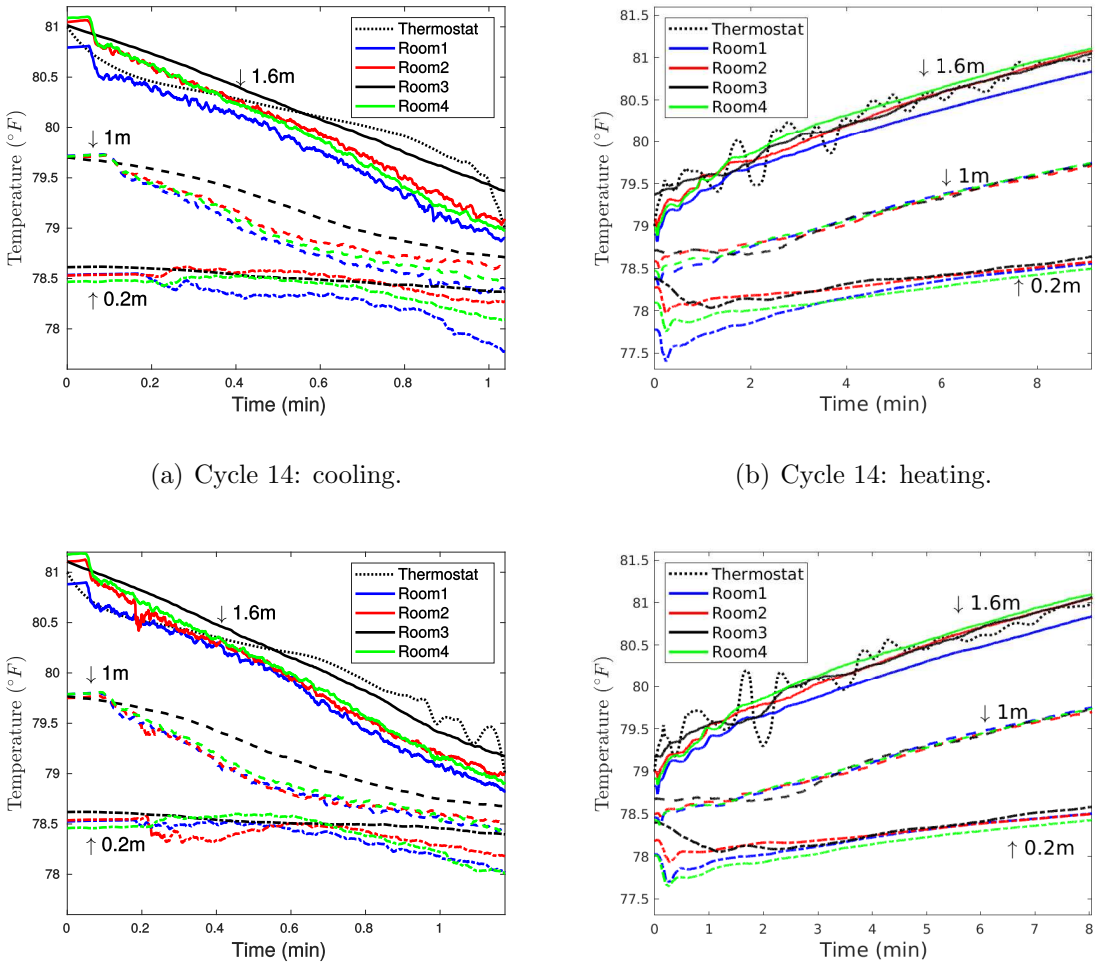

(a) Cycle 14: cooling.

(b) Cycle 14: heating.

(c) Cycle 24: cooling.

(d) Cycle 24: heating.

Figure 5.17: Thermostat Probe Readings as Compared to the Room Averaged Temperatures at Different Heights for the AC Cycles 14 and 24. Line Labels are the Same as in the Caption to Fig. (5.16).

average, the remote sensor probes can track the local room temperatures fairly well, thus offering a promising technology for a smart house HVAC control. While it is expected that a decentralized temperature control system can substantially enhance a thermal comfort of the building occupants and reduce the energy usage by eliminating unnecessary overcooling of the interior spaces, its effect on eradicating or reducing the AC cycle variability is unknown, and needs further investigation.

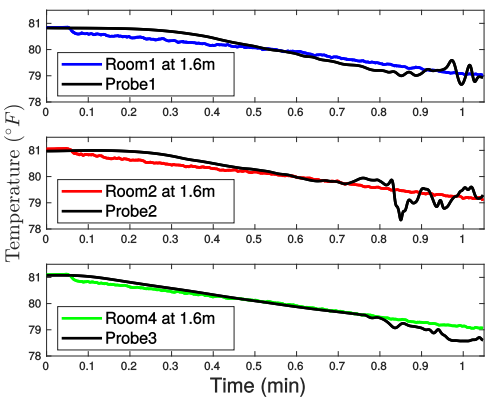

(a) Cycle 25: cooling.

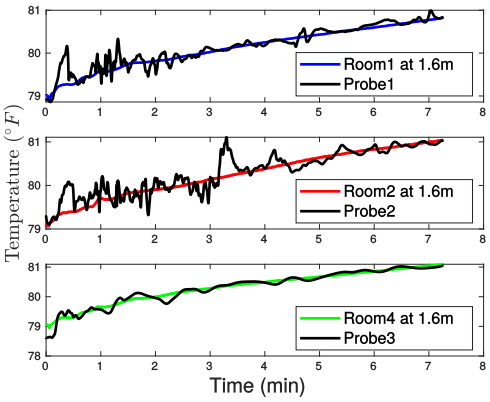

(b) Cycle 25: heating.

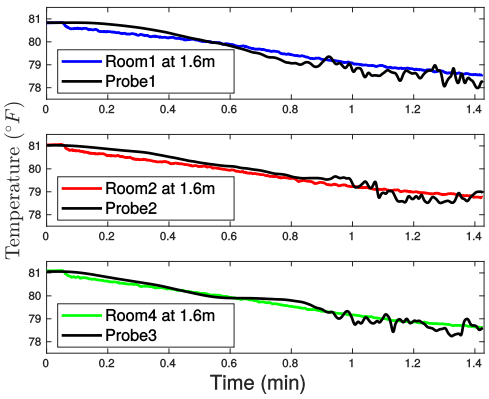

(c) Cycle 26: cooling.

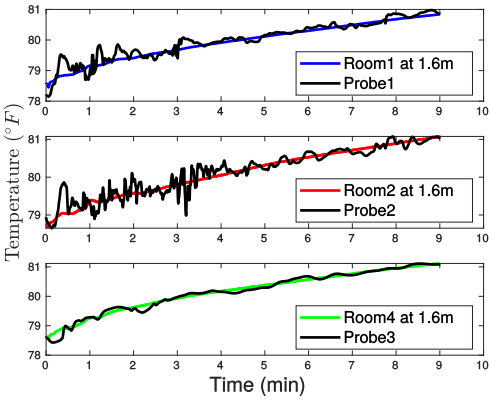

(d) Cycle 26: heating.

Figure 5.18: Temperature at the Remote Sensor Probes Compared with the Room Averaged Temperatures at a Height of 1.6 m.

5.4.5 Interior Temperature Distribution

This section examines the details of the temperature distribution inside the house during the cooling and heating cycles, which can further explain the observed phenomena related to the cycle-to-cycle variability, overcooling, and the differences between the room temperatures. Fig. (5.19) shows the temperature distribution at the end of the cooling stage for the cycles 25 and 26 across a horizontal plane through $z = 1.6\,\mathrm{m}$, i.e., at the thermostat level. The figure shows a footprint of four cooling jets, two in

the middle of both Rooms 1 and 2, and the other two in Room 4, which correspond to the cooling air descending from the air supply vents. The cooling air continues to descend until it hits the floor, upon which it starts coming up along the walls and the interior partitions of the rooms, as can be better viewed in Fig. (5.20) showing a vertical cross-section of the house passing through the $y = 2.1\,\mathrm{m}$ line, i.e., through the center of the vents in the Rooms 1 and 4. The cooling air around the interior partitions between the inner rooms and Room 3 spills out into Room 3, and this is how the hallway is getting cooled, since it does not have its own air supply vent. Comparing Fig. (5.19(a)) and Fig. (5.19(b)), corresponding to the cycles 25 and 26, respectively, we see that the shorter cycle 25, terminated prematurely due to a cold plume impinging on a thermostat probe, leads to the overall higher temperatures inside the house, including Room 3 and the interior rooms; to the contrary, the longer cycle 26 results in significant overcooling of the whole space, and, especially, the interior rooms. Additionally, as seen before from the line plots, the hallway is typically warmer on average than the interior rooms at the thermostat level, supporting the argument that placing a single thermostat probe in a room that is not directly cooled results in the overcooling of the inner rooms.

Figs. 5.21 and 5.22 show the temperature distribution at the end of the heating cycles 25 and 26 across the horizontal plane $z = 1.6\,\mathrm{m}$, and the vertical plane $y = 2.1\,\mathrm{m}$, respectively. As commented before, at the end of the heating cycle the air is much better mixed, the temperature distribution appears to be substantially more uniform, and the turbulent fluctuations are, overall, diminished, except near the walls and the windows, where thermal boundary layers result in a production of small-scale interacting cold and hot plumes. Note that such boundary layers do not form at the floor level, where adiabatic boundary conditions are set up, resulting in a zero mean temperature gradient, which can be seen in Fig. (5.22). From Figures

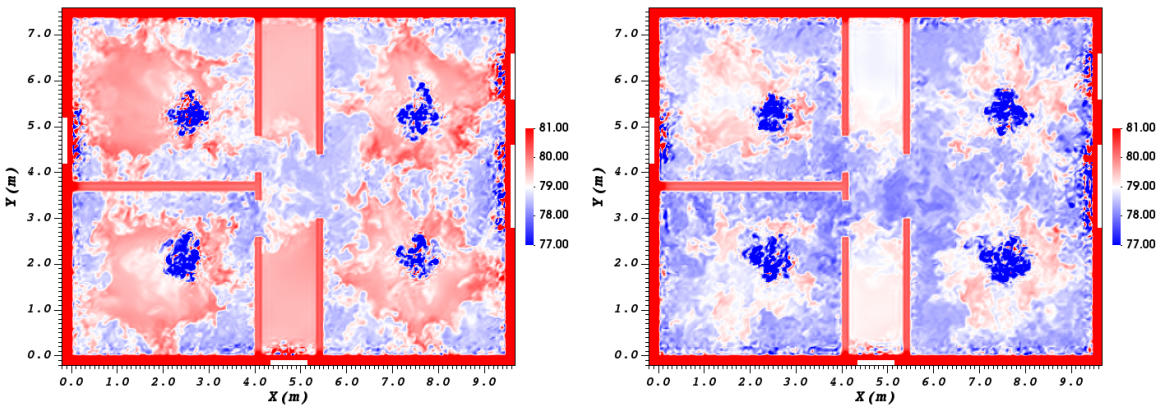

(a) Cycle 25. (b) Cycle 26.

Figure 5.19: Temperature at the End of the Cooling Cycles 25 and 26; Horizontal Slice across the Plane $z = 1.6\,\mathrm{m}$. Temperature is in $^\circ F$.

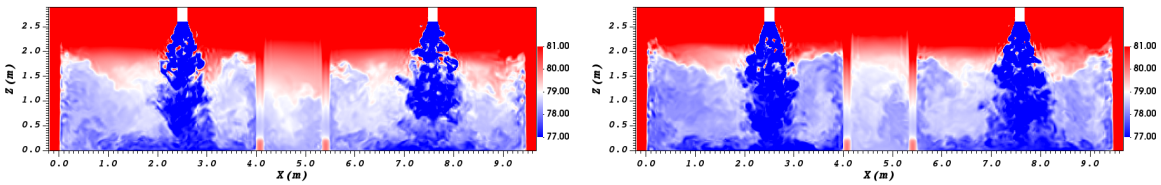

(a) Cycle 25. (b) Cycle 26.

Figure 5.20: Temperature at the End of the Cooling Cycles 25 and 26; Vertical Slice across the Plane $y = 2.1\,\mathrm{m}$. Temperature is in $^\circ F$.

5.16(b), 5.16(d), 5.17(b), 5.17(d), we observe that Room 1 is consistently colder by approximately 0.3 °F at the thermostat level at the end of the heating cycles, which seems to be a permanent feature of the flow, and not an attribute of a cycle variability. Indeed, the flow visualizations in Fig. (5.21) show that the temperature in Room 1 is lower for both the cycles 25 and 26 compared to the rest of the house. This can be explained by the fact that this is the only room in the house (apart from Room 3) that does not have windows. Indeed, Rooms 2 and 4 receive an additional heat through the windows. This strong thermal interaction between the cooled interior air and the hot window surfaces creates a very interesting natural convection pattern shown in Fig. (5.23). It can be seen that the air, warming especially fast through the large windows in the living room, expands and pushes out of the living room,

entering the colder Room 1 and creating a large recirculating vortex in Room 1. The effect of windows, although less significant, can be observed during the cooling cycles as well, resulting in the overall temperatures being the highest in Room 2 during cooling, followed by Room 4, and then Room 1, see Figures 5.16(a), 5.16(c), 5.17(a), 5.17(c). In Room 4, we have a competing effect of larger window surfaces, but also stronger cooling coming from the two vents, which brings the temperature of Room 4 essentially down to the level of Room 1 during cooling, in spite of having windows.

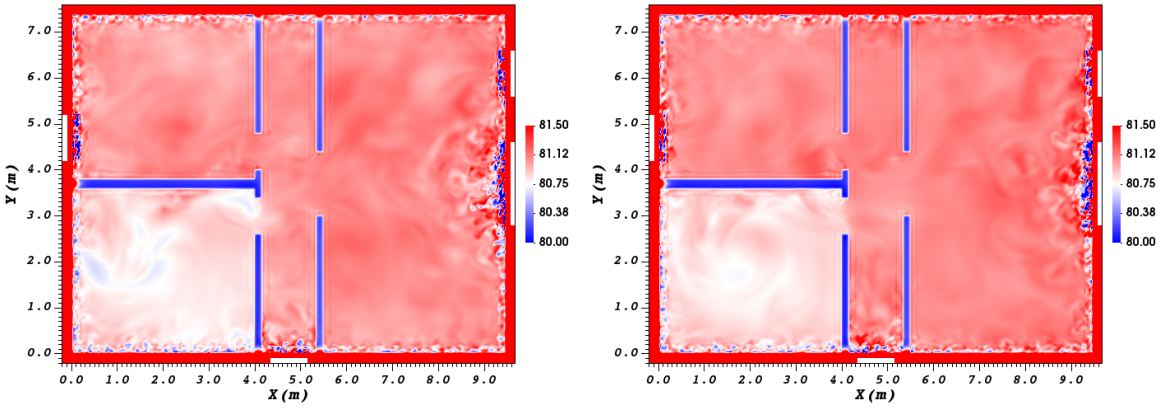

(a) Cycle 25. (b) Cycle 26.

Figure 5.21: Temperature at the End of the Heating Cycles 25 and 26; Horizontal Slice across the Plane $z = 1.6\,\text{m}$. Temperature is in $^\circ F$.

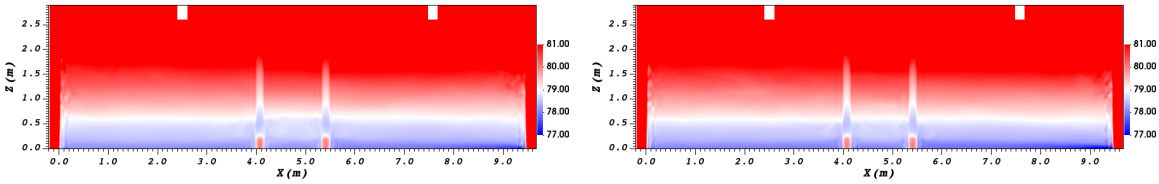

(a) Cycle 25. (b) Cycle 26.

Figure 5.22: Temperature at the End of the Heating Cycles 25 and 26; Vertical Slice across the Plane $y = 2.1\,\text{m}$. Temperature is in $^\circ F$.

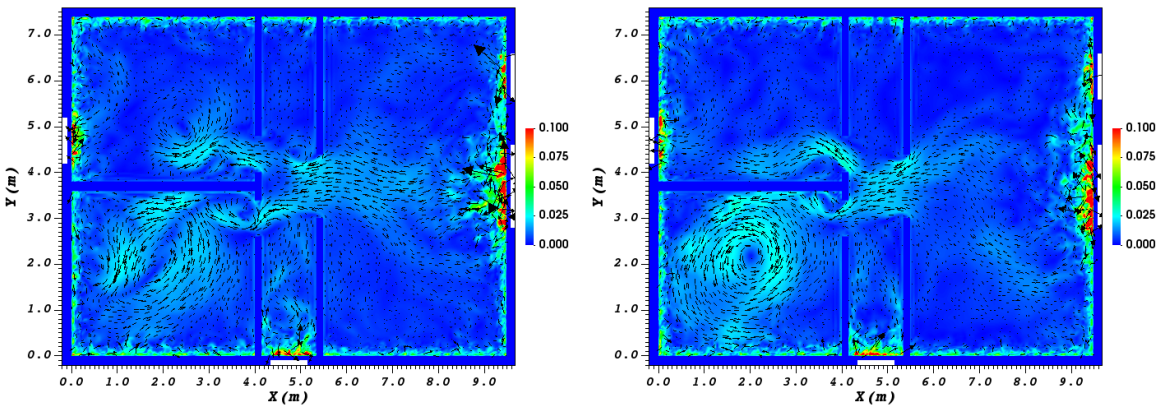

(a) Cycle 25. (b) Cycle 26.

Figure 5.23: Velocity Magnitude and In-plane Velocity Vectors at the End of the Heating Cycles 25 and 26; Horizontal Slice across the Plane $z = 1.6\,\text{m}$. Velocity is in m/s.

5.5 Whole Housing Pre-cooling

In Sec. (5.4.1), it shows that thermostat in Room3 could sort of represent the average temperature of other rooms at the same height, so for whole-housing pre-cooling study, only thermostat reading would be presented. Meanwhile, it is also suggested that heating time would be shortened when the building envelope is heated more as regular AC cycles runs longer. But it is also not reasonable to increase regular AC cycles too much at pre-cooling temperature since there is no steady-state essentially. So in this study, we would run the final heating stage once the time consumption of the regular AC cycle becomes slightly stable.

The thermostat reading is presented in Fig. (5.24) and the time consumption for each stage is shown in Table. (5.6) and Table. (5.7). It shows that pre-cooling strategy could avoid AC being turned on for about 114.14 min maximum by setting the thermostat 6 °F lower for a long time from the upper bound results, so that peak hours would be shifted. Such shifting time is also suggested by Arababadi (2016) thus we could conclude that our approach is validated. However, it should be noticed that

114.14 min is only valid when the thermostat is set to 6 °F lower for a quite long time. It could be 2 hours or even more depending on the thermal insulation performance of each housing. It could be costly if the temperature is set lower compared to regular temperature for a while but the key point is to shift peak hours.

If we assume regular AC cycle consists of 1.5 min cooling and 10 min of heating from the approximation of Table. (5.3), the maximum shifting time 114.14 min is about 10 regular AC cycles, and that is how much cycles it could shift in the cost of pre-cooling.

As for lower bound, the minimum shifting time is just 42.76 min which means if the thermostat is set to 6 °F lower about 352.82 sec which is equivalent to 4 regular cooling stage, right before the local peak hours and it help to shift 42.76 min which is equivalent to 4 regular AC cycles. To some extent, as Arababadi (2016) suggests to pre-cool for at least two hours, it could be concluded that the shifting time is almost equivalent to your pre-cooling time, which means, if you want to save 5 regular AC cycles in peak hours, shift such 5 cooling stages ahead.

However, as we found out in regular AC running and the initial setup of the whole housing pre-cooling, in reality, no housing should reach the temperature we set for the housing envelope as it would be the hottest time during the day, unless AC is running for quite a long time. So 2 hours shifting time should be the maximum even if you pre-cool for more than 3 hours. It is also suggested in Arababadi (2016) that to pre-cool for unnecessary long time is not saving any money at all. But if more than 6 °F temperature difference is set for a decent amount of time, more than 2 hours shifting time could be reached to some extent. However, it would cost more energy potentially.

The room temperature at z=1.6 m at the end of 7th cycle of upper bound and lower bound of cooling and heating stage is presented in Fig. (5.25) and Fig. (5.26). From

Cooling (sec)	100.85	84.25	102.75	78.11	74.2	66.52	73.11
Heating (min)	14.63	17.66	17.71	13.71	11.67	10.82	114.14

Table 5.6: Time Consumption for the Upper Bound of Whole Housing Pre-cooling.

Cooling (sec)	102.82	84.60	92.41	53.43	74.74	75.58	352.82
Heating (min)	17.96	20.6024	19.86	12.51	15.01	13.98	42.76

Table 5.7: Time Consumption for the Lower Bound of Whole Housing Pre-cooling.

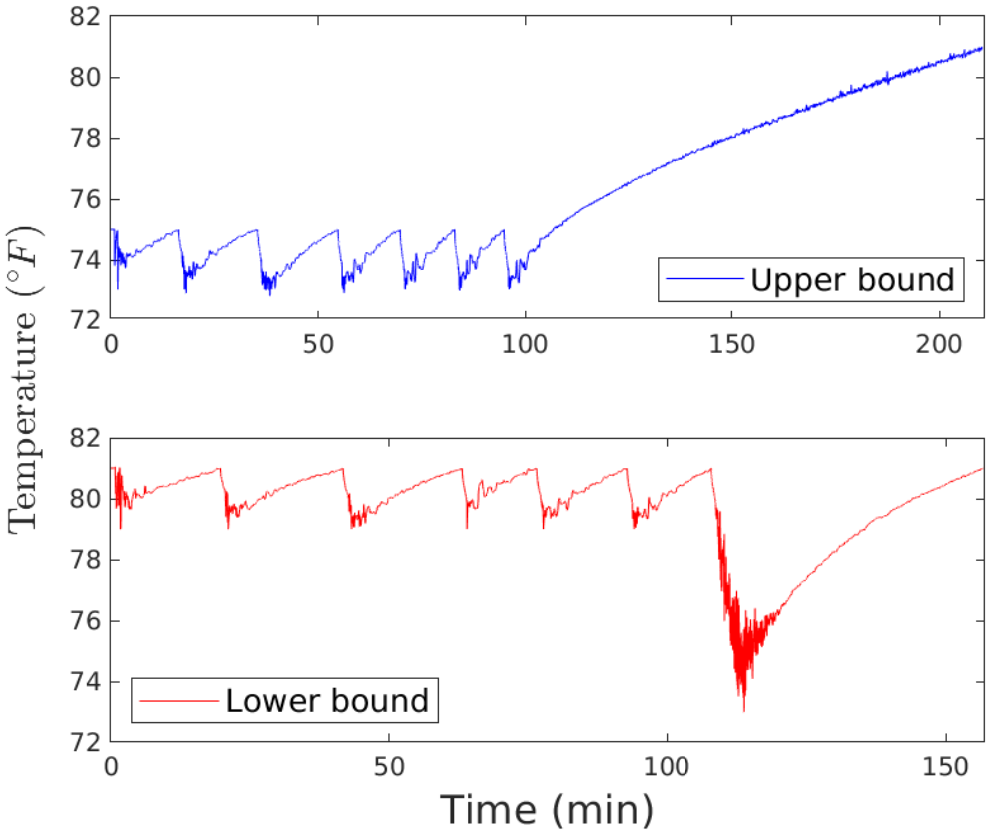

Figure 5.24: Thermostat Reading for Whole Housing Pre-cooling.

Fig. (5.25(a)) and Fig. (5.25(b)), one could see that air temperature from the upper bound is much colder even if they stop at the same criteria. Also, the temperature of partition walls and inner part of the housing envelope is much colder compared from the lower bound one. That would further cause the recovery time from the upper

bound lasts longer than the lower bound one as there is more heating source.

Same conclusion could be drawn from Fig. (5.26), that the upper bound setup keep the housing temperature lower. In other words, once the housing temperature goes back to normal, the upper bound setup would help to make heating stage last longer compared to the lower bound, and thus saves more energy. That actually explain another thing most people do. When someone comes home late, he might turn off the AC in the morning until come back. If that so, partition wall, housing envelope, and furnitures would all reach the same outside temperature and become heat source at night. It would make AC extremely hard to cool back to the normal temperature, and it would be turned on again soon.

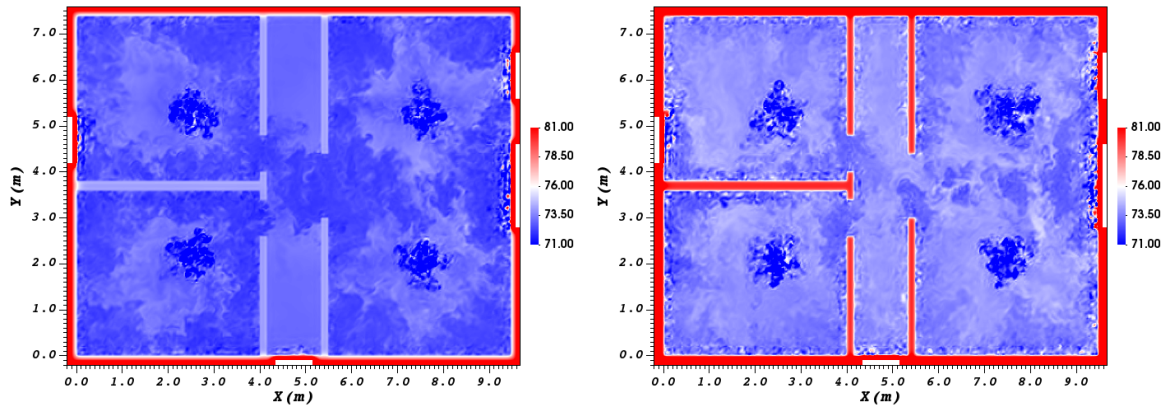

(a) Upper bound. (b) Lower bound.

Figure 5.25: End of 7th Cycle of Upper Bound and Lower Bound Cooling Stage, Room Temperature at z=1.6 m.

5.6 Multi-Zone Housing Pre-cooling

In multi-zone housing pre-cooling study, three more regular cycles were run to let the walls heated more as the first heating stage takes relatively long time indicating heat is not distributed well among the walls. After it runs for 9 cycles and the time consumption of the heating stage becomes stable, a final heating stage is run to see

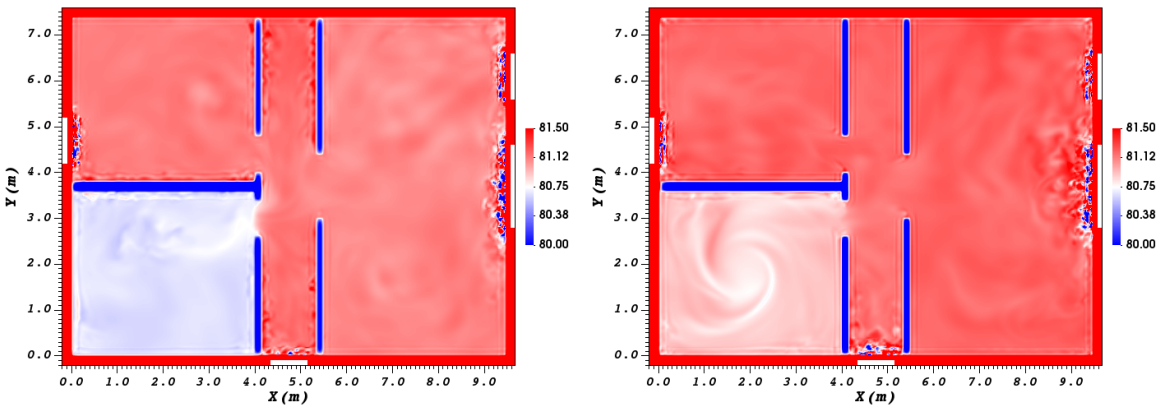

(a) Upper bound. (b) Lower bound.

Figure 5.26: End of 7th Cycle of Upper Bound and Lower Bound Heating Stage, Room Temperature at z=1.6 m.

how much shifting time it could gain from the multi-zone housing pre-cooling.

Cooling (sec)	87.96	61.89	50.33	56.40	55.67	52.38	52.42	58.41	72.18	75.15
Heating (min)	31.33	18.45	14.55	14.16	12.51	11.04	10.66	10.67	11.55	118.00

Table 5.8: Time Consumption for the Upper Bound of Multi-zone Housing Pre-cooling.

Cooling (sec)	102.46	68.95	63.51	80.23	61.14	79.07	64.21	60.40	79.48	79.64
Heating (min)	15.03	12.86	10.04	10.71	8.54	9.40	7.92	6.62	8.20	75.85

Table 5.9: Time Consumption for the Lower Bound of Multi-zone Housing Pre-cooling.

As for the upper bound, shown in Table. (5.8) and Fig. (5.27), it suggests the maximum shifting time it could gain is 118 min, which is almost the same as the results from the whole housing pre-cooling study in Sec. (5.5) which is 114.14 min. And as for the lower bound, shown in Table. (5.9) and Fig. (5.27), the minimum shifting time it could gain is 75.85 min.

Recall that the setting of both upper and lower bound is that the whole surrounding walls of Room1 is fully cooled as an initial condition. The difference is only for the rest as AC turns on during the multi-zone pre-cooling or not. So in reality, the

shifting time would be reduced once pre-cooling is not done for a while, which is the same as whole housing pre-cooling.

There is another major concern of the lower bound that the initial temperature setting of the whole housing is not realistic. The rest of the rooms is already heated fully by the outside, but the partition walls are still cooled. Even if an initial stage is run as prior, such hypothesis is still not that realistic to some extent. But it shows how temperature is influenced in Room1 if the other rooms are not cooled moderately.

As the heating source of Room1 becomes some part of the building envelope and partitioned walls, to cool partitioned walls becomes important. From such study, we suggest that although multi-zone housing pre-cooling is done for a single or multiple rooms, it is better to also turn on the AC of other mini-split as well with moderate temperature. It could help to prolong the shifting time.

To look into the difference between the upper bound and lower bound setup, Fig. (5.28) and Fig. (5.29) are presented. There is an obvious temperature difference between the two partition walls and the housing envelope attached to Room1, as it is much colder in the upper bound setup. That is clearly due to the much hotter surrounding temperature in the lower bound setup.

The lower bound set up in the multi-zone pre-cooling is somehow different from the whole housing pre-cooling, as one is set up with hot surrounding temperature and another is set up with initial regular AC cycles. The reason to do that is to check the influence from the partition walls rather than the strategy itself. It is already confirmed that if multi-zone pre-cooling is set up like the lower bound of whole housing pre-cooling. It would not last time indeed. However, if the surrounding temperature is the same as Room1, it gives a maximum shifting time of the lower bound whole housing pre-cooling set up. So it comes another variant which is the surrounding temperature as if it is hot as outside, it would gives a minimum shifting

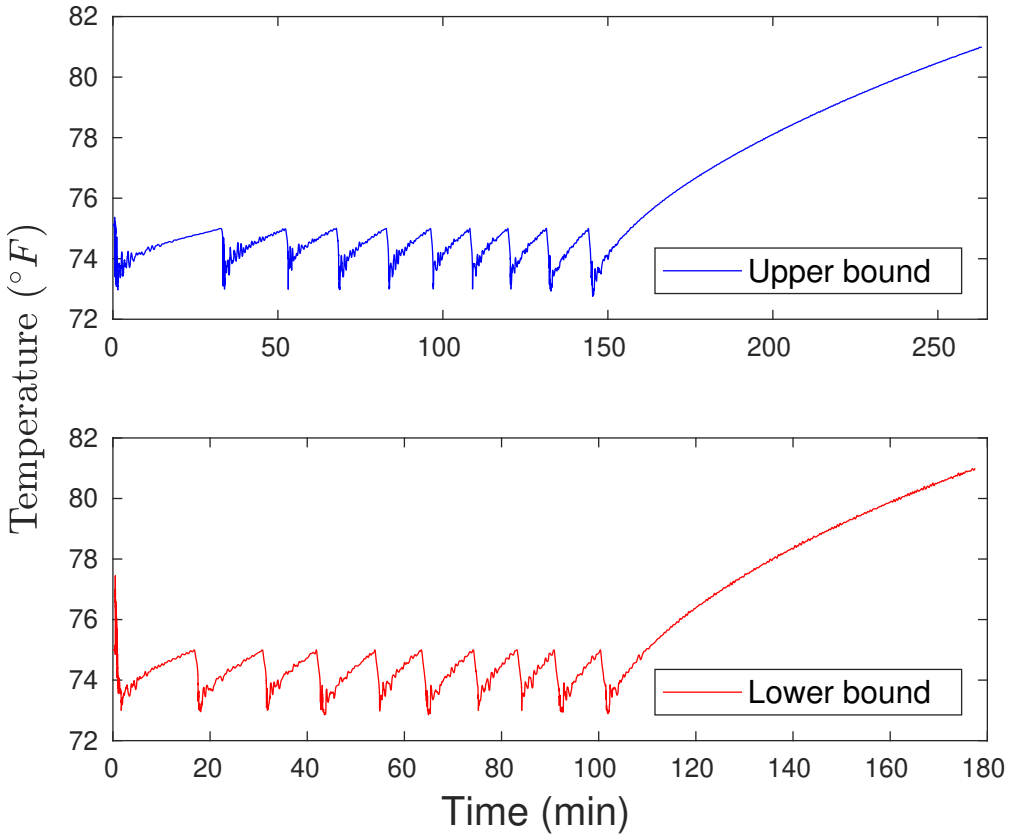

Figure 5.27: Thermostat Reading for Multi-zone Housing Pre-cooling.

time respectively. So it makes sense that the lower bound shifting time of multi-zone pre-cooling is 75.85 min which is more than 42.76 min, as at least, Room1 is well pre-cooled initially.

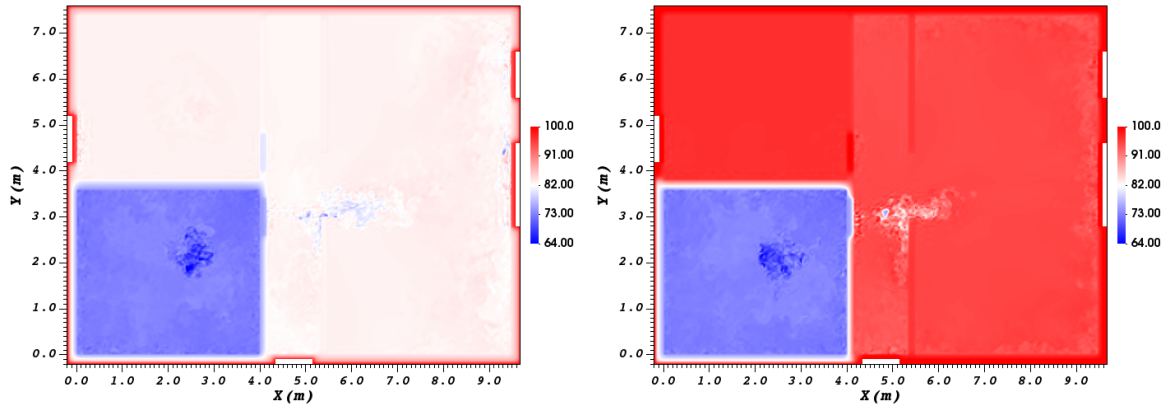

(a) Upper bound. (b) Lower bound.

Figure 5.28: End of 10th Cycle of Upper Bound and Lower Bound Cooling Stage, Room Temperature at z=1.6 m.

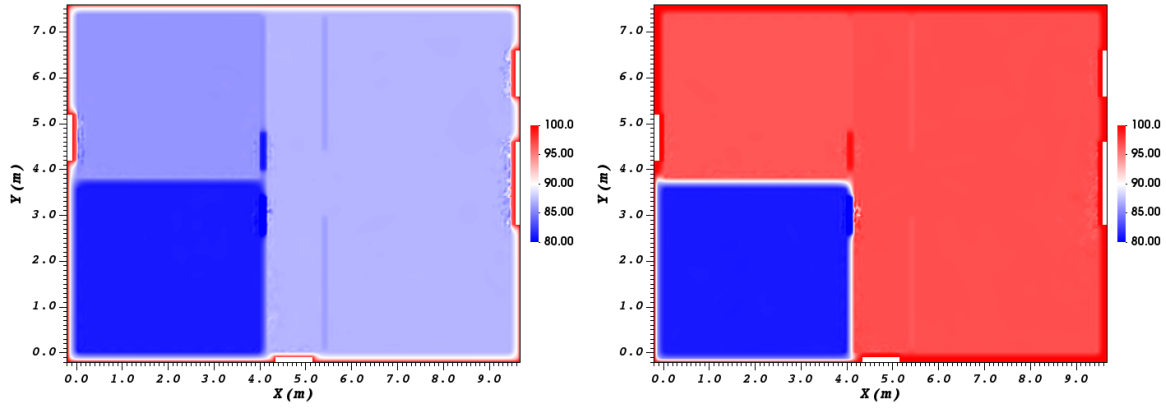

(a) Upper bound. (b) Lower bound.

Figure 5.29: End of 10th Cycle of Upper Bound and Lower Bound Heating Stage, Room Temperature at z=1.6 m.

Chapter 6

CONCLUSIONS

6.1 Summary

Fluid-structure interaction chapter presents a high-order in space and second-order in time computational methodology for a solution of implicit and explicit fluid-structure interaction problem. The methodology is based on a spectral-element formulation of both the solid and the fluid equations. Solid equations adapt a geometrically nonlinear framework using a St. Venant-Kirchhoff material model, while fluid equations solve an incompressible Navier-Stokes equations system on deforming meshes based on Arbitrary Eulerian Lagrangian formulation. The implicit coupling is accomplished via a fixed point iteration approach with Aitken relaxation, which is known to be a robust methodology that allows to achieve stable results in the presence of an added mass effect (Causin *et al.* (2005); Förster *et al.* (2007)). The explicit coupling is accomplished via generalized Robin-Neummann boundary conditions which is also stable. In addition to a development of a high-order solver itself, we have also proposed a comprehensive verification methodology to demonstrate a high-order spatial and a second-order temporal accuracy of the approach in a consistent manner, which consists of h-, p- and temporal refinement tests for both the component solvers, and the coupled fluid-structure interaction problem formulation. Additionally, we have demonstrated a good performance of the methodology on commonly accepted fluid-structure interaction benchmarks, including a flow-induced vibration of a two-dimensional cantilever beam attached to a circular cylinder (Turek and Hron (2006)), and a pressure-driven flow in a three-dimensional pipe with flexible walls

(Fernández *et al.* (2015)).

A polynomial spectral accuracy of the approach with the corresponding h- and p-refinement tests, and the expected second-order temporal convergence of the method, was first demonstrated on an elastostatics and elastodynamics solid formulation using a method of manufactured solutions, and subsequently on a solution of the incompressible fluid flow equations against an analytical solution of convecting Walsh's eddies (Walsh (1992)). For the fluid solver, following a preliminary conclusion achieved by Formaggia and Nobile (2004) on a model problem of a linear advection-diffusion equation, it was demonstrated on an example of the full Navier-Stokes equation system that the 2^{nd}-order BDF scheme in a conservative formulation with a linear in time geometry update (IE-ALE scheme) achieves only a 1^{st} order temporal accuracy on deforming meshes unless the Geometric Conservation Law (GCL) is satisfied. It was also shown that the expected 2^{nd}-order accuracy is recovered if the GCL is implemented. It was also demonstrated for the first time that when the IE-ALE scheme with GCL is applied to a fully coupled FSI problem, where both the fluid and the solid equations are discretized with the second-order schemes (BDF2 for fluid and Newmark for solid), the order of accuracy of the coupled problem reduces to one. To alleviate this problem, a new ALE solver was developed that uses a Crank-Nicholson type geometry update, matching the solid interface update from the Newmark code. Note that GCL is not needed with the CN-type update, because in this case the ALE geometry is updated with the 2^{nd}-order accuracy. A global 2^{nd}-order accuracy of the approach was verified on a fully coupled FSI problem using self-convergence tests. The developed implementation ensures a perfect match of both the interface velocities and displacements between the fluid and the solid solver, thus ensuring a stable and consistent formulation in the considered case of large displacements allowed by a geometrically nonlinear solid formulation.

To allow for a consistent testing of a high-order method on a fully coupled FSI problem, a new computational benchmark has been developed, which consists of a fluid flow in a three-dimensional channel bounded by one rigid and one flexible wall. High-order convergence of spectral element methods can only be achieved for smooth solutions. Special care has thus been taken to develop a benchmark which ensures smoothness of a fully coupled FSI solution in a time-dependent formulation. This involved specification of initial and boundary conditions that are consistent throughout the coupled fluid and solid domains, and are smooth in space and time. The new proposed framework allowed us to demonstrate, for the first time, a possibility of obtaining a high-order spatial convergence with h- and p-refinement on a fully coupled FSI problem, and also confirmed an expected second-order temporal convergence of the CN-ALE scheme for implicit FSI coupling and first-oder temporal convergence for explicit FSI coupling. The convergence study of the fully coupled problem also exemplified a potential need to revisit the definition of the error norms currently employed in single-physics problems, systematically assess their applicability to multi-physics problems, and, perhaps, devise improved error metrics for the FSI problems, to be explored in the future work.

The benchmark was also utilized to assess the influence of the iterative solvers' tolerances on the global error for implicit FSI coupling, which was not highlighted before. A conclusion from this study was that the fluid solver tolerance does not significantly affect the results and can be safely set to a relatively high number resulting in only two fluid solver iterations. However, a tolerance of the FSI solver can have a significant impact on the results, generally reducing the global error by an order of magnitude if the tolerance is reduced by an order of magnitude. The benchmark is also utilized to check the accuracy of the iterative fluid solver while using explicit FSI coupling method. And the conclusion is more iterations for fluid solver would

help the overall accuracy although low iteration number would not affect the stability. The iteration number of fluid solver is up to each problem with the consideration of accuracy versus cost. Developing strongly-coupled FSI approaches that do no rely on fixed-point iterations, including generalized Robin boundary conditions, such as some recent attempts published in Deparis *et al.* (2003); Badia *et al.* (2008); Degroote *et al.* (2009); Yu *et al.* (2013); Banks *et al.* (2014), is therefore a promising avenue to proceed and is worth of an investment.

The developed high-order FSI methodology was ultimately applied to a Direct Numerical Simulation of a turbulent flow in a channel interacting with a hyperelastic compliant wall. This is the first attempt of applying an interface-resolving FSI methodology to a fluid-structure interaction problem involving a turbulent flow and a finite-thickness elastic wall. An ability to predict near-wall turbulent fluctuations with high-order accuracy in the presence of a flexible wall opens up further avenues for research: for example, in the design of passive compliant surfaces capable of controlling near-wall turbulence, which may reduce drag or enhance turbulent mixing and heat transfer, for a variety of engineering applications. According to the solid material properties presented in this study, hyperelastic compliant wall may not reduce drag for its property of containing no damping. The fourth chapter presents a novel physics-based computational methodology for an accurate simulation and analysis of an acoustic transient pressure wave propagation and its interaction with the fluid flow, which is based on coupling CFD with the solution of an inhomogeneous Lighthill's equation. The methodology allows for a comprehensive evaluation of a transient pressure based technique for a detection of leaks in three-dimensional pipe flows.

The results of the analysis show that an analytic wavelet transform that uses a complex-valued wavelet function provides good leak detection capabilities. The

reason behind this improved accuracy is that analytic wavelets: a) have only positive frequencies in their spectrum, and b) provide information on both magnitude and phase of the transformed signal that already has a temporal and frequency dependence owing to the basic wavelet transform properties. These two additional characteristics of the analytic wavelet transform make it especially effective for analyzing highly impulsive signals that, however, contain both low-frequency and oscillatory content, such as the ones found in leak detection applications.

The mode of reflection of an originally plane transient wave from the leak consists of a primary reflected wave which is broadband and can be identified via probing at multiple frequencies, but, additionally, more complex three-dimensional high-frequency modes are also excited, for example, radial waves and azimuthal waves. Radial waves carry large amount of energy at the sides of the pipe that are aligned and opposite to the leak, manifested by high-frequency pressure oscillations at these locations, while the signature of the radial waves is weak at a 90° or -90° azimuthal angle from the leak. At these "sideways" locations, the azimuthal waves are however identified by high-frequency low-amplitude pressure oscillations. Judging from a small magnitude of theses oscillations at the side probes, a conclusion can be made that these tertiary azimuthal modes of reflection are weak in the current case as compared to the primary and secondary planar and radial reflections.

The three-dimensional physics of a sound wave propagation and reflection described above allows us to make some useful conclusions regarding the optimum frequency for a leak detection with the AWT transform methods. Since the primary mode of reflection is broadband and azimuthally invariant, it is recommended that lower frequencies below M1 mode wave are used for a primary leak detection and identification of its streamwise location, as at these frequencies there is a less probability of interference with non-plane modes that obfuscate the analysis.

Moreover, since the plane wave propagates strictly in a streamwise direction, its streamwise velocity is equal to a speed of sound, which makes simple one-dimensional arguments based on Method of Characteristics and the Eq. (4.35) correct at these low frequencies. However, the information about the azimuthal leak position is lost if probing at low frequencies. Higher-frequency probing, due to a difference in pressure readings between the azimuthal probes, would therefore allow for an accurate location of the azimuthal leak position. It is therefore recommended that multi-mode leak detection algorithms are used (i.e., probing at multiple frequencies) for an accurate identification of both a streamwise and an azimuthal position of the leak. For a success of such an approach, since having the probes close to 0° and close to 90° from the leak are essential, we would recommend having at least 4 azimuthal probes around the circumference, however, further studies are required to further optimize this choice.

The presented methodology provides a good accuracy for a leak detection in laminar pipe flow cases with one and two leaks, including the estimation of the peak signal arrival times and the leak longitudinal location along the pipe. At an optimum low-frequency probing of 0.4726 c_0/D, an error of less than 5.25% is obtained for all the cases considered. Additionally, since the signal at a low frequency is supposed to have a minimum interaction with a high-frequency noise, a potential of the success of this leak detection technology in turbulent flows is promising. A presented computational framework can serve as a robust platform for a further development and improvement of leak detection methods and algorithms in three-dimensional complex pipe flow systems. The chapter of conjugate heat transfer for HVAC simulation presents a detailed study of the effect of cyclic on/off operation of the HVAC system on the air flow and temperature distribution inside a model single-floor residential house. The investigation is performed with a validated high-fidelity computational model that

couples the heat conduction process within the building envelope with the interior air flow dynamics, which is modeled by the Large Eddy Simulation of the Boussinesq approximation of the Navier-Stokes equations.

The presented computational model is rigorously validated in this chapter against previous numerical simulations and experiments (Kaminski and Prakash (1986); Posner *et al.* (2003); Tian *et al.* (2007)), as well as versus the field data in the presence of the on/off cycling of the air-conditioning equipment (Cetin *et al.* (2019)). After the validation, the model is applied to document a case study of a medium-size residential house located in the Phoenix, AZ area. The simulations feature an initial development period, followed by 30 cooling and heating cycles, which, combined, represent close to 8 hours of the physical time and thus can be considered as a realistic representation of the obtained statistical information.

It was found that the duration of the cooling and heating cycles varies significantly over the duration of the simulations. On average, both cooling and heating cycles tend to shorten as the simulation progresses, while the effect is more pronounced for the heating cycles. The reason for the shortening of the duration of the heating cycles is a gradual heating of the solid components by the external temperature, which occurs on very long time scales due to a high thermal mass of the wood exterior walls. Cooling cycles, on the other hand, are shortened due to an increase of the efficiency of cooling as the cooling air and the room air become better mixed.

In addition to the slow changing averages, both cooling and heating cycles exhibit a significant degree of cycle-to-cycle variability, with typical values of the standard deviation in the cycle duration as high as 10–13% caused by the turbulent air fluctuations. While the turbulent air temperature fluctuations directly affect the cooling cycles due to a prevalence of small-scale turbulent motions caused by the cooling jet flow at the thermostat probe location, the duration of the subsequent heating cycles

is affected as well. This is due to a premature termination or an excessive duration of the cooling cycles that affect the variability of the room temperature at the end of the cooling stage, which, in turn, influences the successive heating time. As compared to the field data in Cetin *et al.* (2019), a significant degree of variability has been observed there as well, while the EnergyPlus simulations in the same study yielded an almost ideal periodic signal. Since multizone simulation models are inherently incapable of capturing the flow variability due to turbulence, one recommendation could be to include stochastic models representing this effect into the building energy simulation tools. The cycle-to-cycle variability impacts the grid stability, and the need for its accounting in the building energy models is conspicuous. The presented findings of a positive correlation between the cooling and heating time periods within the same AC cycle is an important conclusion in this regard that can help refine the corresponding statistical models. Additionally, a practical mitigation strategy to reduce variability can be proposed geared towards a development of smart thermostat sensors that don't rely solely on instantaneous readings, but consider the time history of a signal so that the turbulent fluctuations can be taken into account, which is partially leveraged with variable capacity systems that monitor the signal for longer durations (Ulpiani *et al.* (2016); Tian *et al.* (2017)).

Another important conclusion of this study is that placing a thermostat into a hallway which does not have its own air supply vent results in overcooling of the inner rooms, and thus reduces the thermal comfort and results in an excessive use of energy. This is in-line with the conclusions of the study in Ulpiani *et al.* (2016), where an on/off HVAC control strategy was found to result in a lower thermal comfort level and less efficient energy usage among other compared control strategies. While a step up would be implementing a variable air volume control that should result in better air mixing and more uniform temperature distribution across the house, this would

require a complete rebuild of the HVAC system, which calls for high investments and might not be immediately affordable for a vast proportion of residents with the existing systems, especially in developing countries. As a more cost-effective alternative, we have also demonstrated a potential success of a remote temperature sensing strategy, substantiating that the sensor probes located within the rooms can track the average room temperatures consistently well. Remote temperature sensors and smart thermostats are readily available on the market and can be easily used with already existing single- and variable-capacity systems. However, whether a decentralized thermostat control will also result in a reduction of the cycle variability is yet unknown and deserves further investigation.

The visualization of the temperature distribution and the air flow within the model house both during the cooling and the heating periods helped further explain the observed phenomena of cycle-to-cycle variability and overcooling. Additionally, a difference between the averaged temperatures within the rooms was also noted, attributed to a glazing effect from the windows, in spite of having a central thermostat with a single deadband setpoint for all the zones. Room 1 which does not have any windows was found to be cooler by 0.3°F at the thermostat level of $z = 1.6$m at the end of the heating cycles. The air flow pattern showed a formation of a large recirculating vortex within Room 1 caused by a natural flow circulation during the heating cycle. During cooling, Room 4 was found to be as cool as Room 1 despite having the windows, due to a presence of an additional cooling vent; however, Room 2 which has a window and only one vent, was consistently the hottest. For the houses that feature a central thermostat system and are incapable of a remote zone control, it can be recommended that the window shades are closed during the day to minimize the glazing effect, or that a computer or other heat sensible equipment is placed into the rooms with fewer windows. To the authors' knowledge, the presented work is the

first study that addresses the effects of cyclic and an on/off AC equipment operation on the temperature distribution within a house, and its effect on the cycle variability that influences energy consumption and its intermittency.

For whole housing pre-cooling, we conclude that the maximum shifting time is 114.14 min and the minimum is 42.76 min, if it is pre-cooled at 74 °F when the normal thermostat setting is 80 °F and the outer temperature is 100 °F. It also suggests from the respect of energy conservation, that what you want to save in the shifting of peak hours would be paid in pre-cooling almost at the same amount. In reality, hotter outside temperature would definitely shorten this time and better insulation would reduce this time, for example, low-E or low solar heat gain windows. It also makes some difference by setting the thermostat to difference temperature. But in generally, the results should be valid.

As for multi-zone pre-cooling, we conclude that it would shift the same amount of peak hours compared to whole housing pre-cooling if everything else remains the same. But a condition should be mentioned that the rest of the rooms should not heated too much, which means AC should be lightly on for the rest before the peak hours to prolong the single room pre-cooling. Otherwise, the shifting time should be reduced to 75.85 min minimum.

6.2 Accomplishments

The present work describes the following specific achievements of my research:

- Developed implicit and explicit partitioned FSI coupling methods in Nek5000.
- Developed implicit solvers for fluid and solid in Nek5000.
- Presented h/p and temporal refinement in FSI.
- Studied 3D turbulent channel with a compliant wall.

- Studied whole-housing envelope regular cooling with CHT.
- Studied whole-housing precooling with CHT.
- Studied multi-zone precooling with CHT.
- Developed Lighthills equation in Nek5000.
- Studied pipe leak detection in 3D laminar pipe flow.
- Analyzed transient pressure signal with AWT.

6.3 Future Directions

Although explicit FSI coupling methodology is fast and stable, the accuracy may further be increased with explicit FSI coupling based on Robin-Robin boundary conditions or iterative but still relatively cheap procedures. For flow with a compliant wall, different material properties should be developed and tried until drag reduction is observed. To further increase the feasibility of using FSI in Nek5000, a multi-mesh FSI coupling should be developed to avoid mesh distortion when a solid is surrounded by fluid.

For better studying HVAC system with CHT in Nek5000, wall model should be implemented as still the results on the heated walls are still a little bit chaotic due to unresolved mesh in this research. Further more, coupling CHT with FSI should be developed for more multiphysics problems.

In acoustic studies, source term accuracy is not analyzed yet and if it is needed, an integration form with Greens function and Ffowcs Williams-Hawkings equation should be developed for the accuracy of the source term and moving objects, if used for noise simulations. A future work would involve a further exploration of the effectiveness of the proposed methodology in application more complicated hydraulics systems, for

example, those involving elbows and junctions, and in turbulent flow. A verification of a scaling of a proposed probing frequency of 10 c_0/L with the AWT transform with different system parameters is also required, including a validation of the developed technology on a field data. Developing data-based correlations invoking data mining and machine learning methodologies utilizing multiple probes, for a better prediction of leak locations and sizes, especially in cases with multiple leaks and complex pipe network systems, would also be interest.

REFERENCES

Adnan, N. F., M. F. Ghazali, M. M. Amin and A. M. A. Hamat, "Leak detection in gas pipeline by acoustic and signal processing - A review", IOP Conf. Series: Materials Science and Engineering **100**, 012013 (2015).

Adrian, R. J., "Hairpin vortex organization in wall turbulence", Phys. Fluids **19**, 041301 (2007).

Aitken, A., "On Bernoulli's numerical solution of algebraic equations", Proceedings of the Royal Society of Edinburgh **46**, 1, 289–305 (1926).

Allen, E. and J. Iano, *Fundamentals of Building Construction: Materials and Methods, 7th Edition* (Wiley, 2019).

Arababadi, R., *Operational and Technological Peak Load Shifting Strategies for Residential Buildings*, Ph.D. thesis, Arizona State Univeristy (2016).

Araujo, M. V., F. D. T. de Luna, E. S. Barbosa, S. R. de Farias Neto and A. G. B. de Lima, "Numerical study of oil flow in tee junction with leaks", Adv. Petrol. Explorat. Develop. **6**, 2, 1–11 (2013).

Badia, S., F. Nobile and C. Vergara, "Fluid-structure partitioned procedures based on Robin transmission conditions", J. Comput. Phys. **227**, 14, 7027–7051 (2008).

Baechler, M. C., J. Williamson, T. Gilbride, P. Cole, M. Hefty and P. Love, "Guide to determining climate regions by county", Pacific Northwest National Laboratory & Oak Ridge National Laboratory **7**, 1–34 (2010).

Baek, H. and G. E. Karniadakis, "Sub-iteration leads to accuracy and stability enhancements of semi-implicit schemes for the navier-stokes equations", J. Comput. Phys. **230**, 12, 4384–4402 (2011).

Baek, H. and G. E. Karniadakis, "A convergence study of a new partitioned fluid-structure interaction algorithm based on fictitious mass and damping", J. Comput. Phys. **231**, 629–652 (2012).

Baik, K., J. Jiang and T. G. Leighton, "Acoustic attenuation, phase and group velocities in liquid-filled pipes III: Nonaxisymmetric propagation and circumferential modes in lossless conditions", J. Acoust. Soc. Am. **133**, 3, 1225–1236 (2013).

Banks, J. W., W. D. Henshaw and D. W. Schwendeman, "An analysis of a new stable partitioned algorithm for FSI problems. Part I: Incompressible flow and elastic solids", J. Comp. Phys. **269**, 108–137 (2014).

Bathe, K.-J., *Finite Element Procedures* (Prentice-Hall, 1996), 1 edn.

Bathe, K.-J. and G. A. Ledezma, "Benchmark problems for incompressible fluid flows with structural interactions", Comput. Struct. **85**, 628–644 (2007).

Bazilevs, Y., K. Takizawa and T. E. Tezduyar, *Computational Fluid-Structure Interaction Methods and Applications* (A John Wiley & Sons, Ltd, 2013).

Beck, S. B. M., M. D. Curren, N. D. Sims and R. Stanway, "Pipeline network features and leak detection by cross-correlation analysis of reflected waves", ASCE J. Hydraulic Eng. **131**, 715–723 (2005).

Ben-Mansour, R., M. A. Habib, A. Khalifa, K. Youcef-Toumi and D. Chatzigeorgiou, "Computational fluid dynamics simulation of small leaks in water pipelines for direct leak pressure transduction", Comp. Fluids **57**, 110–123 (2012).

Benjamin, T. B., "Fluid flow with flexible boundaries", (Springer Verlag Berlin Heidelberg GmbH, 1966), in Proceedings of the 1st International Congress on Applied Mechanics, Munich, Germany, 1964, Henry Görtler, ed.

Benschop, H. O. G., A. J. Greidanus, R. Delfos, J. Westerweel and W.-P. Breugem, "Deformation of a linear viscoelastic compliant coating in a turbulent flow", J. Fluid Mech. **859**, 613–658 (2019).

Berenger, J.-P., "A perfectly matched layer for the absorption of electromagnetic waves", J. Comp. Phys. **114**, 185–200 (1994).

Berselli, L. C., T. Iliescu and W. J. Layton, *Mathematics of Large Eddy Simulation of Turbulent Flows* (Springer Verlag, Berlin, 2006).

Billah, K. Y. and R. H. Scanlan, "Resonance, Tacoma Narrows bridge failure, and undergraduate physics textbook", Am. J. Phys. **59**, 2, 118–124 (1991).

Bilmann, L. and R. Isermann, "Leak detection methods for pipelines", Automatica **23**, 3, 381–385 (1987).

Blackstock, D. T., *Fundamentals of Physical Acoustics* (John Wiley & Sons, 2000).

Booten, C., C. Christensen and J. Winkler, "Energy impacts of oversized residential air-conditioners - Simulation study of retrofit sequence impacts", National Renewable Energy Laboratory NREL/TP-5500-60801 (2014).

Brothers, K. J., "Water leakage and sustainable supply-truth or consequences?", J. Am. Water Works Assoc. **93**, 4, 150–152 (2001).

Brunone, B., M. Ferrante, S. Meniconi and C. Massari, "Effectiveness assessment of pipe systems by means of transient test-based techniques", Procedia Env. Sciences **19**, 814–822 (2013).

Brunone, B., M. Ferrante and L. Ubertini, "Leak analysis in pipes using transients", (2000), in 2nd Annual Seminar on Comparative Urban Projects (Rome, 19-23 June).

Brunone, B., U. M. Golia and M. Greco, "Some remarks on the momentum equation for fast transients", (Universidad Politecnica de Valencia, 1991), 9th Round table, Hydraulic transients with water column separation;Valencia; Spain.

Brunone, B., U. M. Golia and M. Greco, "Effects of Two-Dimensionality on Pipe Transients Modeling ", Journal of Hydraulic Engineering **121**, 906–912 (1995).

Buratti, C., D. Palladino and E. Moretti, "Prediction Of Indoor Conditions And Thermal Comfort Using CFD Simulations: A Case Study Based On Experimental Data", Energy Procedia **126**, 115–122 (2017).

Burman, E. and M. A. Fernández, "Stabilization of explicit coupling in fluid-structure interaction involving fluid incompressibility", Comput. Methods Appl. Mech. Engrg. **198**, 5, 766–784 (2009).

Butler, K. M. and B. F. Farrell, "Three-dimensional optimal perturbations in viscous shear flow", Physics of Fluids A: Fluid Dynamics **4**, 8, 1637–1650 (1992).

Carpenter, P. W. and A. D. Garrad, "The hydrodynamic stability of flow over Kramer-type compliant surfaces. Part 1. Tollmien-Schlichting instabilities", J. Fluid Mech. **155**, 465–5120 (1985).

Causin, P., J. Gerbeau and F. Nobile, "Added-mass effect in the design of partitioned algorithms for fluid-structure problems", Comput. Methods Appl. Mech. Engrg. **194**, 42, 4506–4527 (2005).

Cetin, K. S., "Characterizing large residential appliance peak load reduction potential utilizing a probabilistic approach", Sci. Technol. Built Environ. **22**, 720–732 (2016).

Cetin, K. S., M. H. Fathollahzadeh, N. Kunwar, H. Do and P. C. Tabares-Velasco, "Development and validation of an HVAC on/off controller in EnergyPlus for energy simulation of residential and small commercial buildings", Energy & Buildings **183**, 467–483 (2019).

Chabannes, V., G. Pena and C. Prud'homme, "High-order fluid-structure interaction in 2D and 3D application to blood flow in arteries", J. Comput. Appl. Math. **246**, 1–9 (2013).

Chatterjee, T. and Y. T. Peet, "Regularization modelling for large-eddy simulation in wall-bounded turbulence: An explicit filtering-based approach", International Journal for Numerical Methods in Fluids **88**, 1, 1–17 (2018).

Che, T.-C., H.-F. Duan, P. J. Lee, S. Meniconi, B. Pan and B. Brunone, "Radial Pressure Wave Behavior in Transient Laminar Pipe Flows Under Different Flow Perturbations", Journal of Fluids Engineering **140**, 10, 101203 (2018).

Chen, Q., "Ventilation performance prediction for buildings: A method overview and recent applications", Building and Environment **44**, 848–858 (2009).

Chowdhury, M. A., M. F. Ahmed and M. A. Gaffar, "Water system leak detection in secondary towns of Bangladesh", Water Supply **3**, 343–349 (1999).

Clarke, J., W. Dempster and C. Negrao, "The implementation of a computational fluid dynamics algorithm within the esp-r system", Proc. Building Simulation pp. 166–75 (1995).

Clayton, R. and B. Engquist, "Absorbing boundary conditions for acoustic and elastic wave equations", Bull. Seism. Soc. Amer. **67**, 6, 1529–1540 (1977).

Cockburn, B., G. E. Karniadakis and C.-W. Shu, "Discontinuous Galerkin Methods: Theory, Computation and Applications", in "Lecture Notes in Computational Science and Engineering, vol. 11", (Springer, 1991).

Colombo, A. F. and B. W. Karney, "Energy and costs of leaky pipes: Toward comprehensive picture", J. Water Resour. Plann. Manag. **128**, 6, 441–450 (2002).

Colombo, A. F., P. Lee and B. W. Karney, "A selective literature review of transient-based leak detection methods", J. Hydro-Env. Research **2**, 212–227 (2009).

Courant, R., K. Friedrichs and H. Lewy, "On the partial difference equations of mathematical physics", IBM Journal of Research and Development **11**, 2, 215–234 (1967).

Covas, D., H. Ramos and A. B. Almeida, "Standing wave difference method for leak detection in pipeline systems", J. Hydraul. Engin. **131**, 12, 1106–1116 (2005).

Coxe, D. J., Y. T. Peet and R. J. Adrian, "Vorticity statistics and distributions in drag reduced turbulent pipe flow with transverse wall oscillations", (2019), in Proceedings of 11th Int. Symp. on Turbulence and Shear Flow Phenomena, August 2019, Southampton, UK.

Degroote, J., K.-J. Bathe and J. Vierendeels, "Performance of a new partitioned procedure versus a monolithic procedure in fluid-structure interaction", Comput. Struct. **87**, 11, 793–801 (2009).

Deparis, S., M. A. Fernández and L. Formaggia, "Acceleration of a fixed point algorithm for fluid-structure interaction using transpiration conditions", ESAIM: M2AN **37**, 4, 601–616 (2003).

Deville, M. O., P. F. Fischer and E. H. Mund, *High-Order Methods for Incompressible Fluid FLow* (Cambridge University Press, 2002).

Diao, X., G. Shen, J. Jiang, Q. Chen, Z. Wang, L. Ni, A. Mebarki and Z. Dou, "Leak detection and location in liquid pipelines by analyzing the first transient pressure wave with unsteady friction", Journal of Loss Prevention in the Process Industries **60**, 303–310 (2019).

Dixon, A. E., A. D. Lucey and P. W. Carpenter, "The optimization of viscoelastic coating walls for transition delay", AIAA J. **32**, 256–267 (1994).

Dong, S. and Z. Yosibash, "A parallel spectral element method for dynamic three-dimensional nonlinear elasticity problems", Comput. Struct. **87**, 59–72 (2009).

Dou, Z., A. Rips, N. Welsh, J.-H. Seo and R. Mittal, "Flow-induced flutter of hanging banners: Experiments and validated computational models", in "2018 Fluid Dynamics Conference", (2018).

EIA, "Use of energy explained: Energy use in homes", Https://www.eia.gov/energyexplained/use-of-energy/homes.php (2015).

El Khoury, G. K., P. Schlatter, A. Noorani, P. F. Fischer, G. Brethouwer and A. V. Johansson, "Direct numerical simulation of turbulent pipe flow at moderately high Reynolds numbers", Flow Turb. Combust. **91**, 3, 475–495 (2013).

Engquist, B. and A. Majda, "Absorbing boundary conditions for numerical simulation of waves", Math. Comp. **31**, 139, 629–651 (1977).

et al., P. F. F., "Nek5000 Web page", Http://nek5000.mcs.anl.gov (2016).

Fedorov, A. G. and R. Viskanta, "Three-dimensional conjugate heat transfer in themicrochannel heat sink for electronic packaging", International Journal of Heat and Mass Transfer **43**, 399–415 (2000).

Fernández, M. A., J. Mullaert and M. Vidrascu, "Generalized Robin-Neumann explicit coupling schemes for incompressible fluid-structure interaction: Stability analysis and numerics", Int. J. Numer. Meth. Engng **101**, 3, 119–229 (2015).

Ferrante, M. and B. Brunone, "Pipe system diagnosis by unsteady-state tests. 1. Harmonic analysis", Adv. Water Resources **26**, 95–105 (2003a).

Ferrante, M. and B. Brunone, "Pipe system diagnosis by unsteady-state tests. 2. Wavelet analysis", Adv. Water Resources **26**, 107–116 (2003b).

Ferrante, M., B. Brunone, S. Meniconi, B. W. Karney and C. Massari, "Leak size, detectability and test conditions in pressurized pipe systems", Water Resour. Manage. **28**, 4583–4598 (2014).

Fischer, P., J. Lottes, S. Kerkemeier, O. Marin, K. Heisey, A. Obabko, E. Merzari and Y. Peet, "Nek5000: User's manual", Argonne national laboratory, http://nek5000.mcs.anl.gov/files/2015/09/NEK_doc.pdf (2015).

Fischer, P., J. Lottes, D. Pointer and A. Siegel, "Petascale algorithms for reactor hydrodynamics", J. Phys. Conf. Series **125**, 012076 (2008).

Fischer, P. F., "An overlapping Schwarz method for spectral element solution of the incompressible Navier–Stokes equations", J. Comp. Phys. **133**, 1, 84–101 (1997a).

Fischer, P. F., "An overlapping Schwarz method for spectral element solution of the incompressible Navier-Stokes equations", J. Comput. Phys. **133**, 1, 84–101 (1997b).

Fischer, P. F. and J. S. Mullen, "Filter-based stabilization of spectral element methods", Comptes Rendus de l'Académie des Sciences - Series 1 - Mathematics **332**, 265–270 (2001).

Fish, J. and T. Belytschko, *A First Course in Finite Elements* (John Wiley & Sons, 2007).

Folga, S. M., "Natural gas pipeline technology: Overview", Tech. Rep. ANL/EVS/TM/08-5, argonne National Laboratory (2007).

Formaggia, L., J.-F. Gerbeau, F. Nobile and A. Quarteroni, "On the coupling of 3D and 1D Navier-Stokes equations for flow problems in compliant vessels", Comp. Meth. Appl. Mech. Engrg. **191**, 6, 561–582 (2001).

Formaggia, L. and F. Nobile, "Stability analysis of second-order time accurate schemes for ALE-FEM", Comput. Methods Appl. Mech. Engrg. **193**, 39, 4097–4116 (2004).

Förster, C., W. A. Wall and E. Ramm, "Artificial added mass instabilities in sequential staggered coupling of nonlinear structures and incompressible viscous flows", Comput. Methods Appl. Mech. Engrg. **196**, 7, 1278–1293 (2007).

Froehle, B. and P.-O. Persson, "A high-order disctontinuous Galerkin method for fluid-structure interaction with efficient implicit-explicit time stepping", J. Comput. Phys. **272**, 455–470 (2014).

Funk, J. E., D. J. Wood, S. J. vanVuuren and M. LeChevallier, "Pathogen intrusion into water distribution systems due to transients", (1999), in Proceedings of the 3rd ASME/JSME Joint Fluids Engineering Conference, July 1999, San Francisco.

Gad-el-Hak, M., "Compliant coatings for drag reduction", Prog. Aero. Sci. **38**, 77–99 (2002).

Gad-el-Hak, M., R. F. Blackwelder and J. R. Riley, "On the interaction of compliant coatings with boundary-layer flows", J. Fluid Mech. **140**, 257–280 (1984).

Ganesh, G. A., S. L. Sinha and T. N. Verma, "Numerical simulation for optimization of the indoor environment of an occupied office building using double-panel and ventilation radiator", Journal of Building Engineering **29**, 101139 (2020).

Gerardo-Giorda, L., F. Nobile and C. Vergara, "Analysis and Optimization of Robin-Robin Partitioned Procedures in Fluid-Structure Interaction Problems", SIAM J. Numer. Anal. **48**, 6, 2091–2116 (2010).

German, A. and M. Hoeschele, *Residential Mechanical Precooling* (2014).

Geurts, B., A. K. Kuczaj and E. S. Titi, "Regularization modelling for large-eddy simulation of homogeneous isotropic decaying turbulence", J. Phys. A: Math. Theor. **41**, 344008 (2008).

Geurts, B. J., "Regularization modeling for LES of separated boundary layer flow", Journal of Fluids and Structures **24**, 1176–1184 (2008).

Geuzaine, P., C. Grandmont and C. Farhat, "Design and analysis of ALE schemes with provable second-order time-accuracy for inviscid and viscous flow simulations", J. Comp. Phys. **191**, 296–227 (2000).

Ghazali, M. E., S. B. M. Beck, J. D. Shucksmith, J. B. Boxall and W. J. Staszewski, "Comparative study of instantaneous frequency based methods for leak detection in pipeline networks", Mech. Syst. Signal Process. **29**, 187–200 (2012).

Ghidaoui, M. S., M. Zhao, D. A. McInnis and D. H. Axworthy, "A Review of Water Hammer Theory and Practice", Applied Mechanics Reviews **59**, 1, 49–76 (2005).

Gorter, J. L., "HVAC equipment right-sizing: occupant comfort and energy-savings potential", Energy Eng. **109**, 59–75 (2012).

Guermond, J.-L. and S. Prudhomme, "Mathematical analysis of a spectral hyper-viscosity LES model for the simulation of turbulent flows", Math. Model. Numer. Anal. **37**, 893–908 (2003).

Guillard, H. and C. Farhat, "On the significance of the geometric conservation law for flow computations on moving meshes", Comp. Methods Appl. Mech. Engrg. **190**, 1467–1482 (2000).

Hamilton, J. M., J. Kim and F. Waleffe, "Regeneration mechanisms of near-wall turbulence structures", Journal of Fluid Mechanics **287**, 1, 317–348 (1995).

Henderson, H., D. Parker and Y. J. Huang, "Improving DOE-2's RESYS routine: user defined functions to provide more accurate part load energy use and humidity prediction", In: Proceedings of 2000 ACEEE Summer Study on Energy Efficiency in Buildings, August 20-25, 2000 in Pacific Grove, CA LBNL-46304 (2000).

Henderson, H. I., D. B. Shirey and R. A. Rastad, "Closing the gap: getting full performance from residential central air conditioners, Task 4 - Develop new climate-sensitive air-conditioner, simulation results and cost benefit analysis", New york state energy research and development authority (2007).

Hirt, C. W., A. A. Amsden and J. L. Cook, "An Arbitrary Lagrangian-Eulerian Computing Method for All Flow Speeds", J. Comput. Phys. **135**, 203–216 (1997).

Holzapfel, G. A., *Nonlinear Solid Mechanics: A Continuum Approach for Engineering, 1st edition* (Wiley, 2000).

Horikiri, K., Y. Yao and J. Yao, "Modelling conjugate flow and heat transfer in a ventilated room for indoor thermal comfort assessment", Building and Environment **77**, 135–147 (2014).

Hou, G., J. Wang and A. Layton, "Numerical methods for fluid-structure interaction – A review", Commun. Comput. Phys. **12**, 2, 337–377 (2012).

Hummon, M., D. Palchak, P. Denholm, J. Jorgenson, D. J. Olsen, S. Kiliccote, N. Matson, M. Sohn, C. Rose, J. Dudley, S. Goli and O. Ma, "Grid integration of aggregated demand response, Part 2: Modeling demand response in a production cost model", Tech. Rep. NREL/TP-6A20-58492 (2013).

Ilic, S. M., C. W. Bullard and P. S. Hrnjak, "Effect of shorter compressor on/off cycle times on A/C system performance", University of Illinois at Urbana-Champaign Tech. Report ACRC CR-43 (2001).

Jahanbin, A. and G. Semprini, "Numerical Study on Indoor Environmental Quality in a Room Equipped with a Combined HRV and Radiator System ", Sustainability **12**, 24 (2020).

Jiménez, J., "On the structure and control of near wall turbulence", Physics of Fluids **6**, 2, 944–953 (1994).

Jones, D. H., A. Y. Nehru and J. Skinner, "The impact fretting wear of a nuclear reactor component", Wear **106**, 1–3, 139–162 (1985).

Kaltenbacher, M., M. Escobar, S. Becker and I. Ali, "Numerical simulation of flow induced noise using les sas and lighthill's acoustic analogy", Int. J. Numer. Meth. Fluids **63**, 9, 1103–1122 (2010).

Kaminski, D. and C. Prakash, "Conjugate natural convection in a square enclosure: effect of conduction in one of the vertical walls", International Journal of Heat and Mass Transfer **29**, 1979–1988 (1986).

Kan, J. V., "A second-order accurate pressure-correction scheme for viscous incompressible flow", SIAM J. Sci. Stat. Comput. **80**, 870–891 (1986).

Karamanos, G. S. and G. E. Karniadakis, "A spectral vanishing viscosity method for large eddy simulations", J. Comput. Phys. **163**, 22–50 (2000).

Karim, M. R., M. Abbaszadegan and M. LeChevallier, "Potential for pathogen intrusion during pressure transients", J. Amer. Water Works Assoc. **95**, 5, 134–146 (2003).

Karniadakis, G., M. Israeli and S. Orszag, "High-order splitting methods for the incompressible Navier–Stokes equations", Journal of Computational Physics **97**, 2, 414–443 (1991).

Khalighi, Y., A. Mani, F. Ham and P. Moin, "Prediction of sound generated by complex flows at low mach numbers", AIAA J. **48**, 2, 306–316 (2010).

Kim, E. and H. Choi, "Space-time characteristics of a compliant wall in a turbulent channel flow", J. Fluid Mech. **756**, 30–53 (2014).

Kim, J., P. Moin and R. Moser, "Turbulence statistics in fully developed channel flow at low Reynolds number", Journal of Fluid Mechanics **177**, 133–166 (1987).

Kim, N.-H., *Introduction to Nonlinear Finite Element Analysis* (Springer US, 2015).

Kim, S. H., "Extensive development of leak detection algorithm by impulse response method", J. Hydarul. Eng. **131**, 3, 201–208 (2005).

Kirby, R. M., M. Berzins, J. S. Hesthaven and eds., "Spectral and high order methods for partial differential equations: ICOSAHOM 2014", (Springer, 2014), proceedings of ICOSAHOM conference, June 23-27, 2014, Salt Lake City, UT, USA.

Kirmeyer, G. J., "Pathogen intrusion into the distribution system", (2001), amer. Water Works Assoc. Research foundation, Denver.

Koobus, B. and C. Farhat, "Second order time accurate and geometrically-conservative implicit schemes for flow computations on unstructured dynamic meshes", Comp. Methods Appl. Mech. Engrg. **170**, 103–129 (1999).

Küttler, U. and W. A. Wall, "Fixed-point fluid-structure interaction solvers with dynamic relaxation", Comput. Mech. **43**, 1, 61–72 (2008).

Kuznetsov, G. V. and M. A. Sheremet, "Conjugate natural convection in an enclosure with a heat source of constant heat transfer rate", Int. J. Heat Mass Transfer **54**, 260–268 (2011).

Lai, C. C., "Unaccounted for water and the economics of leak detection", Water Supply **9**, 1–8 (1991).

Lee, T., M. Fisher and W. H. Schwarz, "Investigation of the effects of a compliant surface on boundary-layer stability", J. Fluid Mech. **288**, 37–58 (1995).

Li, B. and G. Alleyne, "Optimal on-off control of an air conditioning and refrigeration system", In: Proceedings of 2010 American Control Conference, Baltimore, MD, USA 978-1-4244-7427-1/10 (2010).

Li, Y. and S.-C. Kong, "Coupling conjugate heat transfer with in-cylinder combustion modeling forengine simulation", International Journal of Heat and Mass Transfer **54**, 2467–2478 (2011).

Lighthill, M. J., "On sound generated aerodynamically i. general theory", Proc. Roy. Soc. London. A. Mathematical and Physical Sciences **211**, 564–587 (1952).

Lilly, J. M. and S. C. Olhede, "Higher-order properties of analytic wavelets", IEEE Transactions on Signal Processing **57**, 1, 146–160 (2008).

Lilly, J. M. and S. C. Olhede, "On the analytic wavelet transform", IEEE Trans. Inf. Theory **56**, 8, 4135–4156 (2010).

Lilly, J. M. and S. C. Olhede, "Generalized Morse wavelets as a superfamily of analytic wavelets", IEEE Trans. Sign. Proc. **60**, 6036–6041 (2012).

Liou, C. P., "Pipeline leak detection by impulse response extracrion", ASME J. Fluids Eng. **120**, 833–838 (1998).

Liu, A. E., "Pipeline accounting and leak detection by mass balance, theory and hardware implementation", (2008), technical Report, Quantum Dynamics, Inc.

Livne, E., "Aircraft active flutter suppression: State of the art and technology maturation needs", J. Aircfaft **55**, 1, 410–450 (2018).

Louati, M. and M. S. Ghidaoui, "High-frequency acoustic wave properties in a water-filled pipe. Part 1: dispersion and multi-path behaviour", J. Hydraulic Res. **55**, 613–631 (2017).

Lu, T., H. T. Li and X. G. Zhu, "Numerical simulation of thermal stratification in an elbow branch pipe of a tee junction with and without leakage", Annals of Nuclear Energy **60**, 432–438 (2013).

Luhar, M., A. S. Sharma and B. J. McKeon, "A framework for studying the effect of compliant surfaces on wall turbulence", J. Fluid Mech. **768**, 415–441 (2015).

Martins, N. M. C., B. Brunone, S. Meniconi, H. M. Ramos and D. I. C. Covas, "Efficient Computational Fluid Dynamics Model for Transient Laminar Flow Modeling: Pressure Wave Propagation and Velocity Profile Changes", Journal of Fluids Engineering **140**, 1, 011102 (2018).

Meier, A., C. Aragon, T. Peffer, D. Perry and M. Pritoni, "Usability of residential thermostats: Preliminary investigations", Building and Environment **46**, 1891–1898 (2011).

Meniconi, S., B. Brunone, M. Ferrante and C. Massari, "Small amplitude pressure waves to diagnose pipe systems", Water Resour. Manage. **25**, 79–96 (2011).

Merrill, B. E. and Y. T. Peet, "Moving overlapping grid methodology of spectral accuracy for incompressible flow solutions around rigid bodies in motion", J. Comp. Phys. **390**, 121–151 (2019).

Merrill, B. E., Y. T. Peet, P. F. Fischer and J. W. Lottes, "A spectrally accurate method for overlapping grid solution of incompressible Navier-Stokes equations", J. Comput. Phys. **307**, 60–93 (2016a).

Merrill, B. E., Y. T. Peet, P. F. Fischer and J. W. Lottes, "A spectrally accurate method for overlapping grid solution of incompressible Navier-Stokes equations", J. Comp. Phys. **307**, 60–93 (2016b).

Merzari, E., A. Obabko and P. F. Fischer, "Spectral element methods for liquid metal reactors applications", (von Karman Institute for Fluid Dynamics, 2017), in Thermohydraulics and Chemistry of Liquid Metal Cooled Reactors, Edited by F. Roelofs & Ph. Planquart, VKI LS 2017-02.

Mirinejad, H., S. H. Sadati, M. Ghasemian and H. Torab, "Control techniques in heating, ventilating and air conditioning (HVAC) systems", J. Computer Science **4**, 777–783 (2008).

Mittal, R. and G. Iaccarino, "Immersed boundary methods", Annu. Rev. Fluid Mech. **37**, 239–261 (2005).

Motazedi, N. and S. Beck, "Leak detection using cepstrum of cross-correlation of transient pressure wave signals", Proceedings of the Institution of Mechanical Engineers, Part C: Journal of Mechanical Engineering Science **232**, 15, 2723–2735 (2018).

Mpesha, W., S. L. Gassman and M. H. Chaudhry, "Leak detection in pipes by frequency response methods", J. Hydraul. Eng. **127**, 2, 134–147 (2001).

Muftuoglu, A. and E. Bilgen, "Conjugate heat transfer in open cavities with a discrete heater at its optimized position", Int. J. Heat Mass Transfer **51**, 779–788 (2008).

Nada, S., H. El-Batsh, H. Elattar and N. Ali, "CFD investigation of airflow pattern, temperature distribution and thermal comfort of UFAD system for theater buildings applications", Journal of Building Engineering **6** (2016).

Newmark, N. M., "A method of computation for structured dynamics", Journal of Engineering Mechanics,ASCE **85**, 67–94 (1959).

Nielsen, P. V. and T. Trytvason, *Computational fluid dynamics and building energy performance simulation* (1998), proceedings of Roomvent, vol.1, Stockholm, Sweden, pp. 101–107.

Nobile, F. and C. Vergara, "An Effective Fluid-Structure Interaction Formulation for Vascular Dynamics by Generalized Robin Conditions", SIAM J. Sci. Comput. **30**, 2, 731–763 (2008).

Obabko, A., E. Merzari, L. Brockmeyer, P. Fischer, T. Sofu, B. Jackson, M. Steer, R. Vaghetto and Y. A. Hassan, "Validation of nek5000 for 37- and 61-pin wire-wrap geometries with conjugate heat transfer", Tech. Rep. 2036–2049, 18th International Topical Meeting on Nuclear Reactor Thermal Hydraulics (NURETH 2019) (2019).

Obabko, A. V., P. F. Fischer, T. J. Tautges, V. M. Goloviznin, M. A. Zaytsev, V. V. Chudanov, V. A. Pervichkno, A. E. Aksenova and S. Karabasov, "Large eddy simulation of thermo-hydraulic mixing in a T-junction", in "Nuclear Reactor Thermal Hydraulics and Other Applications", (Donna Post Guillen, Ed., ISBN 978-953-51-0987-7, 2013).

Olhede, S. C. and A. T. Walden, "Generalized Morse wavelets", IEEE Trans. Sign. Proc. **50**, 2661–2670 (2002).

Orszag, S. A., "Spectral methods for problems in complex geometry", J. Comput. Phys. **37**, 70–92 (1980).

Ovchinnikov, A. L. and B. M. Lapshin, "Low frequency acoustic signal propagation in buried pipelines", J. Phys. Conf. Series **671**, 012031 (2016).

Owowo, J., *Simulation, Measurement and Detection of Leakage and Blockage in Fluid Pipeline Systems*, Ph.D. thesis, University of Manchester, United Kingdom (2016).

Owowo, J. and S. O. Oyadiji, "Finite element analysis and experimental measurement of acoustic wave propagation for leakage detection in an air-filled pipe", Int. J. Struct. Integrity **8**, 4, 452–467 (2017).

Pandey, B., R. Banerjee and A. Sharma, "Coupled EnergyPlus and CFD analysis of PCM for thermal management of buildings", Energy and Buildings **231**, 110595 (2021).

Park, J., T. Kim and C.-s. Lee, "Development of thermal comfort-based controller and potential reduction of the cooling energy consumption of a residential building in kuwait", Energies **12**, 17, 3348 (2019).

Parken, W. H. J., R. W. Beausoliet and G. E. Kelly, "Factors affecting the performance of a residential air-to-air heat pump", ASHRAE Transactions **83**, 839–849 (1977).

Patankar, S. V., *Numerical Heat Transfer and Fluid Flow* (Taylor & Francis, 1980).

Patel, S., P. Fischer, M. Min and A. Tomboulides, "A characteristic-based spectral element method for moving domain problems", J. Scientific Computing **79**, 564–592 (2019).

Patera, A., "A spectral element method for fluid dynamics: laminar flow in a channel expansion", Journal of Computational Physics **54**, 468–488 (1984).

Peet, Y., P. Fischer, G. Conzelmann and V. Kotamarthi, "Actuator line aerodynamics model with spectral elements", AIAA Paper 2013–1210, 51st Aerospace Sciences Meeting, Grapevine, TX (2013).

Peet, Y. and P. F. Fischer, "Heat transfer LES simulations in application to wire-wrapped fuel pins", AIAA Paper 2010–4318, in: 10th AIAA/ASME Joint Thermophysics and Heat Transfer Conference, June 28-July 1 2010, Chicago, IL (2010).

Peet, Y. T. and P. F. Fischer, "Legendre spectral element method with nearly incompressible materials", Eur. J. mech. A, Solids **44**, 91–103 (2014).

Pena, G. and C. Prud'homme, "Construction of a high-order fluid-structure interaction solver", J. Comput. Appl. Math. **234**, 2358–2865 (2010).

Pena, G., C. Prud'homme and A. Quarteroni, "High order methods for the approximation of the incompressible Navier-Stokes equations in a moving domain", Comput. Methods Appl. Mech. Engrg. **209-212**, 197–211 (2012).

Perelman, T., "ON CONJUGATED PROBLEMS OF HEAT TRANSFER", Int. J. Heat Mass Transfer. **3**, 293–303 (1961).

Perera, D. W. U., C. F. Pfeiffer and N.-O. Skeie, "Control of temperature and energy consumption in building - a review", Int. J. Energy Envir. **5**, 471–484 (2014).

Pérez-Lombard, L., J. Ortiz and C. Pout, "A review on buildings energy consumption information", Energy Build. **40**, 1979–1988 (2008).

Persson, P.-O., J. Bonet and J. Peraire, "Discontinuous Galerkin solution of the Navier-Stokes equations on deformable domains", Comput. Methods Appl. Mech. Engrg. **198**, 1585–1595 (2009).

Pezzinga, G., "Evaluation of Unsteady Flow Resistances by Quasi-2D or 1D Models", Journal of Hydraulic Engineering **126**, 778–785 (2000).

PHOENIX, C. O., *BUILDING STANDARDS AND REVIEW PROCESS*, URL `https://www.phoenix.gov/streetssite/Documents/eas_pdf_building_standards_2.pdf` (1997).

Posner, J. D., C. R. Buchanan and D. Dunn-Rankin, "Measurement and prediction of indoor air flow in a model room", Energy and Buildings **35**, 515–526 (2003).

Proctor, J. P., "Field measurements of new residential air conditioners in Phoenix, Arizona", ASHRAE transactions **103**, In: Proceedings of ASHRAE annual meeting, Boston, MA, USA (1997).

Quarteroni, A., F. Saleri and A. Veneziani, "Factorization methods for numerical approximation of Navier-Stokes equations", Comput. Methods Appl. Mech. Engrg. **188**, 1, 505–526 (2000).

Rao, J. S., *Turbomachine Blade Vibration* (New Age International Publishers, 2005).

Rashid, S., S. Qaisar, H. Saeed and E. Felemban, "A method for distributed pipeline burst and leakage detection in wireless sensor networks using transform analysis", Int. J. Distributed Sensor Networks **2014**, 1–14 (2014).

Reddy, R. S., G. Payal, P. Karkulali, M. Himanshut, A. Ukil and J. Dauwels, "Pressure and flow variation in gas distribution pipeline for leak detection", Ieee paper, in Proceedings of IEEE International Conference on Industrial Technology, At Taipei, Taiwan, March 2016 (2016).

Rhodes, J. D., B. Stevens and M. E. Webber, "Using energy audits to investigate the impacts of common air-conditioning design and installation issues on peak power demand and energy consumption in Austin, Texas", Energy & Buildings **43**, 11, 3271–3278 (2011).

Rienstra, S. W. and A. Hirschberg, "An introduction to acoustics", IWDE Report 92-06 (2019).

Rosti, M. E. and L. Brandt, "Numerical simulation of turbulent channel flow over a viscous hyper-elastic wall", J. Fluid Mech. **830**, 708–735 (2017).

Sakievich, P. J., Y. T. Peet and R. J. Adrian, "Large-scale thermal motions of turbulent Rayleigh-Bénard convection in a wide aspect-ratio cylindrical domain", Int. J. Heat Fluid Flow pp. 1–14 (2016).

Semprini, G., A. Jahanbin, B. Pulvirenti and P. Guidorzi, "Evaluation of Thermal Comfort Inside an Office Equipped with a Fan Coil HVAC System: A CFD Approach", Future Cities and Environment **5**, 1 (2019).

Shan, X., W. Xu, Y.-K. Lee and W.-Z. Lu, "Evaluation of thermal environment by coupling CFD analysis and wireless- sensor measurements of a full-scale room with cooling system", Sustainable Cities and Society **45**, 395–405 (2019).

Shehaded, M. and A. I. Shahata, "Modelling the effect of incompressible leakage patterns on rupture area in pipeline", CFD Letters **5**, 4, 132–142 (2013).

Sheldon, J. P., S. T. Miller and J. S. Pitt, "A hybridizable discontinuous Galerkin method for modeling fluid-structure interaction", J. Comput. Phys. **326**, 91–114 (2016).

Shucksmith, J. D., J. B. Boxall, W. J. Staszewski, A. Seth and S. B. M. Beck, "Onsite leak location in a pipe network by cepstrum analysis of pressure transients", J. Amer. Water Works Ass. pp. E457–E465 (2012).

Siegel, R. and M. Perlmutter, "Laminar Heat Transfer in a Channel With Unsteady Flow and Wall Heating Varying With Position and Time", Journal of Heat Transfer **85**, 4, 358–365 (1963).

Silva, R. A., C. M. Buiatti, S. L. Cruz and J. A. F. R.Pereira, "Pressure wave behavior and leak detection in pipelines", Comput. Chem. Eng. **20**, S491–S496 (1996).

Sparn, B., K. Hudon, L. Earle, C. Booten, P. Tabares-Velasco, G. Barker and C. Hancock, "Greenbuilt retrofit test house final report", Tech. rep., National Renewable Energy Lab.(NREL), Golden, CO (United States) (2014).

Sprague, M. A., M. Churchfield, A. Purkayastha, P. Moriarty and S. Lee, "A comparison of Nek5000 and OpenFOAM for DNS of turbulent channel flow", URL `https://www.mcs.anl.gov/~fischer/nek5000/sprague_nek5000_dec2010.pdf` (2010).

Svoma, B. M. and A. Brazel, "Urban effects on the diurnal temperature cycle in Phoenix, Arizona", Climate Research **41**, 1, 21–29 (2010).

Tabares-Velasco, P. C., "Timestep considerations while simulating dynamic behavior of high-performance homes", In: Proceedings of whole buildings xii international conference, Florida, USA (2013).

Taghvaei, M., S. B. M. Beck and W. J. Staszewski, "Leak detection in pipelines using cepstrum analysis", Meas. Sci. Technol. **17**, 367–372 (2006).

Tang, D., C. Yang, S. Kobayashi, J. Zheng and R. P. Vito, "Effect of Stenosis Asymmetry on Blood Flow and Artery Compression: A Three-Dimensional Fluid-Structure Interaction Model", Annals of Biomedical Engineering **31**, 1182–1193 (2003).

Tassou, S. A., C. J. Marquand and D. Wilson, "Comparison of performance of capacity controlled and conventional on/off controlled heat pump", Applied Energy **14**, 241–256 (1983).

Tchuisseu, E. B. T., D. Gomila, D. Brunner and P. Colet, "Effects of dynamic-demand-control appliances on the power grid frequency", Phys. Review E **96**, 1979–1988 (2017).

Tewari, M., F. Salamanca, A. Martilli, L. Treinish and A. Mahalov, "Impacts of projected urban expansion and global warming on cooling energy demand over a semiarid region", Atmospheric Science Letters **18**, 11, 419–426 (2017).

Thomas, P. D. and C. K. Lombard, "Geometric conservation law and its application to flow computations on moving grids", AIAA J. **17**, 1030–1037 (1979).

Thornton, J., R. Sturm and G. Kunkel, *Water Loss Control, 2nd editiion* (McGraw Hill, 2008).

Tian, W., T. A. Sevilla, W. Zuo and M. D. Sohn, "Coupling fast fluid dynamics and multizone airflow models in Modelica *Buildings* library to simulate the dynamics of HVAC systems", Building and Environment **122**, 269–286 (2017).

Tian, Z. F., J. Y. Tu, G. H. Yeoh and R. K. K. Yuen, "Numerical studies of indoor airflow and particle dispersion by large Eddy simulation", Building and Environment **42**, 3483–3492 (2007).

Toh, K., X. Chen and J. Chai, "Numerical computation of fluid flow and heat transfer in microchannels", International Journal of Heat and Mass Transfer **43**, 5133–5141 (2002).

Tomboulides, A. G., J. C. Y. Lee and S. A. Orszag, "Numerical Simulation of Low Mach Number Reactive Flows", Journal of Sci.Comp. **12**, 139–167 (1997).

Tran-Quoc, T. and J. C. Sabonnadiére, "Air conditioner direct load control in distribution networks", In: Proceedings of 2009 ieee bucharest power tech conference, bucharest, romania (2009).

Turek, S. and J. Hron, "Proposal for numerical benchmarking of fluid-structure interaction between an elastic object and laminar incompressible flow", in "Fluid-Structure Interaction", edited by H.-J. Bungartz and M. Schäfer, vol. 53, pp. 371–385 (Springer Berlin Heidelberg, Berlin, Heidelberg, 2006).

Turner, W., I. Walker and J. Roux, "Peak load reductions: Electric load shifting with mechanical pre-cooling of residential buildings with low thermal mass", Energy **82**, 1057–1067 (2015).

Ulpiani, G., M. Borgognoni, A. Romagnoli and C. di Perna, "Comparing the performance of on/off, PID and fuzzy controllers applied to the heating system of an energy-efficient building", Energy and Buildings **116**, 1–17 (2016).

Urbanek, J., T. Barszcz, W. J. Staszewski, S. B. M. Beck and B. Schmidt, "Leak detection in gas pipelines using wavelet-based filtering", Struct. Health Monitor. **11**, 4, 405–412 (2011).

Valencia, A. and F. Baeza, "Numerical simulation of fluidstructure interaction in stenotic arteries considering two layer nonlinear anisotropic structural model", International Communications in Heat and Mass Transfer **36**, 137–142 (2009).

Varghese, S. S., S. H. Frankel and P. F. Fischer, "Direct numerical simulation of stenotic flows. Part 1. Steady flow", Journal of Fluid Mechanics **582**, 253–280 (2007a).

Varghese, S. S., S. H. Frankel and P. F. Fischer, "Direct numerical simulation of stenotic flows. Part 2. Pulsatile flow", Journal of Fluid Mechanics **582**, 281–318 (2007b).

Verkaik, A., M. Hulsen, A. Bogaerds and F. van de Vosse, "An overlapping domain technique coupling spectral and finite elements for fluid-structure interaction", Comput. Fluids **123**, 235–245 (2015).

Visbal, M., P. Morgan and D. Rizzetta, "An implicit LES approach based on high-order compact differencing and filtering schemes", in "16th AIAA Computational Fluid Dynamics Conference", p. 4098 (2003).

Wall, W. A. and E. Ramm, "Fluid–structure interaction based upon a stabilized (ALE) finite element method", in "Computational Mechanics – New Trends and Applications (Proceedings of WCCM IV), CIMNE, Barcelona,1998", edited by S. Idelsohn, E. Oñate and E. Dvorkin (1998).

Walsh, O., "Eddy solutions of the Navier-Stokes equations", in "The Navier-Stokes Equations II — Theory and Numerical Methods", edited by J. G. Heywood, K. Masuda, R. Rautmann and V. A. Solonnikov, vol. 1530, pp. 306–309 (Springer Berlin Heidelberg, Berlin, Heidelberg, 1992).

Wang, H. and Z. J. Zhai, "Advances in building simulation and computational techniques: A review between 1987 and 2014", Energy and Buildings **128**, 319–335 (2016).

Wang, L. L. and Q. Chen, "Evaluation of some assumptions used in multizone airflow network models", Building and Environment **43**, 10, 1671–1677 (2008).

Wang, M., J. B. Freund and S. K. Lele, "Computational prediction of flow-generated sound", Annu. Rev. Fluid Mech. **38**, 483–512 (2006).

Wang, S. and Z. Ma, "Supervisory and optimal control of building HVAC systems: a review", HVAC & R Research **14**, 3–32 (2008).

Wang, X.-J., M. F. Lambert, A. R. Simpson, J. A. Liggett and J. P. Vitkovsky, "Leak detection in pipelines using the damping of fluid transients", J. Hydraul. Eng. **128**, 7, 697–711 (2002).

Wang, X.-J., M. F. Lambert, A. R. Simpson and J. P. Vitkovsky, "Leak detection in pipeline systems and networks: A review", pp. 1–10 (The Institution of Engineers, Austtalia, 2001), conference on Hydraulics in Civil Engineering, Hobart, 28–30 November 2001.

Wang, Z. J., K. Fidkowski, R. Abgrall, F. Bassi, D. Caraeni, A. Cary, H. Deconinck, R. Hartmann, K. Hillewaert, H. Huynh, N. Kroll, G. May, P.-O. Persson, B. van Leer and M. Visbal, "High-order CFD methods: Current status and perspective", Int. J. Numer. Meth. Fluids pp. 1–42, dOI: 10.1002/fld (2012).

Wetter, M. and C. Haugstetter, "Modelica versus TRNSYS - a comparison between an equation-based and procedural modeling language for building energy simulation", In: Proceedings of the simbuild, 2nd national conference of ibpsa-usa, cambridge, MA (2006).

Whittle, A. J., M. Allen, A. Preis and M. Iqbal, "Sensor networks for monitoring and control of water distribution systems", (2013), in 6th Int. Conf. on Struct. Health Monitoring of Intelligent Infrastructure, Hong Kong, December 2013.

Wichowski, R., "Hydraulic transients analysis in pipe networks by the method of characteristics (MOC)", Arch. Hydro-Eng. and Env. Mech. **53**, 3, 267–291 (2006).

Winkler, J., J. Munk and J. Woods, "Effect of occupant behavior and air-conditioner controls on humidity in typical and high-efficiency homes", Energy and Buildings **165**, 364–378 (2018).

Wylie, E. B. and V. L. Streeter, *Fluid Transients* (FEB Press, Ann Arbor, Michigan, 1983).

Xia, Q.-J., W.-H. Huang and C.-X. Xu, "Direct numerical simulation of turbulent boundary layer over compliant wall", J. Fluid Struct. **71**, 126–142 (2017).

Xu, S., D. Rempfer and J. Lumley, "Turbulence over a compliant surface: numerical simulation and analysis", J. Fluid Mech. **478**, 11–34 (2003).

Xu, Y. and Y. T. Peet, "Accuracy and performance of fluid-structure interaction algorithms with explicit versus implicit formulations of the fluid solver", AIAA Paper 2017–3449, in 23rd AIAA Computational Fluid Dynamics Conference, AIAA Aviation Forum and Exposition, Denver, CO, June 2017 (2017).

Xu, Y. and Y. T. Peet, "Verification and convergence study of a spectral-element numerical methodology for fluid-structure interaction", J. Comput. Phys.: X **10**, 100084 (2021a).

Xu, Y. and Y. T. Peet, "Verification and convergence study of a spectral-element numerical methodology for fluid-structure interaction", J. Comput. Phys.: X **10**, 100084 (2021b).

Yu, Y., H. Baek, M. L. Bittencourt and G. E. Karniadakis, "Mixed spectral/hp element formulation for nonlinear elasticity", Comput. Methods Appl. Mech. Engrg. **213–216**, 42–57 (2012).

Yu, Y., H. Baek and G. E. Karniadakis, "Generalized fictitious methods for fluid-structure interactions: Analysis and simulations", J. Comput. Phys. **245**, 317–346 (2013).

Zhai, Z., Q. Chen, P. Haves and J. H. Klems, "On approaches to couple energy simulation and computational fuid dynamics programs", Building and Environment **37**, 857–864 (2002).

Zhai, Z. J. and Q. Y. Chen, "Performance of coupled building energy and CFD simulations", Energy and Buildings **37**, 333–344 (2005).

Zhang, T. and Q. Y. Chen, "Novel air distribution systems for commercial aircraft cabins", Building and Environment **42**, 1675–1684 (2007).

Zhu, X. and J. Kim, "Application of analytic wavelet transform to analysis of highly impulsive noises", J. Sound Vibration **294**, 841–855 (2006).

Zielke, W., "Frequency-Dependent Friction in Transient Pipe Flow", Journal of Basic Engineering **90**, 1, 109–115 (1968).

Zuo, W. and Q. Chen, "Real-time or faster-than-real-time simulation of airflow in buildings", Indoor Air **19**, 1, 33 (2009).

Zuo, W., M. Jin and Q. Chen, "Reduction of numerical diffusion in ffd model", Engineering Applications of Computational Fluid Mechanics **6**, 2, 234–247 (2012).

Zuo, W., M. Wetter, D. Li, M. Jin, W. Tian and Q. Chen, "Coupled simulation of indoor environment, hvac and control system by using Fast Fluid Dynamics and the Modelica *Buildings* library", in "Proceedings of ASHRAE/IBPSA-USA Building Simulation Conference, Atlanta, GA, USA", pp. 56–63 (2014).

Zuo, W., M. Wetter, W. Tian, D. Li, M. Jin and Q. Chen, "Coupling indoor airflow, HVAC, control and building envelope heat transfer in the Modelica *Buildings* library", Journal of Building Performance Simulation **9**, 4, 366–381 (2016).